

# Carnegie Mellon University

## CARNEGIE INSTITUTE OF TECHNOLOGY

### THESIS

SUBMITTED IN PARTIAL FULFILLMENT OF THE REQUIREMENTS

FOR THE DEGREE OF Doctor of Philosophy

TITLE Quantification of Microstructural Evolution Using Moment Invariants

---

PRESENTED BY Lily T. Nguyen

ACCEPTED BY THE DEPARTMENT OF

Materials Science and Engineering

Marc De Graef 05/01/15  
ADVISOR, MAJOR PROFESSOR DATE

Gregory S. Rohrer 05/01/15  
DEPARTMENT HEAD DATE

APPROVED BY THE COLLEGE COUNCIL

Vijayakumar Bhagavatula 06/05/15  
DEAN DATE

**Quantification of microstructural evolution using moment  
invariants**

Submitted in partial fulfillment of the requirements for

the degree of

Doctor of Philosophy

in

Materials Science and Engineering

Lily T. Nguyen

B.S., Metallurgical and Materials Engineering, Colorado School of Mines

M.S., Materials Science and Engineering, Carnegie Mellon University

Carnegie Mellon University  
Pittsburgh, PA

May 2015

*To my family, especially my father.*

*(...and LinhVy and Layton)*

---

## Abstract

The foundation of materials science is that certain aspects of a material's microstructure influence its properties; however, many of these relationships have not yet been established. For example, grain size affects the strength of a material. Instead, a qualitative approach is usually taken to connect microstructure with property or performance, although some quantitative methods have been used such as precipitate size and aspect ratio. The missing link is the quantification of the morphology of certain microstructural features. Although quantitative descriptions of microstructural features have not yet been fully developed, moment invariants (MIs) and other shape descriptors have previously proven to accurately quantify the shapes of secondary gamma-prime precipitates in Ni-based superalloy system. In this thesis, 2D and 3D MIs are used to quantitatively track how different external conditions affect microstructural evolution in several materials systems. This thesis also explores how the MI approach compares to other shape parameters. Three materials systems are considered: the effect of point defect concentration in ferroelastic materials, the onset of rafting in Ni-based superalloys, the effect of an external stress on gamma-prime precipitates in Ni-based superalloys, and annealing of polycrystalline strontium titanate. MIs are computed for each of these materials systems to observe microstructural evolution and were found to adequately describe the changes in these systems. MIs and several other shape descriptors were able to classify whether a microstructure was non-rafted or rafted and to detect the onset of rafting, while the other shape descriptors were unable to be set a criterion. In doped ferroelastic systems, MIs and image entropy are able to distinguish the martensitic transition, the strain glass transition and different strain states: austenite, martensite, premartensitic tweed, and the strain glass state. MIs were also used to distinguish the evolution of the 3D shapes of polycrystalline strontium titanate grains and its Euclidean distance from a cubic shape. It was found that MIs are easily implemented in both 2D and 3D microstructures, as long as the features of interest can be properly segmented. MIs are a powerful tool that can be used in many applications of materials science and engineering.

## ACKNOWLEDGEMENTS

I would first like to thank my funding resources for supporting my research: the Dean's Fellowship at Carnegie Mellon University, the Air Force Office of Science Research under AFOSR Grant No. FA9550-12-1-0475, and UC Santa Barbara for the ICMR Fellowship.

I would especially like to acknowledge my advisor, Marc De Graef for his direction and support during my PhD. I have learned so much about mathematics, microscopy, microstructures, and materials science because of you. I would also like to thank the members of my committee for their helpful suggestions, discussions and insight: Professor Elizabeth Holm, Professor Anthony Rollett, and Dr. Jeff Simmons. I would like to thank my collaborators: from the Ohio State University – Yunzhi Wang, Rongpei Shi, and Dong Wang; from Karlsruhe Institute of Technology – Peter Gumbsch, Melanie Syha, and Andreas Trenkle. Thank you for helping me understand microstructures better and for doing such good work that allowed to me explore how microstructures can be analyzed. I would also like to thank all the staff over the years—from Wean Hall: Jeanna Pekarck, Suzy Smith, Neetha Khan, Val Thompson, Anita Connelly, Angie Pusateri, Bill Pingitore, and to the Roberts Hall people despite the construction: Marygrace Antkowski, Tom Nuhfer, Jason Wolf, Adam Wise. I would like to thank all of my professors over the years as well. From the Colorado School of Mines: Kip Findley, for being my undergraduate advisor and mentor – I am truly thankful for everything you have done for me over my career and instilling an eternal love for metallurgy. To Michael Kaufman, for still remembering me after all this time. From Carnegie Mellon University, I would like to thank Jay Whitacre for mentoring me on public policy and helping me on GSAC. Thank you for your insightful classes and discussions: Warren Garrison, David Laughlin, Henry Piehler, Chris Pistorius, and Greg Rohrer.

---

I would like to thank the members of my group: Patrick Callahan, Emma Humphrey, Shan Hua, Han Leng, Mike Chapman, Prabhat KC, Amy Wang, Saransh, Ryan Harrison, and Isha Kashyap. Your support, words, and laughs have made me a better person. I would like to thank Christine Rooney for her patience in working with me during my last semester. To my students that I have TA'ed over the years; thank you for sharing your love of learning with me and allowing me to attempt to share my knowledge. To my other cohorts: there are too many to name you all, but know that I appreciate each and every one of you. I would especially like to thank Aditya Balasubramanian (AB), Brian DeCost, Vincent DeGeorge, Jillian Epstein, Rachel Ferebee, Chetali Gupta, Brian Lin, Clare Mahoney, Carolyn Norwood, Ellen Reifler, and Miaolei Yan – without your help in classes, research, coffee shops, and writing, I would not be here. We have all helped each other along the way, and it would not have been the same without you. I love you all equally, but alphabetical order causes you to be placed as such, so you can blame it on your family name. I would especially like to thank AB and Clare for helping me through the thesis writing/preparation process and keeping me company, listening to me complain, and giving me advice on how to be a doctor.

I would also like to acknowledge my friends that I have made through ultimate, so thank you for being my throwing buddy over the years and keeping me somewhat in shape. Thank you to Lauren Miller and Svetlana Romanova for living with me and putting up with my crazy hours. Thank you to the friends I made through the Graduate Student Assembly. I would also like to thank my family for all of their support over the years. To the Pittsburgh coffee shops, thank you for supplying the space and caffeine I needed to get through the writing process.

Last, but not least, I would like to thank Frank Perry for his love, patience, support, and kindness. You are without a doubt the person that I am most grateful for, and I will always be thankful for you most of all.

*Lily T. Nguyen*  
*Pittsburgh, PA*

# TABLE OF CONTENTS

Abstract . . . . .	ii
Acknowledgements . . . . .	ii
List of Tables . . . . .	vii
List of Figures . . . . .	viii
List of Symbols . . . . .	xiv
<b>I. Introduction</b> . . . . .	1
1.1 Introduction and motivation . . . . .	1
1.2 Background . . . . .	4
1.2.1 Acquisition of microstructures . . . . .	5
1.2.2 Stereological parameters . . . . .	8
1.2.3 Outlook . . . . .	10
1.3 Hypothesis . . . . .	12
1.4 Document Organization . . . . .	13
<b>II. Theory</b> . . . . .	14
2.1 Moment invariants . . . . .	14
2.1.1 Background . . . . .	14
2.1.2 Computation of moments . . . . .	17
2.1.3 2D moment invariants . . . . .	19
2.1.4 3D moment invariants . . . . .	24
2.1.5 Applications of moment invariants in materials science . .	27
2.1.6 Moment invariants for enabling materials design applications	30
2.1.7 Applications of moment invariants in other fields . . . . .	33
2.2 Other shape descriptors in materials science and engineering . . . .	35
2.2.1 Basic shape parameters . . . . .	36
2.2.2 Shape parameters $\xi$ , $S_{ster}$ , and $\Sigma$ . . . . .	37
2.2.3 Shape quotient . . . . .	38
2.2.4 Minkowski functionals . . . . .	39
2.2.5 Interface shape distribution . . . . .	41
2.2.6 Superellipsoid . . . . .	41
2.3 Comparison metrics . . . . .	46
2.3.1 Euclidean distance . . . . .	47
2.3.2 The Hellinger distance . . . . .	48
2.3.3 The chi-squared distance . . . . .	49

2.4	Summary . . . . .	50
<b>III.</b>	<b>The effect of rafting in Ni-based superalloys . . . . .</b>	<b>51</b>
3.1	Introduction . . . . .	51
3.2	Theoretical and modeling approach . . . . .	53
3.2.1	Phase field model . . . . .	53
3.2.2	3D microstructural image analysis . . . . .	55
3.2.3	2D microstructural image analysis . . . . .	55
3.3	Results . . . . .	57
3.3.1	3D results . . . . .	57
3.3.2	2D results . . . . .	62
3.4	Comparison to other shape descriptors . . . . .	69
3.5	Inversion of the matrix . . . . .	73
3.6	Discussion . . . . .	74
3.7	Conclusions . . . . .	78
<b>IV.</b>	<b>The effect of stress on gamma-prime precipitates in Ni-based superalloys . . . . .</b>	<b>90</b>
4.1	Introduction . . . . .	90
4.2	Materials and methods . . . . .	93
4.3	Results and discussion . . . . .	95
4.4	Conclusions . . . . .	105
<b>V.</b>	<b>The effect of doping on transitions in ferroelastic materials . . . . .</b>	<b>107</b>
5.1	Introduction . . . . .	107
5.2	Theoretical and modeling approach . . . . .	109
5.2.1	Phase field model for strain glass material . . . . .	109
5.2.2	Microstructure image analysis . . . . .	111
5.3	Results and discussion . . . . .	111
5.3.1	Moment invariant analysis . . . . .	111
5.3.2	Image entropy analysis . . . . .	115
5.4	Comparison of MI approach to qualitative analysis . . . . .	119
5.5	Conclusions . . . . .	119
<b>VI.</b>	<b>Grain growth in strontium titanate . . . . .</b>	<b>122</b>
6.1	Introduction . . . . .	122
6.2	Materials and methods . . . . .	123
6.3	Results and discussion . . . . .	125
6.4	Comparison of MI approach to other shape descriptors . . . . .	130
6.5	Conclusions . . . . .	131
<b>VII.</b>	<b>Conclusions . . . . .</b>	<b>133</b>
7.1	Summary . . . . .	133
7.2	Conclusions . . . . .	137
7.3	Future work . . . . .	138
<b>A.</b>	<b>Sensitivity of superellipsoid exponent, <math>n</math> . . . . .</b>	<b>140</b>
	<b>Bibliography . . . . .</b>	<b>177</b>

## LIST OF TABLES

2.1	Shape descriptors for a few isotropic shapes [1]. . . . .	40
3.1	The average number of precipitates per image. The number of precipitates in an image decreases over time. . . . .	57
3.2	Average moment invariants for sorted precipitates by size. . . . .	63
3.3	List of shape descriptors frequently used in materials science analysis [2]. . . . .	69
3.4	Shape descriptor and trend . . . . .	71
4.1	Stresses at which TEM samples were considered. . . . .	93
4.2	The average values of the area, radius, aspect ratio, $\bar{\omega}_2$ , and $\langle \bar{\omega}_i \rangle$ . . . . .	100
5.1	Defect Concentration and Temperature (K) for five different simulation sets. . . . .	112
A.1	Comparison of density maps for various 3D shapes with 5000 2D sections using the Hellinger distance and the chi-squared distance. . . . .	145
A.2	Comparison of density maps to the other shapes in the library. . . . .	146
A.3	Comparison of MIs of cuboid with $n = 4$ to MIs of cuboids from 4.05 to 10 using the Euclidean distance and the chi-squared distance. . . . .	147
A.4	Comparison of MIs of cuboid with $n = 4.5$ to MIs of cuboids from 4.55 to 10 using the Euclidean distance and the chi-squared distance. . . . .	152
A.5	Comparison of MIs of cuboid with $n = 5$ to MIs of cuboids from 5.05 to 10 using the Euclidean distance and the chi-squared distance. . . . .	157
A.6	Comparison of MIs of cuboid with $n = 5.5$ to MIs of cuboids from 5.55 to 10 using the Euclidean distance and the chi-squared distance. . . . .	162
A.7	Comparison of MIs of cuboid with $n = 6$ to MIs of cuboids from 6.05 to 10 using the Euclidean distance and the chi-squared distance. . . . .	166
A.8	Comparison of MIs of cuboid with $n = 6.5$ to MIs of cuboids from 6.55 to 10 using the Euclidean distance and the chi-squared distance. . . . .	170
A.9	Comparison of MIs of cuboid with $n = 7$ to MIs of cuboids from 7.05 to 10 using the Euclidean distance and the chi-squared distance. . . . .	173

## LIST OF FIGURES

1.1	The materials science paradigm, which consists of microstructure, property, processing, and performance. The four tenets are connected to each other and strongly interact with each other on many levels [3]. . . . .	2
2.1	(a) An illustration of the 2D moment invariant space. The second order moment invariant map (SOMIM). Within the region to the left of the parabola, all 2D shapes can be described using moment invariants. Some important shapes are noted on the map. (b) The projected moment invariant map of second and fourth order (PMIM). The curves for ellipses, rectangles, and isosceles triangles are superimposed. <i>Figure adapted with permission from Ref. [4]. Copyrighted by Elsevier.</i> . . . . .	22
2.2	The 3D moment invariant space. The black line is the isotropic shape curve, while the blue lines represent the projections onto the 2D planes. <i>Figure adapted with permission from Ref. [5]. Copyrighted by IOP Science.</i> . . . .	26
2.3	Illustration of the shape parameter $\eta$ . $\eta$ varies from 0 for a circle to 1 for a square. <i>Figure adapted with permission from Ref. [4]. Copyrighted by Elsevier.</i> . . . . .	29
2.4	A schematic that shows the sampling for one-, two-, and three-point correlation functions. A one-point correlation function is shown by a point, a two-point correlation function is shown by a line, and a three-point correlation function is shown by a triangle. Adapted from [6]. . . . .	31
2.5	Schematic illustrating how $\xi$ is measured. The values of $a$ and $d$ for individual particles are $(a_1 + a_2)/2$ and $(d_1 + d_2)/2$ , respectively. <i>Figure adapted with permission from Ref. [7]. Copyrighted by the American Physical Society.</i> . . . . .	38
2.6	The relationships between the 2D affine moment invariant $\bar{\omega}_2$ with $\Sigma$ and $\eta$ . (a) $\bar{\omega}_2$ vs. $\eta$ . (b) $\Sigma$ vs. $\eta$ . (c) $\Sigma$ vs. $\bar{\omega}_2$ . . . . .	39
2.7	2D sections of superellipsoid shapes with varying $n$ exponents. From left to right: (top) 1, 2, 3, 4 (bottom) 5, 7, 15, 50. . . . .	42
2.8	The relationship between the 3D affine moment invariant $\bar{\Omega}_3$ vs. the superellipsoid exponent $n$ . As $n$ increases, the shape becomes closer to a cube. <i>Figure adapted with permission from Ref. [1]. Copyrighted by Elsevier.</i> . . . . .	43
2.9	The SOMIM and PMIM for 5000 random 2D cross-sections through the (a) sphere and (b) the cube. . . . .	44
2.10	2D sections through (100) of cuboids with superellipsoid exponent $n$ between 4.0 and 9.5, in increments of 0.5. . . . .	45

3.1	The starting microstructure for microstructures with a negative and a positive misfit. . . . .	53
3.2	(a) The SOMIM and (b) the PMIM for the starting microstructure for microstructures with a negative and a positive misfit. . . . .	54
3.3	3D representation of the microstructures resulting from the simulation at the ten time steps. The dark regions represent the $\gamma$ matrix while the gray regions represent the $\gamma'$ phase. (a) Microstructures with a negative misfit showing $\gamma'$ plates (b) microstructures with a positive misfit showing $\gamma'$ rods. <i>Figure adapted with permission from Ref. [8]. Copyrighted by Taylor &amp; Francis.</i> . . . . .	56
3.4	Evolution of 3D second-order moment invariants over time, where blue marks the initial time step and the black is the last time step. By computing the MIs within a circular region, the MIs increase with time. (a) negative misfit (b) positive misfit. . . . .	58
3.5	Average of 3D second-order moment invariants over time. (a) average 2nd order 3D MIs, (b) average $\bar{\Omega}_1$ , (c) $\bar{\Omega}_2$ , and (d) $\bar{\Omega}_3$ . . . . .	59
3.6	Moment invariants for the microstructure with a negative misfit using a scan size of $a = 33$ . There is a deviation from the isotropic shape curve that increases with time. . . . .	60
3.7	Moment invariants for the microstructure with a positive misfit using a scan size of $a = 33$ . There is a small deviation from the isotropic shape curve that increases with time. . . . .	61
3.8	The percentage of boxes with $\delta < 0.005$ . If the percentage of boxes is greater than 20%, the microstructure is classified as rafted. Microstructures with a negative misfit were rafted at time step 5 and above, and microstructures with a positive misfit were rafted at time step 6 and above. . . . .	62
3.9	SOMIM and PMIM for precipitates sorted by size. Small precipitates are shown in brown and have high $\bar{\omega}_2$ values. Medium sized precipitates are shown in green and show a range in MI values. Large precipitates are shown in blue and have low MI values. . . . .	63
3.10	Density maps for the microstructure with a negative misfit for the ten time steps (a) SOMIM (b) PMIM. 256 images per time step were analyzed. The region of interest used to determine rafted is shown in the red boxes in the first map of (a) and (b). The peak of the MI distributions shift from the upper right corner to the lower left corner as the $\gamma'$ precipitates directionally coarsen. . . . .	66
3.11	Density maps for the microstructure with a positive misfit for the ten time steps (a) SOMIM (b) PMIM. 256 images per time step were analyzed. The peak of the PMIM shifts from the upper right corner to the lower left corner as the $\gamma'$ precipitates directionally coarsen, as observed in the microstructure with a negative misfit. However, the peak of the SOMIM does not change over time; the biggest change is in the broadening of the MI with decreasing $\bar{\omega}_1$ . . . . .	67

3.12	(a) Fraction of $\gamma'$ precipitates in the SOMIM where $0 \leq \bar{\omega}_1 \leq 0.5$ . (b) Fraction of $\gamma'$ precipitates in the PMIM where $0 \leq \langle \bar{\tau}_i \rangle \leq 0.5$ . The onset of rafting is defined as when at least half of the precipitates are in the selected MI interval. For the microstructure with a negative misfit, this occurred in the SOMIM at time step 3 and in the PMIM at time step 2. For the microstructure with a positive misfit, this occurred at time step 3. . . . .	68
3.13	Images used for analysis using all shape descriptors. . . . .	69
3.14	Various shape descriptors and their evolution over time applied to 2D images. The shape descriptors in green represent descriptors that have identified a rafted microstructure at time step 5 and above, while blue represents shape descriptors with a linear or no relationship, indicating no abrupt change in the system. (a) precipitate count (b) average size, minor axis (c) aspect ratio, perimeter (d) chord length (e) circularity, equivalent ellipse (f) Ferets diameter, major axis (g) solidity (h) averaged MIs (i) fraction of MI distribution in ROI. . . . .	70
3.15	Moment invariant density maps and their evolution over time for one image per time step. (a) SOMIM (b) PMIM. . . . .	72
3.16	Average 2D moment invariants and their evolution over time for one image per time step. (a) average second-order MIs (b) average fourth-order MIs. . . . .	72
3.17	Schematics of where the shapes of the precipitates shift from their cuboidal shape to the rafted shape in (a) SOMIM (b) PMIM. The cuboidal $\gamma'$ precipitates begin the upper right corner and the rafted $\gamma'$ precipitates are in the lower left corner of both maps. . . . .	77
3.18	(a) The SOMIMs and (b) the PMIMs for cross-sections normal to the x-direction in the microstructure with a negative misfit. In these maps, the MIs are computed for the areas of the matrix instead of the $\gamma'$ precipitates. 25 images were analyzed using moment invariants. . . . .	80
3.19	(a) The SOMIMs and (b) the PMIMs for cross-sections normal to the y-direction in the microstructure with a negative misfit. In these maps, the MIs are computed for the areas of the matrix instead of the $\gamma'$ precipitates. 25 images were analyzed using moment invariants. . . . .	81
3.20	(a) The SOMIMs and (b) the PMIMs for cross-sections normal to the z-direction in the microstructure with a negative misfit. In these maps, the MIs are computed for the areas of the matrix instead of the $\gamma'$ precipitates. 25 images were analyzed using moment invariants. . . . .	82
3.21	(a) The SOMIMs and (b) the PMIMs for cross-sections normal to the x-direction in the microstructure with a positive misfit. In these maps, the MIs are computed for the areas of the matrix instead of the $\gamma'$ precipitates. 25 images were analyzed using moment invariants. . . . .	83
3.22	(a) The SOMIMs and (b) the PMIMs for cross-sections normal to the y-direction in the microstructure with a positive misfit. In these maps, the MIs are computed for the areas of the matrix instead of the $\gamma'$ precipitates. 25 images were analyzed using moment invariants. . . . .	84
3.23	(a) The SOMIMs and (b) the PMIMs for cross-sections normal to the z-direction in the microstructure with a positive misfit. In these maps, the MIs are computed for the areas of the matrix instead of the $\gamma'$ precipitates. 25 images were analyzed using moment invariants. . . . .	85

3.24	SOMIMs for cross-sections normal to the x-direction. 256 images were analyzed using moment invariants. . . . .	86
3.25	PMIMs for cross-sections normal to the x-direction. 256 images were analyzed using moment invariants. . . . .	86
3.26	SOMIMs for cross-sections normal to the z-direction. 256 images were analyzed using moment invariants. . . . .	87
3.27	PMIMs for cross-sections normal to the z-direction. 256 images were analyzed using moment invariants. . . . .	87
3.28	SOMIMs for cross-sections normal to the x-direction. 256 images were analyzed using moment invariants. . . . .	88
3.29	PMIMs for cross-sections normal to the x-direction. 256 images were analyzed using moment invariants. . . . .	88
3.30	SOMIMs for cross-sections normal to the z-direction. 256 images were analyzed using moment invariants. . . . .	89
3.31	PMIMs for cross-sections normal to the z-direction. 256 images were analyzed using moment invariants. . . . .	89
4.1	Dark field TEM images of the $\gamma/\gamma'$ microstructure in the DT specimens aged for 120 hours at 640°C. The number below corresponds to the applied stress in MPa. <i>Reprinted with permission from [9]. Copyrighted by Elsevier.</i>	94
4.2	Dark field TEM images of the $\gamma/\gamma'$ microstructure in the RC specimens aged for 120 hours at 640°C. The number below corresponds to the applied stress in MPa. <i>Figure adapted with permission from [9]. Copyrighted by Elsevier.</i> . . . . .	95
4.3	Histograms of the areas of the precipitates in the DT specimens for different stresses (a) 0 MPa, (b) 33 MPa, (c) 53 MPa, and (d) 127 MPa. The average areas are: 122.9, 83.7, 131.6, and 80, respectively, for each of the stresses. .	96
4.4	Histograms of the radii of the precipitates in the DT specimens for different stresses (a) 0 MPa, (b) 33 MPa, (c) 53 MPa, and (d) 127 MPa. The average radius are: 24.77, 20.19, 25.44, and 19.78, respectively, for each of the stresses.	97
4.5	Histograms of the equivalent ellipse aspect ratio $\tau$ for different stresses (a) 0 MPa, (b) 33 MPa, (c) 53 MPa, and (d) 127 MPa. The median aspect ratios are: 1.87, 1.658, 1.646, 1.631, respectively, for each of the stresses. .	98
4.6	Moment invariants vs. stress (a) $\langle \bar{\omega}_i \rangle$ (b) $\langle \bar{\tau}_i \rangle$ , indicating that the average MI values do not change with increasing stress in a DT specimen. . . . .	99
4.7	The SOMIMs and PMIMs for the samples in the DT specimen (a) 0 MPa, (b) 33 MPa, (c) 53 MPa, and (d) 127 MPa. The peak of the distributions for each stress level is between a cube and a circle shape, indicating that the majority of the precipitates have a cuboidal shape with an aspect ratio close to 1. . . . .	100
4.8	Histograms of the $\langle \bar{\omega}_2 \rangle$ at different stresses for different stresses (a) 0 MPa, (b) 33 MPa, (c) 53 MPa, and (d) 127 MPa. The average $\langle \bar{\omega}_2 \rangle$ are: 0.885, 0.884, 0.881, and 0.888, respectively, for each of the stresses. . . . .	101
4.9	$\bar{\omega}_2$ vs. radius, colored by aspect ratio size (a) 0 MPa, (b) 33 MPa, (c) 53 MPa, and (d) 127 MPa. The aspect ratio is colored as: 1 - 1.2: blue, 1.2 - 1.5: forest green, 1.5 - 2: red, greater than 2: black. . . . .	102

4.10	Histograms of the $n$ values at different stresses for different stresses (a) 0 MPa, (b) 33 MPa, (c) 53 MPa, and (d) 127 MPa. The average $n$ are: 9.12, 8.77, 8.54, 8.98, respectively, for each of the stresses. . . . .	103
4.11	Histograms of the Euclidean distance at different stresses for different stresses (a) 0 MPa, (b) 33 MPa, (c) 53 MPa, and (d) 127 MPa. The average $d_{Euc}$ are: 0.437, 0.384, 0.397, 0.376, respectively, for each of the stresses. . . . .	104
4.12	Distance metric vs. stress using chi-squared and Hellinger distances for the SOMIM's and the PMIM's. . . . .	105
5.1	Microstructures resulting from the simulation with various defect concentrations. The temperature decreases from top to bottom. . . . .	113
5.2	The SOMIM and PMIM density maps of the system with a defect concentration of $c = 0$ , with decreasing temperature. A transformation from the parent phase (T=322) to martensite (T=319.2, 274.4, 263.2) with no intermediate states is shown. . . . .	114
5.3	The SOMIM and PMIM density maps of the system with a defect concentration of $c = 0.025$ , with decreasing temperature (in K). This shows a transformation from the parent phase (T=324.8 K) to the premartensitic tweed (T=322, 319.2K) to martensite (T=224 K). . . . .	115
5.4	SOMIM and PMIM density maps for the system with a defect concentration of $c = 0.15$ , with decreasing temperature. This shows a strain glass transition instead of the martensitic transformation, evolving from the parent phase (T=313.6 K) to the frozen strain glass state (T=308K, 288.4, 263.2, 224 K) . . . . .	116
5.5	Image entropy vs. temperature for varying defect concentrations. Note the shift towards the left, from a strongly peaked curve to a decreasing, nearly linear relationship for systems above the critical defect concentration. . . . .	117
5.6	Entropy vs. defect concentration for different simulation temperatures. At intermediate temperatures, the entropy decreases as the defect concentration increases. At the final temperature (224K), the entropy increases with increasing defect concentration until it reaches its maximum at about $c = 0.1$ . . . . .	118
6.1	Three-dimensional representations of the datasets (a) in its initial state and (b) in its annealed state. The grains are colored by crystallographic orientation. . . . .	124
6.2	Two-dimensional cross-sections of the datasets (a) in its initial state and (b) in its annealed state. The grains are colored randomly to distinguish between grain shapes. The black portions are pores. . . . .	125
6.3	(a) Shape quotient vs. volume. (b) Histogram of shape quotient. The blue indicates grains in the initial state and the red indicates grains in the annealed state. It is clearly evident that the shape quotient of the grains increases after annealing. . . . .	126
6.4	Selected grains in their initial and annealed states. . . . .	127
6.5	Shape quotient vs. relative volume change in the (a) initial state (b) annealed state. . . . .	128

---

6.6	Various depictions of using Euclidean distance to measure how far the grains are from a cubic shape. (a) Histogram of the distance from the MIs for a cube. (b) Histogram of the distance from $\bar{\Omega}_3$ for a cube. (c) Change in the the distance from the MIs for a cube, showing that overall, the grains are becoming closer to the cubic shape. (d) change in the distance from $\bar{\Omega}_3$ for a cube. . . . .	129
6.7	(a) Relative volume change. (b) Change in the distance from the MIs for a cube vs. relative volume change. Most of the largest grains have a shape that is closer to the cube shape after annealing compared to its initial state.	130
6.8	Distributions of sphericity values for both annealing states as histograms. .	131
A.1	Density maps for cuboids with $n =$ (a) 5.4, (b) 5.5, (c) 5.6. . . . .	142
A.2	Density maps for cuboids with $n =$ (a) 5.8, (b) 6.0, (c) 6.1. . . . .	143
A.3	Density maps for cuboids with $n =$ (a) 6.15, (b) 6.2, (c) 6.4. . . . .	144

## LIST OF SYMBOLS

MIs	moment invariants
$\bar{\omega}_1$	the similarity 2D second-order moment invariant
$\bar{\omega}_2$	the affine 2D second-order moment invariant
$\bar{\tau}_1$	the similarity 2D fourth-order moment invariant
$\bar{\tau}_2$	an affine 2D fourth-order moment invariant
$\bar{\tau}_3$	an affine 2D fourth-order moment invariant
$\langle \bar{\omega}_i \rangle$	the averaged 2D second-order moment invariant
$\langle \bar{\tau}_i \rangle$	the averaged 2D fourth-order moment invariant
$\bar{\Omega}_1$	a similarity 3D second-order moment invariant
$\bar{\Omega}_2$	a similarity 3D second-order moment invariant
$\bar{\Omega}_3$	the affine 3D second-order moment invariant
$\tau$	the aspect ratio derived from MIs
$A$	aspect ratio calculated as the ratio of major to minor axes
$\Sigma$	a shape parameter used to analyze $\gamma'$ precipitates
SOMIM	second order moment invariant map
PMIM	projected moment invariant map
$d_{Euc}$	Euclidean distance
$d_{CSD}$	chi-squared distance
$\gamma$	the matrix FCC phase in Ni-based superalloys
$\gamma'$	the precipitate phase in Ni-based superalloys
STO	strontium titanate (SrTiO <sub>3</sub> )

## CHAPTER I

### Introduction

#### 1.1 Introduction and motivation

In recent years, our understanding of microstructure-property relationships has seen major advances, in part due to the increased integration of experimental and computational techniques. Our understanding of materials depends on the materials science and engineering paradigm shown in Figure 1.1, consisting of structure, processing, properties, and performance. Structure-property relationships are the fundamental principles that allow us to develop materials better and faster than ever before. Materials scientists are able to determine a material's microstructural parameters relatively well, such as crystallographic orientations, area and volume fractions, and the grain boundary character distribution. These parameters correlate with some of the properties of a material, e.g. the grain size affects the strength of the material. Through materials science the paradigm, we are able to develop more microstructural modeling techniques to design engineering materials with optimal properties. A key part to strengthening microstructure-property relationships is the ability to quantitatively characterize all aspects of microstructures; typically a qualitative approach is taken to link microstructure with property. In this doctoral thesis research, we address the question of how to quantitatively describe the shapes of microstructural constituents.

The field of shape analysis has been applied to materials science and has proven to be a useful tool in microstructural characterization [2]. Shape descriptors have been applied to a variety of fields, ranging from pattern recognition to biology to astronomy [10]. Microstructures consist of many different phases, microstructural features, and can be polycrystalline

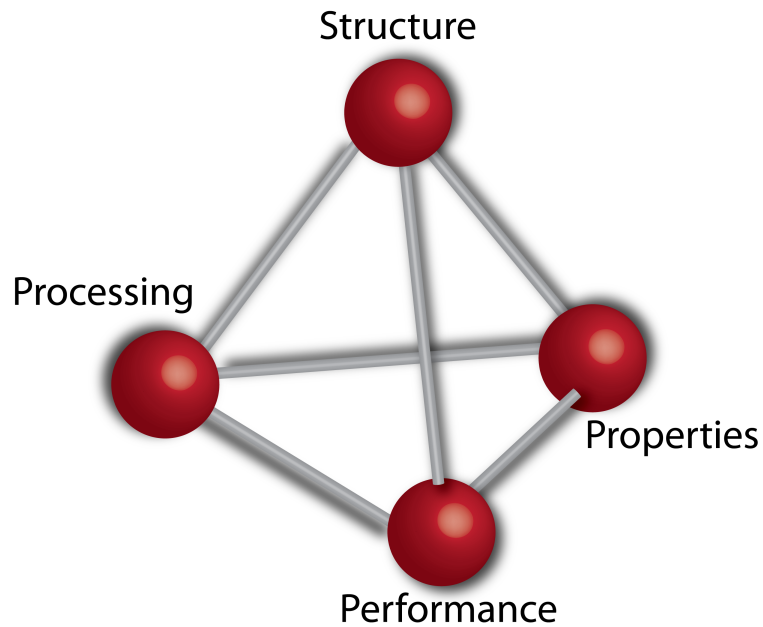


Figure 1.1: The materials science paradigm, which consists of microstructure, property, processing, and performance. The four tenets are connected to each other and strongly interact with each other on many levels [3].

in nature. They are often described in qualitative terms: more spherical, more spread out, spatially clustered. In addition, microstructures are very different from material system to system: polymers do not have a crystalline structure, while deformed metallic grains look different than sintered ceramic materials.

By applying shape descriptors to microstructures, the morphology of certain features can be quantified instead of having to rely on arbitrary and subjective classifiers. It is often the case that two microstructure micrographs are compared to each other and its qualitative differences are noted, leading to ambiguous and subjective classification. While shape and orientation information can now be obtained from the recent advances in electron microscopy, many models do not include any assumptions about shape due to the lack of quantification. Quantitative shape analysis allows the ability to distinguish between microstructures and to use as inputs in models. While others have been able to accurately describe certain phenomena without this shape information and directly from 2D or 3D experimental images [11], having more information is always useful and may better describe experimental observations. Additionally, shape characterization can be used to determine 3D properties that cannot be determined only from 2D sections, to better support theories

on mechanisms for certain phenomena, and to provide a useful tool that can be used in microstructure quantification.

Recently in 2011, President Obama launched the Materials Genome Initiative for Global Competitiveness (MGI) to accelerate the discovery and development of advanced materials systems so that the United States can remain competitive in the 21st century [12]. As a part of this, the U.S. Office of Science and Technology calls for materials technology and development to double the speed of the discovery-to-deployment process of novel materials, at a significantly reduced cost [12]. On average, it takes about twenty years from discovery to distribution for a new material; this time frame is too slow for our fast-paced, constantly changing society. The development of quantitative microstructure-property relationships will undoubtedly help to achieve this goal. Simulation-based techniques help cut down on the need for expensive experimental acquisition and characterization, but this requires accurate and reliable models and algorithms to be valid. However, it is still important to conduct experiments and to be able to compare experimental with simulated results. Therefore, the ability to quantify certain morphological features in experimental microstructures is also important to support these models.

Moment invariants (MIs) have previously been applied to several experimental datasets and synthetically generated microstructures as a solution to the need for a shape descriptor that could automatically detect the microstructural features of interest [1, 4, 5, 13–16]. They are powerful shape descriptors that contain a lot of information about shape while maintaining ease of use and computation speed. The De Graef group has considered the application of moment invariants to objectively and quantitatively describe the morphology of secondary  $\gamma'$  precipitates and grain shapes in Ni-based superalloys in both 2D and 3D [13, 14]. MacSleyne and Callahan have examined both cuboidal  $\gamma'$  precipitates and more complex, dendritic  $\gamma'$  precipitates [13, 14]. Additionally, Callahan has used moment invariants to study grain shapes in experimental and simulated polycrystalline Ni-based superalloys, specifically, IN100 [14]. Although some quantitative parameters are currently used in materials science characterization, they do not provide as much information about the morphology of the microstructural features as moment invariants which offer multiples characteristics that describe shape [2, 6, 17]. Through this work, the moment invariant ap-

proach will further be applied to other Ni-based superalloy microstructures, but also to other materials systems such as ferroelastic materials and perovskite ceramics to examine its microstructural evolution.

## 1.2 Background

Microstructures have been studied for many years, where one of the first reports of metallography was done in 1863 where Henry Clifton Sorby used typical metallographic preparation steps to examine Bessemer steel to study what is considered to be the first true microstructure [18]. The techniques to study microstructures have developed over time as needs have changed; some of the most common sources to study them now include visible light, electrons, a mechanical probe, and ions to name a few [6, 19, 20]. The study of the relationship between microstructures and properties is one of the key components of materials science and engineering. Some of the most important properties of a material are [21]:

- strength: how much force can be exerted on the material
- ductility: a measure of how much the material will permanently stretch by the time fracture occurs
- toughness: indicating the material's resistance to fracture when a crack is present

By understanding its microstructure, the properties of the material can be quantified. Many structure-property relationships have already been established from two-dimensional observations. One relationship is between grain size and the strength of a material; another relationship is between a crack in the material and the time to failure of the material [21]. Other relationships have also been identified, such as relating the microstructure to different electronic or thermal properties.

Microstructural evolution – how a material's structure develops as an external condition such as heat or stress is applied – is commonly studied because the microstructure can often be manipulated by identifying which steps or conditions change the properties. An experiment can be conducted by taking four samples that had the same prior history, then to heat each sample up for different amounts of time and observe how the microstructure changes. Models can also be used to observe how the microstructure changes with time.

Many microstructure-property relationships were established using observations of microstructures in 2D. By using 3D techniques to examine the structures of materials, the true properties can be measured. 3D experimental techniques can be used with simulations in order to determine how microstructures influence physical properties such as fatigue, failure, and deformation. This decreases the time needed to understand a material and its properties, so that material can be applied sooner.

### 1.2.1 Acquisition of microstructures

The acquisition of microstructures is important to understanding the material and its properties and performance. Certain methods can be used, depending on the length scale, availability of equipment, and acquisition time. Traditional 2D microstructure imaging techniques vary depending on the length scale needed to identify the features of interest; a few common techniques include optical microscopy, electron microscopy, and atomic force microscopy. While microstructures have been imaged in two dimensions since the last 1800s, microstructures have also been studied using 3D techniques. In 1918, Forsman used serial sectioning to experimentally collect and examine a steel's microstructure [22]. By constructing a solid model made by combining 2D sections, he was one of the first scientists to obtain a 3D view of a microstructure. This was a significant achievement, as 3D microstructures were also once sketched by hand [23]. The acquisition of 3D experimental datasets has become more readily available, due to the partial or complete automation of experimental data acquisition and the advances in microscopy [1, 6]. Computers have given us the capability to acquire large amounts of data faster than ever and significantly improved the ability to visualize microstructures.

As a result of these advances, three-dimensional (3D) materials science has become its own sub-discipline of materials science and engineering. 3D materials science focuses on the acquisition of 3D data using both experimental and computational techniques to explain materials phenomena [24]. 2D techniques have been used for many years and been relatively successful in describing the properties and performance of materials. However, materials are physically three-dimensional, therefore the 2D information that has been collected in the past is limited in the extent that it can describe 3D materials although stereology has

proved to estimate some quantities reasonably well. The need for three-dimensional data has always been evident, but 3D imaging techniques have progressed only in the last fifteen years.

There are two basic types of methods to acquire 3D experimental data on the nanoscale to millimeter scale. Generally, 3D techniques require a minimum of ten sections per feature to obtain statistically important information [6]. Serial sectioning is one method and images on the macro-to-microscale. This method has been used for almost a hundred years, but has only been widely used in the last fifteen years due to the ability to automate the steps [6]. Serial sectioning experiments consist of two steps that are repeated: an imaging step and a step that removes a small, flat layer of the specimen. The 3D microstructure is then reconstructed from the 2D images.

The sectioning equipment and the 2D characterization instruments are both commonly found in many materials laboratories, so the biggest barrier in serial sectioning is the time available to perform such a repetitious experiment [6]. To acquire the best data, the microstructure is sectioned at the finest possible step size to collect high-resolution data, but these requirements are limited by many factors. The resolution of the imaging machine, the time available, and the precision of the milling machine are just a few of the considerations that must be taken into account. This technique allows for the acquisition of large datasets through sandpaper milling and optical microscopy to higher resolution datasets through ion beam milling and electron microscopy.

The largest disadvantage of this technique is that the sample is destroyed after the experiment, so multiple testing on the sample is not possible. Currently, serial sectioning can be automated by using robots or software for the computer [25]. This reduces acquisition time of the dataset and also the data variability that arises out of readjustments of instrument settings such as brightness and contrast, alignment of the sections, etc. [6]. The resolution of serial sectioning can be quite high, but this technique is also time-consuming.

On the micro-to-macroscale, mechanical serial sectioning has been established using manual polishing techniques, but also as an automated system, such as the LEROY multi-modal system at the Air Force Research Laboratory [26]. LEROY combines a robot with an automated polishing system (Robo-Met.3D) and a dual beam focused ion beam-scanning

electron microscopy (FIB-SEM) to collect experimental datasets. The FIB-SEM has the capability to take SEM images and/or electron backscatter diffraction images (EBSD) to collect both morphological and crystallographic information [6, 25, 27]. However, the FIB-SEM can take on the order of days or weeks to create a 3D dataset, so the TriBeam system was established and uses a femtosecond laser to remove material, which has removal rates that can be four to six orders of magnitude faster than the FIB-SEM technique [28]. This consists of a femtosecond laser installed into a Dual Beam FIB-SEM system, the details of which are in [28]. Currently, there is only one in existence.

X-ray tomography is another type of technique, which uses x-rays to image sections through the material nondestructively. X-ray tomography has commonly been used in medical imaging, e.g. examining tumors in the brain [29]. X-ray tomography illuminates a sample with x-rays and uses the resultant transmitted image to reveal the structure of that material on the micrometer scale [6]. The most common image contrast technique reconstructs a suite of transmission images taken at various projections [6]. Diffraction-contrast techniques use ray tracing methods or other spatial localization methods to define microstructural features [6]. However, these experiments require very high intensity x-rays that can penetrate through the material with an acceptable amount of contrast, although there are some bench-top units with low resolutions [6]. Therefore, these experiments can only feasibly be conducted at synchrotron sources. However, synchrotrons are limited in number, so the availability of this technique is also limited until it is possible to produce high intensity x-rays in an ordinary laboratory setting. Due to the non-destructive nature of this technique, x-ray tomography provides the opportunity for *in-situ* experiments so that microstructures can be collected over time or the ability to process the sample in a way *ex-situ* and to image again [30]. Another non-destructive technique that uses x-rays to image called is high energy diffraction microscopy (HEDM), which uses a near field detector and enables absorption and diffraction experiments [31, 32].

Both serial sectioning and x-ray tomography techniques have been successful in reconstructing 3D data and have also been validated by simulations. Systems are now comprised of multiple instruments that can collect images, chemical, and crystallographic information. Current dataset sizes and resolutions are reasonable, but can also always be improved so

that the 3D experimental techniques can be applied to investigate new materials.

3D datasets can also be generated by creating synthetic microstructures based on statistics from 2D cross-sections. We can start with metallography or EBSD, then use a tool such as Dream.3D, which was developed by Michael Groeber and Michael Jackson to work with digital data, in order to generate realistic synthetic microstructures [33]. Computer simulations can also be used to generate 3D datasets and model microstructural evolution; a few examples are recrystallization, grain growth, and particle coarsening [34]. Some general models can be used to build these 3D datasets: phase field modeling, Monte Carlo simulations, finite element model, fast Fourier transform, or molecular dynamics [6]. Simulations provide another way to look at 3D data without having to conduct costly and time-consuming experiments. However, not all experiments can be performed in 3D due to time constraints, so it is still useful to infer 3D information from available 2D sections. The availability of three-dimensional experimental acquisition techniques makes it possible to obtain more information related to materials science phenomena.

### 1.2.2 Stereological parameters

3D materials science allows access to important geometric information about the material and its microstructure [1]. One method to acquire 3D information without having to perform these time-consuming experiments is through stereology. Stereology is the science behind obtaining 3D information from only 2D cross-sections as described above [35, 36]. By using stereology, useful microstructural quantities can be obtained such as grain size, volume fraction, size distributions of a second phase, and crystal facets [36]. Many of these microstructural quantities are necessary in order to predict material properties such as strength, brittleness, or flexibility. True 3D data can be obtained from the various techniques described earlier. However, these methods are time consuming, so it is also useful to be able to infer 3D information from 2D sections. It is useful to start with stereology so that when 3D information is available, comparisons can be made to confirm the geometrical assumptions that arise from stereology.

In a two-phase system, the amounts of each phase may contribute to the properties of that material. In steel, martensite is a phase that has really high strength and low ductility,

while pearlite has lower strength, but greater ductility than martensite [37]. By heating and cooling the steel, the amounts of each of these phases can be controlled, and the right balance of strength and ductility can be achieved. Since many materials are a mixture of phases, the volume fraction of each phase is important to quantify because it explains the properties of the material. The microstructure of a material is first obtained in 2D using typical microscopy techniques. The area fraction of each phase can then be estimated by calculating the number of pixels in each phase, then dividing by the total number of pixels. Area fraction is the easiest way to estimate the volume fraction, a 3D property, from only 2D information [21]. For a large enough micrograph, area fraction can be a good indicator of the true volume fraction of that phase.

Another important quantity is the true grain size. Two approaches can be used to measure grain size. The first method measures the areas of the grains by basing the grain size on an assumed shape, such as a circle [36]. For a given grain of known area, the diameter of the grain can be estimated by relating  $\pi$  to the area. In the second method, a line of known length is superimposed on the micrograph, then the number of grain boundary intercepts is counted and averaged over the length of the line to estimate grain size [35]. The second approach is recommended because the mean intercept length is related to the surface area per volume [35]. This approach can also be used with a circle instead of a line, counting the number of intercepts, i.e. grain boundaries, that can be counted on the perimeter of the circle [35]. The number of intercepts is divided by the circumference of the circle to obtain the grain size.

Since a grain is three-dimensional, but micrographs are two-dimensional, the 2D micrographs cut the grain in all different directions. This causes the mean sizes to be smaller than the true sizes [36]. However, this is not equal to the grain diameter, so there will always be a spread in the apparent size [36]. The average quantity can be estimated reasonably well if there are many random sections. Thus, assumptions about the grain shape must be made when using 2D techniques. Although it would be useful to be able to measure the particle size and grain size distributions from plane sections, there are limits to the capabilities of estimated average grain size from 2D sections.

Particle sizes can also be estimated by measuring diameters, areas, or chords [36]. Areas

and diameters are types of planar sampling involving measurement of circles. Chords are random lines that cut through a circle and are convenient for use of random test lines, which is a type of linear sampling. As mentioned earlier, the observed sizes are always an underestimate of the actual sizes. Any method for estimating size distributions starts with the largest size class and, based on some assumption about the shape and distribution of the particles, reduces the volume fraction of the next smallest size class by an amount that is proportional to the fraction of the current size class. Chord lengths, which are just any line through the particle, are the most reliable method because they lead to a simple distribution of shapes [35, 36].

Since a 2D image is just a cross-section through a 3D object, depending on where the slice is taken through that feature, the information gathered from the image may be misinterpreted. When materials are examined using two-dimensional techniques, the three-dimensional information about the material is assumed from just that two-dimensional image but may reflect different information a little deeper into the material. The 2D image may not always give an accurate representation of the microstructure. While stereology can be a useful tool to acquire 3D data without using 3D techniques, there are still limitations on what can be estimated by using inference to obtain 3D information. Therefore, the observation of microstructures in three-dimensions provides more complete information about the material without the need for inference.

### 1.2.3 Outlook

Some of the challenges that scientists have discussed for the future of 3D materials science include the never-ending need for higher resolution in data collection, standards for error quantification, and the importance of data management and sharing [24]. While there has been considerable progress, 3D materials science is still a relatively new field where standards are still being developed. Additionally, materials science and engineering will always be a 3D problem, not a 2D one. Thus, 3D materials science is the key to developing accurate models and theories.

3D materials science is a newer field due to the recent advances in data acquisition techniques and computing power. Some of the software improvements include better recon-

struction techniques, automation, and visualization capabilities. Additionally, instruments have improved terms of resolution, accuracy, and imaging and have faster acquisition rates due to advances in milling techniques. Clear, efficient, and accurate representations of grains are the norm now.

While serial sectioning methods have been around for more than a century, it has only been in the last fifteen years where 3D data acquisition has been a viable option. More synchrotron sources are available for use than in the past, and many scientists are being trained in these techniques. Materials science is focused on examining different materials phenomena and being able to understand the mechanisms behind the microstructure in order to develop the best materials. The field of 3D materials science is continually progressing towards better tools to acquire 3D data in faster and cheaper ways, to develop better techniques to manage the data once it has been collected and to understand how much data needs to be collected in order to have enough information. 3D materials science is a key component to ensure the progression of the broader field of materials science and engineering.

Many assumptions that were previously made using 2D sections can now be either confirmed or rejected by the 3D information. 3D materials science can also be used to verify prior 2D knowledge. The acquisition of experimental 3D data can also help scientists develop more accurate models and to use as input parameters. This gives materials scientists more flexibility in designing materials and characterizing their properties. However, 3D materials science is both expensive and time consuming so it needs to be performed on materials that actually need to be analyzed more in-depth. Materials can always be first examined using 2D techniques since they are cheaper and more readily available. When the information gathered seems incomplete, 3D experimental techniques can be a good method to obtain more information.

By understanding the needs of the 3D materials science community, efforts can be made to overcome the current challenges. The community can work together to push 3D materials science forward and to gain a more thorough understanding of materials science and engineering. 3D materials science has already proved that it can contribute to the understanding of materials on a deeper level.

## 1.3 Hypothesis

The overall objective of this work is to use the shape information of the microstructure to help guide materials processing and design activities to achieve optimal properties. The specific goals of this project are to apply moment invariants (MIs) as shape descriptors to a variety of materials systems and to compare them to conventional quantitative tools that have been used in materials science and engineering. The materials systems include: Ni-based superalloys and the evolution of rafting, the effect of stress on a Ni-based superalloy, ferroelastic materials and the effect of defect concentration, and the effect of annealing on grain shape evolution in SrTiO<sub>3</sub>. A secondary goal is to establish an accurate methodology for the quantification of 2D and 3D shapes in both experimental and synthetic microstructures in different materials systems and to establish an accurate comparison metric between them.

The hypothesis is: *moment invariants (MIs) can be used to quantitatively track microstructural changes caused by external conditions.* These external conditions can be either related to processing conditions or operating conditions. The hypothesis will be proven with the following applications:

1. Moment invariants (MIs) can be used to detect the onset of rafting and determine the rafting completion time in Ni-based superalloys.
2. Moment invariants (MIs) can be used to determine how an applied external stress affects the two-phase microstructure in Ni-based superalloys.
3. Moment invariants (MIs) can be used to quantify the strain glass transition in ferroelastic materials.
4. Moment invariants (MIs) can be used to determine the effect of annealing in a polycrystalline strontium titanate.

For each application, the MI approach is compared to other morphological analysis techniques to determine if more information can be determined by using moment invariants than by just using the conventional techniques.

## 1.4 Document Organization

Chapter II provides the background to understand typical materials science shape analysis tools and discusses 2D and 3D moment invariants. This chapter also provides a literature review of how shapes have previously been quantified in microstructures and introduces different comparison metrics that can be used to compute the differences between microstructures. Chapters III to VI discuss various applications of moment invariants to study microstructural evolution. Chapter III examines rafting in Ni-based superalloys. Chapter IV examines the effect of stress on  $\gamma/\gamma'$  microstructures. Chapter V examines the effect of doping on transitions in ferroelastic materials. Chapter VI examines grain shape evolution in polycrystalline perovskite ceramics. Finally, the conclusions and future work are discussed in Chapter 7.

## CHAPTER II

### Theory

The automated recognition of characters and patterns independent of position, size, and spatial orientation has been a goal of many aspects of research ranging from robot vision, astronomy, remote sensing, biology and materials science [10]. To achieve the best results, methods should be sensitive to variations in shape details. Several shape descriptors provide a lot of information about a change in a certain feature, e.g. aspect ratio can capture the elongation of an object. However, there are a lack of shape descriptors that can capture multiple components of shape, such as elongation and irregularity from a circle. In this chapter, we present the use of moment invariants as shape descriptors to quantify microstructural features. Moments and moment invariants are discussed first, followed by other shape descriptors in materials science and engineering, a discussion of comparison metrics, and a brief summary.

#### 2.1 Moment invariants

##### 2.1.1 Background

Many parameters have been developed as shape descriptors, but their use in the materials field has been limited thus far. For example, in the study of  $\gamma'$  precipitates in superalloys, particle aspect ratios have been used to describe the precipitate shape [4, 7]. In others, the radii of particles have been measured, typically using manual techniques [9, 38]. Such approaches are time-consuming and prone to human error. Shape descriptors such as aspect ratio and radius do not always provide all the information that is needed to fully characterize the shape of a particular object. Additionally, they only describe one aspect of the object,

and other information cannot be derived from that aspect. Moment invariants have been chosen as the shape descriptor of choice for this work because of their discriminatory ability to classify shapes. Moments will be discussed first, followed by moment invariants.

Moments are scalar quantities used to characterize a function and capture significant features about it [10]. They have been used for hundreds of years and mathematically, act as projections of a function onto a polynomial basis [10]. For example, the Fourier transform is a projection onto a basis of harmonic functions [10]. Consider moments for a Gaussian distribution in 1D. A zeroth order moment refers to the area or mass of an image, the first to its center of gravity, the second to its variance, the third order to skewness or the asymmetry of the distribution, and the fourth order to kurtosis or the “peakedness” of the distribution. In 2D, the zeroth order moment of a shape function represents the area of the object,  $\mu_{10}$  and  $\mu_{01}$  are proportional to its center of mass, and the second order moments,  $\mu_{20}$ ,  $\mu_{02}$ , and  $\mu_{11}$ , are the moments-of-inertia. In this work, the Cartesian moments are used, which are defined in 2D as [10]:

$$m_{pq} = \iint dx dy x^p y^q D(x, y) = \iint_D dx dy x^p y^q, \quad (2.1)$$

where the order of the moment,  $n$ , is equal to the sum of the exponents  $p + q$  and  $D(x, y)$  describes the shape or indicator function, such that the function is one inside the object and zero outside of it. The central Cartesian moments in 2D are defined as:

$$\mu_{pq} = \iint_D dx dy (x - x_c)^p (y - y_c)^q, \quad (2.2)$$

where  $x_c$ ,  $y_c$  are its center-of-mass coordinates. Central Cartesian moments are invariant to translations and will be used throughout this work. In 2D, the zeroth order moment,  $\mu_{00}$  of an object is equivalent to its area. An object’s centroid can be calculated as  $\bar{x} = \mu_{10}/\mu_{00}$  and  $\bar{y} = \mu_{01}/\mu_{00}$ .

An invariant is described as a functional defined on the space of all admissible image functions  $D(x, y)$  that does not change its value under a degradation operator [10]. The degradation operator comes from the relation between the ideal image  $f(x, y)$  and the

observed image  $g(x, y)$ , given by  $g = D(f(x, y))$ , where  $D$  is the degradation operator [39]. The degradation operator,  $D$ , should not be confused with  $D(x, y)$ , which is the indicator function in Equation 2.1. The degradation operator can be decomposed into two suboperators: the radiometric or graylevel/color operator  $R$  and the geometric/spatial operator,  $G$  [10]. The geometric degradation operator is more commonly used, which is typically a transform of the spatial coordinates and is considered throughout this thesis [10].

There are different types of invariance to consider: translation, rotation, scaling, affine, projective, and elastic geometric are a few examples [10]. Most invariants deal with the geometric distortion of objects, and less work has been focused on radiometric invariants, invariants with respect to changes of the image intensity function [39]. For this work, the degradations of interest are rotation, translation, scaling (isotropic and anisotropic), and affine transforms (anisotropic scaling and skewing).

Moment invariants are combinations of moments that are invariant to certain types of transformations, unconstrained by size, position, or orientation [10]. The German mathematician David Hilbert was the first to study the theory of algebraic invariants in the 19th century [40]. Hu was the first to apply moment invariants to the field of pattern recognition, giving rise to its prominence with his work on making these expressions invariant to rotation [41]. The two types of transformations that are of importance in this work are similarity and affine. Similarity transformations include translation, isotropic scaling, and rotation. Affine transformations include shearing and anisotropic scaling, in addition to the similarity transformations.

Translation invariance is achieved by making the object's centroid coincide with the origin of the coordinate system, which results in a central moment [10]. Uniform scaling invariance is obtained with a proper scaling factor to normalize the moment. Rotational invariance, however, provides a different challenge from translation or isotropic scaling [42, 43]. In 1962, Hu derived his now-famous seven moment invariants to an in-plane rotation around the origin [41]. However, Hu's expressions are no longer used because some of the expressions provide repetitive information. Most of the work on moment invariants is focused on achieving rotation invariance.

Flusser and Suk have shown that there are 80 independent affine invariants with an

order less than or equal to twelve in 2D [10, 42, 44]. Affine moments can be derived from algebraic invariants such as those previously used in the above sections and also from graph theory, tensor algebra, direction solution of proper partial differential equations, or through derivation via image normalization [10, 39, 45]. Out of the moment invariants discussed, affine moment invariants are the most difficult to derive. Affine moments have been applied and successfully distinguished between different patterns through experiments ranging from recognition of simple symmetric patterns to children's mosaics [10]. To correctly identify a microstructural feature, regardless of its position or orientation, it is important to have shape descriptors with invariance with respect to the similarity and affine transformations [10].

### 2.1.2 Computation of moments

The computation of moments in this work is based on the algorithm by Novotni and Klein [46]. Typically, the center-of-mass of the object is not in the origin, so the non-central Cartesian moment is calculated first and then transformed to central moments using the binomial theorem [16]:

$$\bar{\mu}_{pq} = \sum_{k=0}^p (-1)^{p-k} \binom{p}{k} x_c^{p-k} \sum_{l=0}^q (-1)^{q-l} \binom{q}{l} y_c^{q-l} \mu_{kl}. \quad (2.3)$$

The center-of-mass coordinates can be computed as:

$$x_c = \frac{\mu_{10}}{\mu_{00}}; \quad y_c = \frac{\mu_{01}}{\mu_{00}}. \quad (2.4)$$

Consider the case for a one-dimensional moment: The computation of geometric moments of order  $p$  for  $0 \leq p \leq P$  can be done using matrices, where  $f$  is the function sampled at

sample points  $\{x_i\}$ ,  $0 \leq i \leq N - 1$  [46]:

$$\begin{aligned} \begin{bmatrix} M_0 \\ M_1 \\ \vdots \\ M_P \end{bmatrix} &= \begin{bmatrix} \frac{1}{2} \\ \frac{1}{3} \\ \vdots \\ \frac{1}{P+1} \end{bmatrix} \begin{bmatrix} x_0 & x_1 & \cdots & x_N \\ x_0^2 & x_1^2 & \cdots & x_N^2 \\ \vdots & \vdots & \ddots & \vdots \\ x_0^P & x_1^P & \cdots & x_N^P \end{bmatrix} \cdot \\ &\begin{bmatrix} -1 & & & & \\ 1 & -1 & & & \\ & 1 & \cdots & & \\ & & \cdots & -1 & \\ & & & & 1 \end{bmatrix} \begin{bmatrix} f_0 \\ f_1 \\ \vdots \\ f_{N-1} \end{bmatrix} \end{aligned} \quad (2.5)$$

The  $\mathbf{X}$  matrix contains the  $x_N^P$  variables and is a Van der Monde with dimensions of  $(P + 1) \times (N + 1)$ , the matrix  $\mathbf{D}$  contains the -1's and 1's, and the  $\mathbf{F}$  matrix contains the  $f_{N-1}$  variables [46]. Next,  $\mathbf{DF}$  is multiplied to yield  $\mathbf{F}'_0$  of differences [46]:

$$\mathbf{F}'_0 = \mathbf{DF} = \begin{bmatrix} f'_{0,0} \\ \vdots \\ f'_{0,N-1} \\ f'_{0,N} \end{bmatrix} = \begin{bmatrix} -f_0 \\ f_0 - f_1 \\ \vdots \\ f_{N-2} - f_{N-1} \\ f_{N-1} \end{bmatrix}. \quad (2.6)$$

Then, the vectors  $\mathbf{F}'_i$  are generated by multiplying componentwise with the vector of samples  $\mathbf{S} = [x_0, x_1, \dots, x_N]^T$  [46]:

$$\mathbf{F}'_{n+1} = \begin{bmatrix} f'_{n+1,0} \\ \vdots \\ f'_{n+1,N-1} \\ f'_{n+1,N} \end{bmatrix} = \begin{bmatrix} x_0 f'_{n,0} \\ \vdots \\ x_{N-1} f'_{n,N-1} \\ x_N f'_{n,N} \end{bmatrix} \quad (2.7)$$

Therefore, the 1D geometrical moments  $M_p$  are computed by adding up the components of  $\mathbf{F}'_p$  and also multiplying by a factor [46]:

$$M_p = \frac{1}{p+1} \sum_{l=0}^N f'_{p,l}. \quad (2.8)$$

The 2D geometrical moments  $M_{pq}$  on a  $N^2$  grid and the 3D geometrical moments  $M_{pqr}$  can be written as [46]:

$$M_{pq} = \sum_{i=0}^{N-1} \frac{x_{i+1}^{p+1} - x_i^{p+1}}{p+1} \cdot \sum_{j=0}^{N-1} \frac{y_{j+1}^{q+1} - x_i^{q+1}}{q+1} f_{ij} \quad (2.9)$$

$$M_{pqr} = \sum_{i=0}^{N-1} \frac{x_{i+1}^{p+1} - x_i^{p+1}}{p+1} \cdot \sum_{j=0}^{N-1} \frac{y_{j+1}^{q+1} - x_i^{q+1}}{q+1} \cdot \sum_{k=0}^{N-1} \frac{z_{k+1}^{r+1} - x_i^{r+1}}{r+1} f_{ijk}. \quad (2.10)$$

The two- and three-dimensional cases can be split into one-dimensional cases and computed like the 1D case considered above [46].

### 2.1.3 2D moment invariants

For a given order  $n$ , one can derive many moment invariant expressions, but the main difficulty lies in deciding which of those expressions are independent of each other. 2D moment invariants have been studied extensively, and independent forms have been derived [10]. It is important to have independent moment invariant expressions so that there is no redundant information, therefore they cannot be rewritten as linear combinations or products of each other. The moment inertia tensor is [4, 10]:

$$\mathcal{I}_{2D} = \begin{pmatrix} \mu_{20} & -\mu_{11} \\ -\mu_{11} & \mu_{02} \end{pmatrix}. \quad (2.11)$$

The second order moment invariants can be constructed from the trace and the determinant of this matrix [13]:

$$\mathcal{O}_1 = \mu_{20} + \mu_{02}; \quad \mathcal{O}_2 = \mu_{20}\mu_{02} - \mu_{11}^2 \quad (2.12)$$

Therefore, the normalized 2D second order moment invariants (MIs) are [4]:

$$\bar{\omega}_1 = \frac{A^2}{2\pi(\bar{\mu}_{20} + \bar{\mu}_{02})}, \quad (2.13)$$

$$\bar{\omega}_2 = \frac{A^4}{16\pi^2(\bar{\mu}_{20}\bar{\mu}_{02} + \bar{\mu}_{11}^2)}, \quad (2.14)$$

where  $A$  is the surface area of the object and all moments are central moments, indicated by the bar over  $\mu_{ij}$ .

The expressions in Equation 2.13 and 2.14 have been normalized by scaling with respect to the object's area indicated by  $A$ ; this renders them dimensionless, indicated by the bar over the moment invariant expressions [4, 10]. Additionally, when the expressions in Equation 2.13 and 2.14 are scaled by the moment invariant values for the circle such that the second-order moment invariants,  $\omega_i$ , are between 0 and 1 for all 2D shapes, hence the scaling factors of  $1/2\pi$  and  $1/16\pi^2$  in Equations 2.13 and 2.14.

A second order moment invariant map (SOMIM) can be developed using  $\bar{\omega}_1$  and  $\bar{\omega}_2$ , depicting a graphical representation of all 2D shapes as shown in Figure 2.1(a). It has also been shown that  $0 \leq \bar{\omega}_1^2 \leq \bar{\omega}_2 \leq 1$  [4]. For the circle,  $\bar{\omega}_1 = \bar{\omega}_2 = 1$ , and all shapes with isotropic moments of inertia have  $\bar{\omega}_2 = \bar{\omega}_1^2$ ; these include the square and equilateral triangle. All shapes are represented by points to the left of the parabola, whose limits are  $\bar{\omega}_2 = 1$  and the parabola  $\bar{\omega}_2 = \bar{\omega}_1^2$ .

The limit  $\bar{\omega}_2 = 1$  corresponds to the set of all ellipses, for which the second order moment invariant vector is [4]:

$$\bar{\omega}_{\text{ellipse}} = \left( \frac{2\tau}{1 + \tau^2}, 1 \right), \quad (2.15)$$

where  $\tau$  is the aspect ratio of the principal axes. For rectangles, its moment invariants are [4]:

$$\bar{\omega}_{\text{rectangle}} = \left( \frac{6\tau}{\pi(1 + \tau^2)}, \frac{9}{\pi^2} \right), \quad (2.16)$$

and so all rectangles lie on the line  $\bar{\omega}_2 = 0.9119$ . This can also be derived for triangles where  $\bar{\omega}_2 = 27/4\pi^2 = 0.6839$ .

While  $\bar{\omega}_1$  and  $\bar{\omega}_2$  provide some information on the shape, higher order moments in 2D are also necessary to discuss because they are more sensitive to small changes in the shape, in

the same way that skewness and kurtosis provide more subtle information about the shape of a 1D distribution. Higher order 2D moment invariants can be derived using complex moments [14, 16, 39]:

$$C_{pq} = \int \int D(x, y)(x + iy)^p(x - iy)^q dx dy, \quad (2.17)$$

$$C_{pq} = \int_0^\infty \int_0^{2\pi} d\theta dr r^{p+q+1} e^{i(p-q)\theta} D(r, \theta), \quad (2.18)$$

where Equation 2.17 is in Cartesian coordinates and Equation 2.18 uses polar coordinates. In these equations,  $D(x, y)$  and  $D(r, \theta)$  are the indicator function,  $i$  is the imaginary number, and  $r$  and  $\theta$  refer to its polar coordinates. The third order moment invariants are [16]:

$$\sigma_1 = \frac{1}{A^5} [(\bar{\mu}_{30} + \bar{\mu}_{12})^2 + (\bar{\mu}_{03} + \bar{\mu}_{21})^2] \quad (2.19)$$

$$\sigma_2 = \frac{1}{A^{10}} [(\bar{\mu}_{30} - 3\bar{\mu}_{12})(\bar{\mu}_{30} + \bar{\mu}_{12}) \times ((\bar{\mu}_{30} + \bar{\mu}_{12})^2 - 3(\bar{\mu}_{21} + \bar{\mu}_{03})^2) \quad (2.20)$$

$$+ (3\bar{\mu}_{21} - \bar{\mu}_{03})(\bar{\mu}_{21} + \bar{\mu}_{03}) \times (3(\bar{\mu}_{30} + \bar{\mu}_{12})^2 - (\bar{\mu}_{21} + \bar{\mu}_{03})^2)]$$

$$\sigma_3^s = \frac{1}{A^{10}} [(3\bar{\mu}_{12} - \bar{\mu}_{30})(\bar{\mu}_{03} + \bar{\mu}_{21})(3(\bar{\mu}_{30} + \bar{\mu}_{12})^2 - (\bar{\mu}_{21} + \bar{\mu}_{03})^2) \quad (2.21)$$

$$+ (3\bar{\mu}_{21} - \bar{\mu}_{03})(\bar{\mu}_{12} + \bar{\mu}_{30})((\bar{\mu}_{30} + \bar{\mu}_{12})^2 - 3(\bar{\mu}_{21} + \bar{\mu}_{03})^2)]$$

$$\sigma_4^a = \frac{1}{A^{10}} [6\bar{\mu}_{30}\bar{\mu}_{21}\bar{\mu}_{12}\bar{\mu}_{03} + 3\bar{\mu}_{12}^2\bar{\mu}_{21}^2 - \bar{\mu}_{30}^2\bar{\mu}_{03}^2 - 4\bar{\mu}_{30}\bar{\mu}_{12}^3 - 4\bar{\mu}_{03}\bar{\mu}_{21}^3]. \quad (2.22)$$

However, the third order moment invariants are not used because these expressions can not be normalized by the values for a circle, since the values are zero. The independent fourth order 2D moment invariants are defined as [16]:

$$\bar{\tau}_1 = \frac{A^3}{3\pi^2} [\bar{\mu}_{40} + 2\bar{\mu}_{22} + \bar{\mu}_{04}]^{-1}, \quad (2.23)$$

$$\bar{\tau}_2^a = \frac{A^6}{48\pi^4} [\bar{\mu}_{40}\bar{\mu}_{04} - 4\bar{\mu}_{31}\bar{\mu}_{13} + 3\bar{\mu}_{22}^2]^{-1}, \quad (2.24)$$

$$\bar{\tau}_3^a = \frac{A^9}{1728\pi^6} [\bar{\mu}_{40}\bar{\mu}_{22}\bar{\mu}_{04} - \bar{\mu}_{40}\bar{\mu}_{31}^2 + 2\bar{\mu}_{31}\bar{\mu}_{13}\bar{\mu}_{22} - \bar{\mu}_{22}^3]^{-1}, \quad (2.25)$$

where the superscript  $a$  refers to the affine invariants. The pre-factors are chosen so that the three moment invariants are normalized to equal one for the circle. There are also mixed order moment invariants, but they are not discussed here [10, 14].

Five-dimensional (5D) shape descriptors can be obtained by combining  $\bar{\omega}_1$ ,  $\bar{\omega}_2$ ,  $\bar{\tau}_1$ ,  $\bar{\tau}_2$ , and  $\bar{\tau}_3$ . However, since 5-dimensional space is challenging to visualize, it can be simplified by projecting to a lower dimensional space. A useful projection is to average the components of each sub-vector; taking  $(\bar{\omega}_1 + \bar{\omega}_2)/2$  and  $(\bar{\tau}_1 + \bar{\tau}_2 + \bar{\tau}_3)/3$  reduces the 5D description to two dimensions so that points are plotted as  $(\langle\bar{\omega}_i\rangle, \langle\bar{\tau}_i\rangle)$ . This corresponds to projecting the moment invariants onto the diagonals of the respective invariant spaces. These two averaged parameters can be graphed to generate Projected Moment Invariant Maps (PMIMs), as shown in Figure 2.1(b) [16]. Lines have been drawn on the maps where ellipses, rectangles, and triangles lie in the PMIM space. The limits on the ellipse are [16]:  $(\langle\bar{\omega}_i\rangle, \langle\bar{\tau}_i\rangle) = (\frac{1}{2}, \frac{2}{3})$  to (1,1), for the rectangle they are (0.456, 0.504) to (0.933, 0.794), and the limits for the triangle are (0.341, 0.170) to (0.751, 0.354).

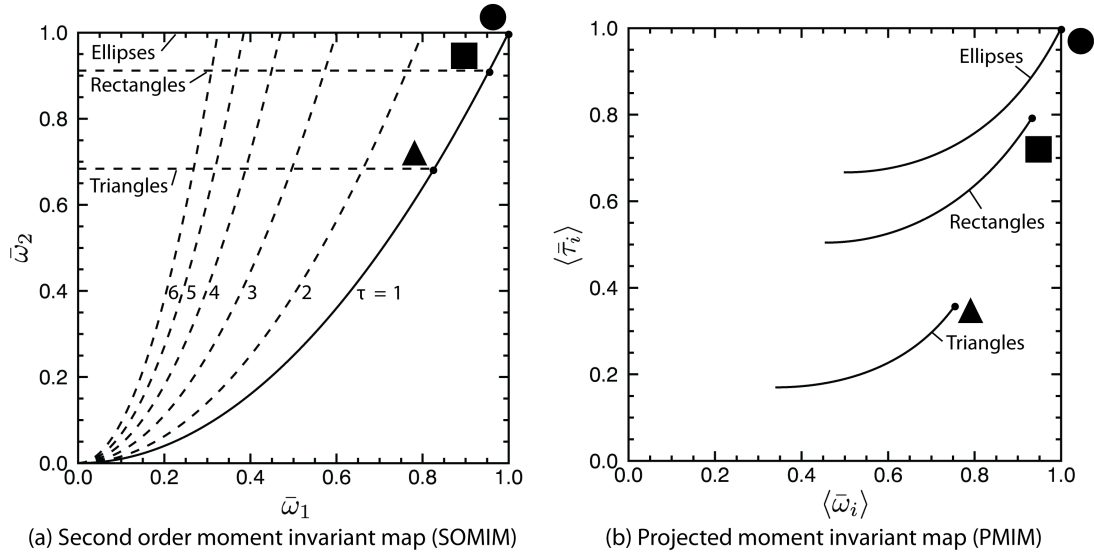


Figure 2.1: (a) An illustration of the 2D moment invariant space. The second order moment invariant map (SOMIM). Within the region to the left of the parabola, all 2D shapes can be described using moment invariants. Some important shapes are noted on the map. (b) The projected moment invariant map of second and fourth order (PMIM). The curves for ellipses, rectangles, and isosceles triangles are superimposed. *Figure adapted with permission from Ref. [4]. Copyrighted by Elsevier.*

The SOMIM and PMIM can be generated as density maps, where each point (either  $(\bar{\omega}_1, \bar{\omega}_2)$  in the SOMIM or  $(\langle\bar{\omega}_i\rangle, \langle\bar{\tau}_i\rangle)$  in the PMIM) is added to the map as a narrow Gaussian peak. The overlapping Gaussians make up the density map and have been normalized to sum up to one over the entire moment invariant domain. The SOMIMs and the PMIMs, can also be generalized to higher order moments. Both SOMIMs and PMIMs serve as

shape descriptors, where the SOMIM represents the 2D moment invariant space, in which all 2D shapes must lie within the parabolic region of Figure 2.1(a). PMIMs incorporate five moment invariants instead of two, so different information can be obtained from the SOMIMs [16]. SOMIMs and PMIMs have both been used to characterize the shapes of 2D objects.

### Equivalent ellipse

Another useful shape frequently used in microstructure modeling is the equivalent ellipse [4, 13,47]. All 2D shapes have an equivalent ellipse, i.e. an ellipse with the same principal second order moments and can be calculated using second order moment invariants. Additionally, the aspect ratio of the 2D shape can be calculated using second order moment invariants. The moment invariants for the equivalent ellipse are [4]:

$$\omega_1^e = 8\pi \frac{\sqrt{\bar{\mu}_{20,P}\bar{\mu}_{02,P}}}{\bar{\mu}_{20,P} + \bar{\mu}_{02,P}}, \quad \omega_2^e = 16\pi^2, \quad (2.26)$$

where  $P$  is the object. The  $\omega_1$  for the equivalent ellipse can be rewritten in terms of the moment invariants of the object  $P$ :

$$\bar{\omega}_1^{ee} = \frac{\bar{\omega}_1^P}{\sqrt{\bar{\omega}_2^P}} \quad (2.27)$$

$\omega_2$  for the equivalent ellipse is always  $16\pi^2$  or  $\bar{\omega}_2 = 1$  in the normalized moment invariant space because  $\bar{\omega}_2$  is an affine moment invariant. In the  $(\bar{\omega}_1, \bar{\omega}_2)$  space, the equivalent ellipse is determined by drawing a parabola that begins at the origin and ends at the point  $(\bar{\omega}_1^e, 1)$ . For aspect ratios  $\tau = 2, 3, 4, 5, 6$ , the dotted lines represent the parabola for that equivalent ellipse, shown in Figure 2.1(a). The parabola can be calculated as [13]:

$$\bar{\omega}_1^2 = \frac{\bar{\omega}_2^P}{(\bar{\omega}_1^P)^2} \quad \bar{\omega}_2 = \frac{\bar{\omega}_2^e}{(\bar{\omega}_1^e)^2}, \quad (2.28)$$

For the equivalent ellipse,  $\bar{\omega}_1$  can be expressed in terms of its aspect ratio of the major and minor axes:

$$\bar{\omega}_1^e = \frac{8\pi\tau}{1 + \tau^2}. \quad (2.29)$$

The aspect ratio of a 2D object can be calculated by:

$$\tau = \frac{1 + \sqrt{1 - (\bar{\omega}_1^e)^2}}{\bar{\omega}_1^e}. \quad (2.30)$$

#### 2.1.4 3D moment invariants

Most of the past work has been on shape descriptors as 2D moment invariants, and moment invariants up to the fourth order have been applied to materials science [4, 13, 14, 16]. 3D moment invariants have also been explored, but are still incompletely known [10, 48–50]. The current knowledge of moment invariants includes three independent second order 3D moment invariants. The Cartesian moments of an object in 3D are defined as [5, 10]:

$$\mu_{pqr} = \iiint dx dy dz x^p y^q z^r D(x, y, z) = \iiint_D dx dy dz x^p y^q z^r, \quad (2.31)$$

where the order of the moment,  $n$ , is equal to the sum of the exponents  $p + q + r$  and  $D(x, y, z)$  describes its shape or indicator function, such that the function is one inside the object and zero outside of it. The central moments are defined as [10]:

$$\bar{\mu}_{pqr} = \iiint_D dx dy dz (x - x_c)^p (y - y_c)^q (z - z_c)^r, \quad (2.32)$$

where  $x_c, y_c, z_c$  are its center-of-mass coordinates.

Past work by MacSleyne includes three independent second order 3D moment invariants, which can be derived from the second rank moment-of-inertia tensor,  $I$  [5]:

$$\mathcal{I}_{3D} = \begin{pmatrix} \mu_{020} + \mu_{002} & -\mu_{110} & -\mu_{101} \\ -\mu_{110} & \mu_{200} + \mu_{002} & -\mu_{011} \\ -\mu_{101} & -\mu_{011} & \mu_{200} + \mu_{020} \end{pmatrix} \quad (2.33)$$

This tensor results in three independent second order moment invariants, defined as:

$$\mathcal{O}_\infty = \mu_{200} + \mu_{020} + \mu_{002}, \quad (2.34)$$

$$\mathcal{O}_\epsilon = \mu_{200}\mu_{020} + \mu_{200}\mu_{002} + \mu_{110}^2 - \mu_{101}^2 - \mu_{011}^2, \quad (2.35)$$

$$\mathcal{O}_\varnothing = \mu_{200}\mu_{020}\mu_{002} + 2\mu_{011}\mu_{101}\mu_{011} - \mu_{200}\mu_{011}^2 - \mu_{020}\mu_{101}^2 - \mu_{002}\mu_{110}^2, \quad (2.36)$$

where  $O_1$  and  $O_2$  are similarity moment invariants, while  $O_3$  is an affine moment invariant.

These invariants can then be normalized with respect to volume to make them dimensionless:

$$\Omega_1 = \frac{3V^{5/3}}{\mathcal{O}_\infty}, \quad \Omega_2 = \frac{3V^{10/3}}{\mathcal{O}_\epsilon}, \quad \Omega_3 = \frac{V^5}{\mathcal{O}_\varnothing}. \quad (2.37)$$

The dimensionless moment invariants  $\bar{\Omega}_i$  are normalized so that their values are between 0 and 1, dividing the dimensionless moment invariants by the expressions for the sphere. The moment invariants for the sphere are derived and are given by [5]:

$$\Omega_1^S = \left(\frac{2000\pi^2}{9}\right)^{1/3}, \quad \Omega_2^S = \left(\frac{2000\pi^2}{9}\right)^{2/3}, \quad \Omega_3^S = \frac{2000\pi^2}{9}. \quad (2.38)$$

The normalized moment invariants are therefore given as:

$$\bar{\Omega}_1 = \left(\frac{9}{2000\pi^2}\right)^{1/3} \times \frac{3V^{5/3}}{\mu_{200} + \mu_{020} + \mu_{002}}, \quad (2.39)$$

$$\bar{\Omega}_2 = \left(\frac{9}{2000\pi^2}\right)^{2/3} \times \frac{3V^{10/3}}{\mu_{200}\mu_{020} + \mu_{200}\mu_{002} + \mu_{110}^2 - \mu_{101}^2 - \mu_{011}^2}, \quad (2.40)$$

$$\bar{\Omega}_3 = \frac{9}{2000\pi^2} \times \frac{V^5}{\mu_{200}\mu_{020}\mu_{002} + 2\mu_{011}\mu_{101}\mu_{011} - \mu_{200}\mu_{011}^2 - \mu_{020}\mu_{101}^2 - \mu_{002}\mu_{110}^2} \quad (2.41)$$

$\bar{\Omega}_1$  and  $\bar{\Omega}_2$  are related to the aspect ratios of a shape, and  $\bar{\Omega}_3$  is a descriptor of shape classes and independent of aspect ratios [5].  $\bar{\Omega}_3$  can also be thought of as a morphological descriptor.

3D moment invariants are derived in the same way as in 2D using Cartesian coordinates. The combinations of higher order moment invariants than order two that are independent and invariant under similarity and affine transformations have yet to be determined [10, 46]. Hadwiger's work on isoperimetric inequalities between moments of inertia in an  $n$ -

dimensional space serve as the foundation upon which the moment invariant expressions in Equations 2.37 can be normalized by the sphere, and all 3D objects lie within the unit cube [51]. The three normalized moment invariants can be represented graphically inside of the unit cube, as shown in Figure 2.2. In the 3D moment invariant space, all isotropic

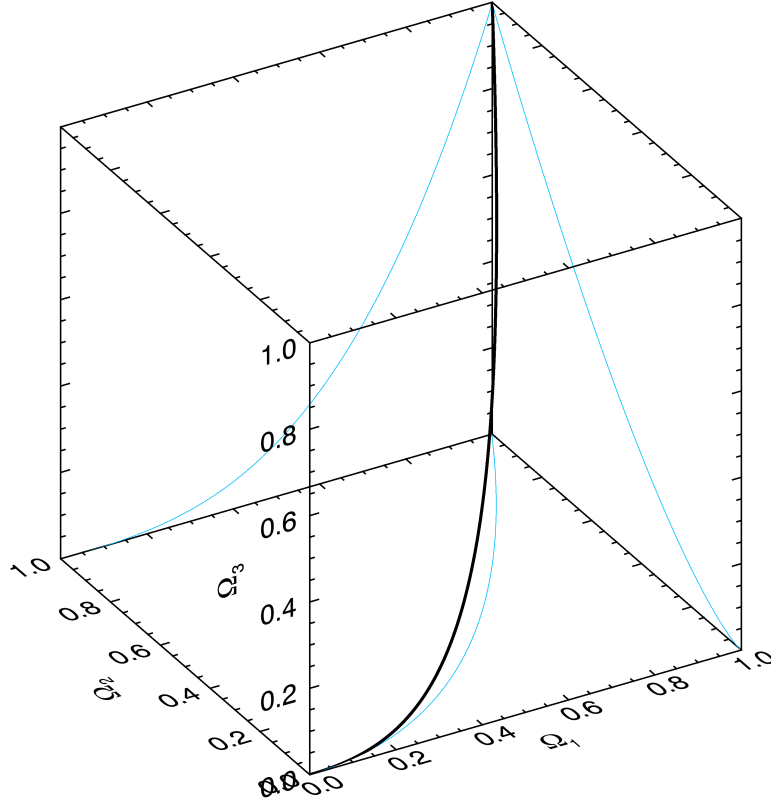


Figure 2.2: The 3D moment invariant space. The black line is the isotropic shape curve, while the blue lines represent the projections onto the 2D planes. *Figure adapted with permission from Ref. [5]. Copyrighted by IOP Science.*

shapes have moment invariants

$$\bar{\Omega}_1^3 = \bar{\Omega}_2^{3/2} = \bar{\Omega}_3. \quad (2.42)$$

and is referred to as the isotropic shape parabola. Alternate approaches to determining 3D moment invariants make use of spherical harmonics, 3D tensors, Cartesian coordinates, and other methods [10, 52]. Recently, Flusser and Suk have computed a list of higher order 3D moment invariants; it is not known yet which of these are independent and which ones are dependent [10].

### Equivalent ellipsoid

The equivalent ellipsoid can also be determined in 3D, like the equivalent ellipse can be determined in 2D. The moment invariants of the ellipsoid are [5]:

$$\bar{\omega}_1(\tau_1, \tau_2) = \left(\frac{2000\pi^2}{9}\right)^{1/3} \frac{3(\tau_1\tau_2)^{2/3}}{1 + \tau_1^2 + \tau_2^2}, \quad (2.43)$$

$$\bar{\omega}_2(\tau_1, \tau_2) = \left(\frac{2000\pi^2}{9}\right)^{2/3} \frac{3(\tau_1\tau_2)^{4/3}}{\tau_1^2 + \tau_2^2 + \tau_1^2\tau_2^2}, \quad (2.44)$$

$$\bar{\omega}_3(\tau_1, \tau_2) = \frac{2000\pi^2}{9} \quad (2.45)$$

These expressions are given in terms of two aspect ratios,  $\tau_1$  and  $\tau_2$ . For the equivalent ellipsoid, its moment invariants are [13]:

$$\bar{\Omega}_1^e = \frac{\Omega_1^P}{(\bar{\Omega}_3^P)^{1/3}}, \quad (2.46)$$

$$\bar{\Omega}_2^e = \frac{\Omega_2^P}{(\bar{\Omega}_3^P)^{2/3}}, \quad (2.47)$$

$$\bar{\Omega}_3^e = \frac{2000\pi^2}{9}, \quad (2.48)$$

where  $P$  refers to the 3D object. The aspect ratios of the equivalent ellipse are [13]:

$$\epsilon_1 = \sqrt{\frac{\mu_y(P)}{\mu_x(P)}}, \quad \epsilon_2 = \sqrt{\frac{\mu_z(P)}{\mu_x(P)}}, \quad a = \frac{15^{1/5} \mu_x(P)^{2/5}}{2^{2/5} (\mu_y(P) \mu_z(P))^{1/10} \pi^{1/5}}, \quad (2.49)$$

where  $\epsilon_1$  and  $\epsilon_2$  are the aspect ratios, and  $a$  is the major axis of the object.

#### 2.1.5 Applications of moment invariants in materials science

The shape of  $\gamma'$  precipitates has been studied extensively using a variety of shape parameters: moment invariants, Minkowski functionals, and the shape quotient are just a few [1, 4, 5, 9, 16, 38]. Due to their relatively cuboidal shape,  $\gamma'$  precipitates are good candidates for the use of moment invariant-based shape descriptors. The application of moment invariants to examine morphological changes include: determining the optimal precipitate shape, how stress affects the microstructure, and how changes in composition or heat treat-

ments in Ni-based single crystal superalloys affect the  $\gamma'$  shape [9, 13, 14, 38].

The first implementation of moment invariants in materials science was done by MacSleyne et al., where moment invariants were used to study the  $\gamma'$  particle shape evolution in 2D phase field simulations [4]. The moment invariant distributions for an experimental and a simulated microstructure were computed and compared to each other. The two-point correlation function was used to determine the locations of the particles and used with moment invariants to determine how well the model describes the real microstructure [4]. The experimental  $\gamma'$  precipitate shapes in René-88DT and UMF-20 superalloys were also studied in 3D using moment invariants [1]. The precipitates in René-88DT were dendritic and analyzed by using  $\bar{\Omega}_3$  and the shape quotient,  $Q$ , while the precipitates in the UMF-20 superalloys were described using moment invariants to find its equivalent superellipsoid [1]. The shape quotient and the superellipsoid are described later in Section 2.2.

Callahan et al. further explored the application of moment invariants by generating a 3D synthetic microstructure and then digitally sectioning along four section planes. The 2D sections are compared to a library of precomputed shapes [16]. Each 3D shape in the library was sectioned along 5000 random directions; then its 2D moment invariants were computed and plotted on its respective SOMIM and PMIM so that a plane in any direction can be detected and matched to the library [16]. Callahan also provided the initial work to detect the changes in  $\gamma/\gamma'$  microstructures. Digital 3D microstructures were created and positioned along preferential directions, then an additional ten microstructures were created with particles that have been elongated by a percentage from 0 to 100%, in increments of 10% [16]. The Hellinger distance was computed for the elongated microstructures to the initial reference microstructure, which is discussed in Section 2.3.2. Callahan also used the Hellinger distance to provide a quantitative comparison between pairs of microstructures, to determine if microstructure  $A$  was more similar microstructure  $B$  or microstructure  $C$  [16].

An area of interest in shape analysis is being able to determine the “optimal shape,” as it may relate to certain materials systems. One area where it has been investigated is the determination of the optimal  $\gamma'$  precipitate shape in Ni-based  $\gamma$ - $\gamma'$  alloys for a given lattice misfit [38]. In one study, 2D moment invariants were applied to a series of platinum group metal (PGM)-containing Ni-based alloys [38]. This calculation was done by manually

measuring the inner and outer square to calculate  $\bar{\omega}_2$ . The two length parameters were measured for an average of 60-75 precipitates per alloy, for a total of seventeen alloys. A shape parameter,  $\eta = A/B$ , was used to characterize the shapes of these alloys, which can be shown in Figure 2.3. A relationship exists between  $\omega_2$ , the second-order 2D affine moment invariant, and the shape parameter,  $\eta$ . This relationship is shown in Figure 2.6(a) and defined as [4]:

$$\omega_2 = \frac{144(\pi(\eta - 1)^2 - 4\eta(\eta - 2))^4}{3\pi(\eta - 1)^2(1 - 2\eta + 5\eta^2) - 16\eta(3\eta^3 - 7\eta^2 + 6\eta - 3)^2} \quad (2.50)$$

Its values range from 0 for the circle, to 1 for the square.  $A$  and  $B$  measure the edge lengths of the inner and outer square. The maximum of the relationship between  $\bar{\omega}_2$  and  $\eta$  is the shape as shown in Figure 2.6(a).

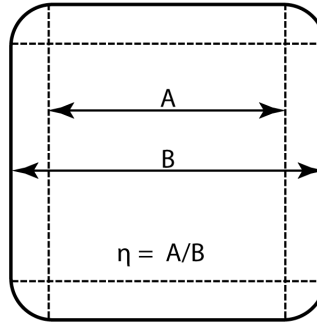


Figure 2.3: Illustration of the shape parameter  $\eta$ .  $\eta$  varies from 0 for a circle to 1 for a square. *Figure adapted with permission from Ref. [4]. Copyrighted by Elsevier.*

This study used a shape parameter  $\eta$  that varies from 0.08 to 0.77; it changes with overall composition and partitioning of elements to the matrix and precipitate phases [38]. The shape parameter,  $\eta$ , peaks at a specific misfit magnitude of 0.4%. Commercial single crystal Ni-based alloys possess near-optimal microstructures as a result of extensive alloy and process development activities. There is an optimal combination of precipitate shape and lattice misfit that results in a cuboidal  $\gamma'$ , but this process can be time-consuming to develop. By being able to estimate the lattice misfit from the  $\gamma'$  precipitate shape, research efforts can be directed.

This study uses another parameter, called the attractor shape,  $\eta_{Att}$ , as the value at which the elastic interaction energy dominates the interfacial energy and stabilizes the

precipitate morphology [4, 38]. One possible application of  $\eta_{Att}$  is to use it to measure the high temperature lattice misfit without having to experimentally determine it, which is both time-consuming and expensive. This range is between  $0.6 < \eta < 0.7$  [38].

### 2.1.6 Moment invariants for enabling materials design applications

Materials science and engineering has also recently shifted to improving and implementing more computational tools with the increases in computational power and knowledge. Tools are needed to characterize and quantify microstructure in a way that facilitates quantification and visualization of structural variance and other data analytics [53, 54]. Improvements in characterization techniques and technology have allowed for the collection of large amounts of 2D and 3D structural information. Several statistical descriptors have been applied to the quantitative description of microstructure [53, 55]:

- n-point correlation functions
- lineal path function and chord length distributions
- information content (entropic) descriptors.

With statistical information about a microstructure, it is desirable to be able to estimate the overall statistics of the material from an ensemble of samples and to relate the measures to macroscale or effective properties [55]. It is also desirable to reconstruct potential individual realizations corresponding to the estimated materials statistics [55]. By optimizing microstructure and processing, superior properties and predictable performance can be obtained, and material optimization can be integrated into the component level design and manufacturing processes.

One of the most popular methods in microstructure quantification is using n-point statistics, where  $n$  refers to a whole number. One-point statistics describe the probability or probability density that is associated with finding a specific local state of interest at a point thrown randomly into the microstructure [53]. One well-known one-point distribution in materials science is the orientation distribution function (ODF) used in texture analysis [56]. Two-point statistics describe the probability density associated with finding a specific local state of interest at two ordered points. Two-point correlation functions can

be used as microstructure descriptors and can account for the anisotropy in the structure. Three-point and higher-point correlation functions become a random triangle and a random quadrilateral and are extensions of one- and two-point correlation functions.

For example, consider a two-phase microstructure where the matrix is one phase, and the other phase is randomly dispersed throughout the matrix phase as shown in the schematic in Figure 2.4. The one-point function  $S_1$  is obtained by randomly assigning a single point onto the micrograph and recording the number of times it lands in one of the phases, such as the dark phase [53]. If there are enough points that are randomly sampled, then  $S_1$  will approach the volume fraction of the dark phase.

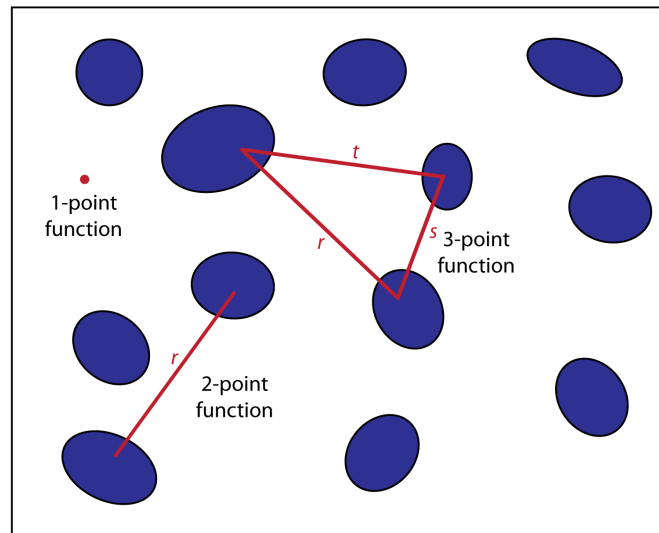


Figure 2.4: A schematic that shows the sampling for one-, two-, and three-point correlation functions. A one-point correlation function is shown by a point, a two-point correlation function is shown by a line, and a three-point correlation function is shown by a triangle. Adapted from [6].

The two-point correlation function  $S_2(r)$  are measured by taking lines of length  $r$  and placing them randomly on the micrograph and recording the fraction of times that both ends of the line are in the dark phase [53]. The variations in  $S_2(r)$  reflect how the two points are correlated in the system. The three-point correlation function  $S_3(r, s, t)$  is the probability that the three vertices of a triangle with sides of lengths  $r$ ,  $s$ , and  $t$  are in the dark phase [53]. N-point correlation functions have been used in other fields such as astronomy, x-ray crystallography, image processing, and electron microscopy [53, 54, 56]. Additionally, efforts have been made to reconstruct the original images from these 2-point correlations

that are directly measured [4,56]. The n-point correlation functions provides the probability that  $n$  points with specified positions are in the dark phase [53].

Therefore it is necessary to examine how moment invariants can be used to inform physical models and how they can be used as an inverse method. Given its moment invariant map, it is not possible to reconstruct a microstructure based on its moment invariant distribution alone [4]. Moment invariants can be used to determine the types of shapes should be found throughout the microstructure. They do not provide any information about the spatial correlation between microstructural features unlike n-point correlation functions, just the shapes of the features. However, moment invariants are a good method to determine how similar two microstructures are to each other. Even if two microstructures seem to look different, moment invariants can show that they are actually similar. One method where moment invariants can be used is to compare the resulting moment invariant distributions of different simulations and determine which simulation best captures the true microstructure [4].

The application of moment invariants in materials science and engineering is still a niche field and growing, but it has found areas of influence. When creating synthetic microstructures using DREAM3D, one of the available options is to choose the  $\bar{\Omega}_3$  distribution of grains [57]. One example is to determine the  $\bar{\Omega}_3$  distribution of an experimental dataset and then use the same distribution as input into the synthetic microstructure. Another option in DREAM3D is to input specific types of shapes, such as ellipsoidal, superellipsoidal, and cuboctahedral [14].

A representative volume element (RVE) can also be determined from a microstructure using moment invariants. The moment invariant distributions for the entire microstructure can be computed and then compared to the moment invariants of varying sizes of the regions of interest until the Hellinger distance shows that the two distributions of the entire microstructure and the smaller region of interest are sufficiently similar. The Hellinger distance is discussed later on Section 2.3.2. The RVE can then be used as the basis upon which to compare other microstructures. This can also be done in two dimensions as well.

It would also be useful to use moment invariants to help describe structure-property relationships. While it is not possible to use moment invariants by themselves, it is possible

that moment invariants can be used with other microstructural parameters to help describe these relationships. The morphology of microstructural features is extremely important to designing the optimal microstructure of a material. For example, moment invariants can be used with volume or area to determine the characteristic morphology of grains. Grains with certain crystallographic orientations may all have the same shape, and therefore moment invariants can be used to detect certain oriented grains without the need for orientation information or to predict orientation in models. For example, the number of facets on a grain may be related to its moment invariants, and other relationships can also be identified. These are just a few examples of the ways that moment invariants can be used with other important microstructural parameters. Moment invariants can help microstructure builders to obtain the same distribution of shapes in simulations as in the experimental or true microstructure.

### 2.1.7 Applications of moment invariants in other fields

Shape analysis is important in many fields ranging from pattern recognition, sedimentary particles, MRI scanning technology, and biology (thermal face recognition) to name a few [10]. Most commonly, moment invariants have been used in the field of pattern recognition. Moment invariants have been used to distinguish in image analysis [39] to study features such as handwritten digits [58], images of military aircraft [59, 60], satellite images [44], alphabet letters [44], texture classification [61], and color object classification [62], to name a few.

The recognition of objects and patterns that have been deformed in some way has been an area of great interest. The three main approaches include: brute force, image normalization, and invariant features [10, 39]. The brute force method is extremely time intensive and requires training of each class with all the different deformed versions, including all rotations, scalings, blurring, etc. The normalization approach transforms the object of interest into a standard position before classification; the disadvantage to this approach is that the object normalization may require the solutions to complex inversion problems. However, the use of invariants provides the ability to discriminate objects of different classes while being insensitive to particular types of deformation. The use of moment invariants can dis-

tinguish between image translation, rotation, scaling, and affine transformations, like we use in materials science and engineering. Moment invariants can also be used with image blurring, convolution with an unknown filter [39].

Much work has been done on geometric distortion of objects; however, the literature on radiometric invariants, or invariants with respect to changes of the image intensity function has been less well-studied [39]. However, intensity changes are important to consider since every image will have these differences. Van Gool introduced affine-photometric invariants, insensitive to the affine transform and to the change of contrast and brightness of the image simultaneously [63, 64]. However, these invariants are insensitive to translation only. These invariants have found applications ranging from face recognition on out-of-focus photographs [65], normalizing blurred images [66], template-to-scene matching of satellite images [45], and blurred digit and character recognition [61, 67], satellite image registration [68].

Magnetic resonance imaging (MRI) has been extremely useful in measuring and characterizing microstructural orientation and organization in biologic tissue, such as cardiac muscle or the central nervous system [69]. The analysis of diffusion tensor magnetic resonance image (DT-MRI) has established connections of diffusion tensor parameters with important tissue properties. Particularly, there is a focus on changes in shape and orientation [70]. A shape metric is any scalar invariant that quantifies some important geometric property of tensor shape, such as overall size or eccentricity. In this application, orientation refers to the complementary degrees of freedom associated with changes in the eigenvectors while keeping the eigenvalues fixed. Therefore, the tensor can be visualized as an ellipsoid when shape and orientation is defined in terms of the tensor eigensystem [70].

Visualizations of the tensor field structure can be created using two sets of orthogonal tensor invariants, one that uses fractional anisotropy (FA) and the apparent diffusion coefficient (ADC) [69, 70]. Tensor shape refers to the degrees of freedom in tensor values spanned by changes in the eigenvalues while keeping eigenvectors fixed. Tensor shape is a trivariate quantity since it is orthogonally decomposed using a set of three orthogonal invariants.

Ennis et al. use two- and three-dimensional colormaps of tensor shape to map tensor size, fractional anisotropy, and mode to color brightness, saturation, and hue [70]. Tensor mode refers to the type of tensor anisotropy from linear anisotropy to orthotropy to planar

anisotropy. For example, a fractional anisotropy map can be color coded for tensor mode and directionally encoded of only linearly anisotropic structures. The different colors represent anywhere from linear anisotropy (blue) to orthotropy (green) to planar anisotropy (red). The directionally encoded colormaps provide a way to display the orientation of anisotropic structures. The highly anisotropic data is indicated by saturating the color intensity by fractional anisotropy. In DT-MRI analysis, tensor shape can be used to show the underlying tissue microstructure and organization. DT-MRI derived maps with tensor mode can be used to assess quality of acquired data and image resolution. Kindlmann et al. created a framework of invariant gradients and rotation tangents to convert shape and orientation (represented by three degrees of freedom each) to tensor contractions along particular pairs of axes [69]. The fourth order diffusion covariance tensor was decomposed into individual and aggregate measures of shape and orientation covariance.

Moment invariants have also been used in many applications, and much work is still being done on the area of moment invariants. They have come a long way from Hu's work on the Fundamental Theorem of Moment Invariants (FTMI) where he came up with seven invariants that have now been corrected so that the moment invariants used now are correct and independent [43,71].

## 2.2 Other shape descriptors in materials science and engineering

The quantification of shape can be difficult because there is not a well-defined and universal quantity. Typically, only one quantity is not sufficient to describe shape. The ideal shape descriptor for microstructural quantification should have the following properties [2]:

- dimensionless: so that its size will not be a factor
- quantitatively describe how far the object deviates from the theoretical ideal or model one
- sensitive to particular shape changes that occur in the process

Typically, a shape descriptor will quantify a deviation from an ideal shape, most frequently a circle or sphere.

### 2.2.1 Basic shape parameters

One common shape factor is aspect ratio, given by [72]:

$$AR = \frac{\text{major axis}}{\text{minor axis}}, \quad (2.51)$$

where the major and minor axes are perpendicular to each other, and  $AR$  is one for a circle or equiaxed shapes. Aspect ratio can also be defined in the other way, so that the aspect ratio is always one for equiaxed shapes and less than one and greater than zero for elongated shapes. However,  $AR$  has some disadvantages because it will be the same for a circle and an equilateral triangle although they have distinctly different shapes, and it cannot detect irregularity. One application where the aspect ratio can be used to distinguish between cold-worked grains with  $AR$  far from one, or near one for equiaxed grains.

There are several 2D shape parameters that are commonly used: the Feret diameter, circularity, and rectangularity. One common shape factor is the Feret diameter, the maximum diameter of the object; it can also be thought of as the longest distance between any two points on the boundary of the object [2]. Circularity is a measure of how close the 2D shape of an object is to a circle, given by the equation [2]:

$$C = 4\pi \frac{A}{P^2}, \quad (2.52)$$

where  $P$  is the perimeter, and  $A$  is the area of the object. It ranges from 0 for an infinitely irregular shape such as a starfish shape and 1 for a circle. However, it is insensitive to any elongations in the object.

Rectangularity is another shape factor that measures how rectangular a shape is [2]:

$$R = \frac{A}{S}, \quad (2.53)$$

where  $A$  is the area of the object and  $S$  is the area of the minimum bounding rectangle. Often, shapes deviate from its ideal shape in more than just its elongation or irregularity. Therefore, it is useful to detect changes in both of these cases. Another commonly used

shape factor capable of accomplishing this task is [2]:

$$f_3 = \frac{d_1}{d_2}, \quad (2.54)$$

where  $d_1$  is the diameter of the maximum inscribed circle and  $d_2$  is the diameter of the maximum circumscribed circle. Shape factors are useful tools to consider the deviation from an ideal shape, and these are just a few of the parameters available. It is important to determine shapes that fit with human classification for clarity. However, this may vary from case to case and in different materials systems.

### 2.2.2 Shape parameters $\xi$ , $S_{ster}$ , and $\Sigma$

Several shape parameters have been used to quantify  $\gamma'$  precipitate shapes include  $\xi$ ,  $\Sigma$ , and  $S_{ster}$ . These parameters all range from 0 to 1 and are used to determine how similar the precipitate shape is to the a circle. The first parameter  $\xi$  is:

$$\xi = \frac{a}{d}, \quad (2.55)$$

where  $a$  is the size of the particle along  $\langle 100 \rangle$  and  $d$  is the size of the particle along a face diagonal, typically along  $\langle 110 \rangle$  [7]. A schematic of how it is measured is shown in Figure 2.5. The parameter  $\xi$  is 1 for a sphere and  $\sqrt{2}/2$  for a cube; therefore cuboidal shapes are in the range of  $1 < \xi < \sqrt{2}/2$ . When the interfaces are concave,  $\xi$  can be smaller than  $\sqrt{2}/2$  and greater than one when particles are ellipsoidal [7].

A second parameter was applied to study  $\gamma'$  precipitates following  $\xi$ , which is defined as [73]:

$$S_{ster} = \frac{(P_i - P_c)}{(P_s - P_c)}, \quad (2.56)$$

where  $P_i$  is the perimeter of the image of the particle and  $P_c$  and  $P_s$  are the perimeters of the area-equivalent circle and square, respectively [73].  $S_{ster}$  is dependent on aspect ratio, whereas  $\Sigma$  is not, so  $\Sigma$  was developed as an alternative.  $\Sigma$  is defined as [9]:

$$\Sigma = \frac{A_p - A_4}{0.5708A_4}, \quad (2.57)$$

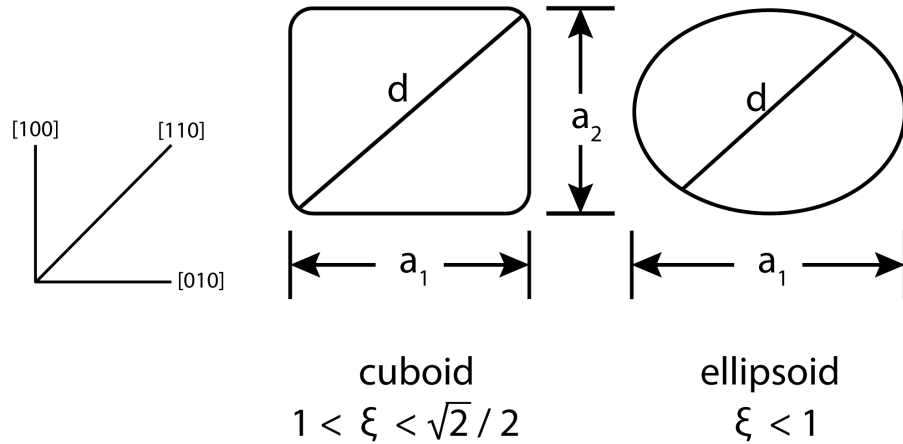


Figure 2.5: Schematic illustrating how  $\xi$  is measured. The values of  $a$  and  $d$  for individual particles are  $(a_1 + a_2)/2$  and  $(d_1 + d_2)/2$ , respectively. *Figure adapted with permission from Ref. [7]. Copyrighted by the American Physical Society.*

where  $A_p$  is the area of the image of the particle,  $A_4$  is the area of the largest 4-sided polygon that contacts the perimeter of the particle, and 0.5708 is a numerical constant that normalizes  $\Sigma$ .  $\Sigma$  is independent of the aspect ratio of the particle. Several relationships have been derived connecting  $\bar{\omega}_2$ ,  $\Sigma$ , and  $\eta$ , as shown in Figure 2.6. These parameters are further discussed and compared to moment invariants in Chapter IV.

### 2.2.3 Shape quotient

The shape quotient,  $Q$ , is a useful shape descriptor in 3D. It is based on an isoperimetric inequality that relates the volume to the surface area of an object:  $36\pi V^2 \leq S^3$  [74]. The shape quotient is defined as:

$$Q = 36\pi \frac{V^2}{S^3}, \text{ where } 0 < Q \leq 1, \quad (2.58)$$

where  $V$  is the volume and  $S$  is the surface area. The shape quotient ranges from 0 for an infinitely complex shape to 1 for a sphere and is an extension of circularity in 3D.  $Q$  decreases as the surface area relative to the volume increases, or an object becomes more complex given its volume. The shape quotient is invariant to similarity transformations and can be treated as a quantitative measure of shape complexity. It has been used by MacSleyne along with moment invariants as another method of quantifying shapes in 3D [1]. Table 2.1

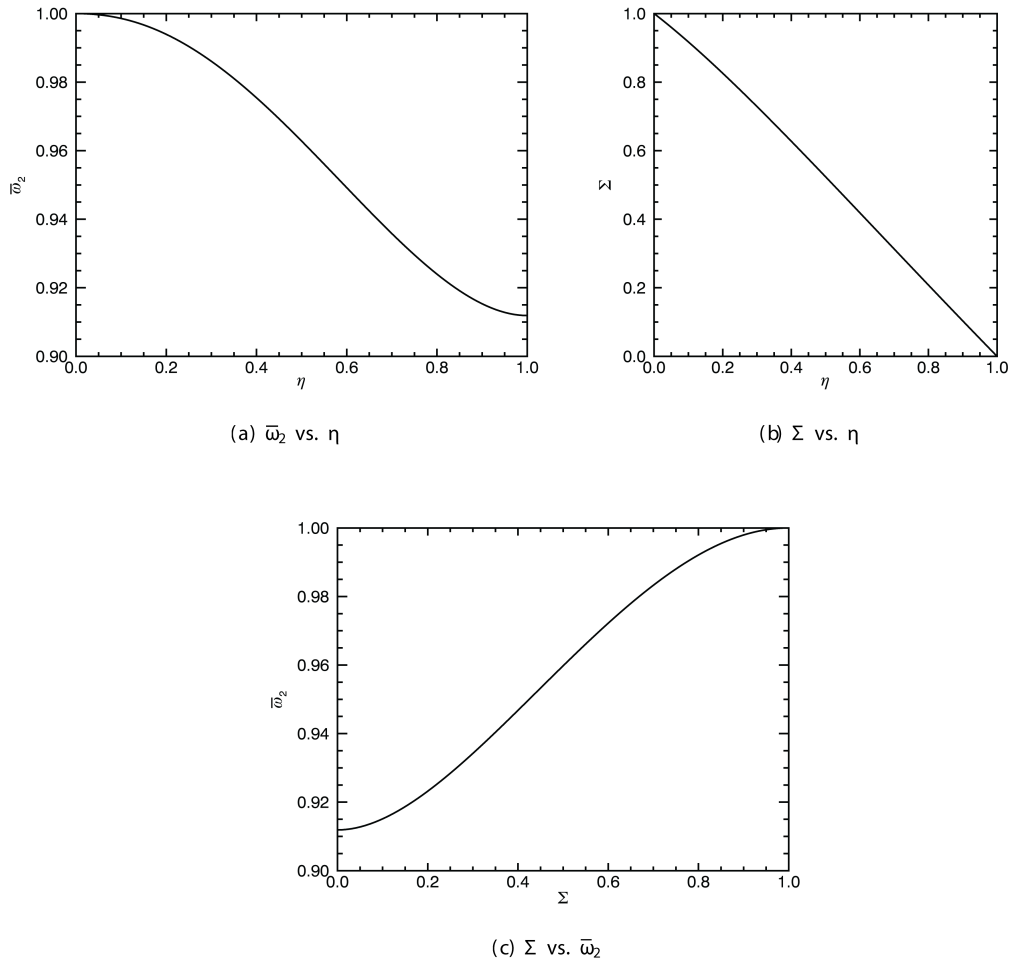


Figure 2.6: The relationships between the 2D affine moment invariant  $\bar{\omega}_2$  with  $\Sigma$  and  $\eta$ . (a)  $\bar{\omega}_2$  vs.  $\eta$ . (b)  $\Sigma$  vs.  $\eta$ . (c)  $\Sigma$  vs.  $\bar{\omega}_2$ .

shows the 3D moment invariants and the shape quotient for a few isotropic shapes. The shape quotient is used in Chapter VI.

### 2.2.4 Minkowski functionals

Minkowski functionals provide a method of classifying shapes based on certain characteristic functions. In 3D, there are four Minkowski functionals due to the relation that there are  $n + 1$  functionals for a given  $n$ -D space [75]:

1.  $V(X)$ : the volume of an object,  $X$
2.  $S(X)$ : the area of the boundary  $\partial X$  of an object,  $X$
3.  $M(X)$ : the integral of mean curvature

Table 2.1: Shape descriptors for a few isotropic shapes [1].

	$\bar{\Omega}_1$	$\bar{\Omega}_2$	$\bar{\Omega}_3$	Shape quotient
Sphere	1	1	1	1
Cube	0.9236	0.8530	0.7879	0.5236
Tetrahedron	0.7400	0.5477	0.4053	0.3023
Octahedron	0.9324	0.8693	0.8106	0.6046
Dodecahedron	0.9851	0.9705	0.9561	0.7547
Icosahedron	0.9891	0.9782	0.9675	0.8288

4.  $K(X)$ : the integral of total curvature

The Minkowski functionals are mathematically defined as:

$$V = \iiint dx dy dz, \quad (2.59)$$

$$S = \int_S dS, \quad (2.60)$$

$$M = \int_S \frac{1}{2}(k_1 + k_2)dS, \quad (2.61)$$

$$K = \int_S k_1 k_2 dS, \quad (2.62)$$

where  $k_1$  and  $k_2$  are the local principal curvatures, also known as the maximum and minimum values of the normal curvatures, and  $\int_S dS$  is the surface integral. The first three Minkowski functionals,  $V$ ,  $S$ , and  $M$ , are invariant with respect to translations and rotations. The last Minkowski functional,  $K$ , is a topological invariant. Volume and surface area are both well-known mathematical quantities, with units of  $\text{length}^3$  and  $\text{length}^2$ , respectively. The integral of mean curvature of a convex object,  $M$ , is related to the mean width,  $\bar{b}$ , by  $M = 2\pi\bar{b}$  and has units of length [51]. The integral of total curvature is the product of the principal curvatures, and the local mean curvature is the average of the principal curvatures [76]. The integral of Gaussian curvature is a dimensionless parameter and is defined by:  $K = 4\pi\chi$ , where  $\chi$  is the Euler characteristic and is equal to no. objects - no. tunnels + no. enclosed voids [13]. Several methods can be used to estimate the Minkowski functionals for discrete binary data. The algorithm by Ohser and Mücklich has been found to estimate these values reasonably well, particularly if the shape has some rounding [13, 75].

### 2.2.5 Interface shape distribution

Another well-used shape descriptor in materials science and engineering is the interface shape distribution (ISD) to study the three-dimensional coarsening behavior in liquid-solid systems [17, 77]. The interface shape distribution,  $P(\kappa_1, \kappa_2)$ , the probability of finding a region of interface with a minimum principal curvature  $\kappa_1$  and maximum principal curvature  $\kappa_2$ , weighted by area [17]. The mean and Gaussian curvatures are measured along the interfaces between the liquid and the solid. The mean curvature is defined as  $(\kappa_1 + \kappa_2)/2$ , and the Gaussian curvature is defined as  $\kappa_1\kappa_2$ . They are useful to determine the direction that coarsening prefers to proceed [17].

### 2.2.6 Superellipsoid

Although the shapes of  $\gamma'$  precipitates can be described using a variety of mathematical expressions, the superellipsoid expression is a useful one to describe  $\gamma'$  shapes and has been used by MacSleyne and Callahan [13, 14]. The superellipsoid is defined as:

$$\left|\frac{x}{a}\right|^n + \left|\frac{y}{b}\right|^n + \left|\frac{z}{c}\right|^n = 1 \quad (2.63)$$

The shape of a superellipsoid is dictated by the value of its exponent, ranging from an octahedron to a sphere to a cuboid to a cube. Selected superellipsoids are shown in Figure 2.7. For the cube, its exponent,  $n$ , is  $\infty$ . A cuboid is an intermediate shape that resembles a cube with rounded corners; as the exponent value increases, the cuboid becomes more cube-like and its corners become less rounded. This makes the superellipsoid a good parameter to describe  $\gamma'$  precipitates, since  $\gamma'$  precipitates at low lattice misfits tend to range from spherical to cuboidal shapes [78].

This exponent takes on certain values for different shapes when  $a = b = c$ :  $n = 1$  corresponds to octahedral shapes, ellipsoids correspond to  $n = 2$ , cuboids have  $n > 2$ , and cube have  $n = \infty$ . The superellipsoid is also useful because its moment invariants can be

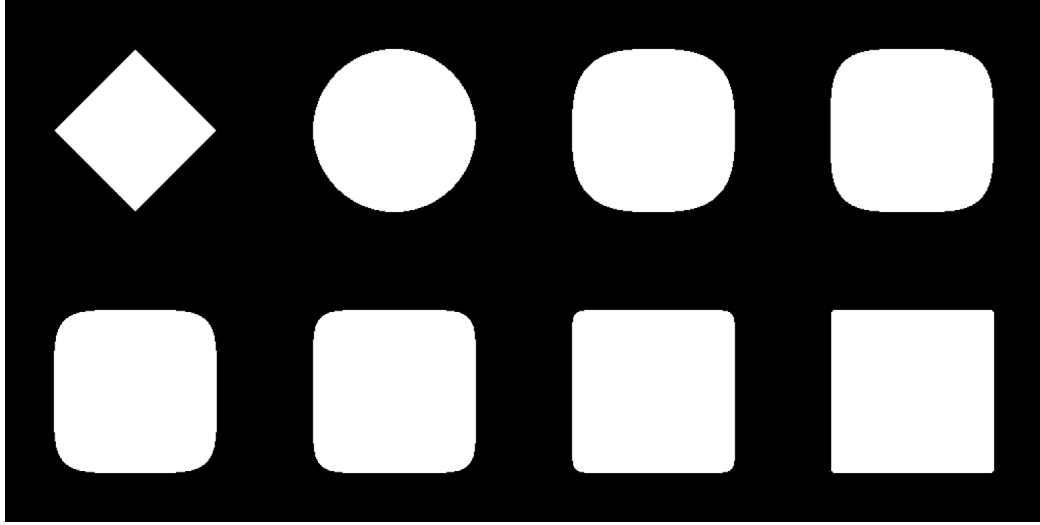


Figure 2.7: 2D sections of superellipsoid shapes with varying  $n$  exponents. From left to right: (top) 1, 2, 3, 4 (bottom) 5, 7, 15, 50.

expressed in closed form (with  $\sigma = a/c$  and  $\tau = b/c$  [5, 16]):

$$\Omega_1^{SE} = F[n] \frac{3(\sigma\tau)^{3/2}}{1 + \sigma^2 + \tau^2}, \quad (2.64)$$

$$\Omega_2^{SE} = F^2[n] \frac{3(\sigma\tau)^{4/3}}{\sigma^2\tau^2 + \sigma^2 + \tau^2}, \quad (2.65)$$

$$\Omega_3^{SE} = F^3[n], \quad (2.66)$$

where

$$F[n] = 20 \frac{\Gamma[1 + \frac{1}{n}]^3 \Gamma[\frac{5}{n}]}{\Gamma[\frac{3}{n}] \Gamma[1 + \frac{3}{n}]^{5/3}} \quad (2.67)$$

and  $\Gamma[x]$  is the complete gamma function. Once the moment invariants for the superellipsoids have been found,  $n$  can be estimated using the relationship between  $\bar{\Omega}_3$  and  $n$ , which exists because of the affine invariance of  $\bar{\Omega}_3$  [5, 16]. The relationship between  $\bar{\Omega}_3$  and the exponent  $n$  is shown in Figure 2.8.

Density maps (SOMIMs and PMIMs) have been computed for cuboids with varying  $n$  values by taking 5000 random sections through a simulated 3D cuboid. Density maps were also computed for the sphere and the cube, as shown in Figure 2.9. A library of pre-computed shapes has been generated to classify experimental shapes. The library can then be compared to experimental shapes, and distance metrics can be used to determine which computed shape most closely resembles the experimental shape. Distance metrics are

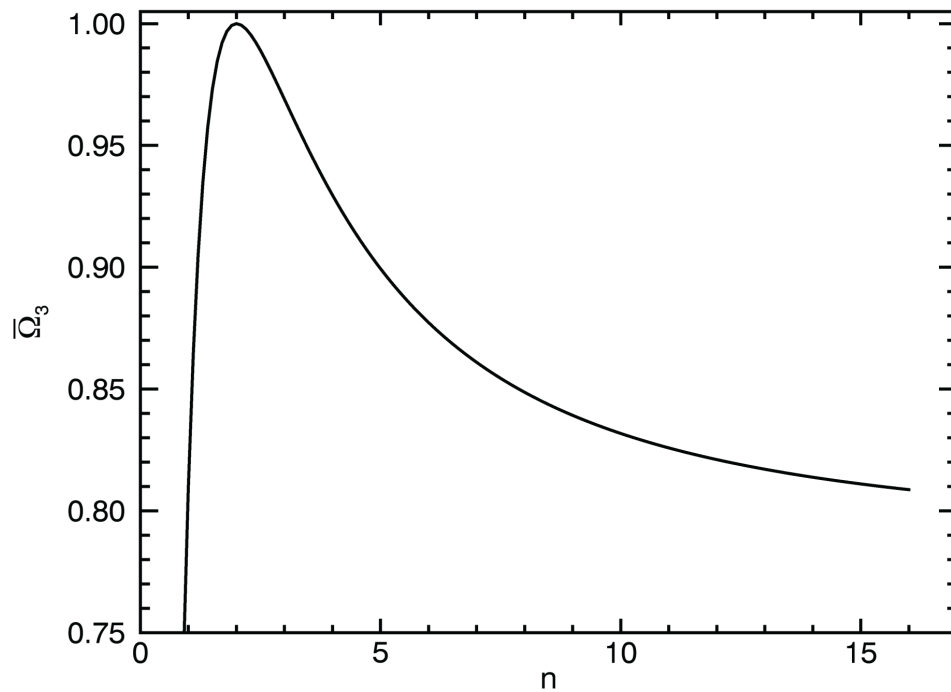


Figure 2.8: The relationship between the 3D affine moment invariant  $\bar{\Omega}_3$  vs. the superellipsoid exponent  $n$ . As  $n$  increases, the shape becomes closer to a cube. *Figure adapted with permission from Ref. [1]. Copyrighted by Elsevier.*

explained in Section 2.3. Appendix A shows an analysis of the sensitivity of the exponent  $n$ , where it was determined that 0.5 increments in the exponent show a noticeable change in the shape. Figure 2.10 shows 2D sections normal to  $\langle 001 \rangle$  of cuboids with exponent values that differ by 0.5. The differences in the cuboids that have exponents that differ by less than 0.5 are so small, that cuboids in 0.5 increments is sufficient to distinguish the shapes.

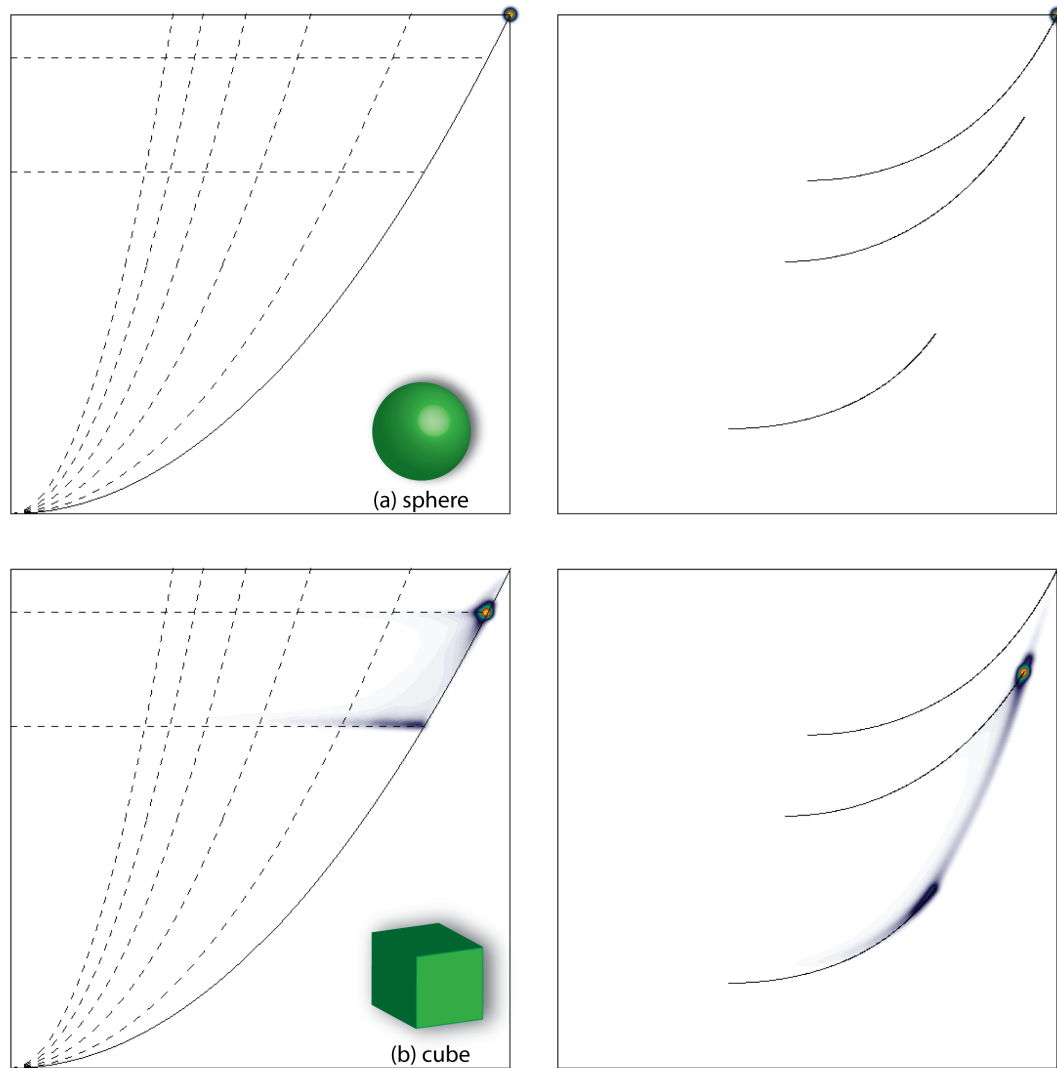


Figure 2.9: The SOMIM and PMIM for 5000 random 2D cross-sections through the (a) sphere and (b) the cube.

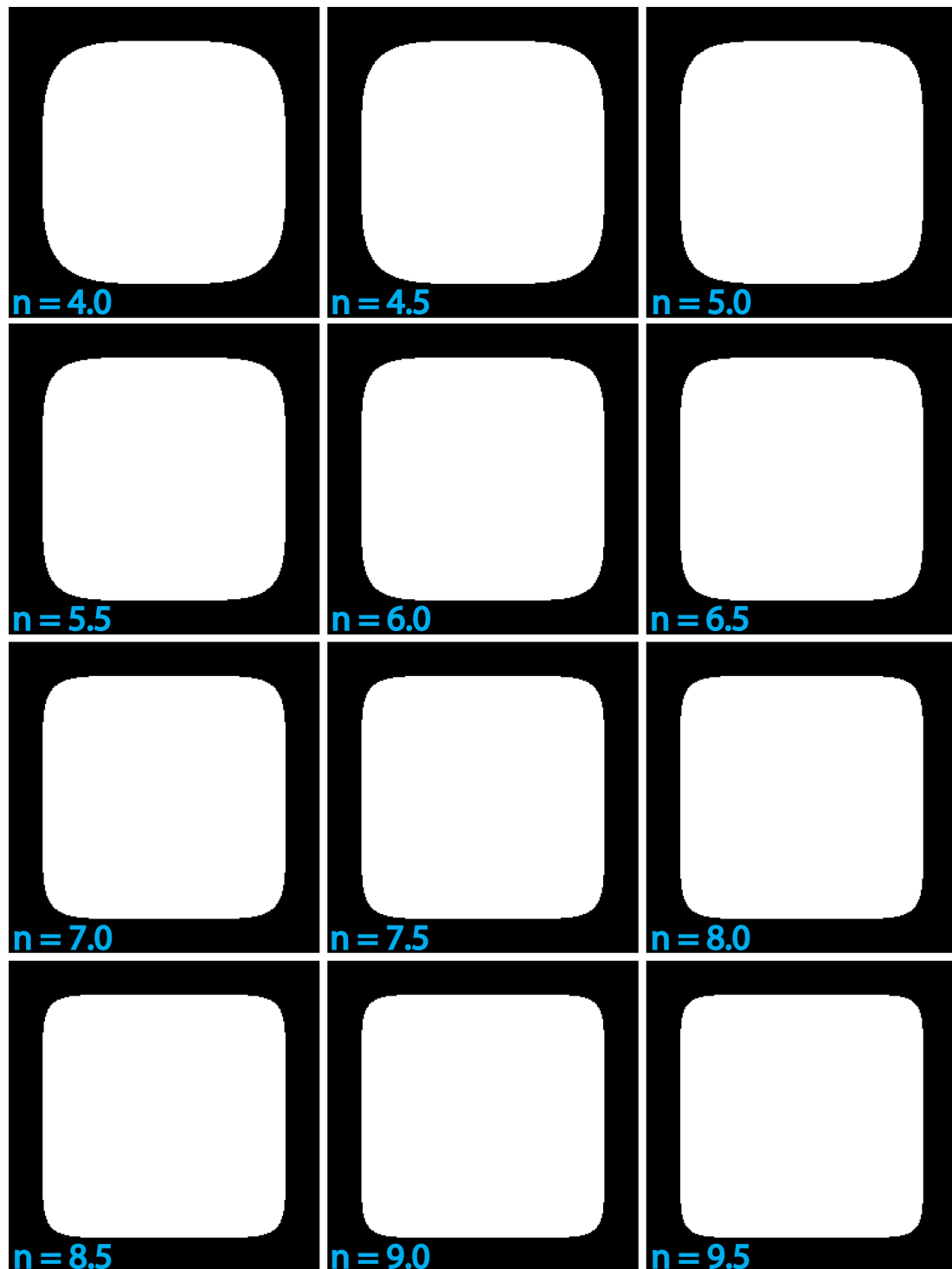


Figure 2.10: 2D sections through (100) of cuboids with superellipsoid exponent  $n$  between 4.0 and 9.5, in increments of 0.5.

## 2.3 Comparison metrics

Moment invariants can be computed for a given microstructure; its SOMIMs and PMIMs can then be generated, which are distributions of certain moment invariants. After the density maps have been computed, distance metrics are used to determine how similar two distributions, or two microstructures, are to each other in a satisfyingly quantitative way.

One of the most common ways to determine how similar two points on a graph are from each other is to compute the distance between them. This concept can also be used to compute the distance between two distributions that are represented in the simplest case, as a histogram. Often it is useful to re-scale a histogram as a probability density function (pdf). Consider  $X$ , a set of  $n$  elements that are discrete and finite. The frequency of each value in the set  $X$  is represented by a histogram  $H(X)$ . Let the number of bins in the histogram be represented by  $d$ . For the distance metrics discussed, the nominal type histogram is considered, where each bin is independent from other bins. The pdf is obtained by dividing each bin of a histogram by the total number of elements,  $n$ , represented as:

$$pdf = \frac{H(X)}{n}. \quad (2.68)$$

As such, the values in the bins in the normalized histogram sum to one. This is equivalent to having an area under the curve equal to one.

Distance metrics are used in many applications: in mathematics, its uses range from geometry, probability, statistics, graph theory, clustering, to more applied fields such as data analysis, pattern recognition, computer vision, astronomy, geography, cosmology, molecular biology, and more [79,80]. Several distance metrics can be used, but the decision of which one to use depends on the measurement type and the representation of objects [81]. Since many measures have been applied to a variety of fields, it can sometimes be difficult to determine which is the most appropriate.

Two probability density functions can be compared to each other using various distance or similarity measures. There is a distinction between the definitions of distance and similarity from a scientific and mathematical point of view. Distance is a quantitative degree of

how far apart two objects are or how dissimilar they are, whereas similarity is how close in proximity two objects are to each other [81]. So for a distance metric of 0, that means that the two objects are the same. For a similarity metric of 0, that means the two objects are completely different. Only distance metrics will be discussed in this chapter. The applicability of a distance metric may be appropriate in one situation, but not in another situation due to the sensitivity of the distance metric and how quickly it increases with changes in the pdf.

A brief overview of some distance metrics is discussed below. Minimum distance estimation has been around since the 1950s and quantifies the degrees of closeness between two sets of data [82]. There are two basic approaches to pdf distance measures: vector and probabilistic [81]. A pdf can be considered a vector because each bin level is assumed to be independent of the other bin levels, such as points in Euclidean space. The distance between two histograms can also be regarded as computing the Bayes probability and equivalent to measuring the overlap between the two pdfs [81].

Many geometrical distances can be applied to compare two probability density functions, but their usefulness depends on the application. Distance metrics can be categorized into different families that are based on the same mathematical property. Three types of families are discussed here.

### 2.3.1 Euclidean distance

The most well-known is the  $L_1$  Minkowski family, which includes the derivations of the Euclidean distance. The  $L_1$  family is also known as the absolute difference and the intersection family is a subset of the  $L_1$  family. The Euclidean distance, also known as the Pythagorean metric, measures the distance between two points. This is a familiar concept, as it is based on the Pythagoras Theorem where  $a^2 + b^2 = c^2$ . The Euclidean distance is computed as:

$$D_{Euc} = \sqrt{\sum_{i=1}^d |P_i - Q_i|^2}, \quad (2.69)$$

where  $P$  and  $Q$  are two pdfs. Related distances to the standard Euclidean distance include the city block distance, the Minkowski distance, and the Chebyshev distance [81]. These are

all considered linear metrics, but metrics can also be computed non-linearly by performing a nonlinear mapping to project the data into another space and evaluate the pairwise data distance as their Euclidean distance in the projected space [80].

The Euclidean distance has been used to determine how different shapes in the moment invariant space are from each other. MacSleyne [4] computed the Euclidean distance between a square and a circle in  $\varphi$  space, which are the 2D second-order moment invariants that have not yet been normalized by the values for a circle:  $d_{\square-\circ} = \frac{\pi-3}{6\pi} = 7.5117 \times 10^{-3}$  and in  $\omega$  space as  $d'_{\square-\circ} = \sqrt{(16\pi^2 - 144)^2 + (4\pi - 12)^2} = 13.9252$ .  $\varphi_i$  is

$$\varphi_1 = \frac{\bar{\mu}_{20}}{A^2} + \frac{\bar{\mu}_{02}}{A^2} \quad (2.70)$$

$$\varphi_2 = \left( \frac{\bar{\mu}_{20}}{A^2} - \frac{\bar{\mu}_{02}}{A^2} \right) + 4 \frac{\bar{\mu}_{11}^2}{A^2} \quad (2.71)$$

However,  $\omega$  is not normalized by the moment invariants for the circle, so the distance in  $\bar{\omega}$  space can be computed as:  $d''_{\square-\circ} = \sqrt{(1 - 0.9549)^2 + (1 - 0.9119)^2} = 0.09897$ .

### 2.3.2 The Hellinger distance

The Hellinger distance, also known as the modified Bhattacharyya coefficient, provides good balance between computation speed, usability, and its ability to distinguish between two distributions  $p$  and  $q$  [14, 83–85]. The Bhattacharyya coefficient  $\beta(p, q)$  measures the similarity of two normalized distributions and is written as [83]:

$$\beta(p, q) = \sum_{i=1}^N \sqrt{p(i) q(i)}, \quad (2.72)$$

where

$$\sum_{i=1}^N p(i) = \sum_{i=1}^N q(i) = 1$$

and  $N$  is the number of bins, and  $p(i)$  and  $q(i)$  have been normalized by the number of observations. The Hellinger distance, a true metric, is a simple comparison descriptor and a modified form of the Bhattacharyya coefficient that is defined as [85]:

$$H(p, q) = \sqrt{1 - \beta(p, q)}. \quad (2.73)$$

A true metric is one that satisfies symmetry and the triangle inequality [86]. The Hellinger distance is used instead of the Bhattacharyya distance because it satisfies symmetry and the triangle inequality [14, 84]. The Hellinger distance has been used previously in materials science and engineering [14]. It can be computed for both the SOMIM and PMIM separately for two given microstructures and can then be combined into one root-mean-square Hellinger distance  $\delta$  value, defined as [14, 16]:

$$\delta = \frac{1}{\sqrt{2}} \sqrt{[H(p_s, q_s)]^2 + [H(p_p, q_p)]^2} \quad (2.74)$$

where  $H(p_s, q_s)$  is the Hellinger distance of the two SOMIMs being compared, and  $H(p_p, q_p)$  is the Hellinger distance of the two PMIMs being compared. Equation 2.74 is the average Hellinger distance to compare both the SOMIM and the PMIM to another SOMIM and PMIM pair.

The Hellinger distance varies from 0 to 1; the more similar the two distributions  $p$  and  $q$  are to each other, the smaller the value of  $\delta$ . This can then be used to compare the moment invariant distributions of a dataset to a set of already computed moment invariant maps, such as the maps in Figure 2.9. It is a useful method to determine whether microstructure  $A$  is most similar to that of microstructure  $B$  or  $C$ . Prior work on the Hellinger distance has shown it to be robust, reliable, and sensitive in the quantification of the similarity of shapes in microstructures [14]. The Hellinger distance is a useful parameter that can be used to compute the “distance between microstructures” [14].

### 2.3.3 The chi-squared distance

Another distance metric is the chi-squared distance, which is used frequently in computer vision applications and is a type of weighted Euclidean distance [87, 88]. There have been various studies in computer vision by comparing images and computing image histograms; the chi-squared distance is frequently chosen as the best distance metric [89]. The chi-squared distance is calculated between the relative counts for each distribution and weight each variable by the inverse of the variable’s overall mean count and is easy to compute. It is based on Pearson’s chi-squared test,  $\chi^2 = \sum_{i=1}^n \frac{(O_i - E_i)^2}{E_i}$ , which is commonly used in

statistics, and can be computed using the equation:

$$\chi = \frac{1}{2} \sum_i \frac{(X_i - Y_i)^2}{X_i + Y_i}, \quad (2.75)$$

where  $X_i$  and  $Y_i$  are two image histograms with an equal number of bins. This metric is a type of Euclidean distance, and normalized distributions are not necessary in order to compute the chi-squared distance. The chi-squared distance is used in addition to the Hellinger distance to compute how different two moment invariants distributions are from each other.

## 2.4 Summary

Several shape descriptors have been described: shape analysis in materials science, moment invariants in 2D and 3D, 2D and 3D shape parameters, Minkowski functionals, and the superellipsoid. Three distance metrics were introduced to distinguish between the shapes of different microstructures: the Euclidean distance, the Hellinger distance, and the chi-squared distance. In the following chapters, selected shape descriptors are applied to various materials systems to study microstructural evolution.

## CHAPTER III

### The effect of rafting in Ni-based superalloys

#### 3.1 Introduction

Superalloys are well known for their use as turbine blades in jet engines due to their excellent mechanical properties at high temperatures, including high strength, high creep resistance, and fatigue resistance [73,90–94]. Precipitate hardening contributes to the strength, due to the presence of an ordered intermetallic L1<sub>2</sub> precipitate phase, known as  $\gamma'$  that is dispersed throughout the FCC ( $\gamma$ ) matrix [78,95]. A high volume fraction of this phase is the key to a superalloy's strength; in nickel-based superalloys, the volume fraction of  $\gamma'$  is about 0.6 or higher [78,95]. The preferred  $\gamma'$  precipitate shape is one that causes as much strain on the matrix as possible while still maintaining coherency and can vary in shape between spherical, cuboidal, plate-like or irregular [78,95].

$\gamma'$  precipitates have different shapes depending on the lattice mismatch; a negative misfit means that the lattice strain in the  $\gamma'$  is larger in the  $\gamma$  matrix, and a positive misfit results in a smaller  $\gamma'$  lattice strain than in the  $\gamma$  phase. The lattice misfit,  $\delta$ , is defined as:

$$\delta = \frac{a_{\gamma'} - a_{\gamma}}{a_{\gamma}}, \quad (3.1)$$

where  $a_{\gamma}$  and  $a_{\gamma'}$  are the lattice parameters of the unconstrained  $\gamma$  and  $\gamma'$  bulk phases, respectively [96]. A near zero misfit results in a spherical shaped precipitate, which does not directionally coarsen as long as the elastic constants of the matrix and the precipitates are similar [95]. A positive misfit results in an intermediate shaped precipitate, one between spherical and cuboidal; the rafting direction of these precipitates is parallel to the applied

stress direction [92,97]. A negative misfit also results in an intermediate shape precipitate, and the rafting direction of the precipitates is perpendicular to the direction of the applied stress [92,97].

Under normal conditions, the magnitude of the lattice misfit determines the shape of the  $\gamma'$  precipitates, which can range from spherical (for misfits in the range 0 to 0.2%), cuboidal (0.5 to 1%), and platelike (above 1.25%) [78,95]. However, when precipitates coalesce, they form long-range, interconnected networks, known as “rafts.” Two types of directional coarsening behavior have been observed in  $\langle 001 \rangle$  oriented nickel-based single crystals [98]:

- Type N:  $\gamma'$  precipitates directionally coarsen normal to the direction of the externally applied stress;
- Type P:  $\gamma'$  precipitates directionally coarsen parallel to the direction of the externally applied stress.

When a single crystal is loaded in tension, a negative misfit crystal forms N-type rafts while positive misfit crystals form P-type rafts; when loaded in compression, the opposite rafting types are observed [92].

Under creep conditions these  $\gamma'$  precipitates can directionally coarsen together and appear plate-like in morphology, which is known as rafting. The creep conditions in commercial alloys are created by the uniaxial tension due to high operational centrifugal forces [94]. The amount of rafting determines the performance and lifetime of turbine blades, so it is necessary to control rafting in superalloys [92]. There are two broad classes of theories of rafting: elasticity-driven and plasticity-driven [9,92,93]. Different models have been developed to simulate rafting in Ni-based superalloys, considering the plasticity in  $\gamma$ -channels in elastically anisotropic and inhomogeneous systems [8]. One of the applications of the moment invariant analysis is to be able to quickly detect if a micrograph contains rafted  $\gamma'$  precipitates or not so that a turbine blade can be taken out of service, if needed. In this chapter, moment invariants can be used to track the change in  $\gamma'$  shape and to determine if rafting has started or occurred. The structure of the chapter is as follows: the phase field model that was used to generate these microstructures is discussed, followed by a discussion of the techniques used. The results in 3D are discussed next, followed the 2D MI

results. Then 2D MIs are compared to other shape descriptors, followed by an evaluation of the  $\gamma$  matrix using 2D moment invariants. This chapter concludes with a discussion and a summary of the results.

## 3.2 Theoretical and modeling approach

### 3.2.1 Phase field model

The datasets are provided courtesy of Rongpei Shi of the Ohio State University and are simulated using phase field modeling, the details of which are described in [8]. The synthetic two-phase  $\gamma/\gamma'$  microstructures were generated using phase field simulations of  $\gamma'$  precipitation without external load (the initial microstructure) and rafting under external load in two Ni-base superalloys (Ni-Al) with positive and negative misfits (i.e.  $\pm 0.3\%$ ) [8]. The simulations were carried out in a 3D system of  $256 \times 256 \times 256$  grid points with a grid size of 20 nm, which represents a system size of  $(5.12\mu\text{m})^3$ . In formulating chemical free energy of the system, four phenomenologically defined order parameters were introduced to characterize the four crystallographically equivalent anti-phase domains of the  $\gamma'$  phase. The individual equilibrium free energies of the  $\gamma$  and  $\gamma'$  phases were linked together by a Landau polynomial of the order parameters. Even though the individual free energies of  $\gamma$  and  $\gamma'$  phase could have been obtained from the CALPHAD thermodynamic database for specific alloys [99, 100], only parabolic polynomials with the common-tangent compositions fitted to the equilibrium compositions from the database were used. The focus is to study directional coarsening during which solute concentrations in the  $\gamma$  and  $\gamma'$  phases are nearly around their equilibrium compositions. The input microstructure shows the  $\gamma/\gamma'$  mi-

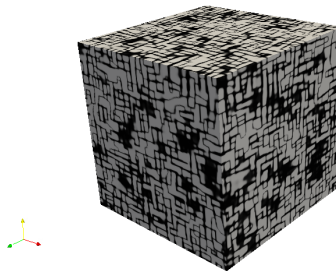


Figure 3.1: The starting microstructure for microstructures with a negative and a positive misfit.

microstructure developed in alloys of lattice misfit  $\delta = \pm 0.3\%$  without external load after 9.44 hours aging at 1300K as shown in Figure 3.1. Without external load, the  $\gamma'$  microstructures developed under positive and negative misfits are identical). Its SOMIM and PMIM is shown in Figure 3.2 The simulated aging process started with a homogeneous super-

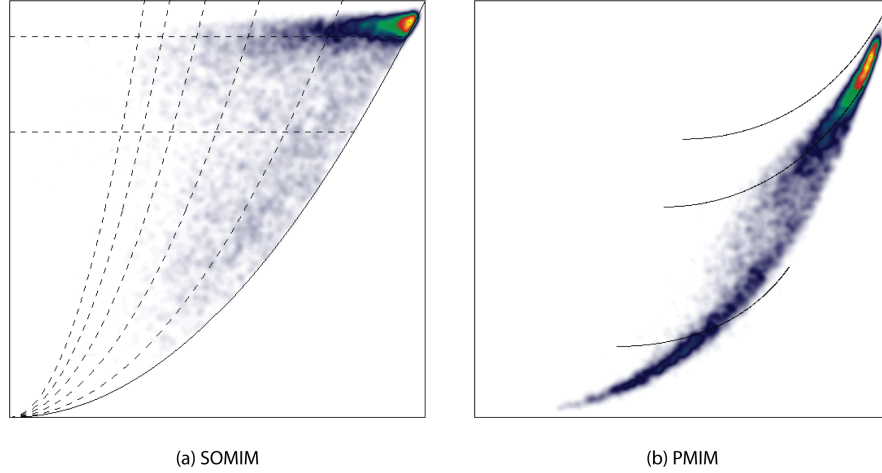


Figure 3.2: (a) The SOMIM and (b) the PMIM for the starting microstructure for microstructures with a negative and a positive misfit.

saturated solid-solution of the  $\gamma$  phase and nucleation of  $\gamma'$  particle was described by the Langevin noise terms (in the first 100 time steps that correspond to 3 minutes in real time). The light shade of gray represents the  $\gamma'$  phase while the dark shade of gray represents the  $\gamma$  matrix. The volume fraction of the  $\gamma'$  phase is about 60% and the sizes of most precipitates are between 160 to 360 nm.

This initial  $\gamma$  and  $\gamma'$  microstructure was then further evolved under a uniaxial tensile load. Dislocation activities in the  $\gamma$  channels under the external load, and their interactions with the  $\gamma'$  particles were considered by introducing a new set of non-conserved order parameters that characterize continuously distributed plastic strain fields associated with the dislocations from each active slip systems. Moreover, the crystalline energy that originally carries periodic interatomic potential with respect to inelastic displacement (or disregistry) is coarse-grained to a constant averaged potential energy that only renormalizes the total free energy. For details about the formulation of the phase field model and the model parameters, the readers are referred to [8].

The N- and P-type rafted microstructures obtained after 9.44 hours aging at 1300K

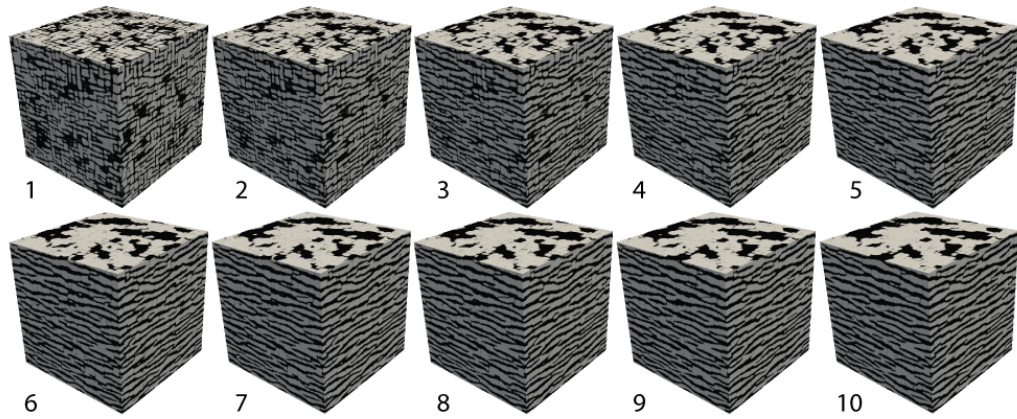
under 152MPa tension along [001] for a negative misfit (-0.3%) and a positive-misfit (0.3%) are shown in Figure 3.3(b) and Figure 3.3(c), respectively. Because sufficient system size has been considered in the phase field simulations, the simulated microstructures are able to capture statistical variations in the morphology and spatial distribution of  $\gamma'$  precipitates observed in experiment [96]. In particular, it can also be seen that the N-type microstructure appears to have more regular alignment across rafted precipitates as compared to the P-type microstructure, at the same level of external load and lattice misfit. This could be attributed to the fact that it is less possible for the P-type  $\gamma'$  rafts ( $\gamma'$  rods in this case) to meet head on with adjacent rafts as compared to the case of the N-type rafts ( $\gamma'$  plates). Figure 3.3 shows examples of the microstructure.

### 3.2.2 3D microstructural image analysis

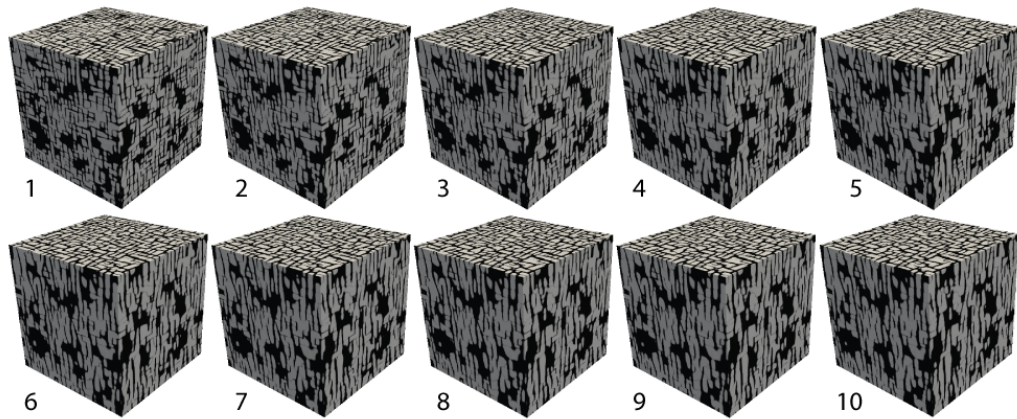
First, a spherical mask can be applied to the  $256^3$  dataset. The three 2nd order 3D MIs are computed for each time step and are plotted on a 3D plot. Since the microstructures at later time steps do not have many precipitates, it is difficult to compare the microstructures at different time steps by only considering the precipitates. An alternative approach is used, one that applies a spherical mask to a smaller region and used to scan across the image. The average precipitate size is taken to be about 0.2% of the microstructure, so a box that is slightly bigger than that is used to be the appropriate box (region of interest) size. A box with a size of  $a = 33^3$  is used to scan throughout the dataset, which is 0.2% of the entire microstructure. This results in 10,941,048 MI triplets. The visualization of data points over ten million data points is difficult to visualize in 3D, so one method is to make 2D plots of the 3D MIs, as a projection. The resulting plots have the following axes:  $\bar{\Omega}_1$  vs.  $\bar{\Omega}_2$ ,  $\bar{\Omega}_1$  vs.  $\bar{\Omega}_3$ ,  $\bar{\Omega}_2$  vs.  $\bar{\Omega}_3$ , which a curve in each depicting the projection of the isotropic shape curve.

### 3.2.3 2D microstructural image analysis

For each 3D dataset, 2D sections were taken normal to the  $y$ -direction, resulting in a total of 256 section images. While the data set could be sectioned along other directions, the  $y$ -direction was chosen because it clearly showed the growth of the  $\gamma'$  precipitates with time. Each image has  $256 \times 256$  pixels and was turned into a binary image by thresholding using



(a) microstructure with a negative misfit



(b) microstructure with a positive misfit

Figure 3.3: 3D representation of the microstructures resulting from the simulation at the ten time steps. The dark regions represent the  $\gamma$  matrix while the gray regions represent the  $\gamma'$  phase. (a) Microstructures with a negative misfit showing  $\gamma'$  plates (b) microstructures with a positive misfit showing  $\gamma'$  rods. *Figure adapted with permission from Ref. [8]. Copyrighted by Taylor & Francis.*

a simple mean threshold. 2D second-order and fourth-order MIs were then computed for each  $\gamma'$  precipitate in each 2D section from a 3D dataset. Due to the coalescing of particles, density maps for the earlier time steps contain more data points than those for the final time steps; the average number of particles per section for each time step is shown in Table 3.1. Since a sufficient number of images and precipitates was used, the density maps show sufficient detail so that the shape evolution can be followed. The distribution of MIs for each time step is represented on both second order moment invariant maps (SOMIM) and projected moment invariant maps (PMIM). These density maps are then used to study how the MI distributions change with respect to stress and time.

Time step	No. of precipitates
1	173
2	94
3	53
4	32
5	22
6	17
7	15
8	13
9	12
10	12

Table 3.1: The average number of precipitates per image. The number of precipitates in an image decreases over time.

### 3.3 Results

3D views of the microstructure at each time step are shown in Figure 3.3. The loading direction is along the [001] direction (vertical), so the negative misfit microstructure is coarsening perpendicular to the direction of loading, and the positive misfit microstructure is coarsening parallel to the direction of loading. Since the  $\gamma'$  precipitates are coarsening, they are also increasing in size. The 3D MI results will be considered first, followed by the 2D MI results. Then, the 2D MI approach is compared to other shape descriptors.

#### 3.3.1 3D results

The 3D moment invariants were computed for microstructures with both types of misfit at each time step considering the entire  $256^3$  dataset and plotted with axes  $\bar{\Omega}_1$ ,  $\bar{\Omega}_2$ , and  $\bar{\Omega}_3$ , as shown in Figure 3.4. The spherical mask causes the MIs to lie along the isotropic shape curve. Figure 3.5 shows plots for each MI by taking the average of the MIs  $((\bar{\Omega}_1 + \bar{\Omega}_2 + \bar{\Omega}_3)/3)$ . When considering the entire dataset, the MIs are increasing with time because the spherical window is becoming more consumed by the precipitates as they grow. From the results of the whole dataset shown in Figure 3.5(a), the average 3D MIs in the negative misfit dataset (indicated in blue) increase linearly until time step 4; from time step 5 and on, the average continues to increase, but very slowly. The average MIs in the positive misfit dataset (indicated in red) never increase linearly, but they are still increasing more quickly in the beginning than towards the end. When considering each of the 2nd order

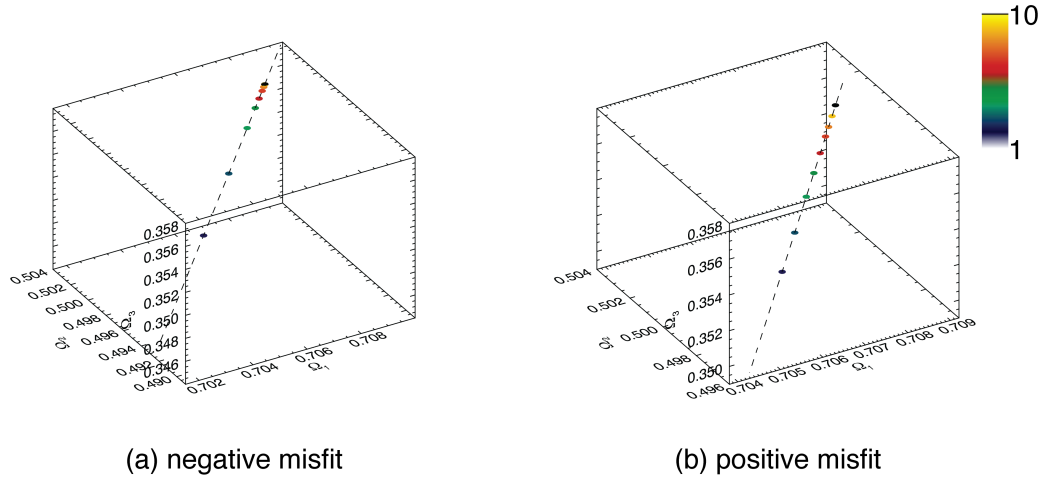


Figure 3.4: Evolution of 3D second-order moment invariants over time, where blue marks the initial time step and the black is the last time step. By computing the MIs within a circular region, the MIs increase with time. (a) negative misfit (b) positive misfit.

MIs individually, they all seem to follow this same trend in both datasets.

The MIs were computed using a box with size  $a = 33^3$ . When plotting the MIs for each cube, they all lie on or close to the isotropic shape curve, so only the region of interest is shown in Figure 3.6 and 3.7. Initially at early times, there is a small distribution of shapes that lie mostly on the isotropic shape curve for both misfits. The distribution of shapes broadens as time continues, and towards the end, there is a deviation from the isotropic shape curve.

The boxes do not seem to deviate much from the isotropic curve, represented as  $\bar{\Omega}_p = (p, p^2, p^3)$ , where  $0 \leq p \leq 1$ . The average  $p$  value, which is the value on the isotropic shape curve that is closest to each ROI, does not change much with time. However, the distribution of minimum distance to the isotropic shape curve from  $p$  changes with time. The standard deviation is small initially; then as the distribution broadens, the standard deviation increases linearly with time. Two parameters were considered to take this deviation into account. First, there is a distribution of the equivalent isotropic shape values for each triplet,  $p$ . The full width half maximum (FWHM) is calculated for each distribution of the equivalent isotropic shape value,  $p$ , to see if the distribution widens with time. The FWHM is:

$$\text{FWHM} = 2\sqrt{2\ln 2} \sigma \approx 2.355\sigma, \quad (3.2)$$

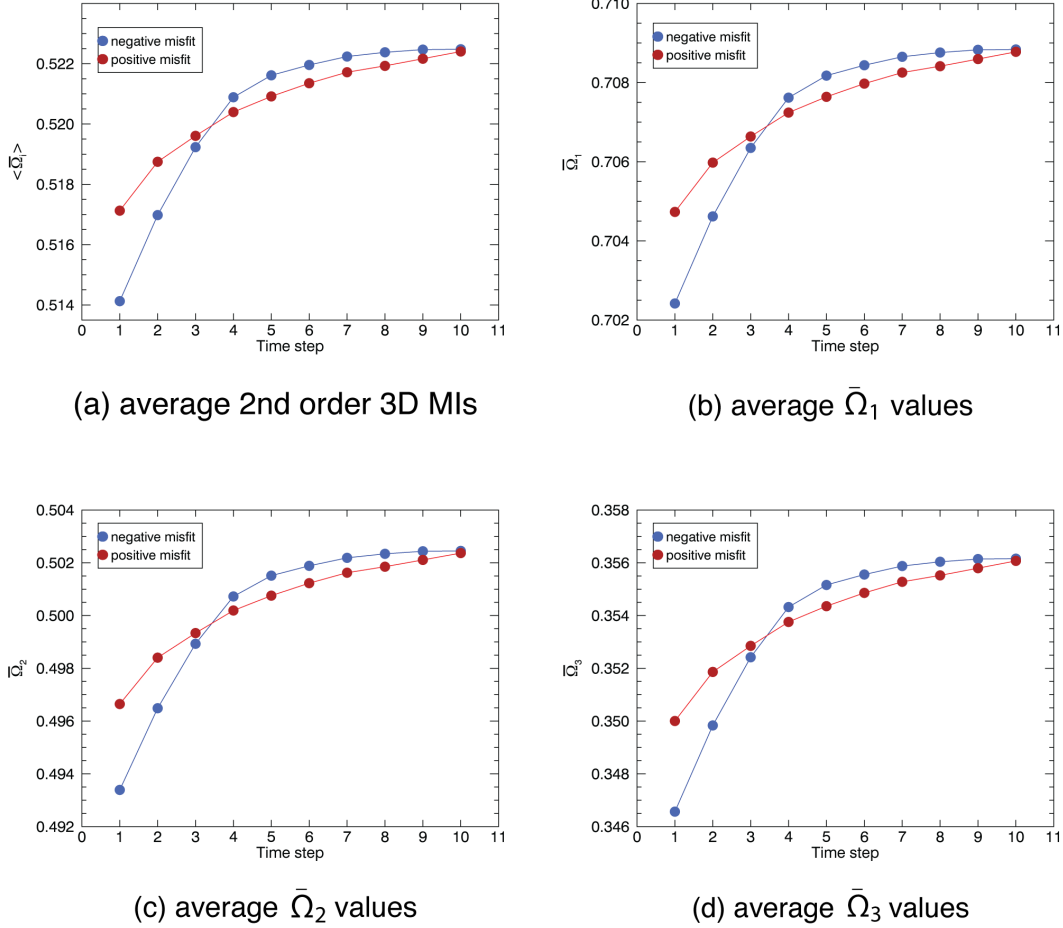


Figure 3.5: Average of 3D second-order moment invariants over time. (a) average 2nd order 3D MIs, (b) average  $\bar{\Omega}_1$ , (c)  $\bar{\Omega}_2$ , and (d)  $\bar{\Omega}_3$ .

where  $\sigma$  is the standard deviation. The minimum distance for each distance from the nearest point on the isotropic shape curve can be considered. The minimum distance is calculated as:

$$\delta = \min \left( \sqrt{(x - p)^2 + (y - p^2)^2 + (z - p^3)^2} \right). \quad (3.3)$$

The percentage of boxes that have a minimum distance,  $\delta$ , greater than 0.005 was found for each time step, and shown in Figure 3.8. The critical value of 20% was chosen to be the number of boxes with a minimum distance greater than 0.005. While most of the distribution is on the isotropic shape curve, the complicated rafting shape will cause a deviation from isotropy despite the circular mask. Using this criterion, the microstructure is rafted at time step 5 for the negative misfit dataset and at time step 6 for the positive

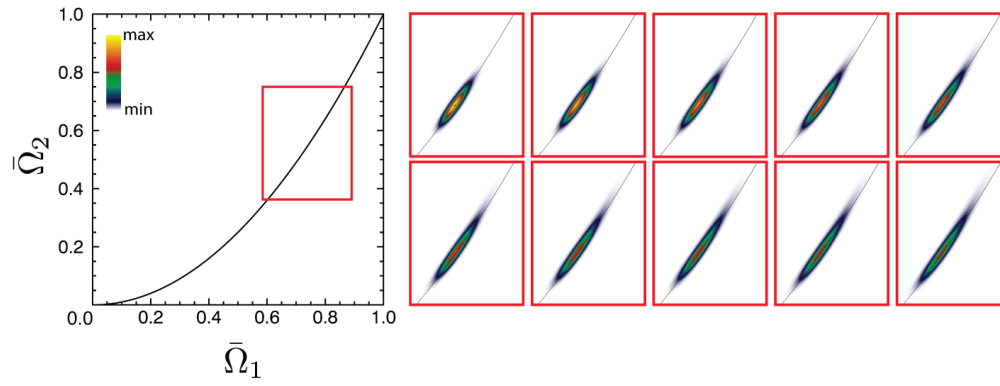
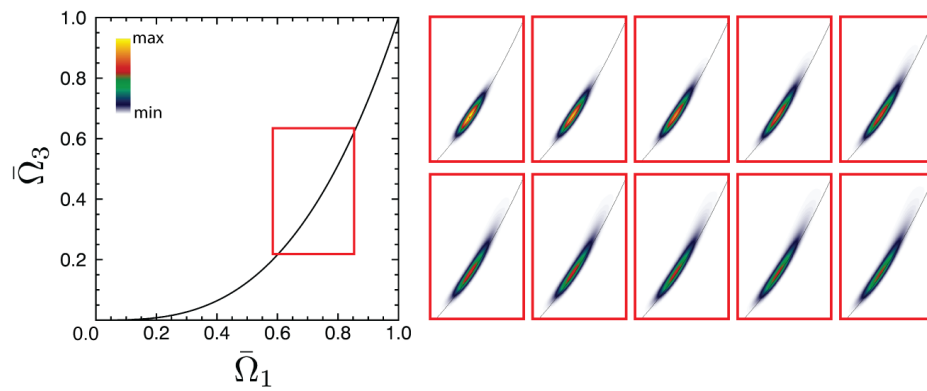
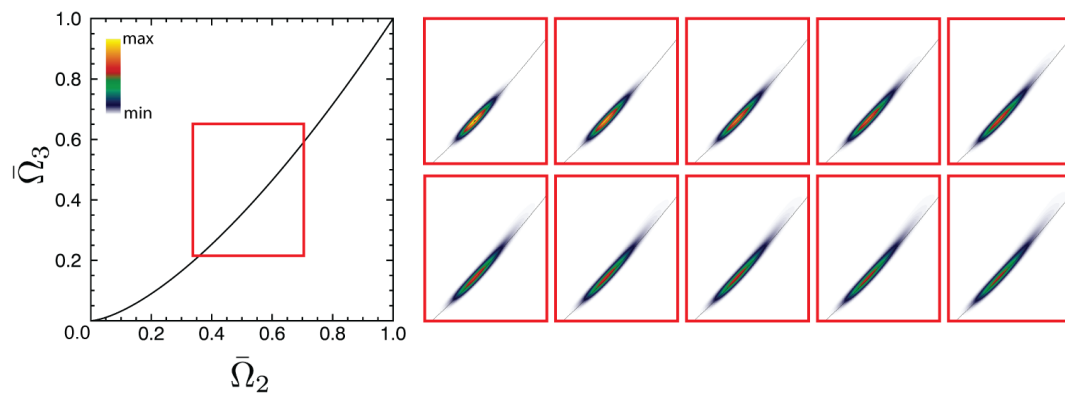
(a)  $\bar{\Omega}_1$  vs.  $\bar{\Omega}_2$ (b)  $\bar{\Omega}_1$  vs.  $\bar{\Omega}_3$ (c)  $\bar{\Omega}_2$  vs.  $\bar{\Omega}_3$ 

Figure 3.6: Moment invariants for the microstructure with a negative misfit using a scan size of  $a = 33$ . There is a deviation from the isotropic shape curve that increases with time.

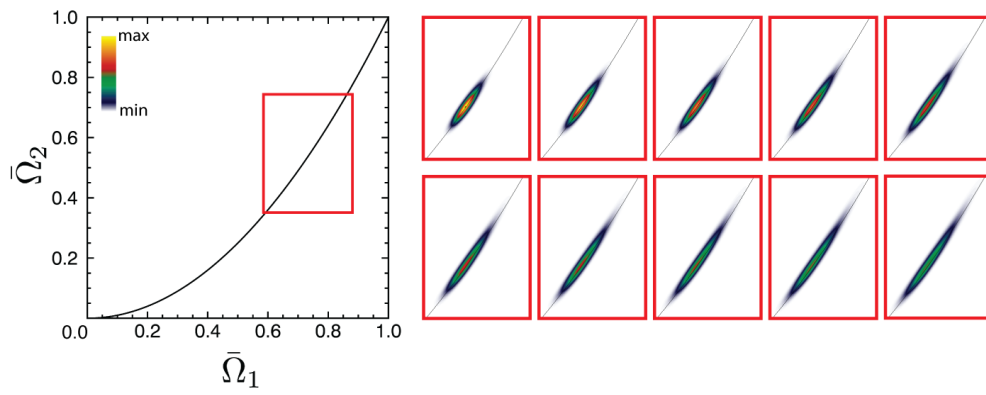
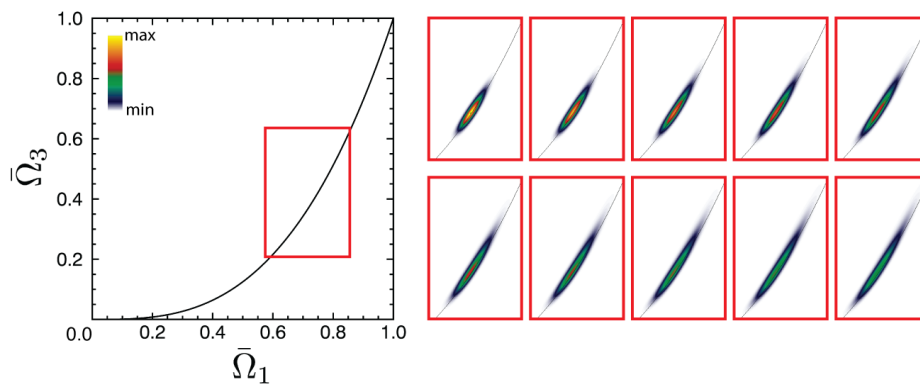
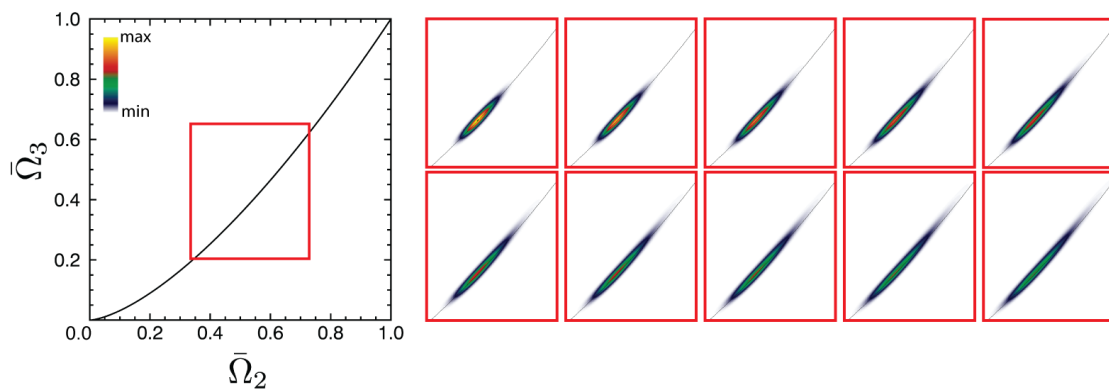
(a)  $\bar{\Omega}_1$  vs.  $\bar{\Omega}_2$ (b)  $\bar{\Omega}_1$  vs.  $\bar{\Omega}_3$ (c)  $\bar{\Omega}_2$  vs.  $\bar{\Omega}_3$ 

Figure 3.7: Moment invariants for the microstructure with a positive misfit using a scan size of  $a = 33$ . There is a small deviation from the isotropic shape curve that increases with time.

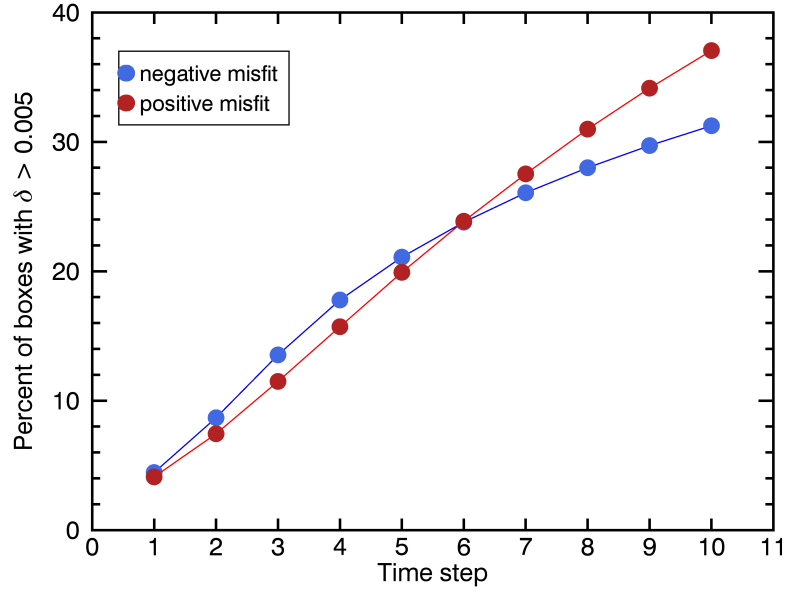


Figure 3.8: The percentage of boxes with  $\delta < 0.005$ . If the percentage of boxes is greater than 20%, the microstructure is classified as rafted. Microstructures with a negative misfit were rafted at time step 5 and above, and microstructures with a positive misfit were rafted at time step 6 and above.

misfit dataset.

### 3.3.2 2D results

By considering the area of the precipitates, it can be assumed that coarsened  $\gamma'$  precipitates will have different shapes than the non-coarsened ones. In Figure 3.9, 2D moment invariant density maps are shown for both microstructures, by classifying precipitates based on size. Moment invariants were calculated for one image from each time step, resulting in ten images being represented on each moment invariant map. Different colors indicate different precipitate sizes. Precipitates are classified as small if they are less than 200 pixels in size, large if they are greater than 2000 pixels in size, and medium if they fall between 200 and 2000. These thresholds were chosen so that medium precipitates lie in the interquartile range of precipitate sizes. Large precipitates consistently have lower moment invariant values (range between 0.114-0.660 with  $\langle \bar{\omega}_2 \rangle = 0.152 \pm 0.094$ ), and the small precipitates have high moment invariant values (range between 0.150-0.981 with  $\langle \bar{\omega}_2 \rangle = 0.911 \pm 0.131$ ). Many of the small precipitates have  $\bar{\omega}_2$  between that of a rectangle and a circle, indicating

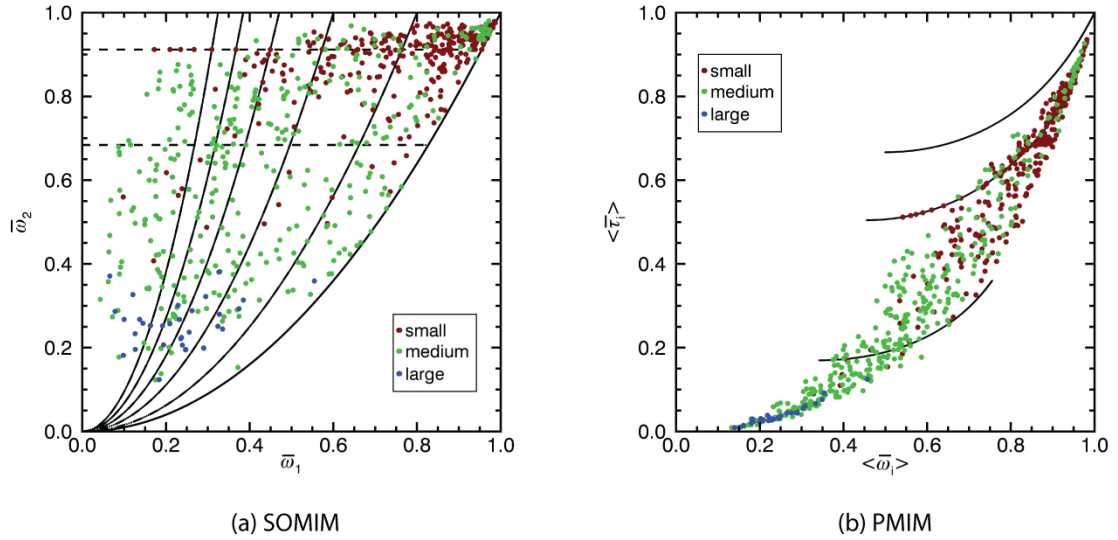


Figure 3.9: SOMIM and PMIM for precipitates sorted by size. Small precipitates are shown in brown and have high  $\bar{\omega}_2$  values. Medium sized precipitates are shown in green and show a range in MI values. Large precipitates are shown in blue and have low MI values.

that they are the typical cuboidal shape expected for this magnitude of lattice misfit. Medium-sized precipitates can vary in moment invariants ( $\langle \bar{\omega}_2 \rangle = 0.565 \pm 0.190$ ) and can be found across the moment invariant map (range between 0.129 to 0.957). Table 3.2 shows the MIs of the precipitates sorted by size. The classification by size indicates that the smaller precipitates shift from the upper right corner to the lower left corner when the precipitates increase in size. Due to differences in the phase field model, the two microstructures will be discussed separately.

Table 3.2: Average moment invariants for sorted precipitates by size.

class	range	average	standard deviation
small	0.150-0.982	0.911	0.131
medium	0.129-0.957	0.565	0.190
large	0.114-0.660	0.152	0.094

### Microstructure with a negative misfit

The SOMIM and PMIM for each time step are shown in Figure 3.10. Initially, the peak of the distribution, indicated in yellow, is in the upper right corner for both the SOMIM and PMIM plots. The majority of  $\bar{\omega}_2$  values are between those of a square and a cube (i.e., between 0.91 and 1), since many of the particles are cuboidal. The majority of the

distribution is also located in the top right corner of the PMIM, with  $\langle \bar{\tau}_i \rangle$  values in the range 0.82–1.

As the microstructure evolves, the  $\gamma'$  precipitates coarsen together and form elongated precipitates. The aspect ratios increase, indicated by a decrease in  $\bar{\omega}_1$  and a shift of the distribution towards the left on the SOMIM. The average  $\bar{\omega}_1$  evolves from 0.92 to 0.17 as the  $\gamma'$  precipitates elongate. As the microstructure continues to evolve (time steps 5 and above), they form raft-like particles that have multiple sides. This causes the majority of the distribution to shift from a peak in the upper right corner to a broad maximum centered in the lower left corner, reflecting the more complicated shape of the typical rafted precipitate.

The coarsening of  $\gamma'$  precipitates also leads to a second peak of moment invariants appearing in the PMIM. The  $\langle \bar{\omega}_i \rangle$  value is centered around 0.90 for the first four time steps and then decreases to 0.35 for the fifth step. The average  $\langle \bar{\tau}_i \rangle$  changes from 0.827 for the second time step to 0.077 for the third step. Since the PMIM tracks the evolution of the second and fourth order moment invariants,  $\langle \bar{\omega}_i \rangle$  decreases because  $\bar{\omega}_1$  decreases with increasing aspect ratio, and  $\langle \bar{\tau}_i \rangle$  decreases because more subtle differences in shape are detected by the higher order moments.

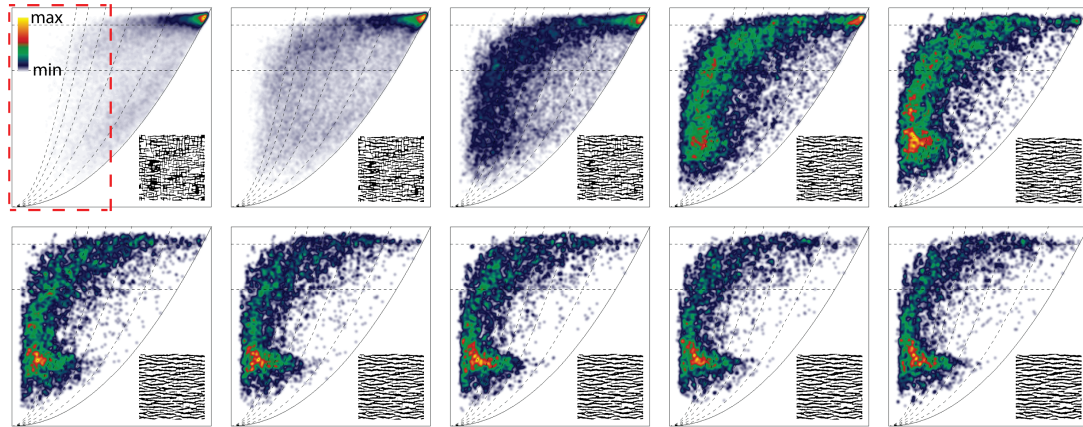
### Microstructure with a positive misfit

The density maps were also computed for the positive misfit microstructure, as shown in Figure 3.11. In the first time step shown in Figure 3.11(a), the distribution is centered in the upper right hand corner, similar to the SOMIM of the negative misfit microstructure. As the microstructure evolves, the distribution broadens horizontally, indicating a slow increase in average aspect ratio, but no other significant shape changes occur. The  $\bar{\omega}_1$  values stay fairly constant between 0.89 to 0.92 for all time steps, whereas the  $\bar{\omega}_2$  values remain in the range 0.89 and 0.90, except for the final time steps 8 and 10, which correspond to  $\bar{\omega}_2$  values of 0.311 and 0.409, respectively. The peak of the SOMIM distribution does not change much with time. In the PMIMs, the range of mean values of  $\langle \bar{\omega}_i \rangle$  is from 0.89 to 0.91, and the range of  $\langle \bar{\tau}_i \rangle$  is from 0.78 to 0.81, with outliers at 0.132 and 0.089 for time steps 8 and 10, respectively. While the  $\gamma'$  precipitates do coarsen and coalesce, the microstructure in Figure 3.3(b) indicates that the precipitates do not form the same type of complex,

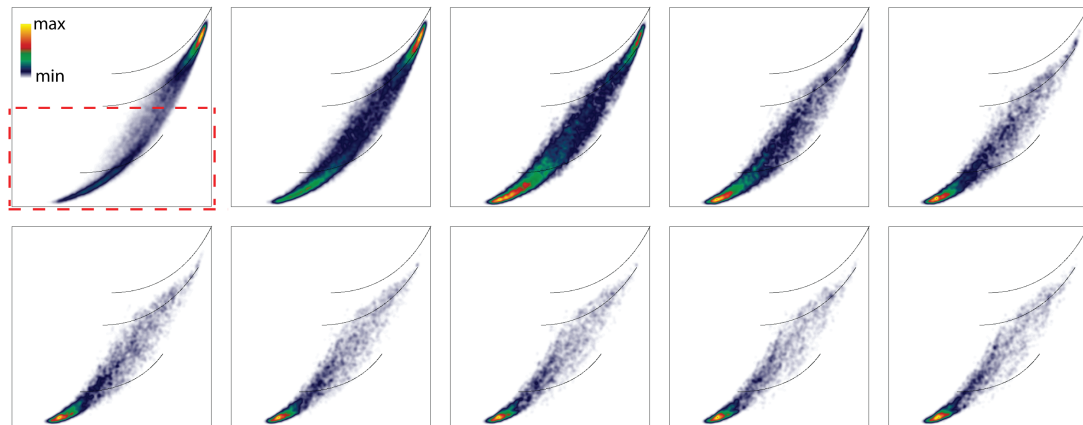
multi-sided chains that are found in the negative misfit microstructure. The PMIMs are shown in Figure 3.11(b), which indicates that the shape evolution, as described by averaged second and fourth order moment invariants, is similar to the evolution of the negative misfit microstructure.

### **Analysis of the moment invariant distribution maps**

All the moment invariant distribution maps show the appearance of a second peak during the evolution of the microstructure, which suggests that a more detailed analysis of the shapes leading to this peak may be useful. In Figure 3.12(a) we display the fraction of precipitates with MIs inside the box outlined in dashed lines in the first time step of Figure 3.10(a); this box corresponds to the range  $0 \leq \bar{\omega}_1 \leq 0.5$ . Note that this box extends along the full range of  $\bar{\omega}_2$ , since initially the evolving shapes maintain some cuboidal aspects, which corresponds to  $\bar{\omega}_2$  in the range 0.9–1; it is only in the later stages of the coarsening process that  $\bar{\omega}_2$  decreases significantly. Similarly, Figure 3.12(b) shows the fraction of precipitates for which  $0 \leq \langle \bar{\tau}_i \rangle \leq 0.5$ , as indicated by the dashed box in Figure 3.10(b). The fractions of precipitates inside the indicated regions were computed as a function of time for both microstructures; when more than 50% of the precipitates have MIs inside the boxes, then the corresponding microstructure is classified as a rafted microstructure. Looking only at the SOMIM distributions, for the microstructure with a negative misfit time steps 3 and above meet this 50% criterion and are hence classified as rafted microstructures; for the positive misfit case, none of the percentages are above the 50% threshold, indicating that none of these microstructures are considered to be rafted, as far as the SOMIM distributions are concerned. For the PMIMs, the higher order moments are more sensitive to the early stages of the evolving  $\gamma'$  shape, and this change is reflected in a change of  $\langle \bar{\tau}_i \rangle$ . Thus, the region of interest in the PMIM corresponds to  $\langle \bar{\tau}_i \rangle$  in the range 0–0.5 or the lower half of the density map. In the negative misfit microstructure, time steps 2 and above meet the 50% criterion and are rafted microstructures according to the PMIM; in the positive misfit case, time steps 3 and above are classified as rafted microstructures. These results suggest that the fraction of precipitates in the selected moment invariant intervals can be used as an indicator for the onset of rafting.

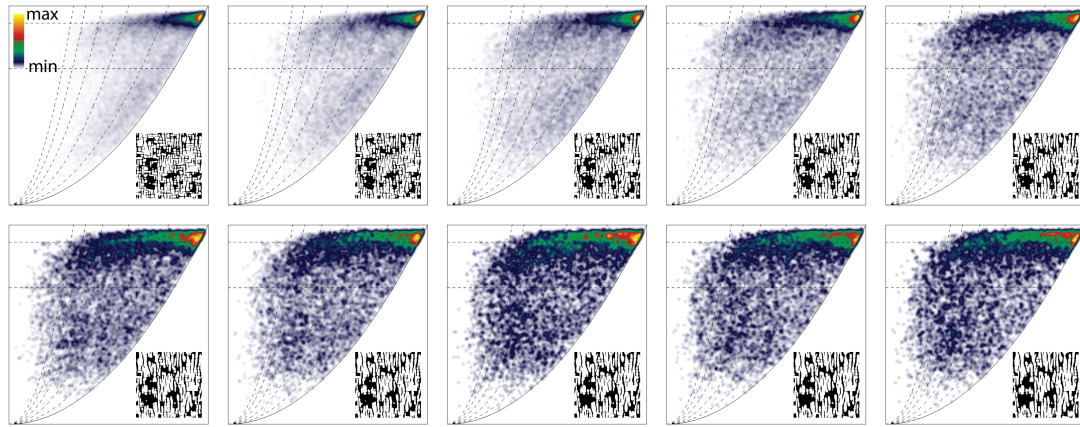


(a) SOMIM - negative misfit

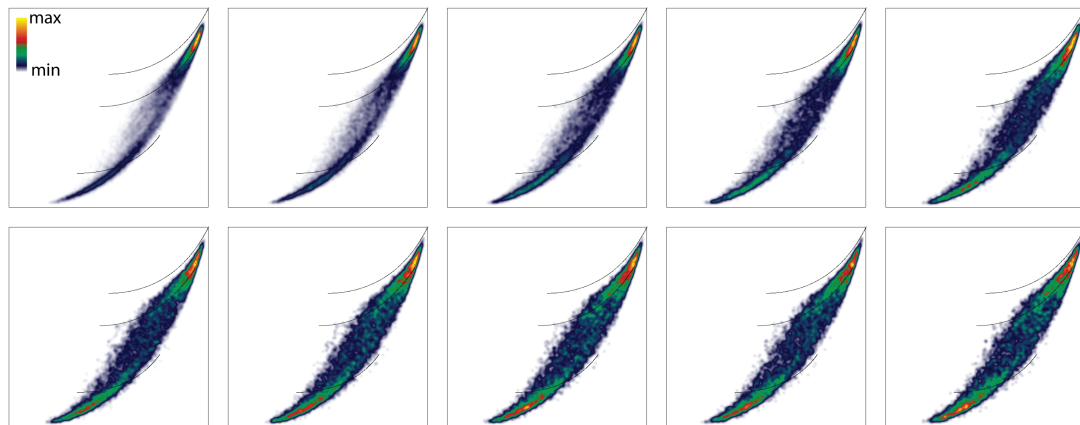


(b) PMIM - negative misfit

Figure 3.10: Density maps for the microstructure with a negative misfit for the ten time steps (a) SOMIM (b) PMIM. 256 images per time step were analyzed. The region of interest used to determine rafted is shown in the red boxes in the first map of (a) and (b). The peak of the MI distributions shift from the upper right corner to the lower left corner as the  $\gamma'$  precipitates directionally coarsen.



(a) SOMIM - positive misfit



(b) PMIM - positive misfit

Figure 3.11: Density maps for the microstructure with a positive misfit for the ten time steps (a) SOMIM (b) PMIM. 256 images per time step were analyzed. The peak of the PMIM shifts from the upper right corner to the lower left corner as the  $\gamma'$  precipitates directionally coarsen, as observed in the microstructure with a negative misfit. However, the peak of the SOMIM does not change over time; the biggest change is in the broadening of the MI with decreasing  $\bar{\omega}_1$ .

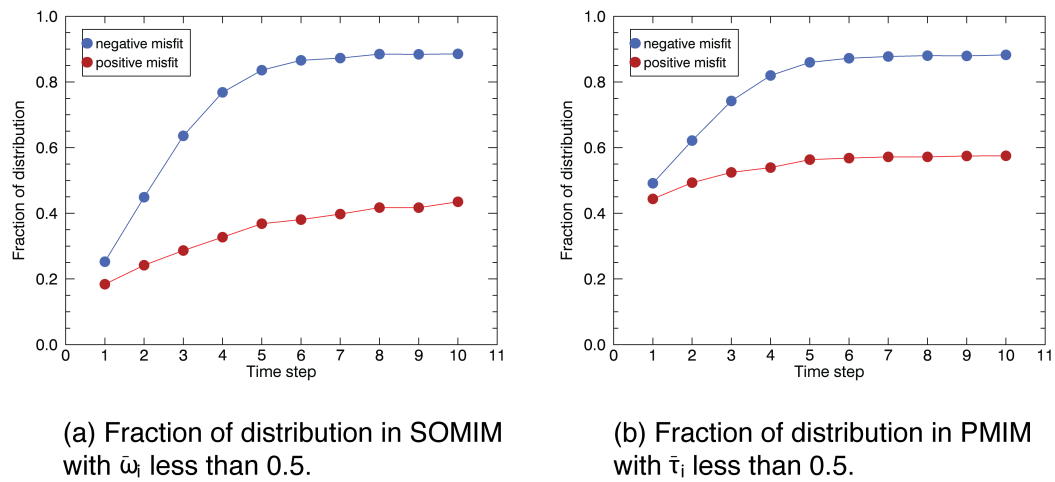


Figure 3.12: (a) Fraction of  $\gamma'$  precipitates in the SOMIM where  $0 \leq \bar{\omega}_1 \leq 0.5$ . (b) Fraction of  $\gamma'$  precipitates in the PMIM where  $0 \leq \langle \bar{\tau}_i \rangle \leq 0.5$ . The onset of rafting is defined as when at least half of the precipitates are in the selected MI interval. For the microstructure with a negative misfit, this occurred in the SOMIM at time step 3 and in the PMIM at time step 2. For the microstructure with a positive misfit, this occurred at time step 3.

### 3.4 Comparison to other shape descriptors

Many parameters have been used to describe the shape of  $\gamma'$  precipitates. Typical shape descriptors used for analysis in materials science and engineering include: area fraction, aspect ratio, chord length, circularity, equivalent ellipse, Feret's diameter, moment invariants, perimeter, solidity, and precipitate count [2]. They are typically represented in one of several ways: a histogram, a scatter plot, an average, or as a correlation with another parameter.

Table 3.3: List of shape descriptors frequently used in materials science analysis [2].

Shape descriptor	Description
Area fraction	percentage of non-zero pixels
Aspect ratio	ratio of the major axis to minor axis
Chord length	length of particle in a certain direction
Circularity	$4\pi^{area}/perimeter^2$ , how close it is to a circle shape
Equivalent ellipse	the aspect ratio of the shape if fitted to its equivalent ellipse
Feret's diameter	longest distance between any two points along the particle's boundary
Moment invariants	combinations of moments invariant to similarity or affine transformations
Perimeter	length of the outside boundary of the particle
Solidity	ratio of area to convex area, determined by the gift wrap algorithm

These shape descriptors were applied to one image per time step (Figure 3.13), resulting in ten images that were morphologically analyzed. Generally, the average is reported, which is done in Figure 3.14. The change in the system is identified as when there is a change in the

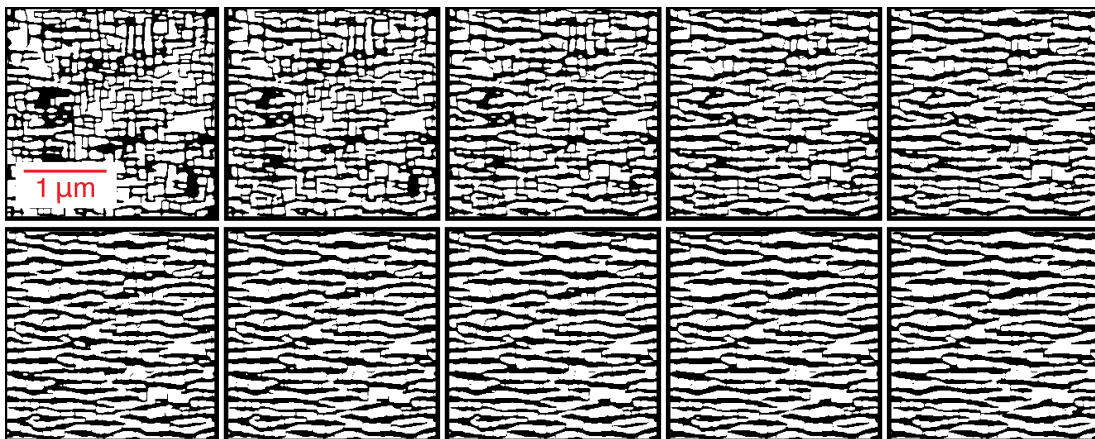


Figure 3.13: Images used for analysis using all shape descriptors.

trend of the parameter of interest. Moment invariant density maps were also computed and shown in Figure 3.15; the average moment invariants are shown in Figure 3.16. ImageJ is a common tool used to analyze different regions of interest and was used to calculate a series of parameters: precipitate size, aspect ratio, Feret's diameter, circularity, and perimeter [101].

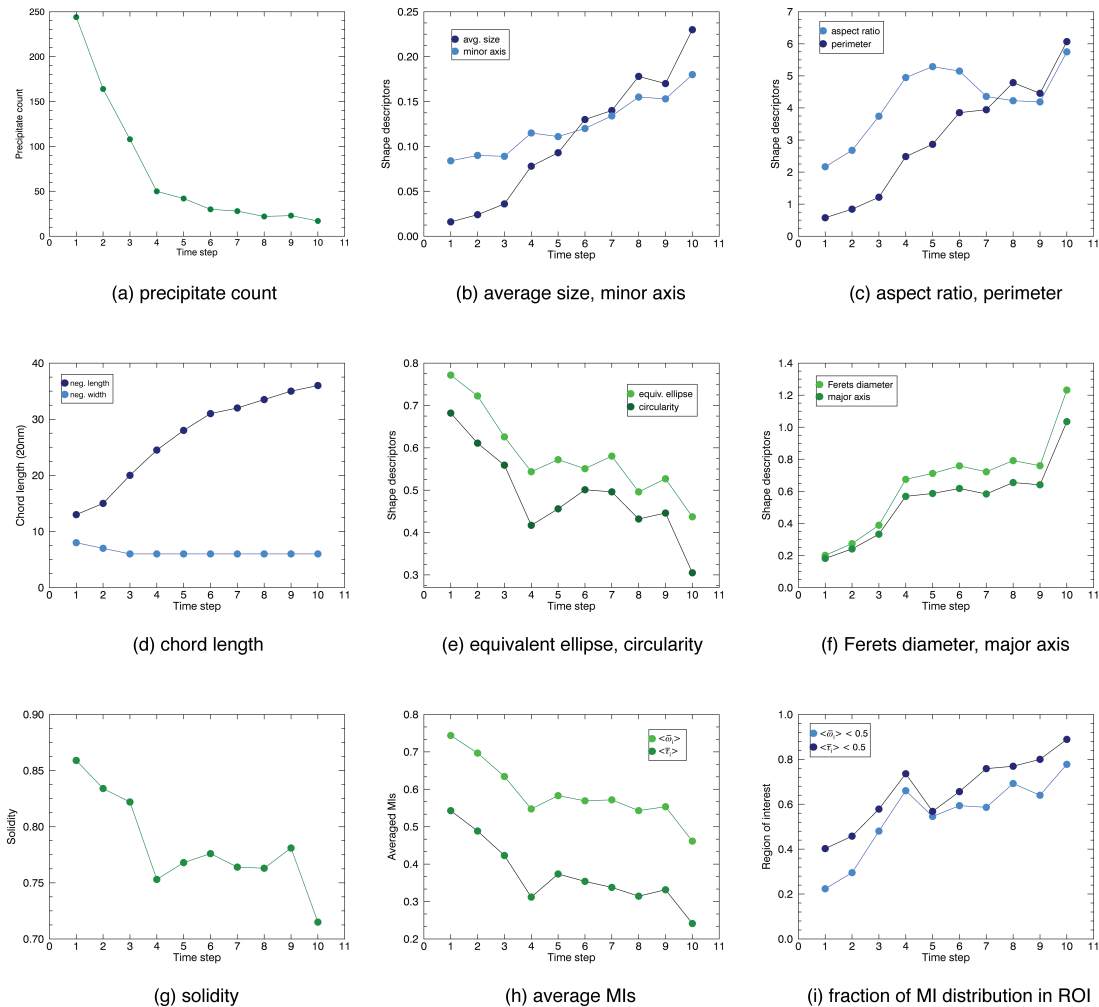


Figure 3.14: Various shape descriptors and their evolution over time applied to 2D images. The shape descriptors in green represent descriptors that have identified a rafted microstructure at time step 5 and above, while blue represents shape descriptors with a linear or no relationship, indicating no abrupt change in the system. (a) precipitate count (b) average size, minor axis (c) aspect ratio, perimeter (d) chord length (e) circularity, equivalent ellipse (f) Ferets diameter, major axis (g) solidity (h) averaged MIs (i) fraction of MI distribution in ROI.

Several trends can be seen when plotting the average of each parameter with time, as shown in Table 3.4. Depending on how the parameter is measured, it will increase or

Table 3.4: Shape descriptor and trend

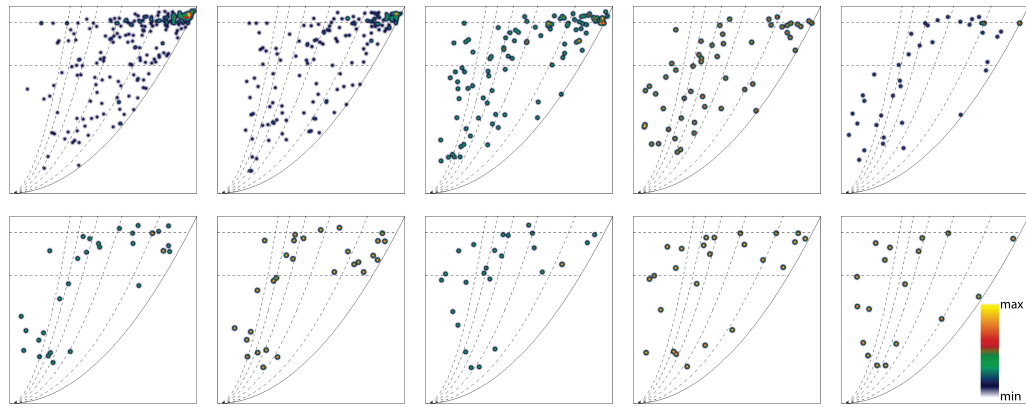
Shape descriptor	Change in sys.	Trend
No. of ppt.	5	linearly decreasing, smaller linear decrease
Avg. size of precipitates	n/a	linearly increasing
Aspect ratio	n/a	no trend
Chord length	n/a	linearly increasing
Chord width	n/a	constant
Circularity	5	decreasing linearly, constant, spike at the end
Equivalent ellipse	5	decreasing linearly, constant, spike at the end
Feret's diameter	5	linearly increasing, constant, spike at the end
Major axis	5	linearly increasing, constant, spike at the end
Minor axis	n/a	linearly increasing
Moment invariants	5	linearly increasing, constant, spike at the end
Perimeter	n/a	linearly increasing
Solidity	5	linearly decreasing, constant, spike at the end

decrease with time as the particles coalesce. While some of these shape descriptors have different trends, they are characterized by a contrast in the trend at the rafting completion time. However, this may be difficult to create a criterion for any dataset, instead of a criterion specific to this dataset. In this case, it is easy to create a criterion because there is such a wide range of microstructures.

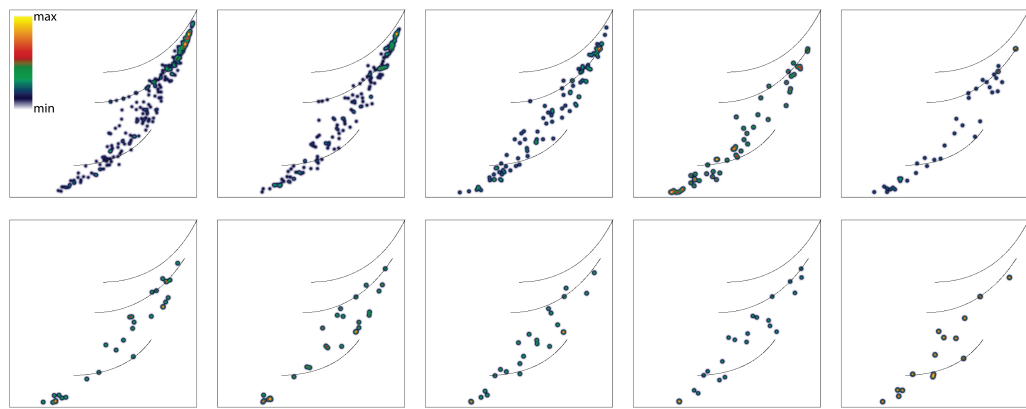
Previously, the time at which there was a change in the trend was chosen to be the rafting completion time, indicated that there is now a rafted microstructure. Using that criteria, these shape descriptors identified the rafting completion time to be:

- **time step 5:** equivalent ellipse, circularity, Feret diameter, major axis, solidity, precipitate count
- **linear:** average size, aspect ratio, minor axis, perimeter, chord length, chord width

Moment invariants are proposed as the shape descriptor of choice because they contain a large amount of information that was contained in many of the other shape descriptors. While some of these shape descriptors adequately describe the evolution of the precipitates over time, they only contain one aspect of the precipitates' changes. However, MIs can consolidate some of these aspects.

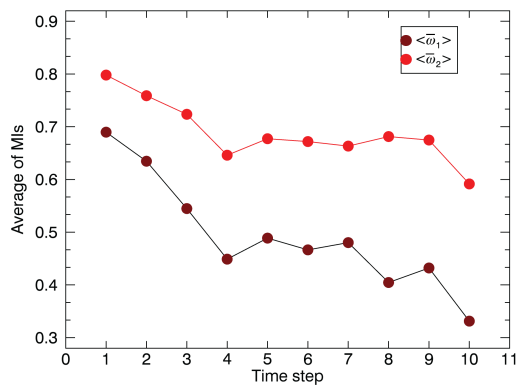


(a) SOMIM

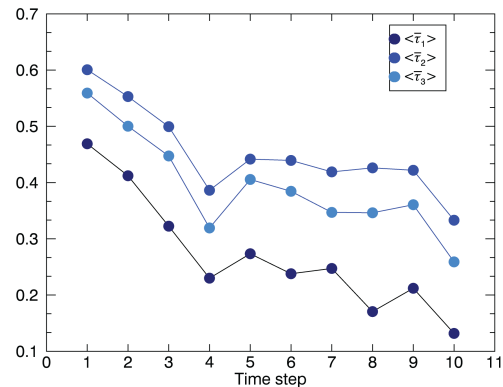


(b) PMIM

Figure 3.15: Moment invariant density maps and their evolution over time for one image per time step. (a) SOMIM (b) PMIM.



(a) average 2nd order MIs



(b) average 4th order MIs

Figure 3.16: Average 2D moment invariants and their evolution over time for one image per time step. (a) average second-order MIs (b) average fourth-order MIs.

### 3.5 Inversion of the matrix

It is also interesting to consider the portions of the microstructure that are occupied by the  $\gamma$  matrix. Figures 3.18 – 3.23 show the SOMIMs and PMIMs when the  $\gamma$  phase is being analyzed using moment invariants. For the off-direction of the microstructures, which is the  $z$ -direction for the negative misfit microstructure and the  $x$ -direction for the positive misfit microstructure, the density maps do not change much with time. This is expected since the density maps computed for the  $\gamma'$  precipitates in these cross sections also do not change. However, the directions of interest show a change in the microstructure, which are the  $y$ -directions in both microstructures with misfits, the  $x$ -direction for the negative misfit, and the  $z$ -direction for the positive misfit. The number of areas that are considered per time step increases with time, so the density maps are more densely populated by the end.

For the microstructure with a negative misfit (Figures 3.19 and 3.20(a)), the distribution in the SOMIMs starts in the lower left corner near the isotropic shape curve, then the distribution becomes more spread out along the isotropic shape curve throughout the MI space and  $\bar{\omega}_2$  increases. For the microstructure with a positive misfit, the distribution in the SOMIMs (Figure 3.21) starts in the lower left hand corner near the isotropic shape curve. Then a second peak of shapes of higher  $\bar{\omega}_2$  values develops with longer times. In the PMIMs (Figures 3.19 and 3.20(b)), the distribution is on the lower left corner, then it becomes more densely populated. The distribution spreads out, but the peak remains in the same location.

The analysis of the  $\gamma$  matrix can yield some interesting results. In these results, the  $\gamma$  matrix shows a change in the system with increasing stress. However, the analysis of the  $\gamma$  phase in general can be difficult because of the interconnectivity in the initial stages. The edges of the micrographs affect how the  $\gamma$  phase is being analyzed by the moment invariant calculation. Therefore, the usefulness of the matrix MI analysis will depend on the size of the micrograph and how much of the matrix is considered.

### 3.6 Discussion

Two types of rafting have been identified previously by [92]: n-type rafting ( $\gamma'$  precipitates coarsen normal to the applied loading direction) and p-type rafting ( $\gamma'$  precipitates coarsen parallel to the applied loading direction). For an applied tensile stress, a negative misfit microstructure undergoes n-type rafting while a positive misfit microstructure undergoes p-type rafting [8]. Typical  $\gamma'$  precipitate shapes in a microstructure with a lattice misfit of  $\pm 0.3$  are cuboidal and aligned along the  $\langle 001 \rangle$  direction. As the system is subject to the applied stress, the  $\gamma'$  precipitates directionally coarsen together, forming a wavy morphology that is characterized by zigzag shapes. The variations in  $\gamma'$  precipitate size, shape, and spatial distribution all contribute to the rafted microstructure with a wavy morphology that is similar to experimental observations of rafting [8].

Since the microstructures have been simulated to represent an experimental microstructure, characterization of the precipitate shapes have been difficult compared to the simulations with perfectly aligned and identical precipitates [8]. The p-type rafts were defined as  $[001]$  rods, while n-type rafts were referred to as  $(001)$  plates [8]. Zhou et al. [8] discussed some initial characterization of the phase-field constructed microstructures using average chord length and average aspect ratio. The average chord length was measured in 2D along the rafting directions for each type of rafting: the width of the rafts and the length of the rafts [8]. The initial average chord length for the starting microstructures is 192 nm for both directions and corresponds to the average edge length of the cuboidal  $\gamma'$  precipitates before the applied external stress [8]. The average  $\gamma$  channel width is 36 nm and has been estimated from the volume fraction [8]. Using chord length, the raft width remains fairly constant during rafting, and the raft length increases with time [8]. The aspect ratio and the average chord length increase almost linearly initially, then gradually slow down after time step 5 [8]. The rafting completion time has been defined as the moment when the aspect ratio increase begins to slow down, which is about 3.87 hours for the n-type rafting and 4.72 hours for the p-type rafting [8].

3D moment invariants were used to classify different  $\gamma'$  precipitates due to the availability of 3D datasets. However, there are only eleven precipitates in the last time step due to

coarsening. Instead, a box with a spherical filter was used to gather a sufficient amount of information. Figures 3.6 and 3.7 show that the peak of the distribution and the average MI value do not change much with time. The boxes have MIs that are deviating from the isotropic shape curve, indicated by the blue. Initially, datasets with both misfits have boxes with MIs that have isotropic shapes. At later times, the rafted precipitates indicate a deviation from isotropy, and its MI distributions broaden.

However, it is also useful to consider the evolution of these microstructures in 2D. 2D cross-sections were taken through three directions, normal to the x, y, and z directions, which are shown in Figures 3.24 – 3.31. As alternative 2D shape descriptors to chord length, moment invariants and precipitate size are used to characterize the  $\gamma'$  precipitate evolution with increasing stress. Rafted precipitates have large areas compared to non-rafted ones, so it is useful to consider both precipitate size and moment invariants to classify non-rafted vs. rafted precipitates as shown in Figure 3.9. Since the particles are coarsening together, the number of particles per image decreases, but the area of each precipitate increases. Moment invariants are scale invariant, so this change is not detected in the moment invariant maps.

Small precipitates in the  $\gamma/\gamma'$  microstructure are oriented along one of the  $\langle 001 \rangle$  directions and are cuboidal in shape. Small precipitates are found in the SOMIM with  $\bar{\omega}_2$  values typically between  $0.91 < \bar{\omega}_2 < 1$ . However, large precipitates are rafted, indicating that their shapes are long in length and connected so that they have zigzag shapes. These shapes can be found in the lower left corner of the SOMIM. Medium-sized precipitates are found throughout the SOMIM because they are in an intermediate stage between non-rafted and rafted. They tend to have greater aspect ratios than the smaller precipitates because some directional coarsening has already occurred.

Moment invariants are calculated for each time step of each microstructure. Non-rafted microstructures have  $\gamma'$  precipitates that, depending on the magnitude of the lattice misfit, are a shape between the square and the circle. For these microstructures, the magnitude of the lattice misfit is  $\pm 0.3\%$ , so the  $\gamma'$  precipitates have cuboidal shapes that are oriented along the  $[001]$  direction. If images are normal to the  $\langle 001 \rangle$  direction, then a non-rafted microstructure will have density maps similar to the first SOMIM and PMIM in Figure 3.10 and 3.11, for the negative and positive misfits, respectively. Many of the precipitates are in

the upper right corner and have values between 0.91 and 1.

While the  $\gamma'$  precipitates in the negative and positive misfit microstructures both directionally coarsen, the moment invariant approach is able to detect the coarsening faster than just by visual inspection. For instance, the changes between time step 3 and 4 in Figure 3.3(a) are so minor that it is difficult to see the changes in time step 4. However, the SOMIM and PMIM in Figure 3.10 show that the second class of shapes is present in time step 4.

The density maps show a distinct shift in the shapes detected initially compared to the shapes of the  $\gamma'$  precipitates in the final microstructures. As stress is applied to the system, the  $\gamma'$  precipitates directionally coarsen and become larger in size and lose their isotropy by becoming more elongated. The  $\bar{\omega}_2$  values still indicate a rectangular shape, but the  $\bar{\omega}_1$  values become smaller and can be seen in the second image of Figure 3.10(a). This is detected more readily in the PMIMs due to the higher order moment invariants since higher order moments are more sensitive to the small changes in shape. The PMIM detects the evolution of the  $\gamma'$  precipitates more readily than the second-order moments, which contain overall shape information.

New shapes appear on the SOMIMs and the PMIMs as the  $\gamma'$  precipitates coarsen together and connect to form these many-sided rafts. There are two main types of shapes that are on the SOMIM: non-rafted, cuboidal  $\gamma'$  precipitates that are found in the upper right corner and rafted, many-sided  $\gamma'$  precipitates that are found in the lower left corner. Rafting in terms of moment invariants can be defined as when the peak of the distribution is in the lower left corner of the PMIM. More specifically, to define rafting completion time in a manner similar to the method using the average aspect ratio, it is defined as when the fraction of  $\gamma'$  precipitates in the ROI stops increasing linearly with time. Using the SOMIM, this is at time step 4 for n-type rafting and at time step 5 for p-type rafting. Using the PMIM, rafting is completed at time step 5 for n-type and p-type rafting.

The moment invariant approach also indicates that p-type rafting occurs more slowly than n-type rafting. The region of interest approach is used to quantify the onset of rafting and indicates that rafting starts to occur in time step 2 for n-type and in time step 3 for p-type. P-type rafting took longer to complete rafting than n-type rafting due to the

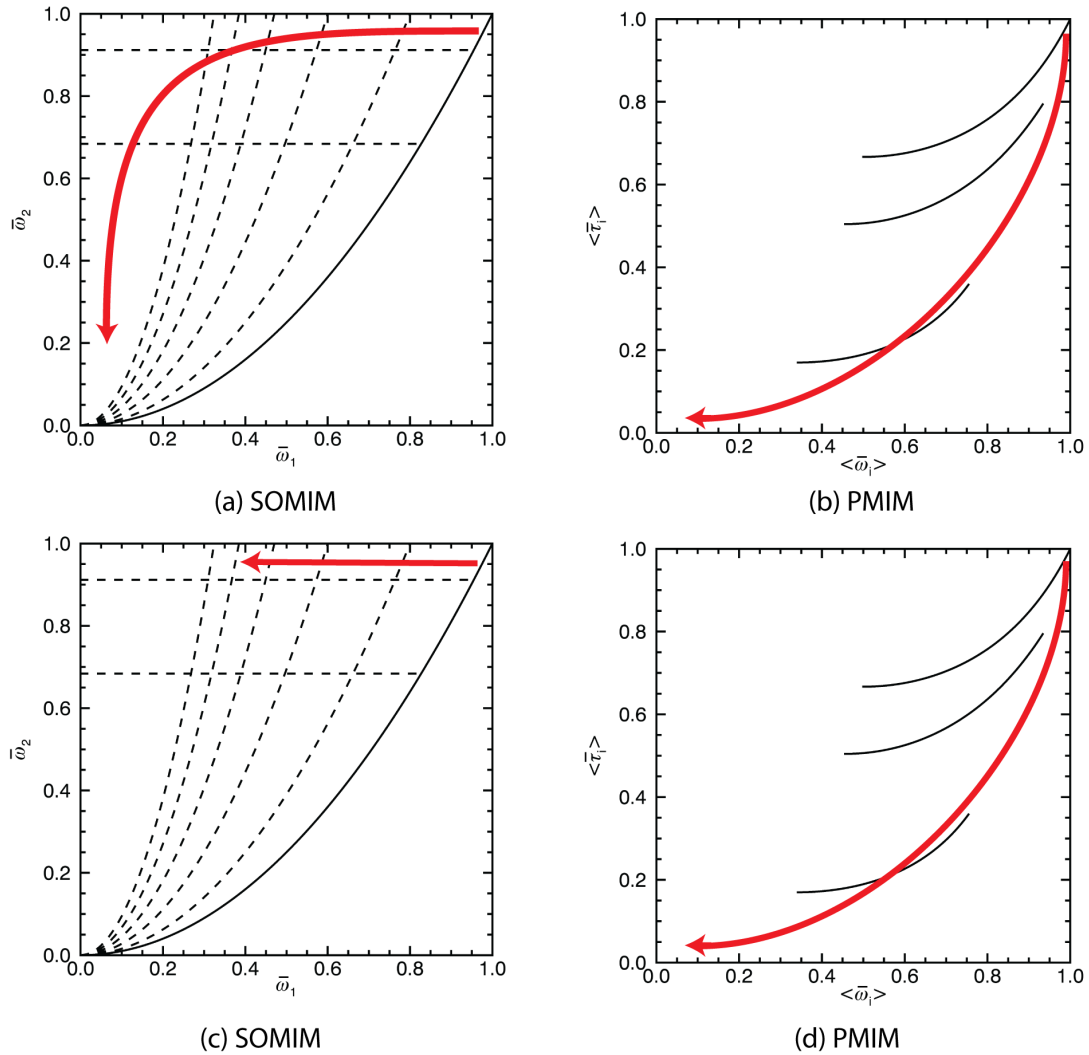


Figure 3.17: Schematics of where the shapes of the precipitates shift from their cuboidal shape to the rafted shape in (a) SOMIM (b) PMIM. The cuboidal  $\gamma'$  precipitates begin in the upper right corner and the rafted  $\gamma'$  precipitates are in the lower left corner of both maps.

spatial variation in the  $\gamma'$  precipitate alignment in the starting microstructure, which is in agreement with literature [8]. It is less probable for the p-type  $\gamma'$  rafts (as  $\gamma'$  rods) to meet with adjacent rafts, unlike the n-type rafts (as  $\gamma'$  plates) [8]. Hence, the p-type rafted microstructures do not look as well-aligned as the n-type. Figure 3.17 shows a schematic on the SOMIM and the PMIM of how the cuboidal  $\gamma'$  precipitates respond to an external stress. For a microstructure with a negative misfit as shown in Figure 3.17(a) and (b), the peak of the distribution begins in the upper right corner in both maps due to the cuboidal shapes. Then the peak shifts to the lower left corner, as indicated by the arrows

upon rafting. The resulting shift to the lower left corner is accompanied by an increase in precipitate size. A new peak of shapes is detected in the SOMIM and the PMIM due to the rafted  $\gamma'$  precipitates. For a microstructure with a positive misfit as shown in Figure 3.17(c) and (d), the peak of the distribution also begins in the upper right corner in both maps. The PMIM for positive misfit precipitates behaves in the same manner as the negative misfit precipitates, but the peak in the SOMIM does not develop in the lower left corner. Instead, the peak maintains the same  $\bar{\omega}_2$  but the spread in  $\bar{\omega}_1$  increases. The positive misfit precipitates elongate, but they do not form as many sides as in the microstructure with a negative misfit so they retain their cuboidal shape as shown in Figure 3.17(c).

### 3.7 Conclusions

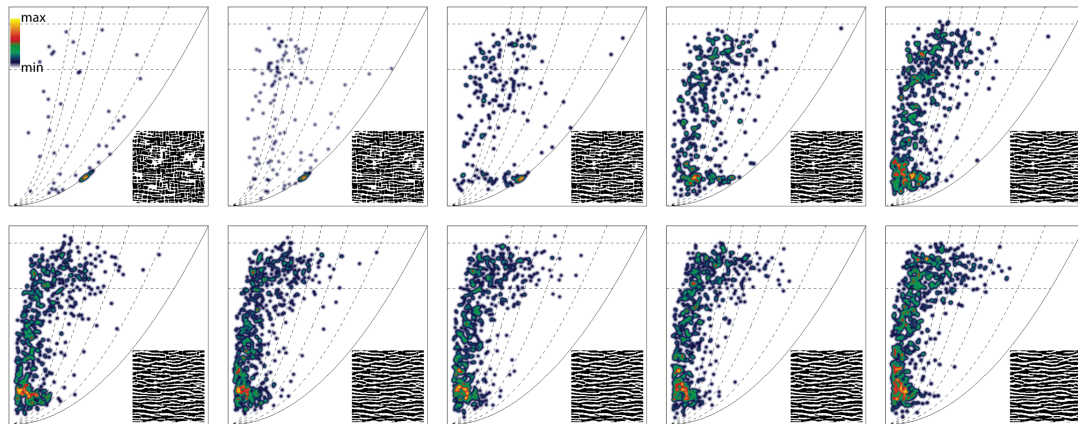
Moment invariants are used to analyze  $\gamma'$  precipitates in Ni-based superalloys subject to an applied external stress. Microstructures with a negative lattice misfit and a positive lattice misfit were studied. By tracking how the shapes of  $\gamma'$  evolve over time, the onset of rafting can be identified. The characteristics of non-rafted and rafted microstructures can also be quantified using moment invariants. While 2D and 3D moment invariants were both used, they both show similar results. Therefore for these datasets, the 2D approach is sufficient to classify when the microstructure has rafted. The SOMIM can be used to distinguish between a microstructure with a negative misfit versus a positive misfit. In a microstructure with a negative misfit, the rafted microstructures are located in the lower left corner of the SOMIM while they retain high  $\bar{\omega}_2$  and decrease in  $\bar{\omega}_1$  for a microstructure with a positive misfit. Microstructures with either misfit have a PMIM that shifts from the upper right corner to the lower left corner.

The MI approach can be used to determine if a microstructure is rafted or not. A 2D section of the material can be obtained using microscopy. Then the image can be segmented, and the MIs for each precipitate can be computed. Then, its MI maps can be created. The fraction of precipitates in the select moment invariant intervals can be computed, then using preset criteria, the microstructure can be classified as either non-rafted or rafted.

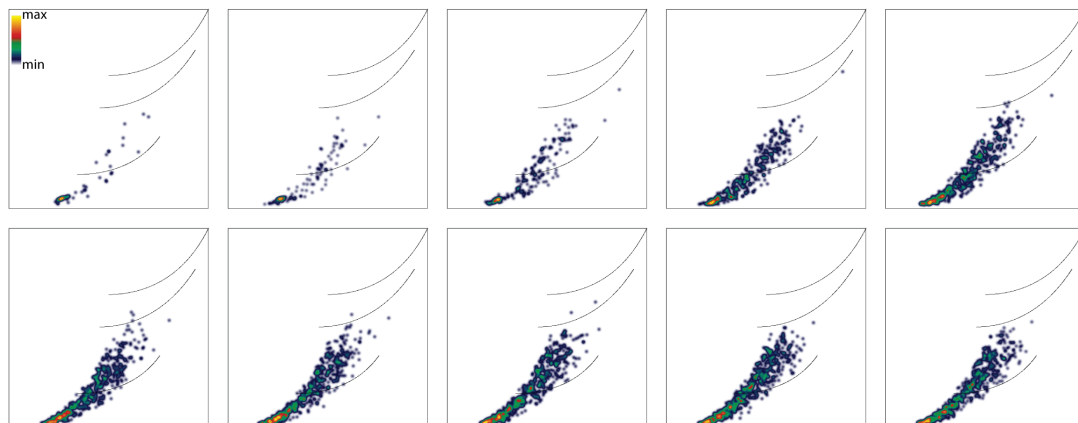
Some conclusions can be drawn about typical  $\gamma'$  precipitate shapes and rafting in Ni-based superalloys:

- Using boxes with size  $p = 33^3$ , rafting is completed in the microstructure with a negative misfit at time step 5 and in the positive misfit microstructure at time step 6.
- For a non-rafted microstructure, cuboidal  $\gamma'$  precipitates are the typical shape with this lattice misfit. Cuboidal precipitates have  $\bar{\omega}_2$  the affine 2D second order moment invariant, that is between 0.91 and 1.
- Rafted microstructures contain many large  $\gamma'$  precipitates with  $\bar{\omega}_2$  between 0.2-0.4.
- The microstructure with a negative misfit can be distinguished from a positive misfit based on its SOMIMs. Microstructures with a negative misfit have MIs in the SOMIM that shift from the upper left corner initially (high  $\bar{\omega}_1$  and  $\bar{\omega}_2$ ), to the lower left corner during rafting (low  $\bar{\omega}_1$  and  $\bar{\omega}_2$ ). Microstructures with a positive misfit have MIs in the SOMIM that have similar  $\bar{\omega}_2$  values throughout the rafting process; the change in the SOMIM is reflected in the decrease in  $\bar{\omega}_1$ .
- The onset of rafting is defined as when more than 50% of the  $\gamma'$  precipitates are in selected regions of interest in the SOMIM and PMIM. For n-type rafting, it occurred in time step 2 and for p-type rafting, it occurred in time step 3.
- The rafting completion time was previously defined as when the average aspect ratio stops increasing linearly with time. In terms of moment invariants, rafting completion time is defined as when the fraction of  $\gamma'$  precipitates in the ROI stop increasing linearly with time. N-type rafting is completed at time step 4 using the SOMIM criterion and at time step 5 using the PMIM criterion. P-type rafting is completed at time step 5 using the PMIM criteria.
- Six of the twelve shape descriptors that were used to analyze the shapes of  $\gamma'$  precipitates were able to define the microstructure as rafted at time step 5 and later, which was in agreement with the MI approach: circularity, equivalent ellipse, Feret diameter, major axis, solidity, and precipitate count. The other six shape descriptors were unable to detect rafting: average size, aspect ratio, perimeter, minor axis, chord length, and chord width.

From these conclusions, it is determined that the hypothesis is supported. MIs are capable of determining the state of the microstructure (non-rafted or rafted), and MIs were able to detect rafting as well or sooner than the other shape descriptors that were analyzed. Additionally, MIs were able to be used to set a criterion for the onset of rafting, which was not done using the shape descriptors.

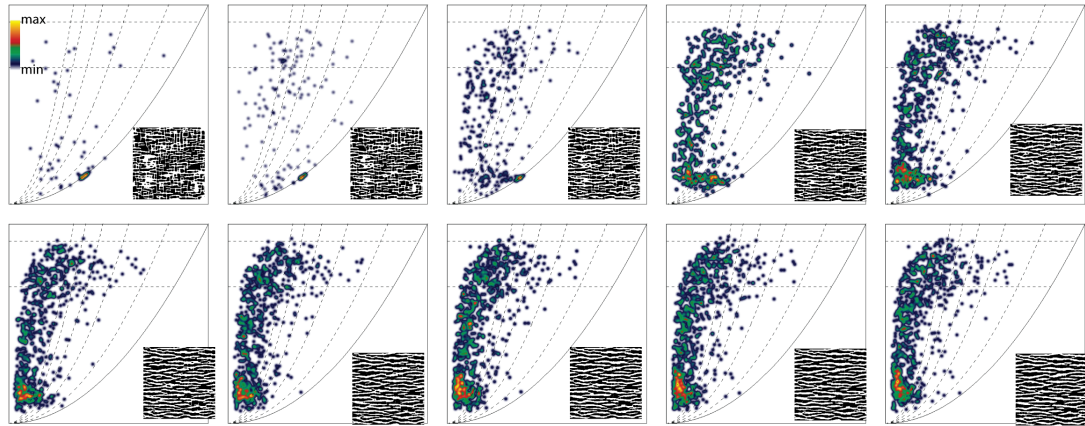


(a) SOMIM - negative misfit , normal to the x direction

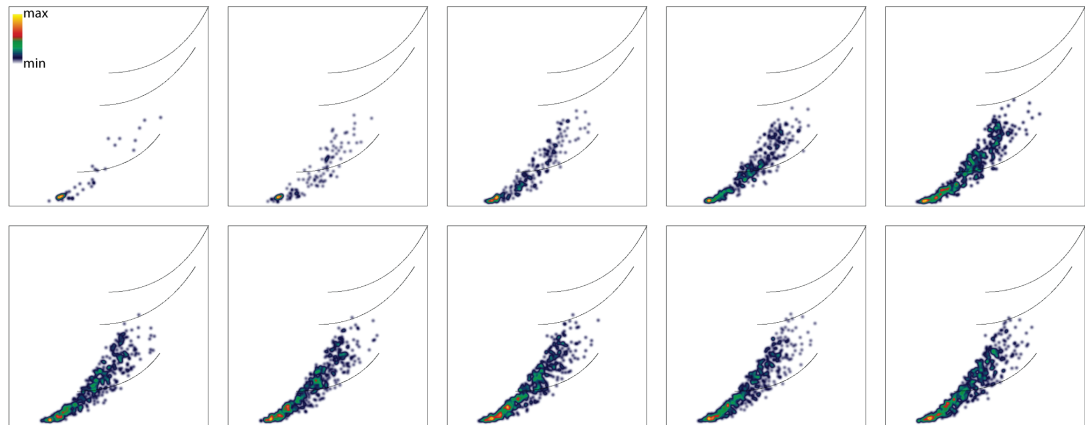


(b) PMIM - negative misfit, normal to the x direction

Figure 3.18: (a) The SOMIMs and (b) the PMIMs for cross-sections normal to the x-direction in the microstructure with a negative misfit. In these maps, the MIs are computed for the areas of the matrix instead of the  $\gamma'$  precipitates. 25 images were analyzed using moment invariants.

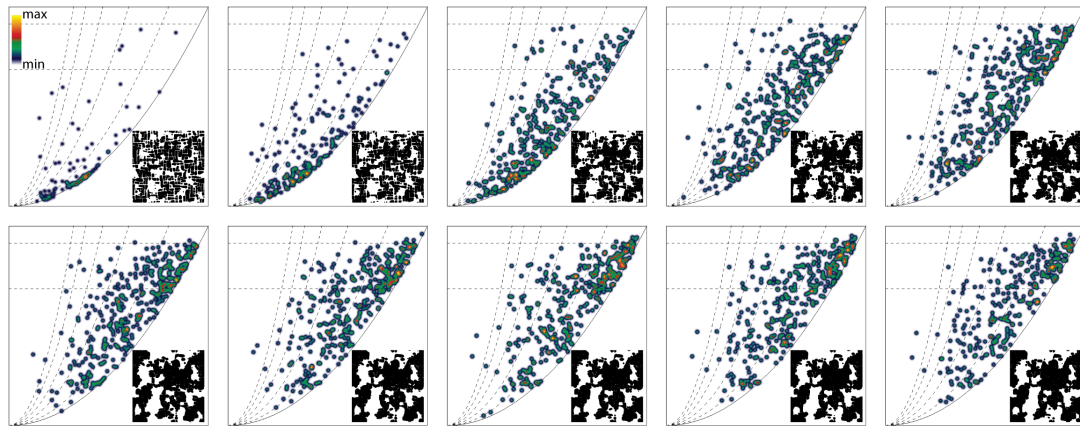


(a) SOMIM - negative misfit , normal to the y direction

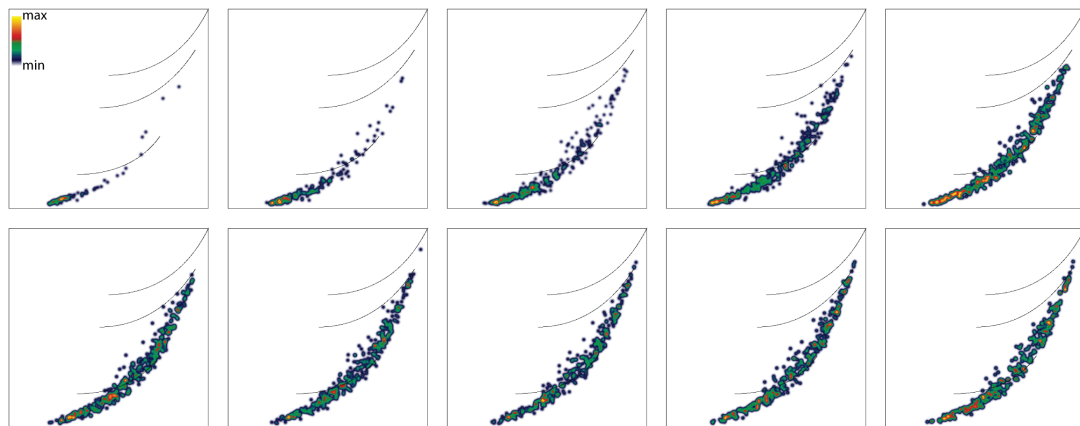


(b) PMIM - negative misfit, normal to the y direction

Figure 3.19: (a) The SOMIMs and (b) the PMIMs for cross-sections normal to the y-direction in the microstructure with a negative misfit. In these maps, the MIs are computed for the areas of the matrix instead of the  $\gamma'$  precipitates. 25 images were analyzed using moment invariants.

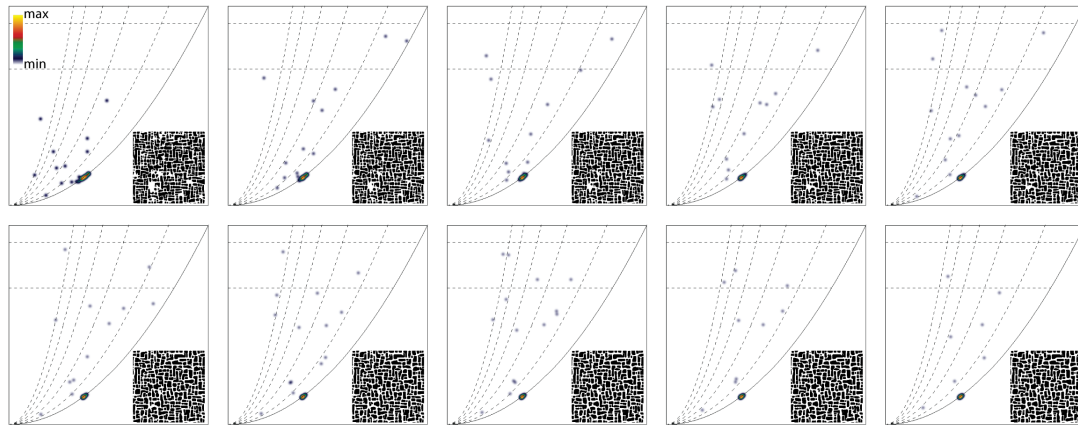


(a) SOMIM - negative misfit , normal to the z direction

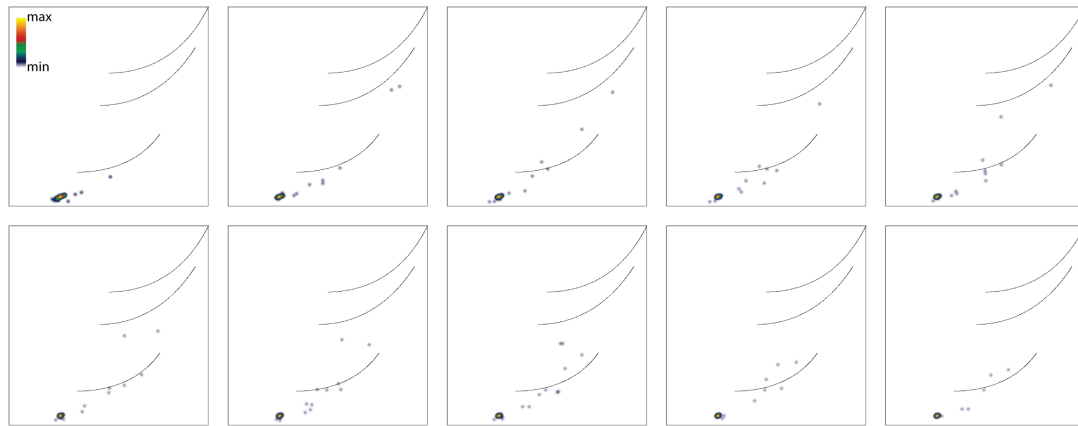


(b) PMIM - negative misfit, normal to the z direction

Figure 3.20: (a) The SOMIMs and (b) the PMIMs for cross-sections normal to the z-direction in the microstructure with a negative misfit. In these maps, the MIs are computed for the areas of the matrix instead of the  $\gamma'$  precipitates. 25 images were analyzed using moment invariants.

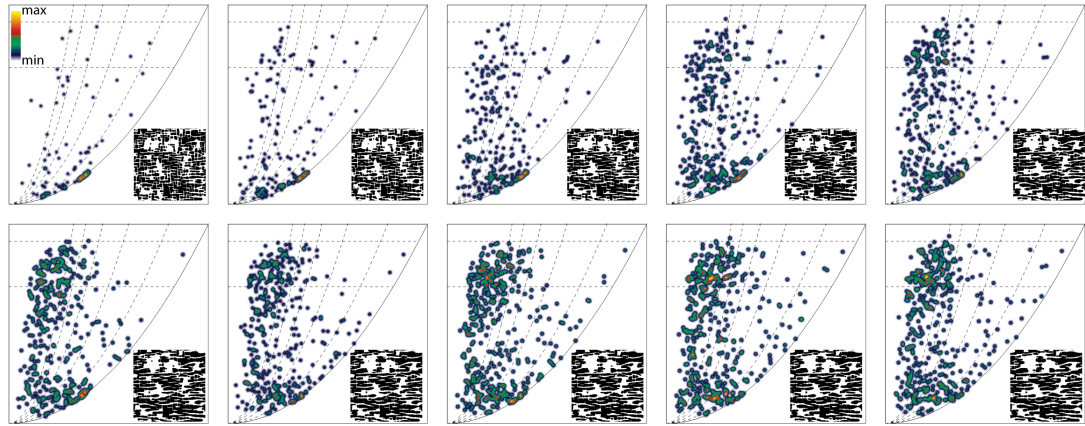


(a) SOMIM - positive misfit, normal to the x direction

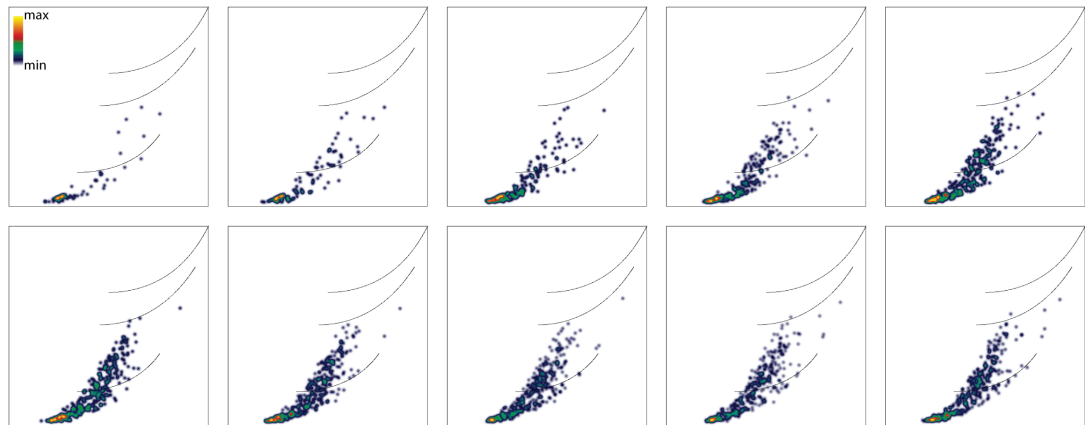


(b) PMIM - positive misfit, normal to the x direction

Figure 3.21: (a) The SOMIMs and (b) the PMIMs for cross-sections normal to the x-direction in the microstructure with a positive misfit. In these maps, the MIs are computed for the areas of the matrix instead of the  $\gamma'$  precipitates. 25 images were analyzed using moment invariants.

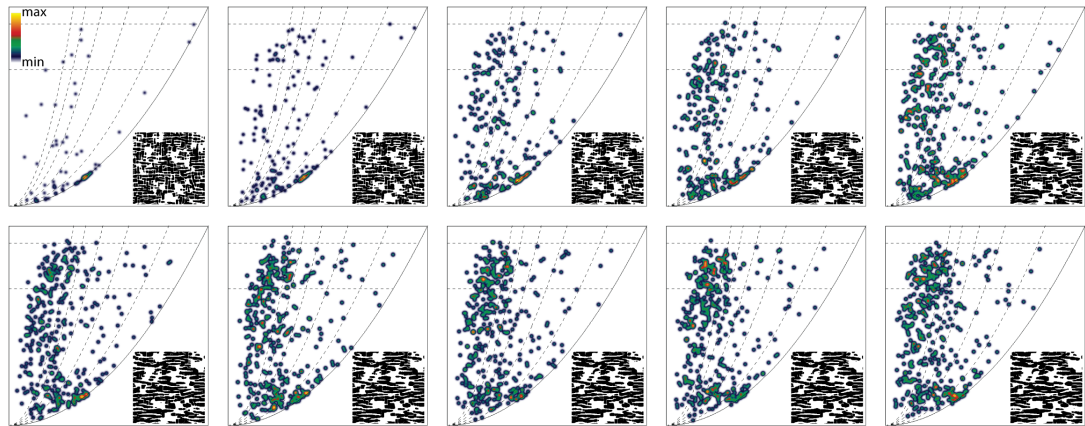


(a) SOMIM - positive misfit , normal to the y direction

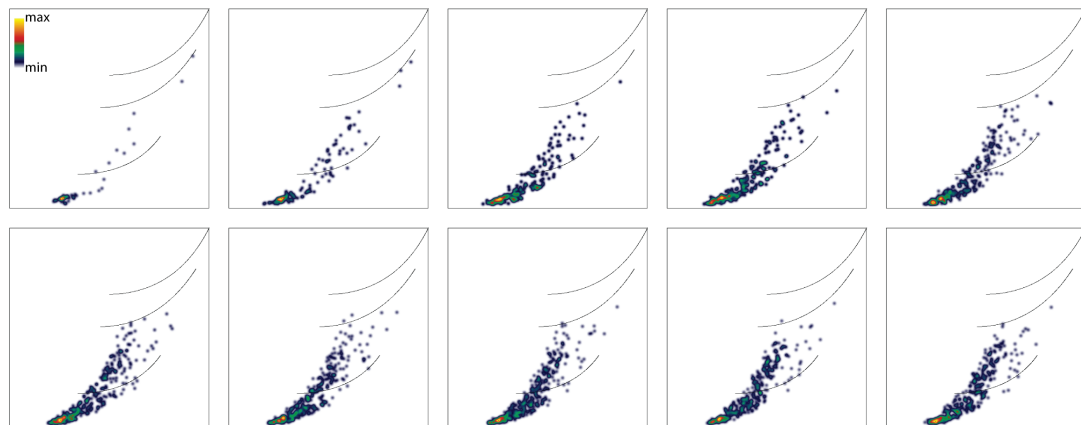


(b) PMIM - positive misfit, normal to the y direction

Figure 3.22: (a) The SOMIMs and (b) the PMIMs for cross-sections normal to the y-direction in the microstructure with a positive misfit. In these maps, the MIs are computed for the areas of the matrix instead of the  $\gamma'$  precipitates. 25 images were analyzed using moment invariants.



(a) SOMIM - positive misfit , normal to the z direction



(b) PMIM - positive misfit, normal to the z direction

Figure 3.23: (a) The SOMIMs and (b) the PMIMs for cross-sections normal to the z-direction in the microstructure with a positive misfit. In these maps, the MIs are computed for the areas of the matrix instead of the  $\gamma'$  precipitates. 25 images were analyzed using moment invariants.

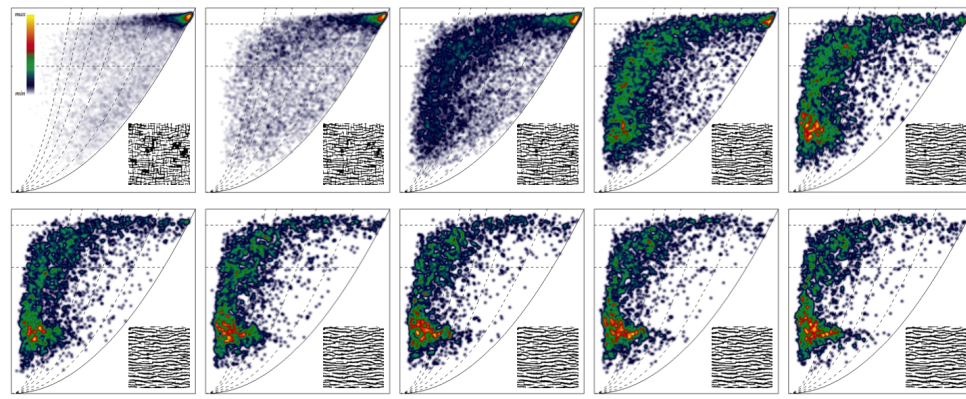


Figure 3.24: SOMIMs for cross-sections normal to the x-direction. 256 images were analyzed using moment invariants.

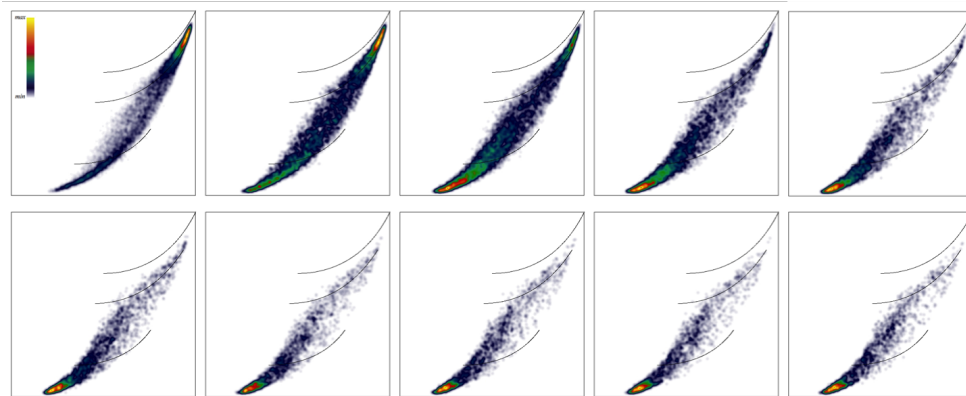


Figure 3.25: PMIMs for cross-sections normal to the x-direction. 256 images were analyzed using moment invariants.

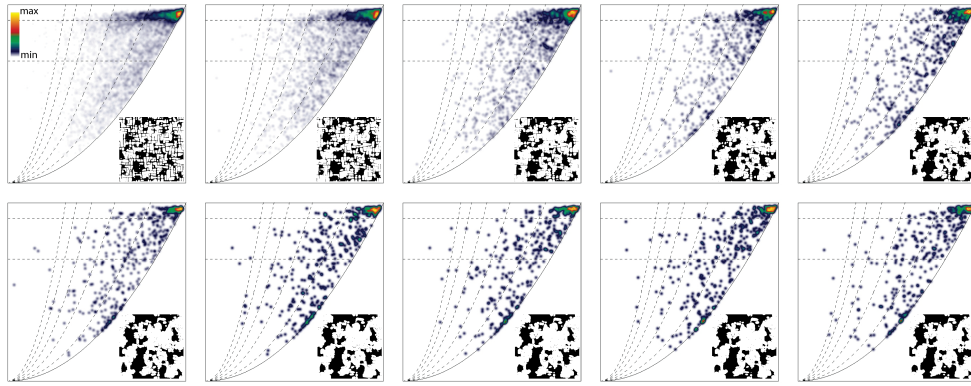


Figure 3.26: SOMIMs for cross-sections normal to the z-direction. 256 images were analyzed using moment invariants.

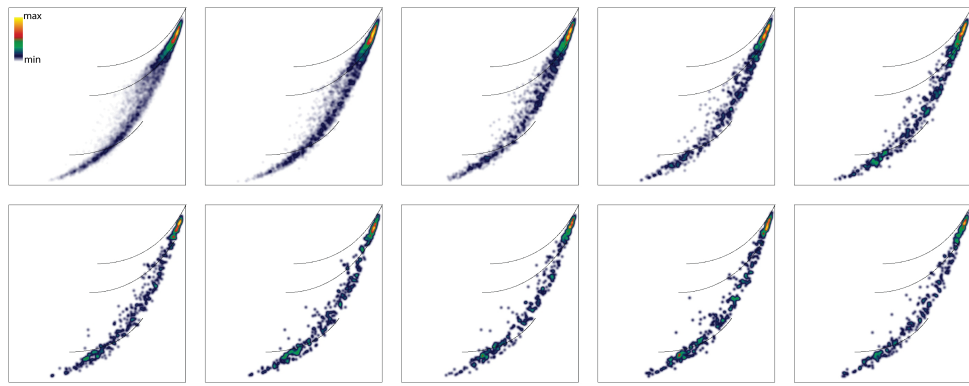


Figure 3.27: PMIMs for cross-sections normal to the z-direction. 256 images were analyzed using moment invariants.

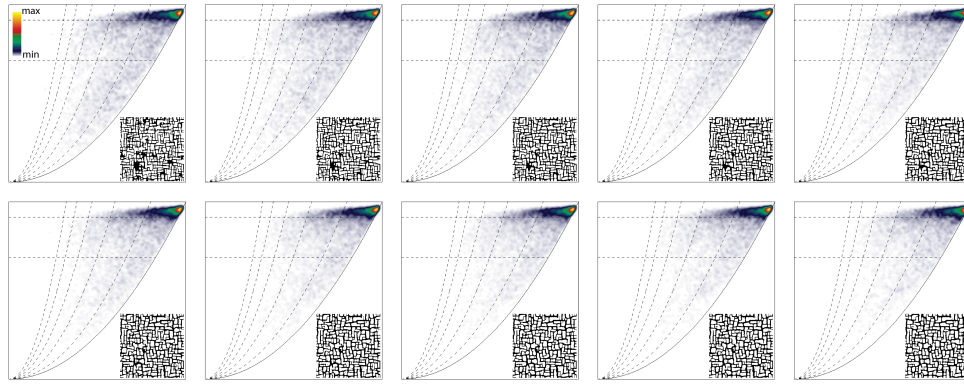


Figure 3.28: SOMIMs for cross-sections normal to the x-direction. 256 images were analyzed using moment invariants.

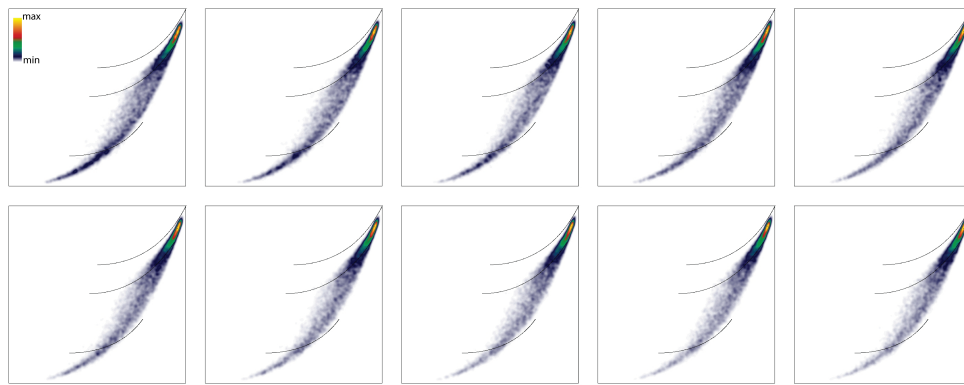


Figure 3.29: PMIMs for cross-sections normal to the x-direction. 256 images were analyzed using moment invariants.

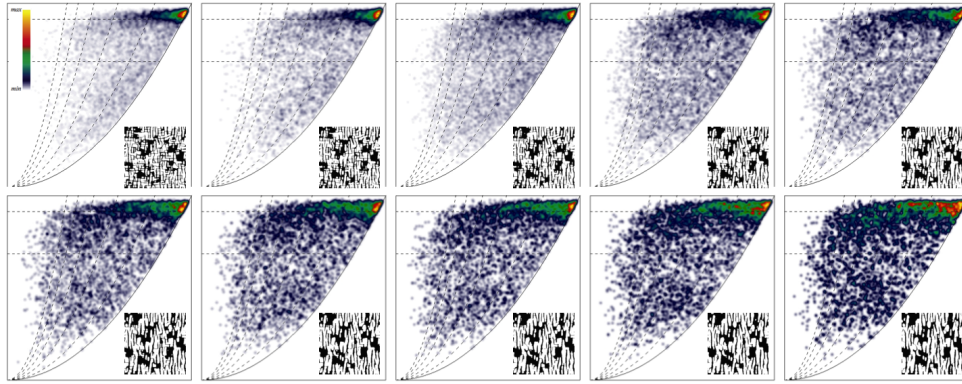


Figure 3.30: SOMIMs for cross-sections normal to the z-direction. 256 images were analyzed using moment invariants.

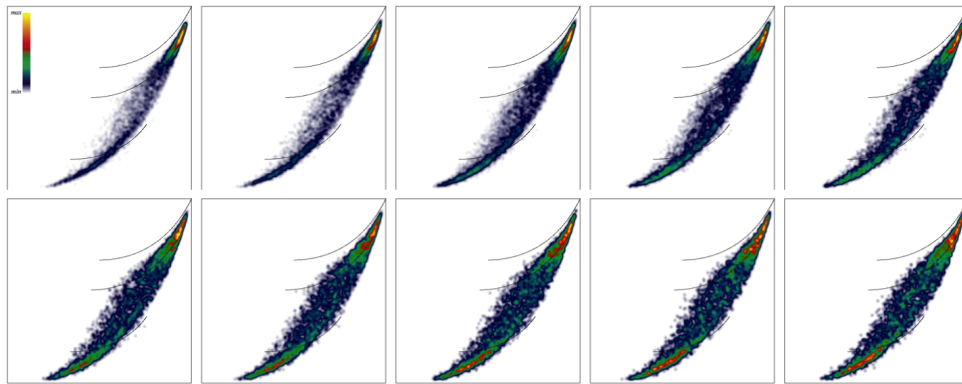


Figure 3.31: PMIMs for cross-sections normal to the z-direction. 256 images were analyzed using moment invariants.

## CHAPTER IV

# The effect of stress on gamma-prime precipitates in Ni-based superalloys

### 4.1 Introduction

Ni-based superalloys are discussed in Chapter III, but a brief overview of their microstructure will be discussed in this chapter as well. The shapes of  $\gamma'$  precipitates typically range from spherical to cuboidal to plate-like, depending on the lattice misfit between  $\gamma$  and  $\gamma'$  [78]. The study of the morphological evolution of  $\gamma'$  precipitates is important because of the coarsening of  $\gamma'$  precipitates that occurs due to an externally applied stress [78,96]. An external stress is applied parallel to  $[100]$  to systems with a small negative lattice misfit between the  $\gamma$  and  $\gamma'$  phases, and its resulting microstructure is studied [9]. However, systems where the external stress is applied parallel to other directions, such as  $\{110\}$  have also been studied [9].

Several shape descriptors have been applied to the study of  $\gamma'$  shapes in superalloy systems. Although they have already been discussed in Chapter II, it is useful to give a review of them in this chapter. The most commonly used is aspect ratio  $A$ , to measure how non-equiaxed the precipitates become after a certain stress or aging time. However, this only measures its change in shape in its elongation and does not provide any information about how similar the  $\gamma'$  precipitate shape is to a circle or a square shape. Therefore, other parameters have been developed to describe  $\gamma'$  shapes.

One of the first shape parameters that was used to quantify the morphological evolution

of  $\gamma'$  shapes is [7]:

$$\xi = \frac{a}{d}, \quad (4.1)$$

where  $a$  is the size of the particle along  $\langle 100 \rangle$  and  $d$  is the size of the particle along a face diagonal, typically along  $\langle 110 \rangle$  [7]. The parameter  $\xi$  is 1 for a sphere and  $\sqrt{2}/2$  for a cube; therefore cuboidal shapes are in the range of  $1 < \xi < \sqrt{2}/2$ . When the interfaces are concave,  $\xi$  can be smaller than  $\sqrt{2}/2$  and greater than one when particles are ellipsoidal [7]. Maheshwari et al. measured  $\xi$  for precipitates in Ni-Al alloys with various Al contents and aging times; they then plotted the parameter  $\xi$  over different  $a$  values, showing that  $\xi$  decreases with increasing particle length  $a$  [7]. Therefore, larger precipitates are closer to a cube shape than a sphere. The parameters  $a$  and  $d$ , however, were measured by hand; therefore, they were not used in other observations.

The next progression in analyzing the morphology of  $\gamma'$  precipitates was examined by Fährmann et al., who defined a stereological curvature parameter called  $S_{ster}$ , defined as [73]:

$$S_{ster} = \frac{(P_i - P_c)}{(P_s - P_c)}, \quad (4.2)$$

where  $P_i$  is the perimeter of the four-fold symmetric particle image, and  $P_c$  and  $P_s$  are the perimeters of the area-equivalent circle and square.  $S_{ster}$  ranges from 0 for a circle to 1 for a square, and it reasonably indicates the extent to which the sides of the particle have become less convex [73]. Particles with convex interfaces have  $S_{ster} < 1$ .  $S_{ster}$  is best used with particles that have an aspect ratio  $A < 1.5$ . Otherwise  $S_{ster}$  can be misleading and indicate concave interfaces that are not present or a maximum value of one when  $A \geq 2.3$  [73, 102]. Therefore,  $S_{ster}$  is best used for concave shapes with low aspect ratios, which makes its use limited in shape analysis. Fährmann measured the average aspect ratio,  $\bar{A}$ , and the curvature parameter  $\bar{S}_{ster}$  on microstructures with different lattice misfits ( $\delta = -0.3\%$ ,  $-0.15\%$ ,  $-0.1\%$ ,  $+0.4\%$ ,  $+0.65\%$ ) at different aging times; it was found that the larger the absolute value of the lattice misfit and the larger the particle, the more non-equiaxed the particle is [73].

Li et al. proposed another shape parameter [102]:

$$\Sigma = \frac{A_p - A_4}{0.5708A_4}, \quad (4.3)$$

where  $A_p$  is the area of the image of the particle,  $A_4$  is the area of the largest 4-sided polygon that contacts the perimeter of the particle, and 0.5708 is a numerical constant that normalizes  $\Sigma$ .  $\Sigma$  varies between 0 for a square to 1 for a circle. The advantage of  $\Sigma$  is that it is independent of the aspect ratio.  $\Sigma$  and  $A$  are both measured using the Image-Pro Plus<sup>TM</sup> software package [9]. It measures the average curvature of the precipitate-matrix interface reasonably well. Li et al. measured  $\Sigma$  and  $A$  for  $\text{Ni}_3\text{X}$  precipitates in 5 different binary Ni alloys: Ni-Al, Ni-Ga, Ni-Ge, Ni-Si, and Ni-Ti [102]. Precipitates were segregated by radius size, then  $\Sigma$  was measured for each precipitate [102]. It was found that as stress increases, the precipitates in a given size range become slightly more cuboidal.  $\Sigma$  has also been used to indicate that  $\gamma/\gamma'$  interfaces become more planar with increasing aspect ratios and with increasing applied compressive stress, especially for higher volume fractions through the work of Prikhodko and Ardell [9].

Ardell and Prikhodko have examined  $\gamma/\gamma'$  microstructures in Ni-13.36Al alloys aged at 640°C under uniaxial compression from 0 to 150 MPa [9, 103]. Experiments were performed on specimens of two different geometries: doubly-tapered (DT) and right cylindrical (RC). The different geometries affected the microstructure and how it changed with applied stress. Transmission electron microscopy (TEM) was used to look at a section normal to the axis of the applied stress [9, 103]. This is appropriate for this microstructure because  $\gamma'$  has a negative lattice misfit with the  $\gamma$  matrix [103]. It was predicted that in the early stages, the  $\gamma'$  shapes are nearly equiaxed. As the microstructure develops, the  $\gamma'$  precipitates will grow in size and start to coarsen [7, 9, 102]. Their work examined how an applied stress influences the morphology of  $\gamma'$  precipitates, and if coarsening promotes or delays the onset of the cuboidal shape [103]. There are several key points that have been concluded from qualitative observations on RC specimens [9]:

- Increasing applied stress results in decreasing precipitate sizes.

- Aging time increases precipitate sizes.
- Precipitates become slightly more cuboidal in shape with increasing aging time and align along the elastically soft  $\langle 001 \rangle$  directions.
- Larger precipitates have aspect ratios that are greater than one.
- Coalescing of precipitates is more frequently observed in microstructures with larger volume fractions.
- The shape of  $\gamma'$  precipitates under stress-free conditions become less spherical and have larger aspect ratios as their sizes increase.

Initially two parameters were used to characterize the morphology: the aspect ratio,  $A$ , and the shape parameter  $\Sigma$ . The measurements were made from scanned and enlarged dark field (DF) electron micrographs. Moment invariants can be compared to the approach taken by Prikhodko and Ardell to determine if there is any additional information that can be interpreted from the DT specimens. Moment invariants are applied to images taken at different stress levels for both types of specimens and will be used with aspect ratio to determine the morphological evolution of  $\gamma'$  precipitates in a Ni-Al system.

## 4.2 Materials and methods

The specimens have a nominal composition 13.36 at.% Al. The experiments were performed by Prikhodko on cylindrically symmetric specimens with a certain geometry: the first sample has a doubly-tapered (DT) shape and the second sample has a right cylindrical (RC) shape. All samples were aged at  $640^\circ$ . The DT samples were then aged between 10 to 1021 hours

Table 4.1: Stresses at which TEM samples were considered.

	stress 1 (MPa)	stress 2 (MPa)	stress 3 (MPa)	stress 4 (MPa)
DT	0	33	53	127
RC	0	23	53	151

with applied stresses ranging from 30 to 130 MPa. The RC samples were aged for 120 hours under stresses ranging from 0 to 151 MPa. TEM samples were made in the plane normal to the axis of the applied stress, normal to  $[100]$ . Dark field (DF) TEM images were taken

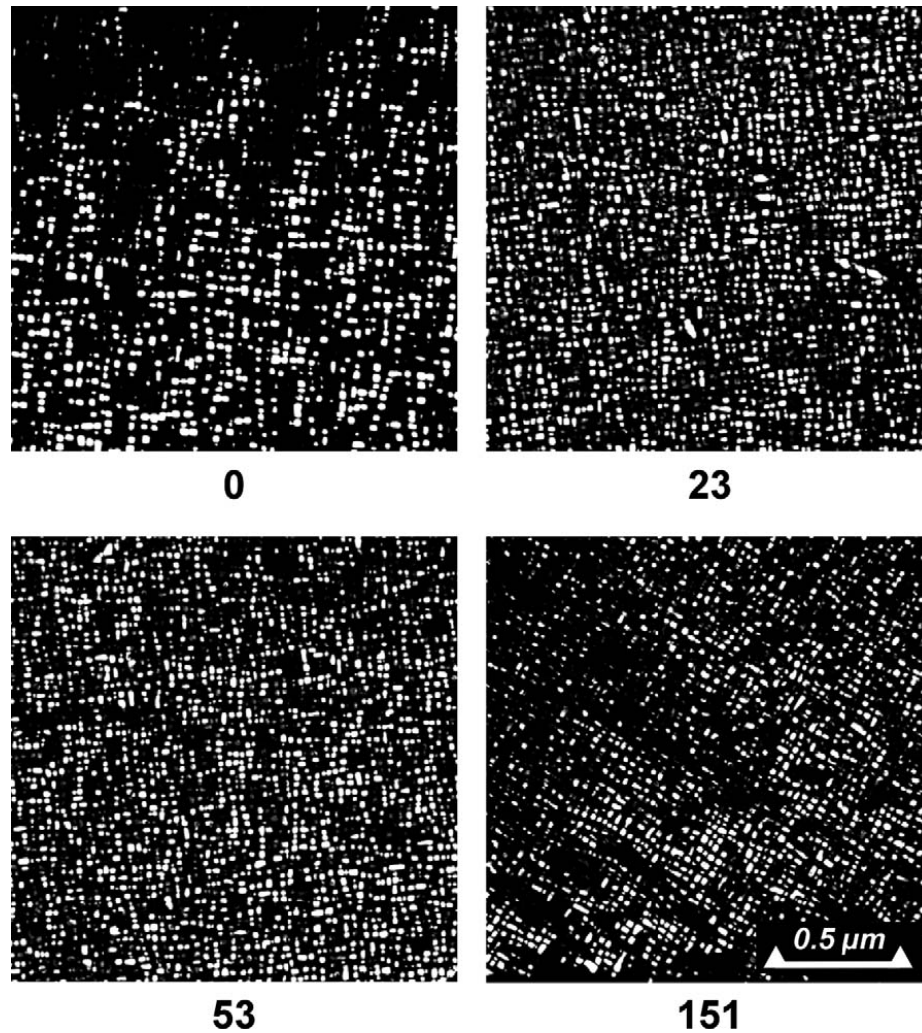


Figure 4.1: Dark field TEM images of the  $\gamma/\gamma'$  microstructure in the DT specimens aged for 120 hours at  $640^\circ\text{C}$ . The number below corresponds to the applied stress in MPa. *Reprinted with permission from [9]. Copyrighted by Elsevier.*

at various stresses for the DT specimens and are shown in Figure 4.1. The TEM images of the RC specimens are shown in Figure 4.2.

2D moment invariants are used to quantify the shape evolution of  $\gamma'$  precipitates at the stresses listed in Table 4.1 for the DT specimens. The 2D moment invariants are then plotted on SOMIMs and PMIMs as density maps. The MIs for the precipitates are compared to 2D sections of cuboids with varying exponent  $n$  values. Additionally, the equivalent ellipse aspect ratios are computed for each precipitate. Then the change of the distributions with increasing stress is measured by computing the distance from the MI distributions from the microstructure at zero stress.

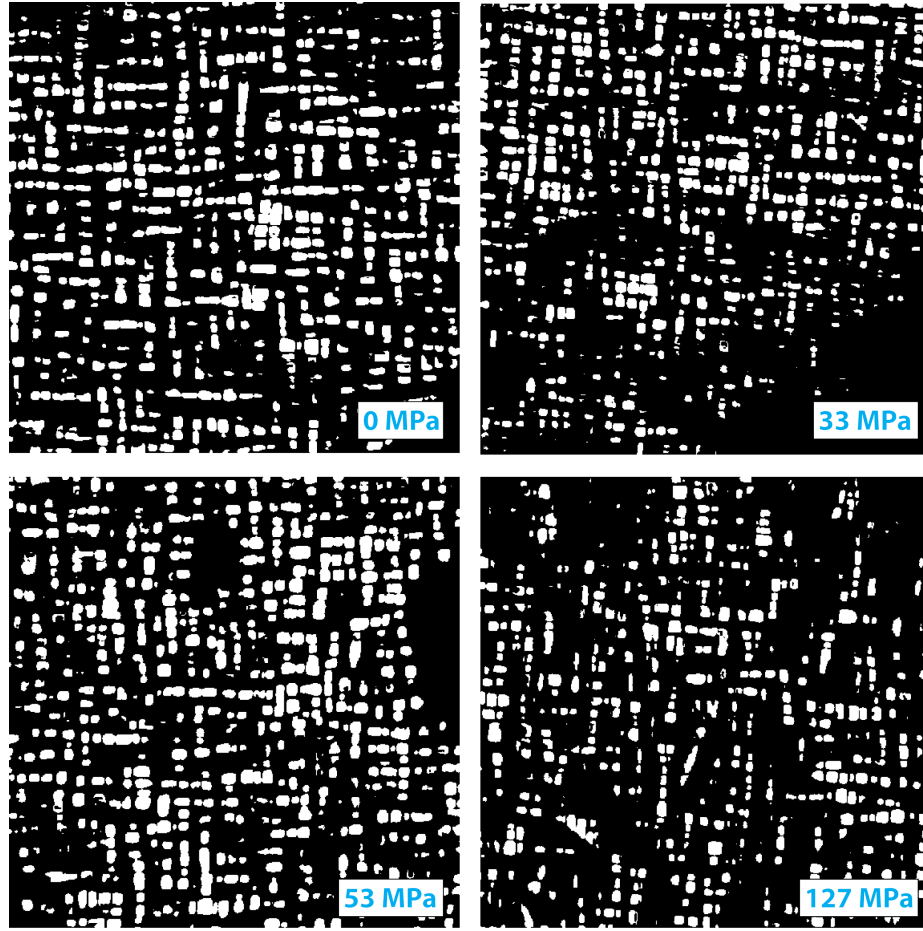


Figure 4.2: Dark field TEM images of the  $\gamma/\gamma'$  microstructure in the RC specimens aged for 120 hours at 640°C. The number below corresponds to the applied stress in MPa. *Figure adapted with permission from [9]. Copyrighted by Elsevier.*

### 4.3 Results and discussion

In the initial analysis, three parameters were considered: the radius, the aspect ratio, and  $\Sigma$ . The size of the precipitates is measured by their radius, which is calculated as [9]:

$$r = r_{min} \frac{A + 1}{2}, \quad (4.4)$$

where  $r_{min}$  is the radius of the smallest circle inscribed in its image and  $A$  is the aspect ratio. The precipitates were separated by size, and the  $\Sigma$  and  $A$  values were considered in these groups. Prikhodko showed the results from the  $\Sigma$  analysis via four plots [9]:

- $\Sigma$  vs.  $r$ , as scatter plots colored by aspect ratio and as another plot with  $\Sigma$  as an average.

- $A$  vs.  $r$ , as scatter plots and as another plot with  $A$  as an average.
- $\Sigma$  vs.  $\sigma$ , six plots separated by radius size.
- $A$  vs.  $\sigma$ , six plots separated by radius size.

The moment invariant approach is chosen as an alternative to using the shape parameters  $\Sigma$  and  $A$  to characterize the morphological evolution of  $\gamma'$  precipitates with increasing stress. Through this analysis, a series of relationships are determined. Prikhodko and Ardell determined previously that as applied compressive stress increases, the  $\gamma/\gamma'$  interfaces become more planar and the aspect ratio increases [9]. This is particularly true for larger volume fractions, as in the RC specimens which have a larger volume fraction compared to the DT specimens. However, we will only consider results from the DT specimens here.

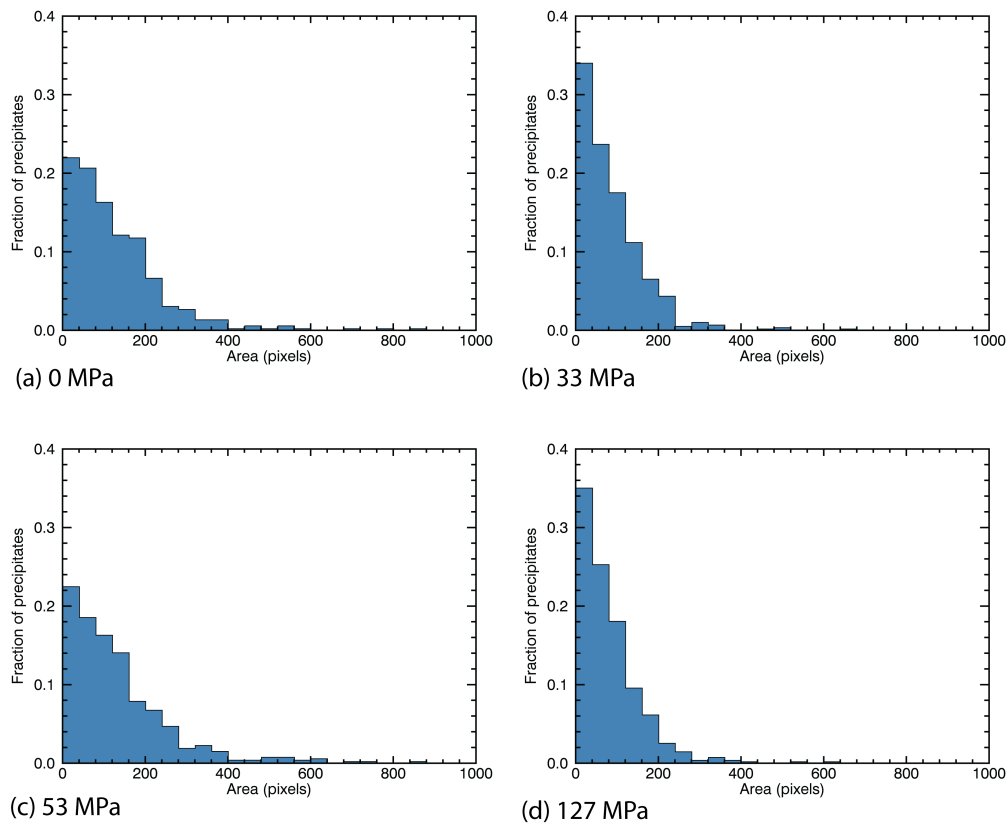


Figure 4.3: Histograms of the areas of the precipitates in the DT specimens for different stresses (a) 0 MPa, (b) 33 MPa, (c) 53 MPa, and (d) 127 MPa. The average areas are: 122.9, 83.7, 131.6, and 80, respectively, for each of the stresses.

In the DT specimens, Prikhodko and Ardell determined that  $\Sigma$  and aspect ratio stay fairly constant with increasing stresses for all particle radii; the average precipitate size stays constant as well [9]. In the RC specimens, increasing applied stress leads to decreasing particle sizes, and an applied stress causes the shapes of  $\gamma'$  precipitates to become more non-equiaxed [73, 78]. The volume fraction of  $\gamma'$  influences how much the shapes are affected, and this is less pronounced in smaller volume fraction alloys. As  $\gamma'$  precipitates grow, they become more planar and the aspect ratios increase due to the increased elastic interactions between precipitates. The shape parameters  $\Sigma$  and  $A$  are less strongly affected by stress in the DT specimens than in the RC specimens [9]. To provide a comparison between the moment invariant approach and the  $\Sigma$  approach, it is useful to separate the precipitates by size and by aspect ratio and consider their moment invariants in this manner.

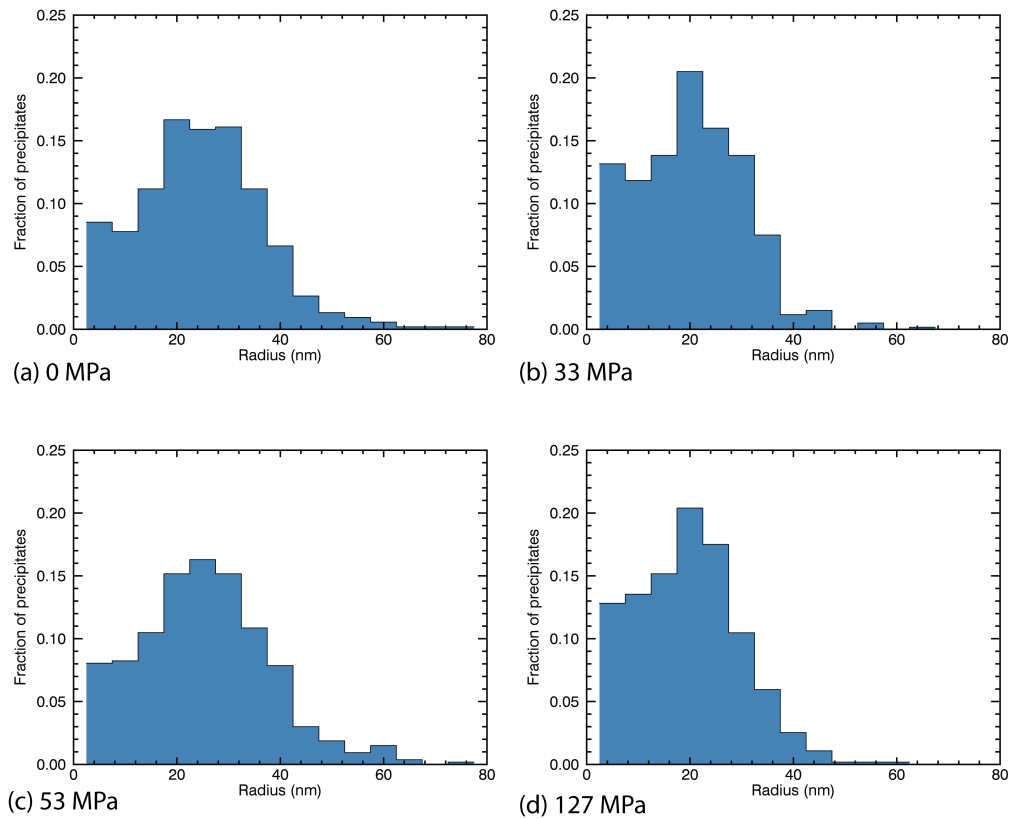


Figure 4.4: Histograms of the radii of the precipitates in the DT specimens for different stresses (a) 0 MPa, (b) 33 MPa, (c) 53 MPa, and (d) 127 MPa. The average radius are: 24.77, 20.19, 25.44, and 19.78, respectively, for each of the stresses.

Figure 4.3 shows histograms of the areas of the precipitates for each of the stresses. The average areas fluctuate with increasing stress, but the sizes are in the same range at every stress level. The area of each precipitate was then converted to its radius, by calculating the radius as if the precipitate was a circle using  $r = \sqrt{\frac{A}{\pi}}$ . Histograms of the radii of the precipitates are shown in Figure 4.4 and show larger precipitate sizes than observed by Prikhodko et al. [9].

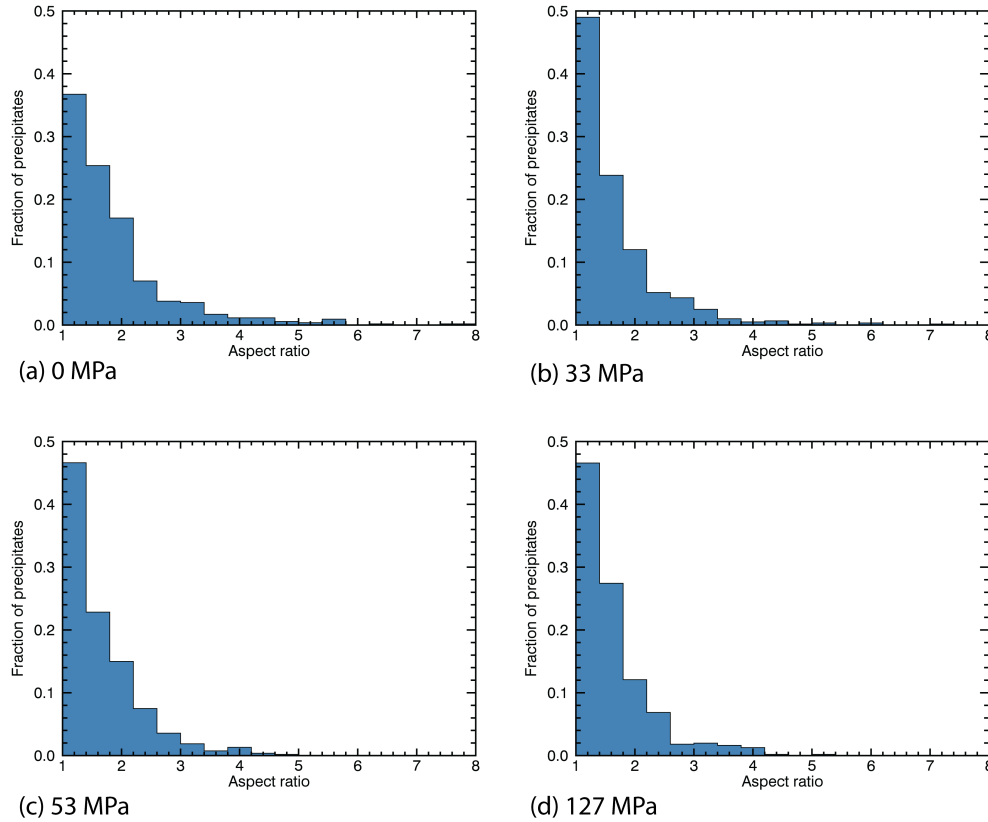


Figure 4.5: Histograms of the equivalent ellipse aspect ratio  $\tau$  for different stresses (a) 0 MPa, (b) 33 MPa, (c) 53 MPa, and (d) 127 MPa. The median aspect ratios are: 1.87, 1.658, 1.646, 1.631, respectively, for each of the stresses.

The aspect ratio is also calculated to determine if there is any morphological change in  $\gamma'$  shape. The aspect ratio was also computed for the precipitates, and the histograms are shown in Figure 4.5. The average aspect ratio decreases after stress is applied to the microstructure. However, this does not agree with the expectation that the  $\gamma'$  precipitates become more planar as they grow; instead they decrease in aspect ratio [9]. One possible explanation is that the stresses applied only cause strain in the elastic region and the

precipitates needed more time to fully become cuboidal and to align along the elastically soft cube  $\langle 001 \rangle$  directions. Additionally, more precipitates were considered in Prikhodko's analysis, which may explain this difference.

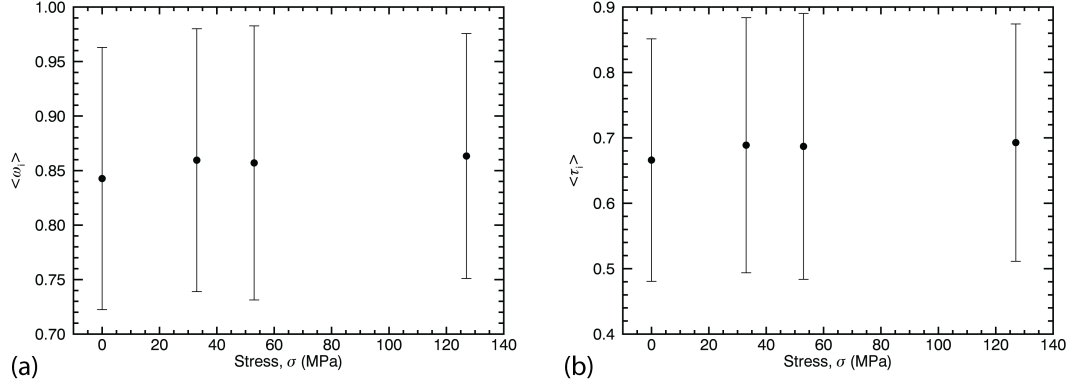


Figure 4.6: Moment invariants vs. stress (a)  $\langle \bar{\omega}_i \rangle$  (b)  $\langle \bar{\tau}_i \rangle$ , indicating that the average MI values do not change with increasing stress in a DT specimen.

Moment invariants were calculated for the  $\gamma'$  precipitates in the DT specimens in Figure 4.1. The precipitates that are on the edge of the image are not included in the calculation. Figure 4.6 shows the range of the averaged 2nd and 4th order moment invariants,  $\langle \bar{\omega}_i \rangle$  and  $\langle \bar{\tau}_i \rangle$ , indicating that the average moment invariants do not change much with stress. Figure 4.7 shows the density maps for the samples at each stress. The first row in Figure 4.7 shows the SOMIMs for the micrograph at each stress, while the second row in Figure 4.7 shows the PMIMs. The density maps do not seem to change much as the stress increases, but the final microstructure at 127MPa does seem to have less precipitates that deviate from a cuboidal shape. The peak of the distribution is located around  $(\bar{\omega}_1, \bar{\omega}_2) = (0.82, 0.89)$ . The  $\bar{\omega}_2$  for all rectangles is 0.911, so the  $\gamma'$  precipitates have a  $\bar{\omega}_2$  that is quite close to that of the rectangle. The  $(\bar{\omega}_1, \bar{\omega}_2)$  for a square is  $(0.955, 0.912)$ , so the distribution has values that have aspect ratios larger than one, but they are still relatively close. It is also useful to consider only  $\bar{\omega}_2$ , the affine moment invariant.  $\bar{\omega}_2$  does not change much with increasing stress, as shown in Figure 4.8. However, the histograms also show that the fraction of precipitates with  $\bar{\omega}_2$  greater than the value for a rectangle, 0.911, slightly increases with increasing stress. Initially, at zero stress, only 57% of the precipitates have an  $\bar{\omega}_2$  value above 0.911 compared to 63% at 127 MPa.

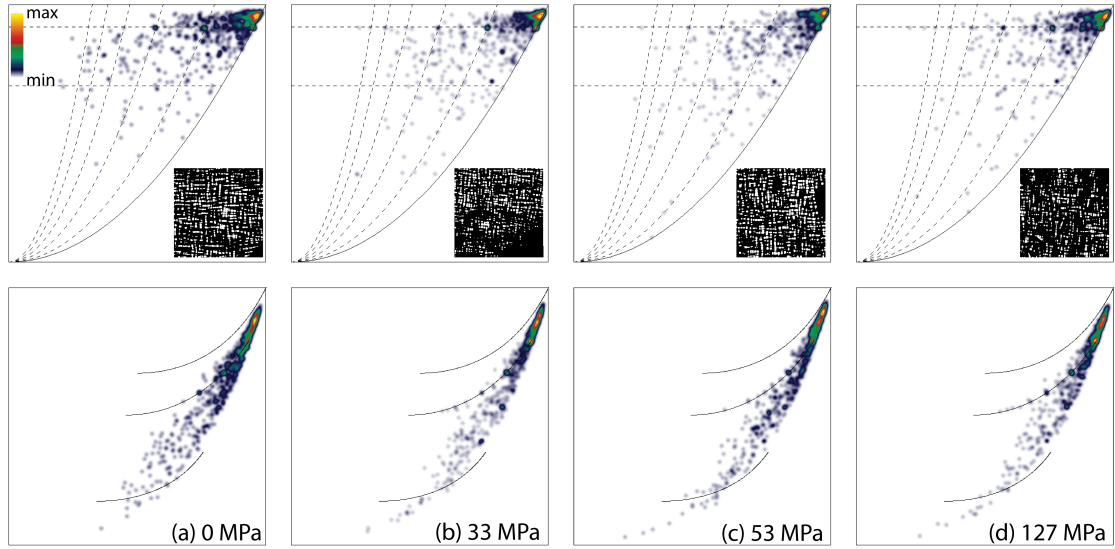


Figure 4.7: The SOMIMs and PMIMs for the samples in the DT specimen (a) 0 MPa, (b) 33 MPa, (c) 53 MPa, and (d) 127 MPa. The peak of the distributions for each stress level is between a cube and a circle shape, indicating that the majority of the precipitates have a cuboidal shape with an aspect ratio close to 1.

Table 4.2 shows the average values of precipitate size and shape descriptors. The averages of the moment invariants do not show much a change with increasing stress; however, the aspect ratio decreases with increasing stress. It is also interesting to show  $\bar{\omega}_2$  vs. ra-

Table 4.2: The average values of the area, radius, aspect ratio,  $\bar{\omega}_2$ , and  $\langle \bar{\omega}_i \rangle$ .

stress (MPa)	area (pixels)	radius (nm)	AR	$\bar{\omega}_2$	$\langle \bar{\omega}_i \rangle$
0	$122.898 \pm 111$	$24.769 \pm 12$	$1.875 \pm 0.941$	$0.885 \pm 0.094$	$0.843 \pm 0.120$
33	$83.658 \pm 78$	$20.185 \pm 10$	$1.658 \pm 0.741$	$0.884 \pm 0.107$	$0.860 \pm 0.121$
53	$131.603 \pm 124$	$25.436 \pm 13$	$1.646 \pm 0.622$	$0.881 \pm 0.119$	$0.857 \pm 0.126$
127	$80.002 \pm 75$	$19.778 \pm 10$	$1.631 \pm 0.627$	$0.888 \pm 0.108$	$0.863 \pm 0.112$

dus, to be able to compare to Prikhodko's results. Figure 4.9 shows  $\bar{\omega}_2$  vs. radius, colored by aspect ratio. While it is somewhat difficult to distinguish between the different colors, the final microstructure has more precipitates with large aspect ratios and larger sizes with high  $\bar{\omega}_2$  values.

The moment invariants for each precipitate were also compared to the moment invariants for cuboids with exponent  $n$  from 4 to 10, in increments of 0.05. The precipitate was then assigned a superellipsoid exponent value based on the  $n$  that the precipitate matched to best. The cuboids were sectioned normal to the [100] direction, so that they are in the same

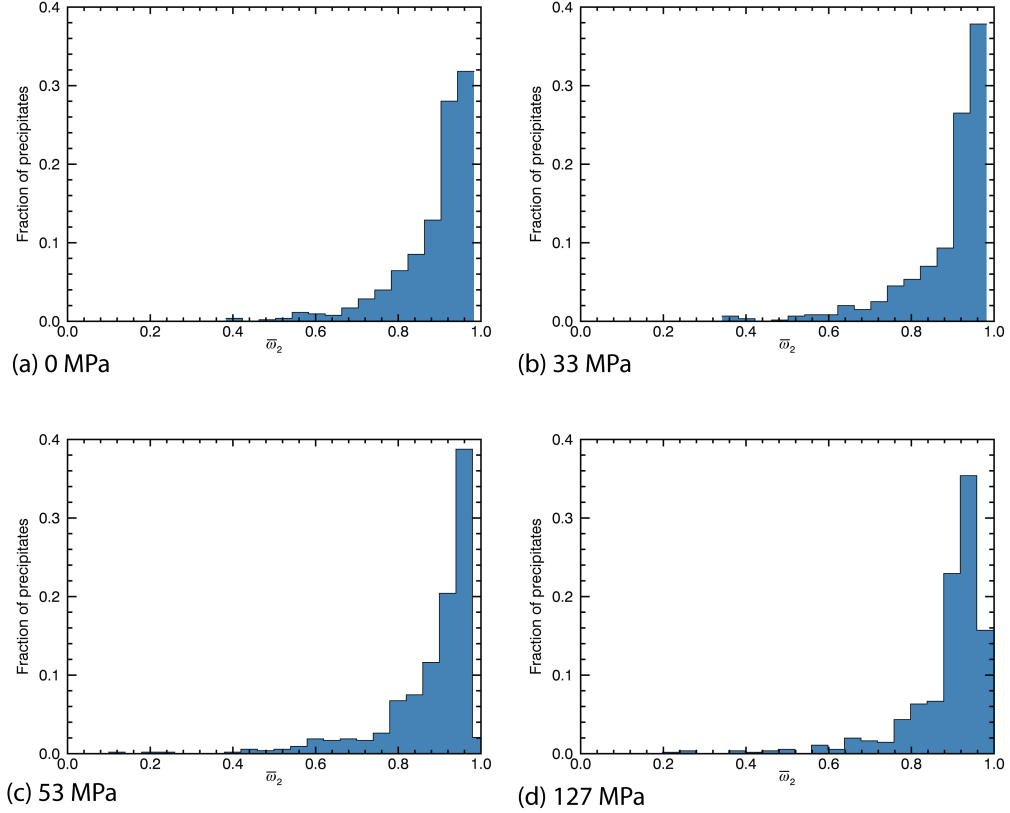


Figure 4.8: Histograms of the  $\langle \bar{\omega}_2 \rangle$  at different stresses for different stresses (a) 0 MPa, (b) 33 MPa, (c) 53 MPa, and (d) 127 MPa. The average  $\langle \bar{\omega}_2 \rangle$  are: 0.885, 0.884, 0.881, and 0.888, respectively, for each of the stresses.

plane as the  $\gamma'$  precipitates being considered. Their 2D moment invariants were computed, then the precipitates were compared to the moment invariants for the cuboids by computing the Euclidean distance. The Euclidean distance from the MIs for the cuboids is calculated as:

$$d = \sqrt{(\bar{\omega}_1^p - \bar{\omega}_1^c)^2 + (\bar{\omega}_2^p - \bar{\omega}_2^c)^2 + (\bar{\tau}_1^p - \bar{\tau}_1^c)^2 + (\bar{\tau}_2^p - \bar{\tau}_2^c)^2 + (\bar{\tau}_3^p - \bar{\tau}_3^c)^2}, \quad (4.5)$$

where  $^p$  refers the MI value for the precipitate, and  $^c$  refers to the value for the cuboid. Figure 4.10 shows the histograms for the cuboids that the precipitates are closest to, and Figure 4.11 shows the histograms for the minimum Euclidean distance to a cuboid. The average distances decrease with increasing stress, and the average  $n$  value of the  $\gamma'$  precipitates decreases with increasing stress.

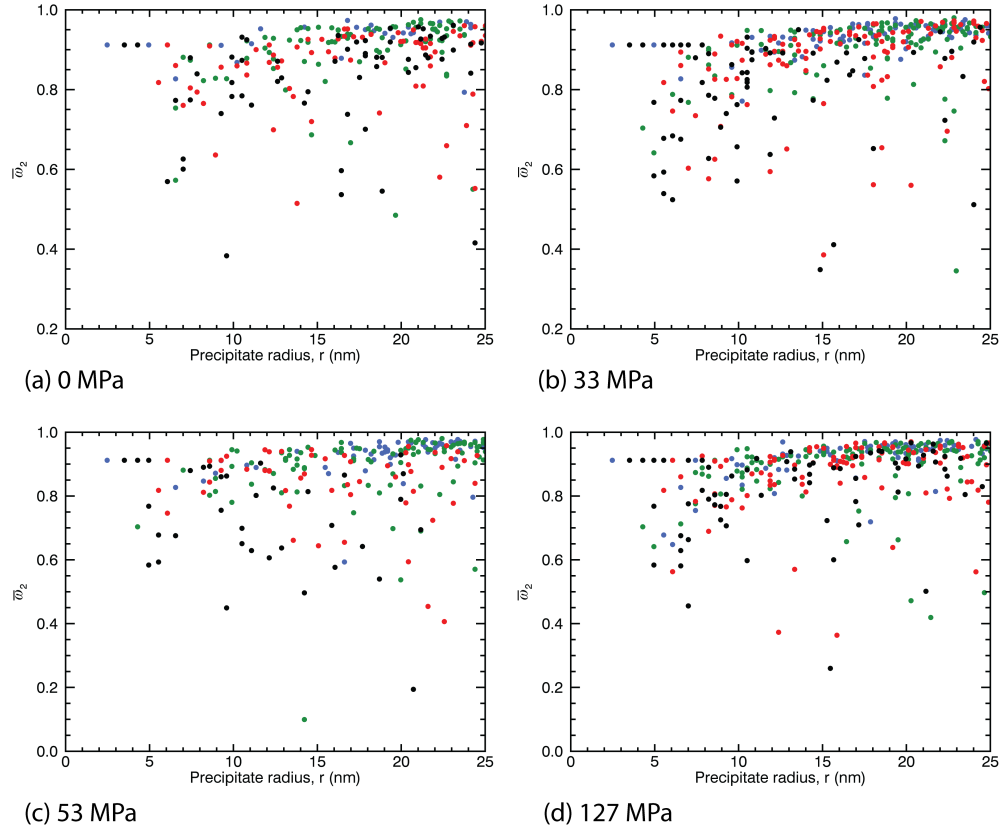


Figure 4.9:  $\bar{\omega}_2$  vs. radius, colored by aspect ratio size (a) 0 MPa, (b) 33 MPa, (c) 53 MPa, and (d) 127 MPa. The aspect ratio is colored as: 1 - 1.2: blue, 1.2 - 1.5: forest green, 1.5 - 2: red, greater than 2: black.

The distance metrics can also be used to consider how much the  $\gamma'$  precipitates have changed once stress is applied. The Hellinger distance and the chi-squared distance are computed to compare the density maps computed for the stresses 33, 53, and 127 MPa to the density maps for stress at 0 MPa, shown in Figure 4.7. The SOMIM and PMIM in Figure 4.7(a) are compared to the maps in Figures 4.7(b)-(d). The results are shown in Figure 4.12. However, the distance metrics show the same amount of change in the density maps calculated at the different stresses. Thus, the SOMIMs for stresses at 33, 53, and 127 MPa are all the same distance away from the SOMIM for stress at 0 MPa, with a Hellinger distance of about 0.45 and a chi-squared value of about 0.17. The PMIMs for stress at 33, 53, and 127 MPa have a Hellinger distance of about 0.35 and a chi-squared distance of about 0.26. The average Hellinger distance for both maps is about 0.4. The SOMIMs for stresses at 33, 53, and 127 MPa are more similarly distributed to stress at 0 MPa than

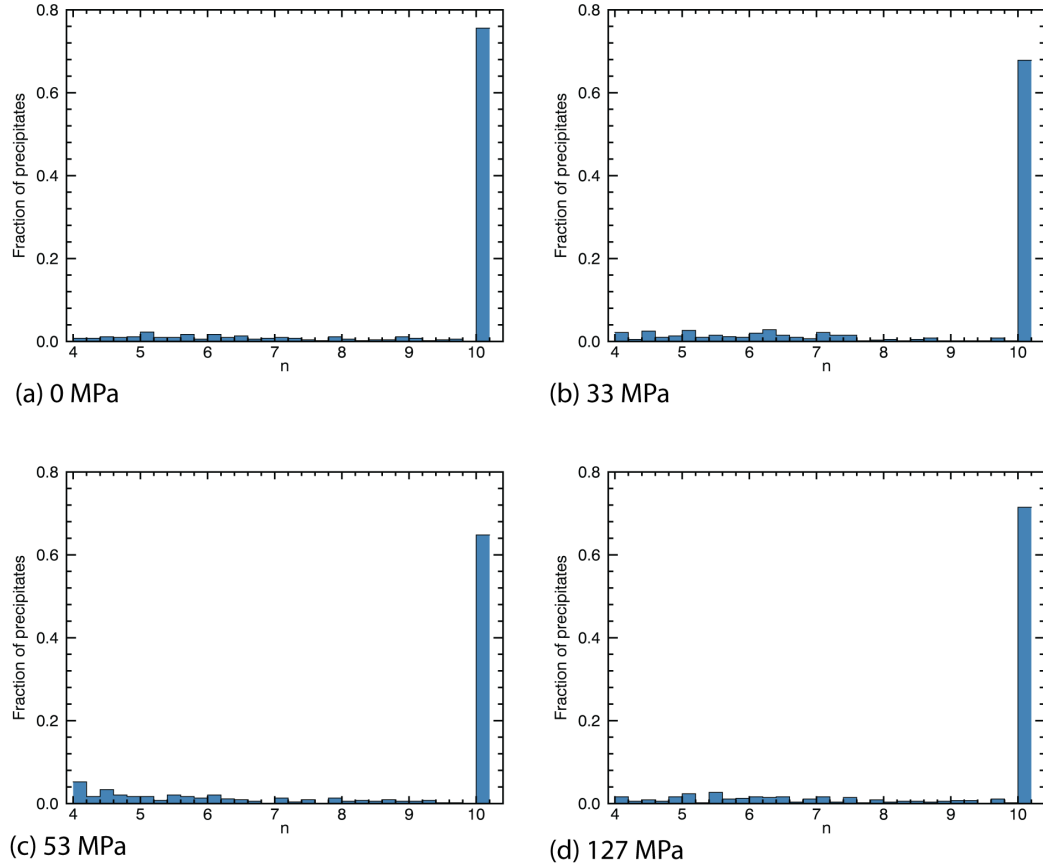


Figure 4.10: Histograms of the  $n$  values at different stresses for different stresses (a) 0 MPa, (b) 33 MPa, (c) 53 MPa, and (d) 127 MPa. The average  $n$  are: 9.12, 8.77, 8.54, 8.98, respectively, for each of the stresses.

comparing the PMIMs of those stresses to the PMIM at no stress.

There are some discrepancies between the chi-squared distance and the Hellinger distance results. For the distances computed between the SOMIMs, the chi-squared distance shows that the SOMIMs between the stress at 0 MPa and stress at 127 MPa are more similar than that of stress at 33 or stress at 53. Using the Hellinger distance metric, the SOMIMs between stress = 0 and stress = 33 are the most similar, followed by stress = 127, then stress = 53. The precipitates in stress = 53 MPa are the most different from stress at 0 MPa. The two distance metrics agree with each other when considering the PMIMs. The stress at 127 MPa is most similar to stress at 0 MPa, followed by stress at 33 MPa and stress = 53 MPa. However, the distances between the maps at different stresses do not differ much from the initial map for stress at 0 MPa, and it is difficult to say if there

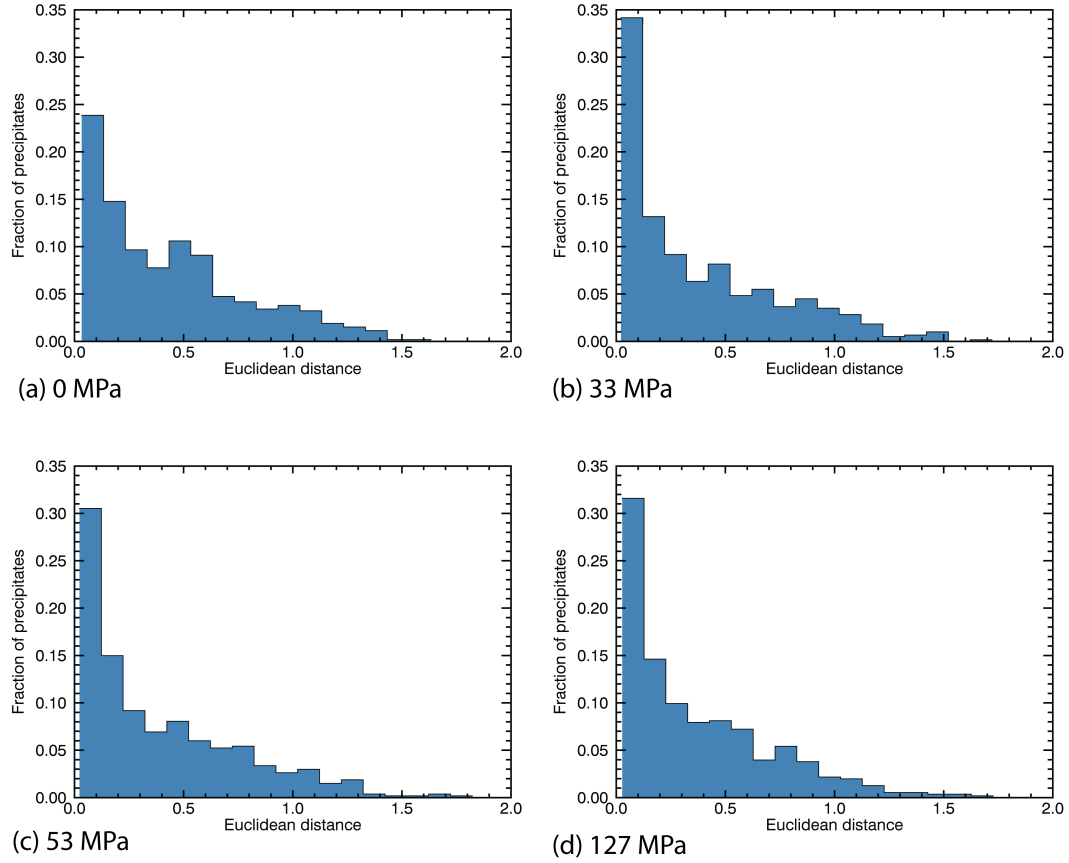


Figure 4.11: Histograms of the Euclidean distance at different stresses for different stresses (a) 0 MPa, (b) 33 MPa, (c) 53 MPa, and (d) 127 MPa. The average  $d_{Euc}$  are: 0.437, 0.384, 0.397, 0.376, respectively, for each of the stresses.

is any morphological evolution with increasing stress. The analysis using distance metrics show that all the microstructures are fairly similar to each other. These results agree with those found by Prikhodko and Ardell in [9]. By considering the shapes of all precipitates throughout the entire microstructure at each stress level, each microstructure has similar shapes throughout it.

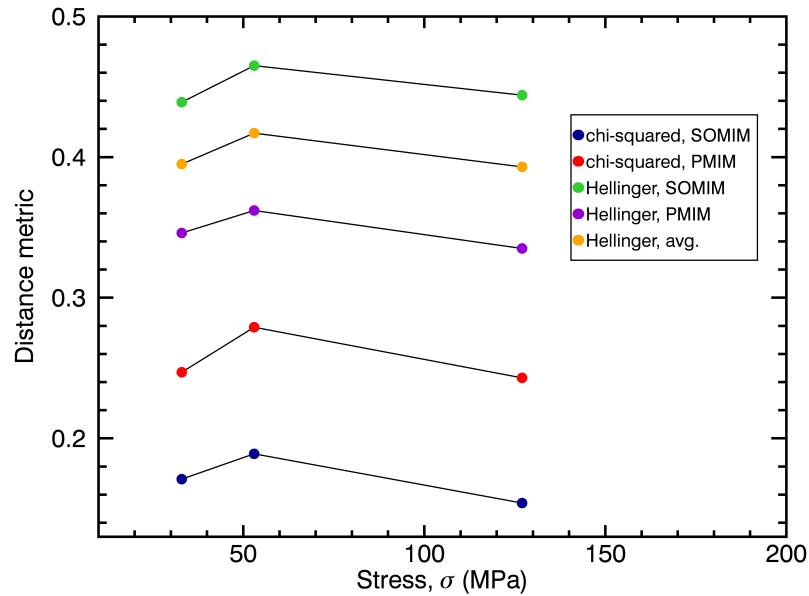


Figure 4.12: Distance metric vs. stress using chi-squared and Hellinger distances for the SOMIM's and the PMIM's.

## 4.4 Conclusions

The moment invariants were computed from micrographs from the DT specimens at stress of 0, 33, 53, and 127 MPa. By considering only the averages of the moment invariants, it is difficult to distinguish between the microstructures at different stresses. This is in agreement with Prikhodko's work, where the DT specimens all showed similar precipitate shapes [9]. However, the average aspect ratio was found to decrease with increasing stress, while the aspect ratio calculated by Prikhodko was found to stay relatively constant with increasing stress. When the precipitates are sorted by size, the larger precipitates tended to have larger aspect ratios, while smaller precipitates tended to have smaller aspect ratios. This conclusion was consistent with Prikhodko's results using  $\Sigma$  and  $A$ . The superellipsoid exponent  $n$  was also found to slightly decrease with increasing stress, which was found to somewhat agree with Prikhodko's  $\Sigma$  analysis.

With increasing stress, the present study found that:

- The aspect ratio decreases.

- The average moment invariants are approximately the same.
- Using the Hellinger distance, the density maps for all stress levels are fairly similar.
- The radius size is approximately the same.
- The superellipsoid exponent  $n$  slightly decreases.

Overall, the results using moment invariants seemed to agree with the results using  $\Sigma$  and  $A$  to quantify the morphology of the  $\gamma'$  precipitates. The only discrepancy was in aspect ratio, where the aspect ratio derived from the moment invariants decreased with increasing stress while the aspect ratio from Prikhodko's work stayed relatively constant. Only one image per stress level was evaluated in this study, so the discrepancy could be due to the consideration of more precipitates in Prikhodko's study or in the differences in how aspect ratio was calculated. However, the moment invariant approach was able to detect that the  $\gamma'$  precipitates become slightly less cuboidal with increasing stress, which is not detected using  $\Sigma$ . The results do not strongly suggest a great change in shape for these precipitates, indicating that moment invariants do not provide much additional information that was not previously described by aspect ratio and  $\Sigma$ . However, moment invariants do provide a way to link other shape descriptors such as the superellipsoid exponent  $n$  and aspect ratio to describe the evolution of the  $\gamma'$  precipitates. Therefore the hypothesis is not strongly supported by the MI analysis applied to the microstructures of the DT specimens.

## CHAPTER V

### The effect of doping on transitions in ferroelastic materials

#### 5.1 Introduction

The class of ferroelastic materials, which encompasses most shape memory alloys (SMAs) and superelastic materials, is an important class of functional materials and plays a crucial role in many modern technologies. These materials are defined by the non-linear strain-stress hysteresis and generally characterized by the existence of two distinct strain states, the strain liquid (a strain-disordered paraelastic state known as the parent phase or austenite at high temperature) and the strain crystal (a long-range strain-ordered ferroelastic state known as martensite at low temperature). The ferroelastic (or martensitic) transition between these two states under the influence of a temperature change or an applied stress gives rise to the technologically important shape memory effect and superelasticity [104, 105].

Recent experimental work [8, 106, 107] and simulations [108–110] have found that point defect doping will destroy the normal ferroelastic transition and produce a new strain state, a strain glass state, that is analogous to cluster-spin glasses in ferromagnetic systems and relaxors in ferroelectric systems [111]. Strain glass has shown abnormal characteristics, such as nanosized ferroelastic domains, frequency dispersion of the modulus and internal friction, a continuous phase transition and so on [107, 112–115]. However, the physical nature of the strain glass state, i.e., the correlation between nanosized ferroelastic domains and long range ordered martensitic domains, as well as the correlation among different nanosized ferroelastic domains, is still unclear. A strain glass is a frozen and disordered strain state with short range order [106] due to point defects causing random local stresses and strains that inhibit the long-range ordering of strains [111]. Some of the properties of

strain glass make it an interesting candidate for possible technological applications; these include a “smeared” elastic modulus peak with frequency dispersion, the disappearance of a heat flow peak, and a small thermal hysteresis [113]. The strain glass state can be qualitatively identified by frozen nanodomains, no change in the average structure, and non-ergodicity.

The strain glass state was first reported in  $\text{Ti}_{48.5}\text{Ni}_{51.5}$  [106]; later Zhang et al. [116] built a detailed phase transition phase diagram and reported that the martensitic alloy  $\text{Ti}_{50-x}\text{Ni}_{50+x}$  exhibits the strain glass state when doped with  $x > 1.3$  excess Ni as a point defect [106]. Several other alloy systems also exhibit the strain glass state:  $\text{Ti}_{50}\text{Ni}_{50-x}\text{Fe}_x$  with a critical Fe doping level of  $5 < x_c < 6$  [107] and combinations of elements with Ti such as  $\text{TiNi-X}$ ,  $\text{Ti-Pd-X}$ , etc., where  $X$  is an alloying element such as Fe, Cr, Mn, Co, V, etc. [111].

While martensitic microstructures have been studied extensively, the key microstructural features of a strain glass state is still poorly understood. The presence of point defects, such as excess Ni in a  $\text{Ti}_{50-x}\text{Ni}_{50+x}$  alloy, causes a strain glass transition to occur when the excess concentration  $x$  is above a critical value  $x_c$  [116]. Doping at a defect concentration lower than the critical value  $x_c$  changes the normal martensitic phase transition temperature; the system forms a premartensitic tweed, a precursor that has a quasi-dynamic disordered strain state and is identified by its cross-hatched appearance in electron diffraction contrast images [106]. At or above the critical defect concentration, the normal martensitic phase transition is suppressed and a strain glass state forms, which is also represented by a static disordered strain state and is similar in appearance to the premartensitic tweed [116]. However, premartensitic tweed is distinct from the strain glass state [111].

Wang et al. [110, 113] implemented a phase field model based on the Landau theory of phase transitions to study the effect of point defects on a ferroelastic system. The model assumes that point defects change the thermodynamic stability of martensite globally and create local lattice distortions that break up the symmetry of the Landau potential [110, 113]. However, the microstructural nature such as domain size, distribution, shape, etc. of the strain glass state are still unclear.

In this chapter, moment invariants and image entropy are used to analyze the mi-

crostructure images produced by the model in [110] for different dopant concentrations at different temperatures to quantitatively determine the correlation between nanosized ferroelastic domains and long range ordered ferroelastic domains and among different nanosized ferroelastic domains. The different microstructural states will be easily distinguished from each other using these quantitative techniques.

## 5.2 Theoretical and modeling approach

### 5.2.1 Phase field model for strain glass material

For simplicity, a single crystal undergoing a generic square to rectangle (2D) martensitic transformation is considered [117]. The Landau free energy (2-4-6 potential) without considering the effect of point defects is described by Equation (5.1) and the global transition temperature effect (GTTE) and the local field effect (LFE) caused by defects are described by Equations (5.2) and (5.3), respectively [110, 118]:

$$f_{ch}(\eta_1, \eta_2) = \frac{1}{2}A_1 (\eta_1^2(\mathbf{r}) + \eta_2^2(\mathbf{r})) - \frac{1}{4}A_2 (\eta_1^4(\mathbf{r}) + \eta_2^4(\mathbf{r})) + \frac{1}{4}A_3 (\eta_1^2(\mathbf{r}) + \eta_2^2(\mathbf{r}))^2 + \frac{1}{6}A_4 (\eta_1^2(\mathbf{r}) + \eta_2^2(\mathbf{r}))^3 \quad (5.1)$$

$$A_1 = A_1^0 (T - T^0(c)), \text{ and } T^0(c) = T^{00} + b \cdot c \quad (5.2)$$

$$f_l(\mathbf{r}) = \sum_{i,j=1,2;m=1,3,5} \eta_i^{local}(\mathbf{r}) \eta_j^m(\mathbf{r}) \quad (5.3)$$

The total free energy also includes the non-local gradient terms and the coherency elastic strain energy  $E_{el}$ :

$$F = \int d^2r \left[ \frac{1}{2}\beta(\nabla\eta_1)^2 + \frac{1}{2}\beta(\nabla\eta_2)^2 + f_{ch}(\eta_1, \eta_2) + f_L(\mathbf{r}) \right] + E_{el} \quad (5.4)$$

where

$$E_{el} = \frac{1}{2} c_{ijkl} \sum_{p=1}^2 \sum_{q=1}^2 \varepsilon_{ij}^{00}(p) \varepsilon_{ij}^{00}(q) \int \eta_p^2(\mathbf{r}) \eta_q^2(\mathbf{r}) d^3r - \frac{1}{2} \sum_{p=1}^2 \sum_{q=1}^2 \int \frac{d^2k}{(2\pi)^2} B_{pq} \left( \frac{\mathbf{k}}{k} \right) \{ \eta_p^2(\mathbf{r}) \}_k \{ \eta_q^2(\mathbf{r}) \}_k^* \quad (5.5)$$

In these equations,  $\eta_i(\mathbf{r})$  ( $i=1,2$ ) are the long range order (lro) parameters characterizing the martensitic phase;  $\eta_i^{local}(\mathbf{r})$  ( $i=1,2$ ) describes the local field caused by the static point defects;  $b$  characterizes the GTTE strength;  $c$  is a dimensionless average defect concentration measured in terms of area fraction in the simulations;  $T^{00}$  is the critical transition temperature without defects; and  $T^0(c)$  describes the critical transition temperature at defect concentration  $c$ . The coefficients in the Landau polynomial (normalized by the typical transformation “chemical” driving force  $\Delta f = 1.85 \times 10^6 \text{ J/m}^3$  [119]) are:  $A_1^0 = 0.05 \cdot (T - T^0)$ ,  $A_2 = 30$ ,  $A_3 = 19$ , and  $A_4 = 10$ .

The interfacial energy between the austenite and martensite is assumed to be  $\gamma = 0.05 \text{ J/m}^2$ , which yields a length scale  $l_0 = 0.94 \text{ nm}$ . The corresponding gradient energy coefficient is  $\beta = 4.5$ . For an elastically isotropic system, the elastic modulus can be described through the shear modulus  $G = 40 \text{ GPa}$  and the Poisson ratio  $\nu = 0.3$ . The elastic modulus is assumed to be the same for both phases (i.e., homogeneous modulus assumption). The elastic energy described in Equation (5.5) associated with the martensitic transformation or strain glass transition was described using the phase field microelasticity theory based on Green’s function solution [120].

Microstructural evolution during martensitic and strain-glass transitions is characterized by solving the stochastic time-dependent Ginsburg-Landau equation of the long range order parameters:

$$\frac{d\eta_p(\mathbf{r}, t)}{dt} = -M \frac{\partial F}{\partial \eta_p(\mathbf{r}, t)} + \xi_p(\mathbf{r}, t), \quad p = 1, 2, \quad (5.6)$$

where  $M$  ( $M=1$  in our simulation) is the kinetic coefficient and  $\xi_p(\mathbf{r}, t)$  is the Langevin random noise term. The system size considered in the simulations is  $256l_0 \times 256l_0$  (i.e.,  $240 \text{ nm} \times 240 \text{ nm}$ ). Periodic boundary conditions were applied along both dimensions.

### 5.2.2 Microstructure image analysis

Each simulated image had a size of  $256 \times 256$  pixels and was turned into a binary image by thresholding using a simple mean threshold algorithm [121]. Each binary image was then analyzed by scanning a window across the image, and the 2D second and fourth order moment invariants were computed for each window position. An initial range of window sizes from  $9 \times 9$  to  $37 \times 37$  pixels was used to determine the optimal window size for the simulated microstructures. It was found that a window size of  $17 \times 17$  pixels, which corresponds to representative elements with an area that is about 0.4% of the total image area, resulted in moment invariant maps with a sufficient number of data points as well as a clear evolution of the maps with respect to the relevant simulation parameters. The distribution of moment invariants is represented on both second order moment invariant maps (SOMIM) and projected moment invariant maps (PMIM). These density maps can be used to study how the MI distributions change with respect to temperature and defect concentration.

The microstructure images were also characterized using a second image descriptor, the image entropy [122]. For a given image  $A$ , with gray levels in the range  $[0 \dots 255]$ , an image histogram  $h(i)$  is obtained, which counts the number of pixels with gray level  $i$ . After normalization by the number of pixels,  $N$ , the image entropy is computed from the values  $p(i) = h(i)/N$  as  $H(A) = -\sum_{j=0}^{255} p_j \ln p_j$ . In thermodynamic terms, the image is regarded as an ideal solution of 256 components, and the image entropy is equal to the configurational entropy of mixing of this ideal solution [123]. Although images can be scaled to a smaller interval, using the full 0 to 255 grayscale provides the ability to better distinguish between microstructural differences.

## 5.3 Results and discussion

### 5.3.1 Moment invariant analysis

Moment invariant density maps were generated for each condition in Table 5.1. Figures 5.2 to 5.4 show the SOMIM and PMIM for each microstructure and transformation type of Figure 5.1: austenite to martensite (Figure 5.2), austenite to premartensitic tweed to martensite

(Figure 5.3), and austenite to strain glass (Figure 5.4). While the point defect concentration  $c$  may slightly alter the starting microstructure, which is generated using identical noise terms (random number seed and noise amplitude), the density maps have similar moment invariant distributions, with mostly isotropic shapes dispersed through the structures, as shown in Figure 5.1. The premartensitic tweed and the strain glass microstructures look similar, and their density maps show similar microstructural shapes and shape distributions.

Table 5.1: Defect Concentration and Temperature (K) for five different simulation sets.

Concentration	Temp 1	Temp 2	Temp 3	Temp 4	Temp 5
0.0	-	322	319.2	274.4	224
0.01	330.4	322	308	252	224
0.025	324.8	322	319.2	282.8	224
0.03	330.4	322	308	252	224
0.05	322	319.2	316.4	308	224
0.06	330.4	322	308	252	224
0.07	322	316.4	308	280	224
0.08	322	316.4	308	280	224
0.1	316.4	308	294	277.2	224
0.125	313.6	308	294	280	224
0.15	313.6	308	288.4	263.2	224
0.2	313.6	308	288.4	268.8	224

When  $c = 0$ , the system transforms from its paraelastic parent phase to a poly-twinned martensitic microstructure at a narrow temperature range (i.e., a sharp phase transition) that is typical of ferroelastics, as shown in Figure 5.1. Figure 5.2 shows the density map of the austenite-martensite transformation. The starting microstructure exhibits a narrow range of moment invariants located on or near the isotropic shape parabola  $\bar{\omega}_2 = \bar{\omega}_1^2$ . As the system cools down, the austenite transforms to martensite and displays a broader, more diffuse range of moment invariants, with a peak near the upper right corner (1, 1) point. The high moment invariant values are due to the poly-twinned nature of the martensite; since the interfaces between the twins are quite straight and the mask chosen to isolate the region of interest is a circle, the majority of moment invariant values will be close to those of the circle. Window positions that intersect the straight inter-variant boundaries give rise to the long curved distribution tails in Figure 5.2.

When  $0 < c < c_{crit}$ , the parent phase first changes to premartensitic tweed before

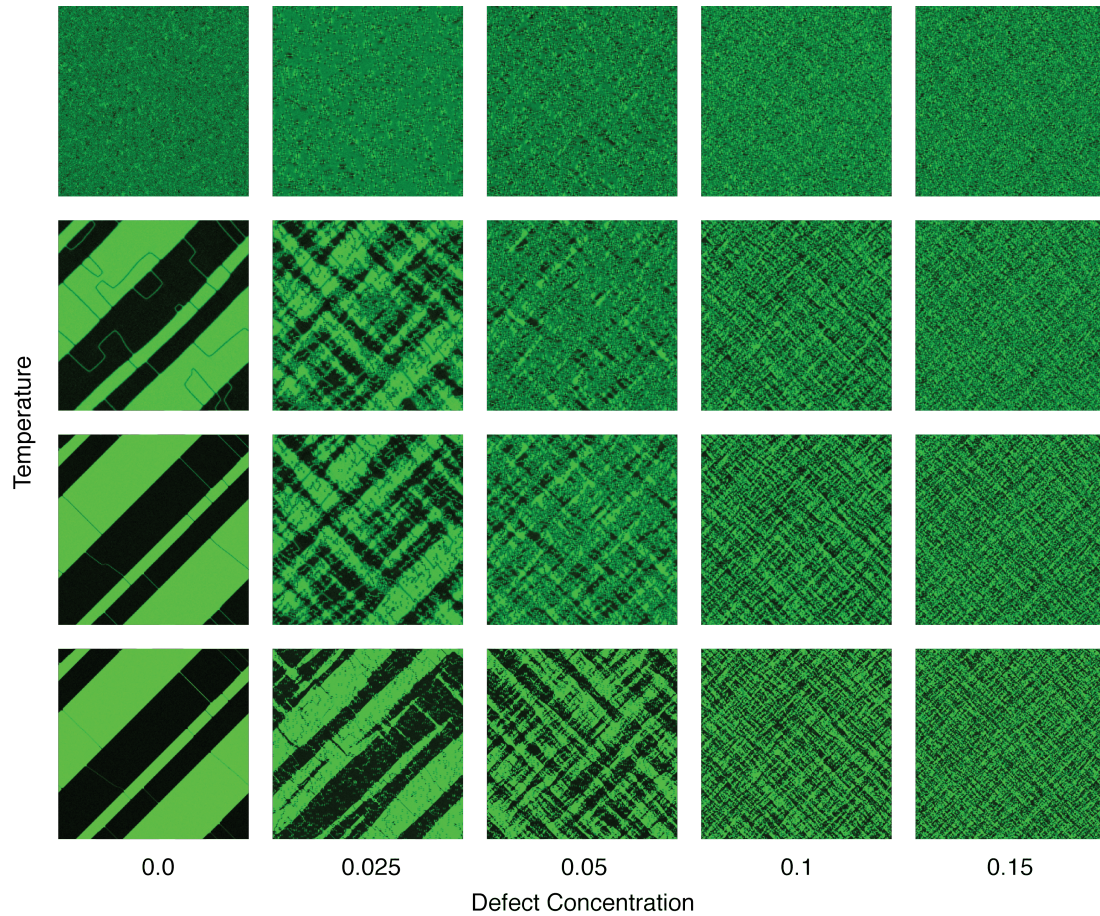


Figure 5.1: Microstructures resulting from the simulation with various defect concentrations. The temperature decreases from top to bottom.

transforming into martensite at the martensite start temperature. The moment invariant density map evolution for this type of transformation is shown for  $c = 0.025$  in Figure 5.3. The parent phase with a low defect concentration has similar density maps to that of the undoped parent phase, with a mostly isotropic shape distribution. The premartensitic tweed exists at intermediate temperatures, which is characterized by a cross-hatched structure. This structure results in isotropic shapes that are distributed along the entirety of the isotropic shape parabola in the SOMIM. As the system cools, the distribution of moment invariants sharpens from the broad distribution at higher temperatures to one that becomes once again centered near  $(1, 1)$ , similar to the  $c = 0$  case. The tweed microstructure changes into regular martensite upon further cooling because there are not enough point defects dispersed throughout the system to disrupt the long-range strain order; hence, the final microstructure at low defect concentrations is similar to that of the undoped system and

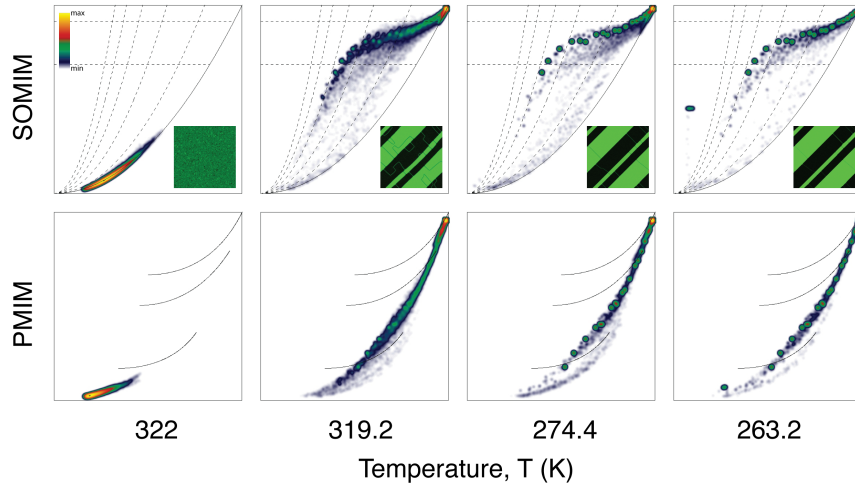


Figure 5.2: The SOMIM and PMIM density maps of the system with a defect concentration of  $c = 0$ , with decreasing temperature. A transformation from the parent phase ( $T=322$ ) to martensite ( $T=319.2, 274.4, 263.2$ ) with no intermediate states is shown.

exhibits martensite. While the density maps for the final temperature in  $c = 0$  and  $c = 0.025$  do not look the same, the maxima of both distributions are located near the upper right corner  $(1, 1)$ , which are the moment invariants for the circle. Thus, the key identifying feature of the martensite microstructure is that its density maps peak near the point  $(1, 1)$  for the circular window used to determine the MIs.

For  $c > c_{crit}$ , the parent phase changes to a glass, similar to the premartensitic tweed, then to its final state as a strain glass with static nanodomains. As the microstructure cools from the parent phase, the density maps (Figure 5.4) do not change much and only move up slightly along the isotropic parabola. Since the initial structure becomes frozen as it cools, at the final temperature similar density maps to those at the initial temperature are expected. Thus, the strain glass state is characterized by density maps that are centered along the lower portion of the isotropic shape parabola, and the peak near  $(1, 1)$  never develops because the microstructure details remain much smaller than the circular window size used to determine the MIs.

The moment invariant density maps for the different microstructure states are clearly distinct and in principle allow for the microstructure types to be identified directly. The austenitic microstructure is characterized by a disordered strain state with MIs along the isotropic shape parabola in the range  $[0.3, 0.9]$ , depending on the point defect concentra-

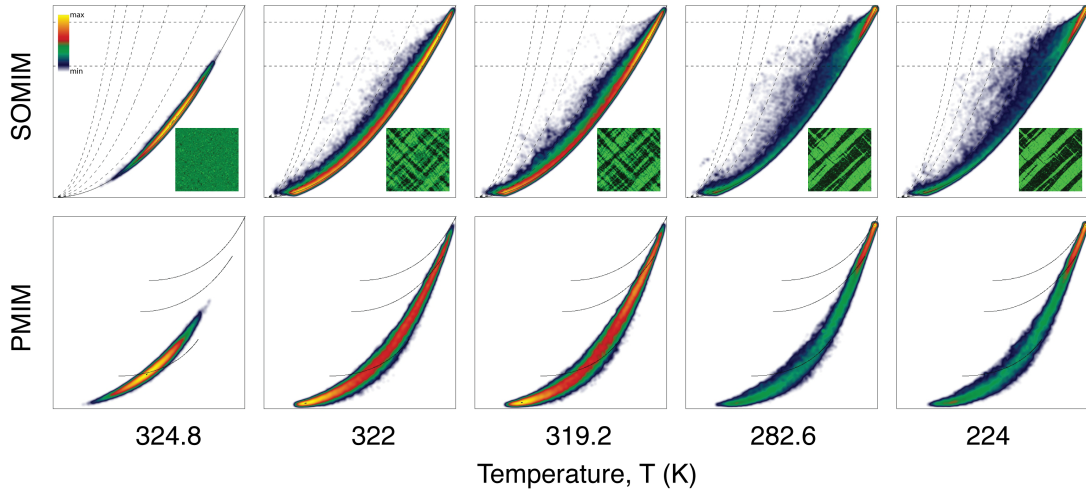


Figure 5.3: The SOMIM and PMIM density maps of the system with a defect concentration of  $c = 0.025$ , with decreasing temperature (in K). This shows a transformation from the parent phase ( $T=324.8$  K) to the premartensitic tweed ( $T=322, 319.2$  K) to martensite ( $T=224$  K).

tion in the system. The martensite phase has a moment invariant distribution that is centered around  $(1, 1)$  due to the shape of the computational window (circular). The premartensitic tweed and the strain glass have density maps that are broadly similar to those of the parent phase, but vary in their details depending on the size of the nanodomains. As defect concentration increases, the domain size decreases, which shifts the moment invariant distributions. While the normal transformation has density maps that show different distributions for different temperatures, the density maps for systems with high defect concentrations do not change much as the system cools, and they are clearly distinguishable from those of the other microstructural states.

### 5.3.2 Image entropy analysis

The image entropy,  $H$ , is a measure of statistical randomness in an image and was computed at different defect concentrations  $c$  and temperatures, which is shown in Figure 5.5. Results obtained for systems have defect concentrations below the critical value for strain glass are shown in different shades of blue, while those obtained for systems having defect concentrations above the critical values are shown in different shades of red. The defect concentrations are identified as having a martensitic transition or a strain glass transition based on the linearity of the relationship between entropy and temperature. A line of best fit is applied to each defect concentration, and an  $R^2$  value greater than 0.9 means that there is

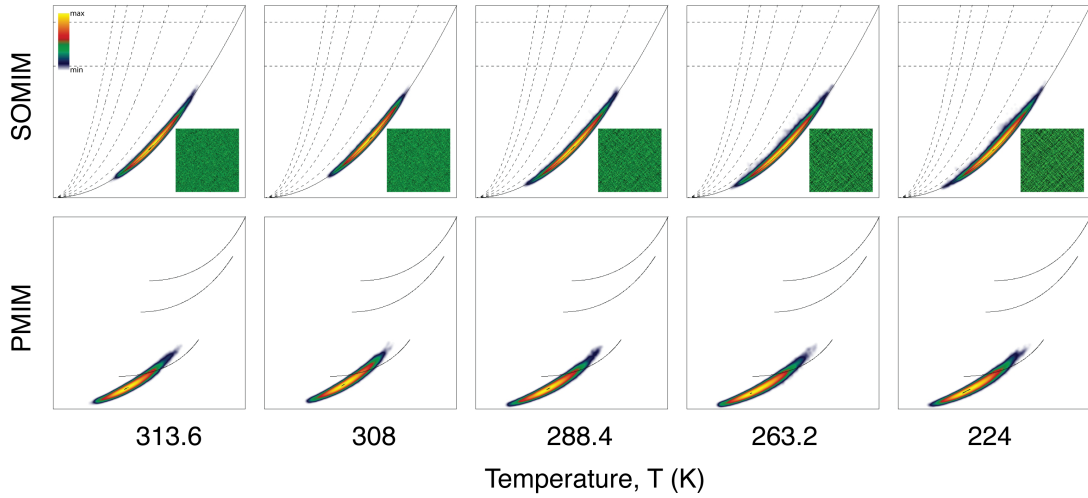


Figure 5.4: SOMIM and PMIM density maps for the system with a defect concentration of  $c = 0.15$ , with decreasing temperature. This shows a strain glass transition instead of the martensitic transformation, evolving from the parent phase ( $T=313.6$  K) to the frozen strain glass state ( $T=308$  K,  $288.4$ ,  $263.2$ ,  $224$  K) .

a nearly linear relationship between entropy and temperature for that defect concentration.

Low entropy images generally have little contrast between light and dark regions, whereas high entropy images tend to have a lot of texture and contrast. Hence, the strain glass microstructures will have a higher image entropy because of the strain disorder that is frozen into the system, while the martensitic microstructures will have a low image entropy due to the uniformity of the image contrast within the martensite variants. The parent phase has a relatively low image entropy at all defect concentrations since the microstructure does not change substantially with  $c$ ; this is also supported by the moment invariant analysis.

For the undoped ( $c = 0$ ) system, a rapid change occurs upon cooling from austenite to martensite with no intermediate state, so the image entropy rapidly changes from low to high during the transition and finally back to low for the uniform martensite variants. The highest image entropy occurs at  $T = 319.2$  K, likely because the martensitic plates are not fully developed at that temperature. The image entropy gradually decreases as the system cools down further.

The image entropy of systems with low defect concentrations starts out low, then increases quickly as the system cools. The entropy stays constant or decreases for the rest of the cooling process. The image entropy is at a peak at intermediate temperatures for

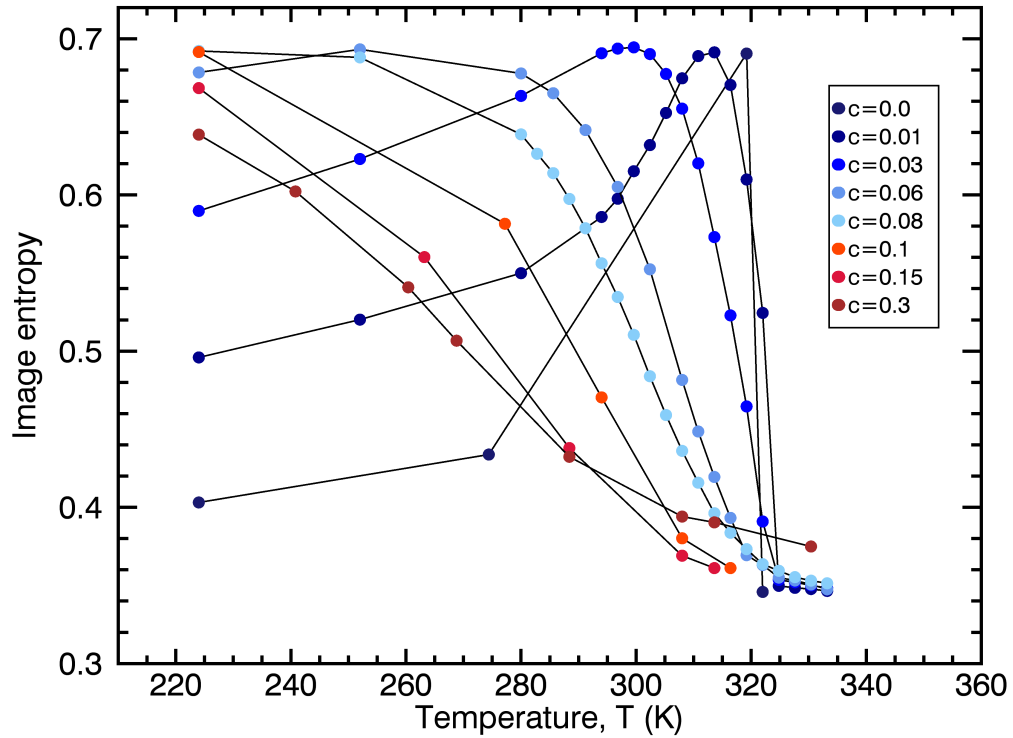


Figure 5.5: Image entropy vs. temperature for varying defect concentrations. Note the shift towards the left, from a strongly peaked curve to a decreasing, nearly linear relationship for systems above the critical defect concentration.

systems with low defect concentrations (below 0.08). While the final microstructures are martensite, the interfaces between the two variants are not as sharply defined as in the undoped system, so they have higher entropy than in the undoped martensite. The higher the point defect concentration, the higher the image entropy of the final martensite microstructure.

Systems with high defect concentration start out with a low image entropy that steadily increases in nearly linear fashion upon cooling and can be fitted to a linear relationship. The formation of the martensitic nanodomains causes the entropy to increase, and so systems with more point defects will have a higher image entropy. However, the image entropy reaches a maximum and then decreases in systems with a low point defect concentration because the nanodomains in the precursory tweed structure transforms into micron scale martensitic twin plates. The image entropy displays a continuous change with temperature,

which suggests a continuous transition. Whether or not one can determine an equivalent “image heat capacity” according to the image entropy is a topic of ongoing research.

Figure 5.6 shows the image entropy versus the defect concentration for selected temperatures. The entropy for the lowest temperature increases as defect concentration increases until the critical defect concentration, where the entropy is at a maximum. The entropy of the states with defect concentrations higher than the critical defect concentration decreases slightly from the maximum entropy found at  $c = 0.1$ ; however, these microstructures still have high entropy as compared to the entropy for low defect concentrations at 224 K.

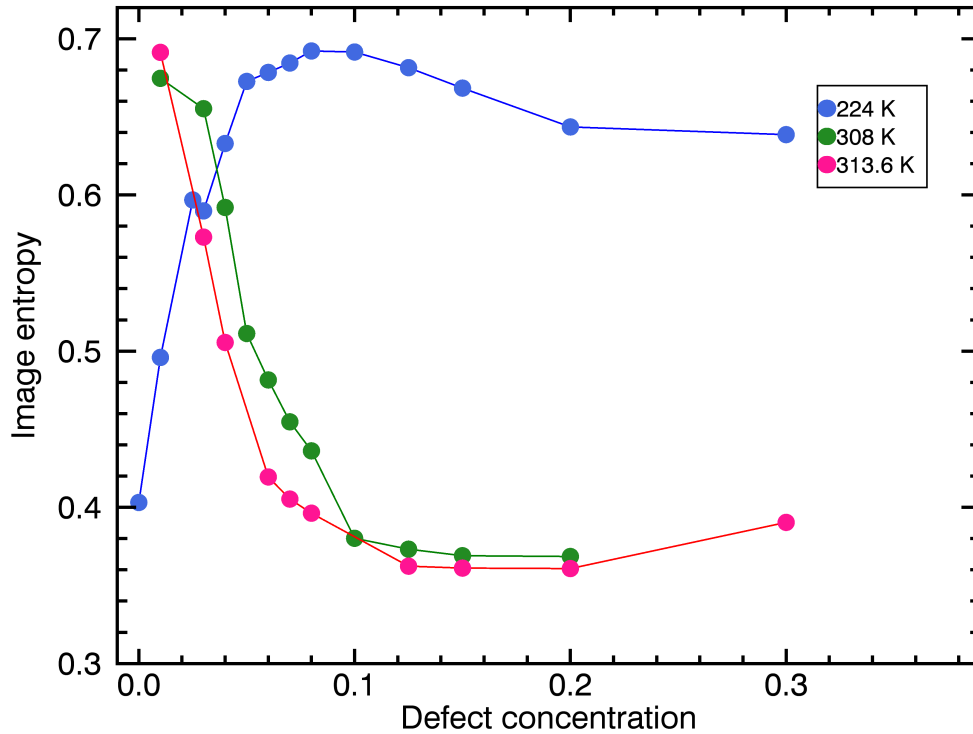


Figure 5.6: Entropy vs. defect concentration for different simulation temperatures. At intermediate temperatures, the entropy decreases as the defect concentration increases. At the final temperature (224K), the entropy increases with increasing defect concentration until it reaches its maximum at about  $c = 0.1$ .

We conclude from these simulations that the strain glass state produces microstructures with a high image entropy, while the starting microstructure has low image entropy at all point defect concentrations. The premartensitic tweeds display a range of image entropies.

Figure 5.5 shows that systems with low defect concentrations in the range  $[0, 0.08]$  have an entropy that displays no systematic relationship with respect to temperature. For higher concentrations, above 0.1, the entropy follows a nearly linear relationship with temperature. The critical point defect concentration is thus determined to be  $c = 0.1$ , when the system switches from undergoing a martensitic transition to a strain glass transition.

## 5.4 Comparison of MI approach to qualitative analysis

There are four microstructural states of interest in these materials systems: the austenite parent phase, the low temperature martensitic phase, the pre-martensitic tweed, and the strain glass state. Austenite is usually only qualitatively assessed; with its disordered state, it is difficult to make any quantitative assessments. Martensite is easier to quantify; the number of domains can be counted, the width of the domains can be assessed, and the orientations can be used to distinguish martensite. However, premartensitic tweed and the strain glass state pose similar issues to austenite in terms of quantification. Since these states also do not have long range order, it can be difficult to determine an adequate quantitative tool that can consider both the local and the global microstructure. Therefore, moment invariants provide a good method to quantify these types of microstructures that can both determine the global microstructure and can also provide the a representative region of interest.

## 5.5 Conclusions

The strain glass transition in ferroelastics can be induced by doping with point defects. Different microstructural states can exist in a doped ferroelastic system, such as premartensitic tweed and a strain glass state, in addition to the typical austenite and martensite states. We have successfully used moment invariants and image entropy to automatically distinguish between these states. While the parent phase has a relatively narrow distribution of moment invariants, a system with low defect concentration as it is cooled displays a much greater spread in its moment invariant distribution. However, for a system with high defect concentration, the moment invariant distribution changes only by a small amount, indicating that it is indeed a frozen version of its former disordered strain state.

The parent phase consists of equiaxed structural fluctuations randomly dispersed throughout the system. Its SOMIM has a small range of moment invariant values that lie near the isotropic shape parabola. The tweed structure has moment invariant maps that lie along the entirety of the parabola; due to the complex cross-hatched state, when viewed through a small circular window, nearly all window positions reveal a close to isotropic intensity distribution, thus producing parabolic moment invariant maps. The strain glass state consists of nanosized martensitic domains that decrease in size as defect concentration increases. The strain glass has density maps similar to those of the parent phase, with a narrow distribution of moment invariants that lie along the isotropic shape parabola. The strain glass state can be distinguished from the premartensitic tweed because it has a smaller spread in moment invariant distribution.

Systems that undergo a martensitic transformation are characterized by a broad moment invariant distribution, with a peak centered near the circle point with coordinates (1, 1). However, systems that display a strain glass transition tend to have moment invariant distributions that do not change much upon cooling. These systems tend to have more complex shapes in their strain domain microstructure, giving rise to MI distributions away from the circle point. Since the calculated moment invariants all lie near the isotropic shape parabola  $\bar{\omega}_2 = \bar{\omega}_1^2$ , the shapes detected by the moment invariant windowing technique are nearly isotropic.

In terms of image entropy, we find that both the parent phase and the final martensitic phase display low image entropy whereas the premartensitic tweed state has an intermediate image entropy. The strain glass state displays varying entropy values as well, but systems with high defect concentrations have higher entropy values than systems with low defect concentrations because of how the nanodomains finally rearrange in the microstructure. Systems with defect concentrations equal or greater than  $c_{crit} = 0.1$  display an image entropy that decreases nearly linearly with temperature, or, equivalently, increases linearly with time.

Moment invariants have been shown to be capable of characterizing the range of strain domain shapes that can occur in the different microstructural states of a ferroelastic system. Image entropy can be used to identify the critical defect concentration, which, for the

computational model employed in this paper, is  $c_{crit} = 0.1$  and is in agreement with the value determined independently by heat capacity calculations in [113].

Using the moment invariant analysis with image entropy allows for the identification of all the strain states considered. While moment invariants were able to distinguish between austenite, martensite, and premartensitic tweed, it was difficult to use moment invariants to distinguish between austenite and the strain glass state. Image entropy was able to identify the transition that the system is undergoing (martensitic transformation or strain glass transition), but it was difficult to use image entropy to distinguish between premartensitic tweed, martensite, and the strain glass state. However, image entropy can distinguish between austenite and the strain glass state. Therefore, the hypothesis is supported because both MIs and image entropy can be used to fully quantify the microstructural states in doped ferroelastic systems.

## CHAPTER VI

### Grain growth in strontium titanate

#### 6.1 Introduction

The materials properties of perovskite ceramics are determined by their grain and grain boundary characteristics such as size, morphology, and crystallographic orientation [124]. Some of the interest in polycrystalline perovskite ceramics comes from the observation of a grain growth anomaly, which may be due to the interface anisotropy of these materials [124–126]. Strontium titanate is one type of perovskite that has shown this deviation from the expected Arrhenius type of behavior, although the origins of the anomaly are not clear [127].

One common way to control the size and shape of grains is by annealing the material at an elevated temperature. At higher temperatures, grains grow because it is more energetically favorable for the material as a whole to have less surface area. This phenomenon is known as grain growth or coarsening, where the average size of the crystals within a polycrystalline material increases [21]. Interfacial energy is the driving force for grain growth because the interfacial area decreases and the associated energy decreases as the average size increases [125]. The general equation for grain growth is written as [21]:

$$d - d_0 = (kt)^n, \tag{6.1}$$

where  $d$  is the grain size,  $d_0$  is the initial grain size,  $k$  is the growth factor,  $t$  is the annealing time, and  $n$  is an exponent that is ideally 0.5 [124,125]. However, most experiments have an exponent value,  $k$ , less than 0.5 [125]. Typical coarsening theories can predict the

size and evolution of crystals for systems with isotropic surface energies, but anisotropic interfaces affect the grain growth [124, 125]. When the interfaces are anisotropic, a bimodal grain size distribution may occur and can lead to abnormal grain growth [124, 125, 127]. Although there is a large amount of literature on strontium titanate, the grain growth of bulk  $\text{SrTiO}_3$  and its driving force have not been studied extensively [124]. However, studies have investigated the morphological evolution of  $\text{SrTiO}_3$  crystals coarsening in a titania rich liquid and surface energy anisotropy [125], and there have been both experimental [124, 127, 128] and simulations [129–131] where the focus is the grain growth of strontium titanate.

The study of perovskite ceramics has been important to understand the relationship between interface anisotropies and microstructural evolution. By investigating strontium titanate ( $\text{SrTiO}_3$ ), a model system for perovskite ceramics, the morphology and crystallographic orientation of the individual grains can be examined. One proposed explanation for the non-Arrhenius behavior is that there is a decrease in the relative grain boundary energy of low mobility interfaces with increasing temperature [130]. Another explanation could be a change in grain boundary faceting of strontium titanate with temperature [130].

The 3D microstructure of strontium titanate specimens has been investigated using x-ray diffraction contrast tomography (DCT) by Melanie Syha at the Karlsruhe Institute of Technology. The characterization of the grain shapes in two different processing states, before and after annealing, is achieved through the use of 3D moment invariants as the principal shape descriptors to analyze voxelized representations of the grains extracted from the 3D reconstructions. The shape quotient and the distance from each grain to the cube are both used to examine the evolution of the grains. The 10% largest grains are also exclusively examined. By conducting annealing experiments, the growth kinetics of strontium titanate can be examined to investigate its deviation from the usual Arrhenius behavior and can then be compared to simulations.

## 6.2 Materials and methods

The specimen was prepared at Karlsruhe Institute of Technology by mixing  $\text{SrCO}_3$  and  $\text{TiO}_2$  using a molar Sr/Ti ratio of 0.996. The powder was milled and calcined in multiple steps; then the specimen was sintered for 1 hour at  $1600^\circ\text{C}$  in oxygen, then cut and ground

to a cylindrical shape. After the first DCT investigation, the specimen was annealed ex-situ for 1 hour at 1600°C in air. The details of the DCT investigation are outlined in [127].

X-ray diffraction contrast tomography (x-ray DCT), a non-destructive technique, was used to collect the 3D grain shapes and their crystallographic orientation. X-ray tomography was discussed previously in Chapter I. In materials science, the sample is subjected to x-rays that provide image contrast between the different microstructural features [6]. Computer programs are then used to reconstruct the 3D microstructure, using phase or diffusion contrast information. X-ray DCT has been shown to be a good method to reconstruct the 3D microstructure of perovskite materials [127, 132]. Two datasets were analyzed on the same sample, one in its initial state and one after annealing. Both datasets have a system size of 506 x 506 x 398 voxels and a voxel edge length of 0.7 microns.

Figure 6.1 depicts three-dimensional microstructure reconstructions of the specimen in its initial and annealed states. The crystallographic orientation is encoded in the colors of each grain. The second DCT experiment was conducted on a slightly smaller volume of

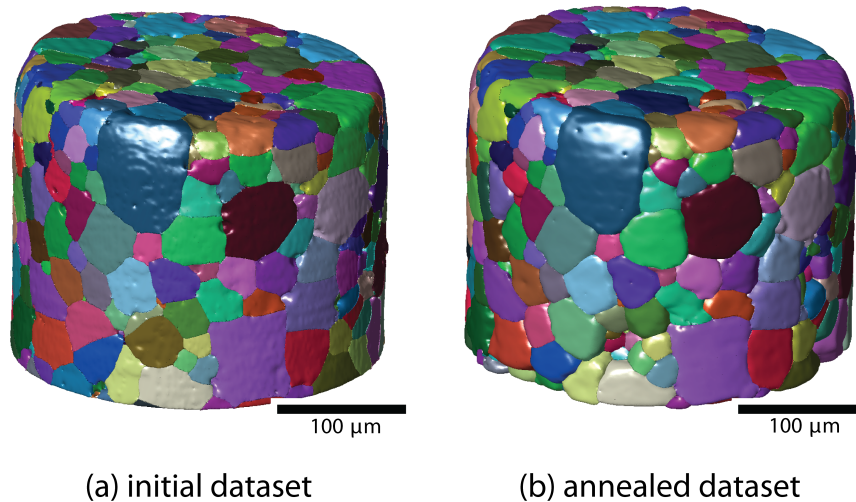


Figure 6.1: Three-dimensional representations of the datasets (a) in its initial state and (b) in its annealed state. The grains are colored by crystallographic orientation.

the specimen. There are 849 grains identified in the initial state, of which 351 grains are connected with the surface, and 498 grains are bulk grains. The annealed state contains 797 grains, with 387 surface grains and 416 bulk grains. Two-dimensional cross-sections through the datasets are shown in Figure 6.2.

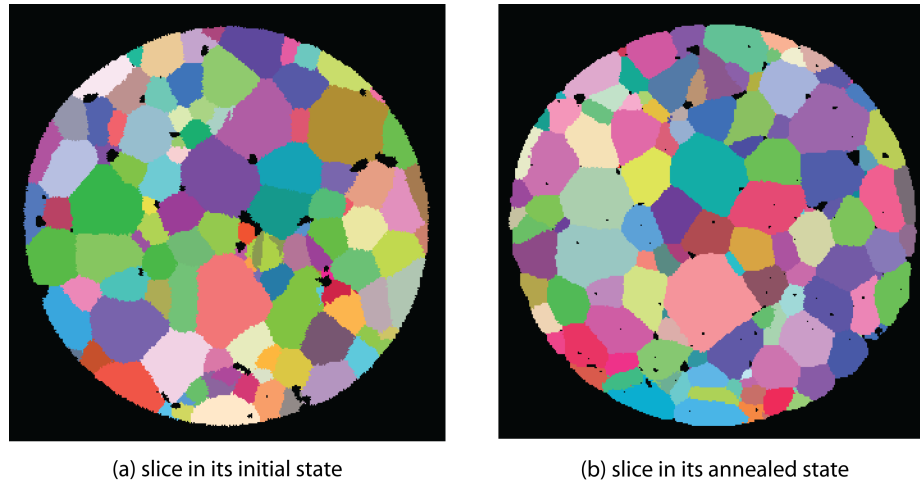


Figure 6.2: Two-dimensional cross-sections of the datasets (a) in its initial state and (b) in its annealed state. The grains are colored randomly to distinguish between grain shapes. The black portions are pores.

397 grains were considered in the shape analysis, grains that could be found in both states and contained at least ten voxels. Several quantitative tools were used in this analysis: 3D moment invariants, shape quotient, Euclidean distance, and relative volume change. The shape quotient was calculated by first computing the Minkowski functionals, then using the first two functionals to calculate  $Q$ . The Minkowski functionals were computed using the approach taken by Ohser; the specifics of which can be found in [75].

### 6.3 Results and discussion

It was previously qualitatively observed in [127] that these grains seemed have a cubic shape and that the largest grains would be more likely than smaller grains to have a cubic shape. In addition, the largest grains would have a small relative volume change rate, close to zero. To verify these observations, a quantitative approach was taken.

For these datasets, the average relative volume change was  $\Delta V/v_0 = 0.19$  per bulk grain, indicating that the microstructure exhibits moderate grain coarsening. For the grains that were considered in the quantitative analysis (the ones that were found in both annealing states), the average relative volume change is  $-0.118 \pm 0.153$ , indicating that the grains that were found in both states tended to shrink with annealing. This is in agreement with the behavior of grain size distributions obtained during annealing experiments on dense SrTiO<sub>3</sub>

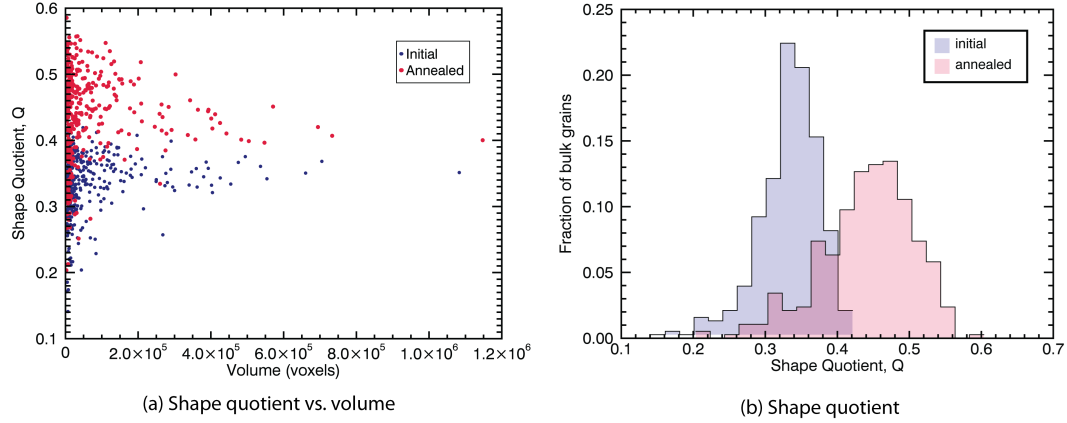


Figure 6.3: (a) Shape quotient vs. volume. (b) Histogram of shape quotient. The blue indicates grains in the initial state and the red indicates grains in the annealed state. It is clearly evident that the shape quotient of the grains increases after annealing.

specimens at  $1550^\circ$  [124, 130].

Initially, the shape quotient was used to determine the complexity of the grain shapes. The volume distributions for both states are similar, as shown in Figure 6.3(a), but there is a clear indication that the shape quotient increases for the annealed grains compared to the initial grains with similar volumes. Histograms of the shape quotient for both annealing states are shown in Figure 6.3(b). The average shape quotient,  $\bar{Q}$ , is  $0.348 \pm 0.026$  in the initial state and  $0.430 \pm 0.035$  in the annealed state. This suggests that the grains are growing closer to a less complex shape, which can be observed in Figure 6.4. Grains with a small relative volume change of an absolute value of 0.2 or less seem to have slightly higher shape quotient values in both states, as shown in Figure 6.5. Thus, grains that do not change much in size have a smaller surface area to volume ratio than grains that are growing or shrinking.

The moment invariants were calculated for each grain. However, the distributions appear similar, and it is therefore difficult to distinguish any changes in the system based on the distributions alone. Since it was hypothesized that the grains may be close to a cubic shape, the distance for the moment invariants for each grain to those of a cube is calculated for each grain. The moment invariants for a cube are  $(\bar{\Omega}_1, \bar{\Omega}_2, \bar{\Omega}_3) = (0.924, 0.854, 0.788)$ . The

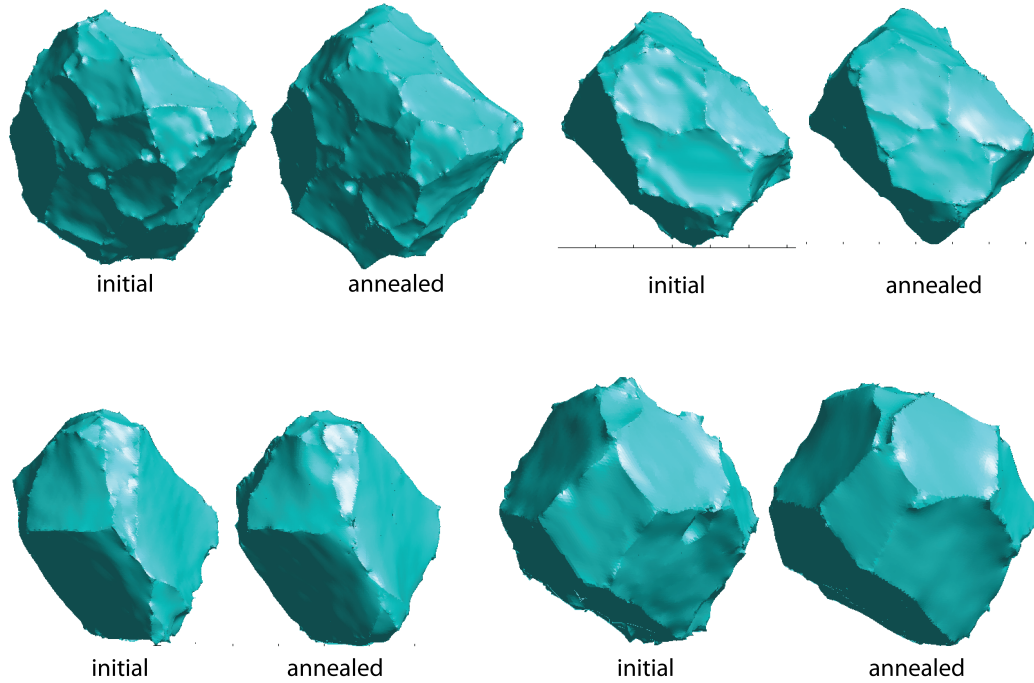


Figure 6.4: Selected grains in their initial and annealed states.

distance calculated is the Euclidean distance, which is calculated as:

$$d = \sqrt{(\bar{\Omega}_1^g - \bar{\Omega}_1^c)^2 + (\bar{\Omega}_2^g - \bar{\Omega}_2^c)^2 + (\bar{\Omega}_3^g - \bar{\Omega}_3^c)^2}, \quad (6.2)$$

where  $^g$  refers to the value for a grain and  $^c$  refers to the value for the cube. For reference, the Euclidean distance between a cube and a sphere is 0.269 and can be considered a fairly large distance between two shapes. Initial and annealed grains have about the same distance away from a cube, with average  $\bar{d}$  values of  $0.137 \pm 0.077$  and  $0.136 \pm 0.11$ , as shown in Figure 6.6(a). However, the distribution of the distances calculated for the annealed grains has a larger range.

Since some grains may be non-equiaxed and could have a rectangular shape as opposed to a strict cubic shape, it is also useful to consider only  $\bar{\Omega}_3$  as a shape descriptor due to its invariance under affine transformations. The histograms for the distance from the  $\bar{\Omega}_3$  value for a cube are shown in Figure 6.6(b), with average values of  $0.0158 \pm 0.069$  before annealing and  $0.0083 \pm 0.0008$  after annealing. Thus, annealed grains are closer to an affine cube shape than in their initial states. The distribution in Figure 6.6(c) also shows that

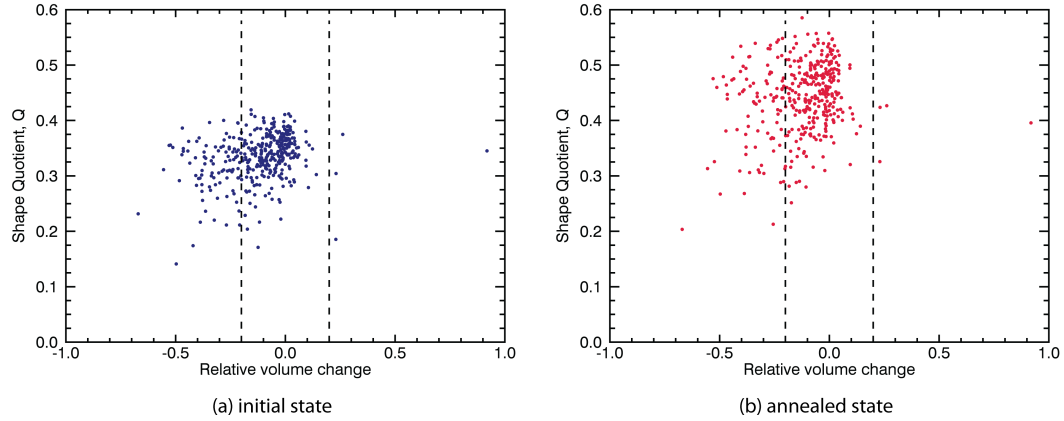


Figure 6.5: Shape quotient vs. relative volume change in the (a) initial state (b) annealed state.

the annealed grains have moment invariants that are becoming closer to those of a cube than the initial grains, indicated by a negative change in distance and a median value of  $-0.012 \pm 0.063$ . In Figure 6.6(d), the change in the distance from  $\bar{\Omega}_3$  is very small, with an average value of  $-0.015 \pm 0.055$ .

The largest 10% (37 grains) were exclusively examined, since it was assumed that larger grains may not change much. Figure 6.7(a) shows the relative volume change of the largest grains which is quite small, with a relative volume change of less than 0.15 for all large grains. The annealed grains are closer to a cube shape than the initial grains, regardless of whether the grain shrinks, grows, or stays relatively constant in volume. The distance from the cube's moment invariants for the large grains, shown in Figure 6.7(b), is  $0.129 \pm 0.013$  before annealing and  $0.100 \pm 0.019$  after annealing. The change in the distance from a cube shape decreases for all the grains except for two, and the average change in distance is  $0.027 \pm 0.107$ . Thus, annealing causes the grains to have a shape closer to a cube than in the initial state.

While the overall grain shape remains fairly equiaxed throughout the experiment, the average Euclidean distance to a cube shape decreases by a factor of two. Accordingly, a large number of grains evolve towards a more cubic shape. This effect is pronounced for the 10% largest grains, which show a reduced Euclidean distance to a cube compared with the Euclidean distance averaged over all bulk grains. Initially, their Euclidean distance is reduced by 6%, in the annealed state, it is 26% smaller than the bulk average. These grains

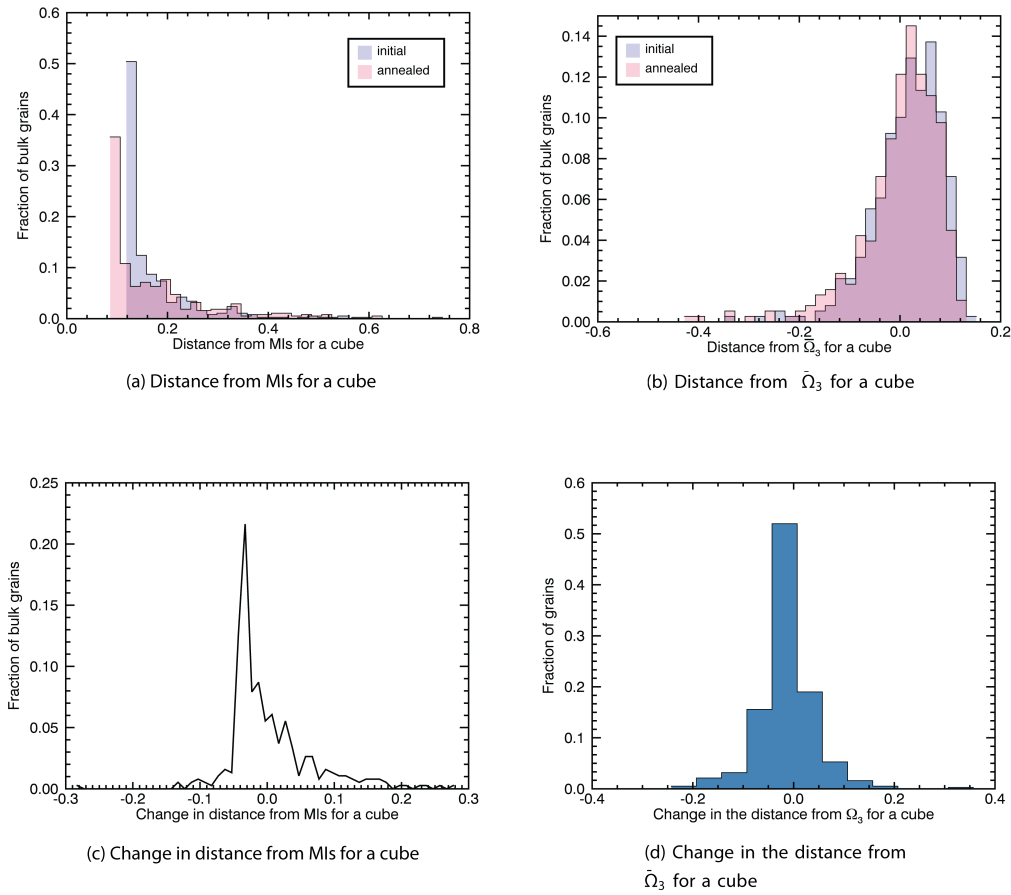


Figure 6.6: Various depictions of using Euclidean distance to measure how far the grains are from a cubic shape. (a) Histogram of the distance from the MIs for a cube. (b) Histogram of the distance from  $\bar{\Omega}_3$  for a cube. (c) Change in the the distance from the MIs for a cube, showing that overall, the grains are becoming closer to the cubic shape. (d) change in the distance from  $\bar{\Omega}_3$  for a cube.

do also show a reduced relative volume change rate of 0.15 compared with the average relative volume change rate of the bulk (0.19).

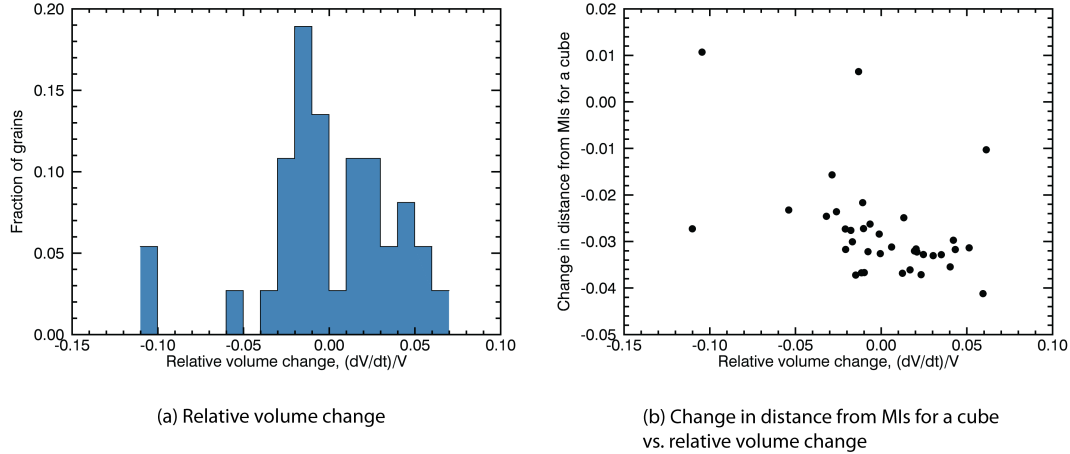


Figure 6.7: (a) Relative volume change. (b) Change in the distance from the MIs for a cube vs. relative volume change. Most of the largest grains have a shape that is closer to the cube shape after annealing compared to its initial state.

## 6.4 Comparison of MI approach to other shape descriptors

There are not many 3D shape analysis tools that have been applied to study 3D microstructures, and thus many of the observations are qualitative. As shown in [127], many grains appeared to have a rather cubic shape. In order to quantify the evolving shape of the grains, sphericity distributions of both annealing states are compared in figure 6.8. Since calculating sphericity values from voxel data is highly discretization dependent and requires a voxel size that is small compared to the average feature size [26], the sphericity is measured on topology conserving triangulated surface meshes of individual grains according to:

$$\Psi = \frac{\pi^{\frac{1}{3}}(6V_G)^{\frac{2}{3}}}{O_G}, \quad (6.3)$$

where  $V_G$  denotes the volume of a grain and  $O_G$  the grain's surface area. The average sphericity  $\bar{\Psi}$  is  $0.80 \pm 0.06$  in the initial and  $0.81 \pm 0.15$  in the annealed state. For comparison, the sphericity of a cube is 0.806. The grains have a sphericity value that is close to the cube. Therefore, the sphericity considered as an average does not show much of a change in the grain shape, compared to using comparisons of the moment invariants of the grains to the moment invariants of the cubes or the shape quotient nor is there an obvious shift in its distribution.

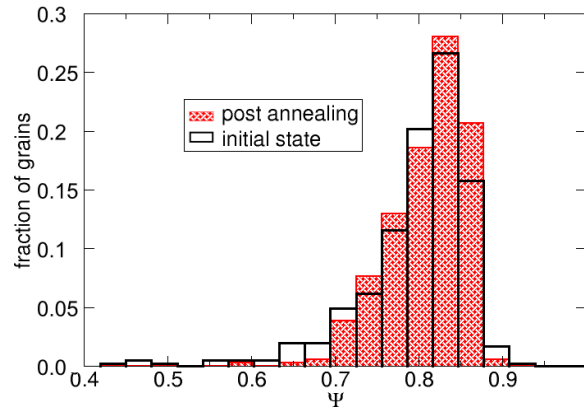


Figure 6.8: Distributions of sphericity values for both annealing states as histograms.

## 6.5 Conclusions

Several conclusions can be made about the microstructural evolution of polycrystalline strontium titanate. Only grains found in both states of annealing were considered. The overall average grain shape seems to be fairly equiaxed throughout annealing, with only minor changes in volume and shape. However, this conclusion can only be made about grains that can be found in both annealing states, not the ones that either disappeared or appeared during annealing. Annealing causes the average Euclidean distance to a cube shape to decrease by a factor of 2 and is even larger when considering the Euclidean distance to  $\bar{\Omega}_3$  for an affine cube. Therefore, many of the grains evolve towards a more cubic shape. When the largest grains are considered, they have a smaller relative volume change compared to the consideration of all bulk grains. The distance from the MIs for a cube does not change much for the largest grains, and large grains are close to a cubic shape before and after annealing. Therefore, the grains in these investigations appear to become closer to a cubic shape, even with annealing for only one hour.

Visual inspection of the grains makes it difficult to distinguish a change in grain shape upon annealing, and the analysis using sphericity does not show any significant change in grain shape. However, while the changes during annealing were not large according to the MI and shape quotient analysis, it does show that the grains are indeed showing a trend towards increasing cubicity. While the shape quotient showed a more drastic change in a grain's shape, MIs were better able to capture the grain becoming more cubic instead of

just a decrease in surface area as captured by the shape quotient. Therefore, the hypothesis is partially supported by this analysis: MIs and the shape quotient can be used together to examine the changes in the STO grains upon annealing, but they cannot be used separately to fully describe grain shapes.

## CHAPTER VII

### Conclusions

#### 7.1 Summary

The goals of this project are to apply moment invariants as shape descriptors to a variety of materials systems and to compare them to conventional quantitative tools that have been used in materials science and engineering. Moment invariants were successfully applied to three materials systems and were able to quantify the shapes of the microstructural features of interest. The hypothesis of this work is: *moment invariants (MIs) can be used to quantitatively track microstructural changes caused by external conditions.* These external conditions can be either related to processing conditions or operating conditions. The hypothesis was validated by applying other quantitative techniques to the same datasets and comparing the results using those techniques to the results using the moment invariant approach.

The hypothesis was validated with the following applications:

1. *Moment invariants (MIs) can be used to detect the onset of rafting and determine the rafting completion time in Ni-based superalloys.*

3D moment invariants are able to detect when rafting is completed in the microstructures, but they were not used to describe the onset of rafting. 2D moment invariants are used to detect when the onset of rafting occurs in these microstructures and to determine the rafting completion time. A criteria of half of the precipitates below the region of interest (ROI) was chosen to determine whether or not the microstructure was rafted. The rafting completion time using 2D moment invariants is defined as when the fraction of  $\gamma'$  precipitates in the ROI stop increasing linearly with time

or there is a change in the trend. Rafting can be detected and is observed when precipitate size increases and there is a shift of the peak of the MI distribution in the SOMIM and the PMIM from the top right corner to the lower left corner.

Twelve shape descriptors and microstructural parameters were also used on the same 2D images as those analyzed by the moment invariant approach. The shape descriptors that are able to detect rafting include: the number of precipitates, circularity, equivalent ellipse, Feret diameter, major axis, and solidity. The shape descriptors that are unable to detect a change in the system include: average size, aspect ratio, chord length, chord width, minor axis, and perimeter. While several shape descriptors can detect a change in the system, many of these parameters can be derived from moment invariants or are related to a change relative to another shape such as circularity, for example. These parameters contain only one aspect of the changes in the precipitates; however, MIs consolidate some of these aspects. Moment invariants can detect the elongation of the particles upon directional coarsening, and they can detect the complexity in the rafted, zigzag precipitate. The hypothesis is validated; MIs are capable of quantifying the onset of rafting and the differences between non-rafted and rafted  $\gamma'$  precipitates. This presents the first attempt to quantify the onset of rafting and a rafted microstructure.

2. *Moment invariants (MIs) can be used to determine how an applied external stress affects the two-phase microstructure in Ni-based superalloys.*

These microstructures were initially analyzed by Prikhodko using aspect ratio  $A$  and the shape parameter,  $\Sigma$ . It was found that  $\Sigma$ ,  $A$ , and precipitate size are not strongly affected by increasing applied stress [9]. Moment invariants are used with the superellipsoid exponent,  $n$ , to determine how the the roundness of the corners of the precipitates change with stress. This approach found that increasing stress causes the aspect ratio to decrease and the superellipsoid exponent  $n$  to slightly decrease. Therefore, increasing stress causes the  $\gamma'$  precipitates to become slightly less cuboidal, i.e. its corners are becoming slightly more rounded.

The aspect ratio used by Prikhodko was calculated by taking the ratio of the major

and minor axes of the precipitate, while the aspect ratio that we used was calculated by deriving it from its equivalent ellipse. This difference in the calculation of the aspect ratio may explain why the aspect ratios derived from MIs were found to decrease while Prikhodko's average aspect ratio stayed relatively the same with increasing stress. The hypothesis is partially validated; MIs were used with other shape descriptors the superellipsoid exponent  $n$  and the aspect ratio to detect slight changes in shape with increasing stress. However, it is difficult to say whether or not the MI results provide additional information to the approach using  $\Sigma$  and  $A$ .

3. *Moment invariants (MIs) can be used to quantify transitions in doped ferroelastic materials.*

MIs and image entropy were used in analyzing transitions in Ni-doped Ni-Ti systems. The MIs can easily distinguish between austenite, martensite, and premartensitic tweed. Each of these three states have MI peaks in different locations. The strain glass state has a microstructure similar to that of austenite, with a slightly higher  $\bar{\omega}_2$  peak than in the austenite. Image entropy was used to determine the critical defect concentration of these materials systems and classify the transformation or transition that is occurring based on its microstructural evolution. In these microstructures, moment invariants are able to classify which state the system is at a given defect concentration and temperature.

Image entropy is useful to determine the critical defect concentration, but it is not as useful to classify the state of the system because premartensitic tweed and the strain glass state have varying image entropy values. Moment invariants can also be used to determine the critical defect concentration by determining when the system no longer forms premartensitic tweed. Since these microstructures are difficult to segment, other shape analysis techniques are not as readily applied to these microstructures as in segmented microstructures. Therefore it can be difficult to distinguish between strain states by visual inspection. The hypothesis is validated; MIs and image entropy can be used to determine the strain state and to quantify the transition of the system. This is the first attempt to distinguish between strain states purely based on microstructure.

4. *Moment invariants (MIs) can be used to determine the effect of annealing in polycrystalline strontium titanate.*

Moment invariants were used to analyze 3D grain shapes in polycrystalline strontium titanate at two time steps, one before annealing and one after annealing. Previously, it was determined that grains appear to be more cubic using a qualitative assessment. Since it was previously assumed that the grains might have cubic shapes, the moment invariants were calculated for each grain and then compared to the moment invariants for a cube. The Euclidean distance was used to determine a grain's similarity to a cube, and the distance to the affine moment invariant for a cube was also considered. Annealing causes the average Euclidean distance to a cube shape to decrease by a factor of two; grains become closer to a cubic shape. By studying only large grains, they were found to be close to a cubic shape before and after annealing and their relative volume change is small.

Since the grains are three-dimensional, the shape quotient and the sphericity were also used to analyze grain shapes. The distributions of the shape quotient show an increase after annealing, indicating that the grains grow closer to a cube shape in their annealed state. Sphericity does not show much of a change in grain shape before and after annealing and is more useful to compare how close grains are to a sphere shape. However, the focus of the study is to examine if the grains become closer to a cubic shape after annealing. For these datasets, moment invariants and shape quotient are both useful to show that the grains become more cubic after annealing. The shape quotient only contains information about shape complexity, so it is difficult to state how close to a cube shape the grains are becoming. Sphericity does not comment on how close the grains become to a cube shape. Therefore the hypothesis is partially supported; moment invariants can be used to quantify if a grain becomes more cubic after annealing, but its change in shape is more readily identified with the shape quotient. This is the first study of how close 3D grain shapes are to a cube shape.

## 7.2 Conclusions

This thesis provides a quantitative comparison of shape descriptors that can be used in materials science and engineering applications. Moment invariants were used to study microstructural evolution in three materials systems, and the characteristics of several microstructures were quantified for the first time. Since many different shapes can be found in microstructures, there is not a universal shape descriptor that is been used across materials systems. However, moment invariants can fill this void. Previously, the application of moment invariants in materials science and engineering has been mostly in the analysis of  $\gamma'$  precipitates in Ni-based superalloys, both in 2D and 3D. The work done by MacSleyne and Callahan demonstrated the ability to use moment invariants to examine microstructures and analyzed  $\gamma'$  precipitates with spherical to cuboidal to dendritic  $\gamma'$  precipitates [13,14]. This thesis features the application of moment invariants in  $\gamma/\gamma'$  systems, but it also applies the moment invariant approach to other materials systems as well, showing versatility and ease of use. Although moment invariants are applied to features that have clearly defined boundaries, MIs can also be used on systems that do not have clearly defined boundaries, such as austenite. Moment invariants are not widely known throughout the materials science community, the recent Materials Genome Initiative may prove to be the right vehicle for making the moment invariant approach more widely used and applied.

Moment invariants can also be used to help with research related to Integrated Computational Materials Engineering (ICME), dedicated to improved competitiveness and national security [133]. ICME aims to improve computational materials science tools to accelerate materials development and merge design with manufacturing [133]. Moment invariants are another tool that can be used in ICME, specifically to help bridge the gap between experimental and simulated microstructures. By using moment invariants in microstructure quantification, more accurate models can be predicted to describe the actual phenomena that is occurring. Additionally, there have been many advances in three-dimensional microscopy and characterization techniques in recent years. Since two-dimensional microscopy has been used throughout materials science for many years, a larger amount of shape analysis tools have been applied to analyze these kinds of micrographs. However, three-dimensional

characterization is less established than two-dimensional approaches; there is a lack of quantitative tools in 3D that used to analyze microstructures. Moment invariants are one way to describe microstructures and can be used to analyze these three-dimensional microstructural features.

A quick search of the term “morphology” in Google Scholar yields over three million results, showing how important the characterization of morphology is in all types of fields. Moment invariants provide an easy method to quantify the shapes of microstructural features regardless of their position, orientation, or size. Moment invariants are powerful shape descriptors that can be used in many applications. One of the most useful aspects of moment invariants is that only moment invariants need to be computed on the microstructural features, and other shape descriptors can be derived from them, such as aspect ratio and the superellipsoid exponent,  $n$ . While moment invariants were used in methods similar to that in [13, 14], they were also used in novel methods such as using a spherical mask to serially image across the microstructure and to determine an object’s distance from an ideal shape of interest. Moment invariants were used to quantify some key microstructural features that have only been qualitatively assessed in the past. This thesis shows that moment invariants serve as a powerful quantitative tool to analyze microstructural evolution, but they may also be used in a broader context.

### 7.3 Future work

There is still a large amount of future work, as the application of moment invariants in materials science and engineering is still being developed. The first part is already in progress by a graduate student, which is to determine if odd order moments, such as the third order moment invariants, can be normalized in such a way that they do not become zero for symmetric shapes.

The analysis in Chapter IV can be developed further to include the analysis on RC specimens. However, due to time constraints, it was not explored in-depth in this thesis. For the ferroelastic systems discussed in Chapter V, there are other interesting microstructures to consider, which is to analyze how the Von Mises stress changes with different defect concentrations. There are additional polycrystalline strontium titanate datasets with more

annealing times, and there is also a dataset that was analyzed using DCT that was also acquired through destructive serial sectioning on the TriBeam system [28]. It would be interesting to see how the grain shapes in the same dataset vary between the non-destructive x-ray tomography technique and the destructive serial sectioning technique.

There are some other opportunities for future work. The connectivity of the  $\gamma$  or the  $\gamma'$  phases can be explored as a function of time, temperature, or stress level using methods such as percolation threshold. The 2D MI scan approach was used to examine microstructures in ferroelastics; however, the differences between serial sampling versus random sampling can be explored.

Future work may also include:

- One of the interesting possibilities is to link the changes in shape with properties within the microstructure. For example, the shapes of the  $\gamma'$  precipitates were associated with certain time steps, but it would also be interesting to link the shapes of the precipitates with the strength of the material.
- One interesting possibility is to use n-point correlations with moment invariants as inputs for a synthetic microstructure. It would be interesting to incorporate moment invariants to determine the starting grain shapes in simulations and see how the grains act according to the model parameters and measure their change using MIs.
- It would also be interesting to find the relationship of moment invariants with other shape descriptors that are not described here. For example, relationships between  $\Sigma$ ,  $\eta$ , and  $\bar{\omega}_2$  have been established. The relationship between  $\bar{\Omega}_3$  and  $n$  has also been established.
- Other materials systems can also be analyzed using the moment invariant approach as well. While the relationship of moment invariants with the shape descriptors for  $\gamma'$  precipitates has been fairly established, it would be useful to consider more complex shapes. One application would be to use moment invariants to characterize the morphology martensite in high strength steels, especially considering martensite as laths, blocks, packets, and grains.

## APPENDIX A

### Sensitivity of superellipsoid exponent, $n$

The use of superellipsoids with moment invariants is useful to distinguish between different  $\gamma'$  precipitates. Experimental micrographs can be taken of these  $\gamma'$  precipitates and then compared to a library of ideal cuboidal shapes to determine what shapes the experimental shapes best match. To be able to determine the number of shapes that need to be added to the library, it is important to determine the precision needed to distinguish between different cuboids and different shapes although there is still an unlimited number of pre-computed shapes that can be added to the library. For example, how different is  $n = 6.0$  from  $n = 6.15$  or  $n = 6.2$ ?

To begin, it is important to consider the largest distance in the analysis of  $\gamma'$  precipitates. The largest distance to consider is that between the sphere and the cube in 3D, or the circle and the square in 2D, due to the interest in  $\gamma'$  precipitate shapes. The Euclidean distance between the 3D MIs for the sphere and the cube is 0.269 and the chi-squared distance is 0.0199. The Euclidean distance between 2D second MIs for the circle and the square is 0.0990 and the chi-squared distance is 0.00255. These values will serve as reference as the largest distances being considered.

An analysis was conducted on the distances between the moment invariants for cuboids with different  $n$  values and determined through two ways. To be able to compare 2D sections such as in a typical micrograph and determine its 3D information, stereology must be applied. The first method was to compare the MI distributions of the random sections through the cuboids. The method chosen is to take a large number (5000) of random 2D sections through the material. The 2D second and fourth order MIs are computed for each

section, then plotted on its SOMIM and PMIM as density maps. The Hellinger distances (H) and the chi-squared distances (CSD) between the cube maps and the sphere maps are:  $H_{SOMIM} = 0.974$ ,  $H_{PMIM} = 0.975$ ,  $H_{avg} = 0.975$ ,  $CSD_{SOMIM} = 0.980$ ,  $CSD_{PMIM} = 0.981$ , and  $CSD_{avg} = 0.980$ .

At low  $n$  values (below 4), the shapes are more easily distinguished from each other, even by visual inspection. At high  $n$  values (above 7), the corners are only slightly rounded, and many of the sections will have shapes similar to the sections taken through a cube. Therefore, the density maps of the  $n$  values of interest were chosen to be in the 4 to 7 range, specifically in the 5.5 to 6.5 range: 5.4, 5.5, 5.6, 5.8, 6.0, 6.1, 6.15, and 6.4. The comparisons between these maps are shown as the Hellinger distance and the chi-squared distance in Table A.2.

The cuboids were also considered only as one 2D section. A 2D slice was taken through the middle of each cuboid, sectioned normal to the (100) plane. The cuboids that were considered had exponent values of  $n$  between 4 to 10 in increments of 0.05, resulting in 70 cuboids being analyzed. Cuboids with three edge lengths were considered (in pixels): 60, 100, and 200. The second and fourth order moment invariants were computed for each slice. Then the distance between the cuboid slices are computed using the Euclidean distance and the chi-squared distance. The tables below show the comparison of one cuboid to the rest of the cuboids being considered and contain the comparison for cuboids of edge length 60 and 100. From the tables, the 0.05 increments show a small change in the distances; the Euclidean distance between cuboids with exponents that differ by less than 0.5 is less than 0.001. From the sensitivity analysis, 0.5 increments are sufficient to compare different cuboidal shapes in both 2D and 3D.

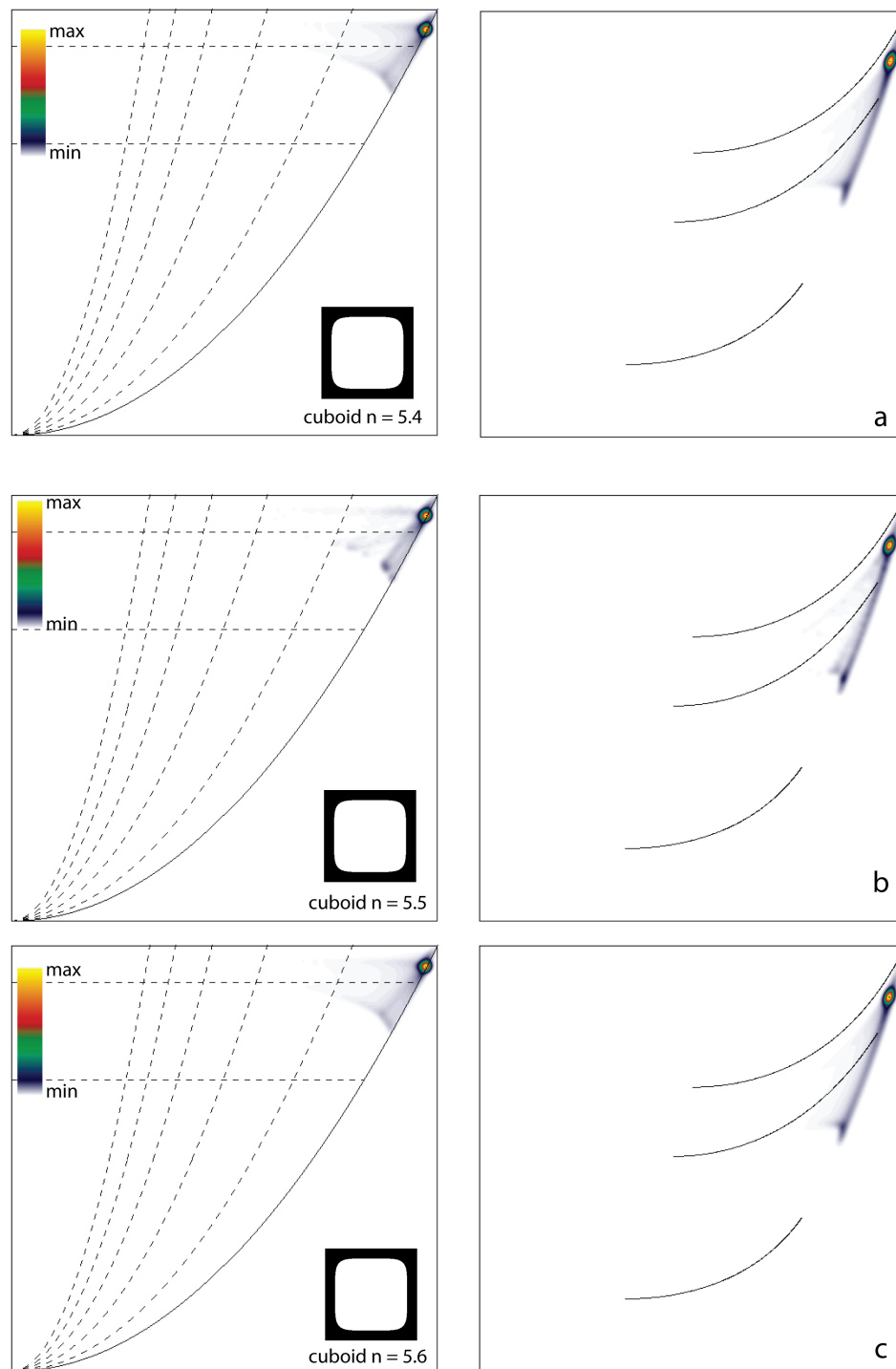


Figure A.1: Density maps for cuboids with  $n = (a) 5.4, (b) 5.5, (c) 5.6$ .

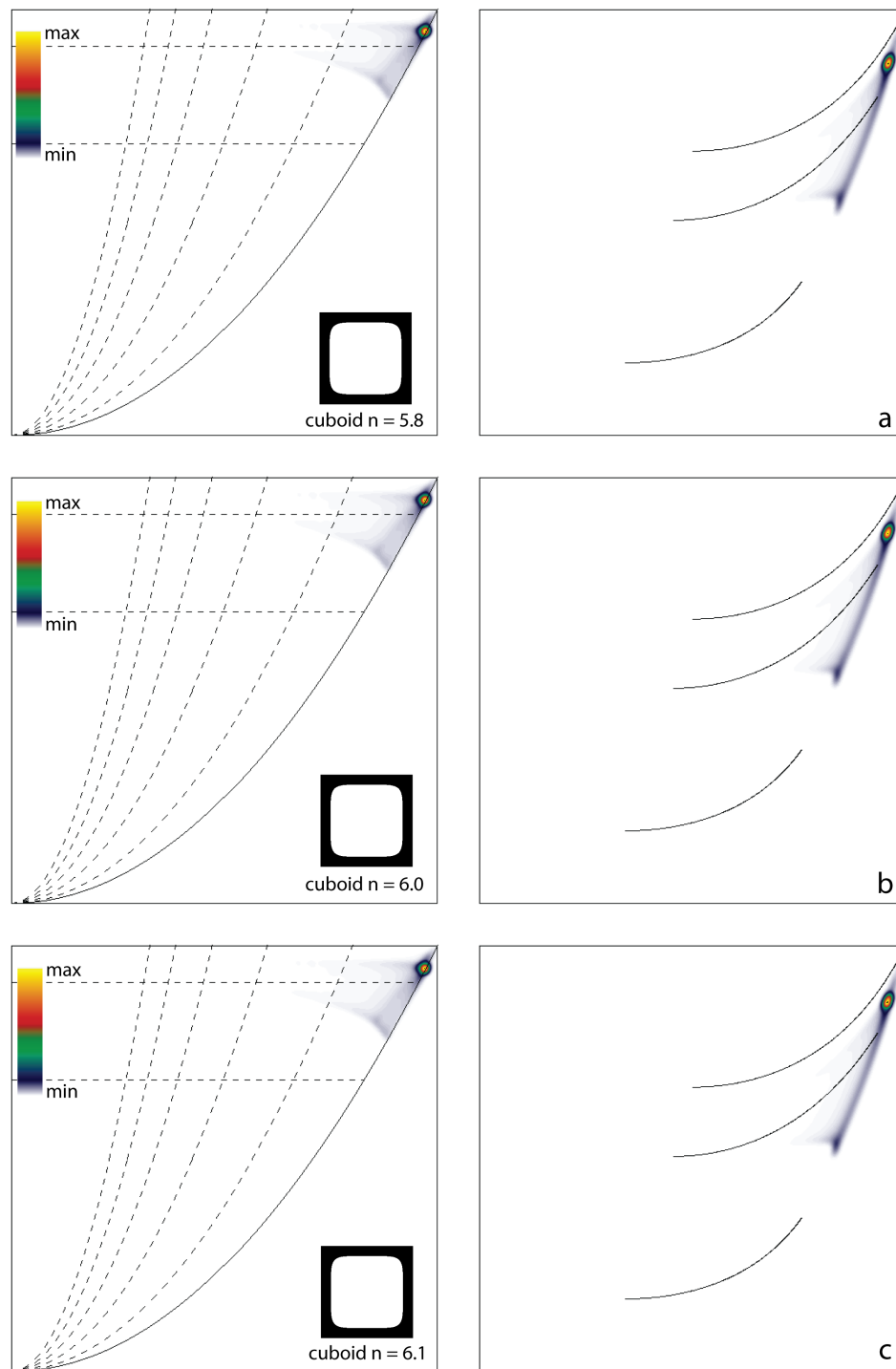


Figure A.2: Density maps for cuboids with  $n =$  (a) 5.8, (b) 6.0, (c) 6.1.

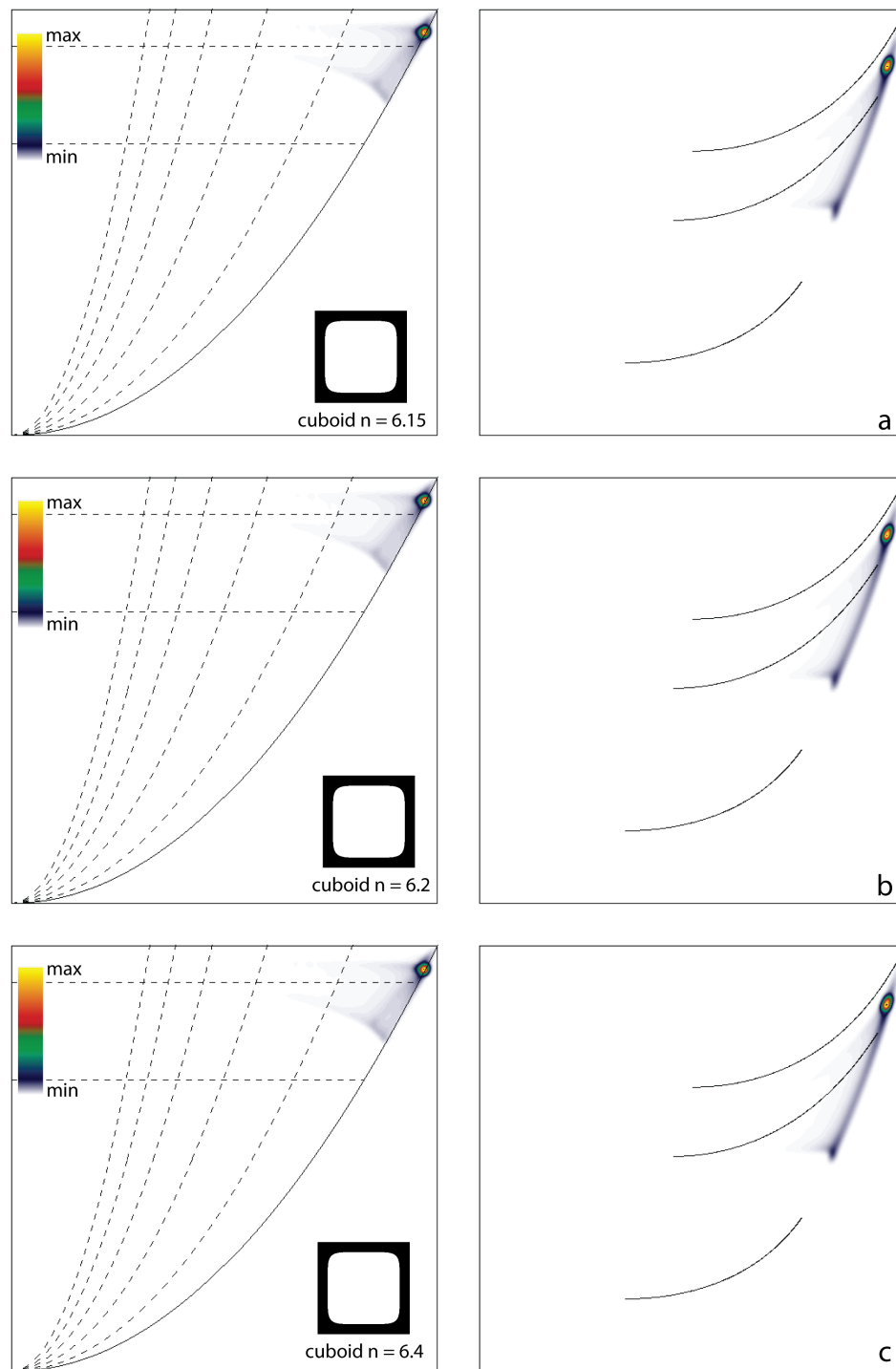


Figure A.3: Density maps for cuboids with  $n =$  (a) 6.15, (b) 6.2, (c) 6.4.

Table A.1: Comparison of density maps for various 3D shapes with 5000 2D sections using the Hellinger distance and the chi-squared distance.

Shape 1	Shape 2	step size	$H_{SOMIM}$	$H_{PMIM}$	$H_{avg}$	$CSD_{SOMIM}$	$CSD_{PMIM}$	$CSD_{avg}$
cube	sphere	n/a	0.974	0.975	0.975	0.980	0.981	0.980
5.4	6.4	1	0.331	0.383	0.358	0.225	0.167	0.196
5.4	6	0.6	0.237	0.277	0.258	0.125	0.089	0.107
5.6	6	0.4	0.178	0.207	0.193	0.074	0.053	0.064
5.8	6.2	0.4	0.161	0.190	0.176	0.061	0.043	0.052
6	6.4	0.4	0.157	0.186	0.172	0.059	0.042	0.050
5.8	6	0.2	0.088	0.103	0.096	0.020	0.014	0.017
6	6.2	0.2	0.086	0.105	0.096	0.020	0.014	0.017
5.4	5.5	0.1	0.139	0.114	0.127	0.023	0.034	0.028
5.5	5.6	0.1	0.144	0.115	0.130	0.023	0.035	0.029
6	6.1	0.1	0.049	0.059	0.054	0.007	0.005	0.006
6.1	6.2	0.1	0.045	0.054	0.050	0.006	0.004	0.005
6.1	6.15	0.05	0.022	0.023	0.022	0.001	0.001	0.001
6.15	6.2	0.05	0.033	0.037	0.035	0.003	0.002	0.002

Table A.2: Comparison of density maps to the other shapes in the library.

Shape 1	Shape 2	SOMIM	PMIM	Product
6.4	6.2	0.0845	0.1010	0.0931
6.4	6.15	0.1095	0.1293	0.1198
6.4	6.1	0.1215	0.1450	0.1337
6.4	6	0.1567	0.1862	0.1721
6.4	5.8	0.2214	0.2577	0.2402
6.4	5.6	0.2861	0.3320	0.3099
6.4	5.4	0.3315	0.3833	0.3583
6.4	5.5	0.3499	0.3893	0.3701
6.4	cube	0.6716	0.6611	0.6663
6.4	sphere	0.9427	0.9569	0.9498
5.8	6	0.0882	0.1034	0.0961
5.8	5.6	0.1120	0.1322	0.1225
5.8	6.1	0.1266	0.1511	0.1394
5.8	6.15	0.1369	0.1636	0.1508
5.8	6.2	0.1606	0.1901	0.1760
5.8	5.4	0.1817	0.2152	0.1992
5.8	5.5	0.2050	0.2086	0.2068
5.8	6.4	0.2214	0.2577	0.2402
5.8	cube	0.7020	0.6813	0.6917
5.8	sphere	0.9363	0.9511	0.9437
6.2	6.15	0.0327	0.0372	0.0350
6.2	6.1	0.0451	0.0537	0.0496
6.2	6.4	0.0845	0.1010	0.0931
6.2	6	0.0860	0.1049	0.0959
6.2	5.8	0.1606	0.1901	0.1760
6.2	5.6	0.2377	0.2783	0.2588
6.2	5.4	0.2891	0.3386	0.3148
6.2	5.5	0.3080	0.3409	0.3249
6.2	cube	0.6810	0.6661	0.6736
6.2	sphere	0.9406	0.9552	0.9479

Table A.3: Comparison of MIs of cuboid with  $n = 4$  to MIs of cuboids from 4.05 to 10 using the Euclidean distance and the chi-squared distance.

length (pixels)	shape 1	shape 2	$\bar{\omega}_i$ Euc-dist	$\bar{\omega}_i$ CSD	$\bar{\tau}_i$ Euc-dist	$\bar{\tau}_i$ CSD
60	4	4.05	8.432E-04	1.826E-07	3.261E-03	2.914E-06
60	4	4.1	2.125E-03	1.160E-06	8.262E-03	1.874E-05
60	4	4.15	2.681E-03	1.847E-06	1.025E-02	2.889E-05
60	4	4.2	3.299E-03	2.797E-06	1.259E-02	4.357E-05
60	4	4.25	3.720E-03	3.558E-06	1.422E-02	5.563E-05
60	4	4.3	5.311E-03	7.257E-06	2.026E-02	1.132E-04
60	4	4.35	5.984E-03	9.214E-06	2.279E-02	1.434E-04
60	4	4.4	6.474E-03	1.079E-05	2.471E-02	1.686E-04
60	4	4.45	6.907E-03	1.228E-05	2.629E-02	1.910E-04
60	4	4.5	8.330E-03	1.787E-05	3.161E-02	2.767E-04
60	4	4.55	8.592E-03	1.902E-05	3.264E-02	2.951E-04
60	4	4.6	9.116E-03	2.141E-05	3.469E-02	3.335E-04
60	4	4.65	9.641E-03	2.395E-05	3.664E-02	3.724E-04
60	4	4.7	1.114E-02	3.199E-05	4.221E-02	4.952E-04
60	4	4.75	1.165E-02	3.502E-05	4.419E-02	5.432E-04
60	4	4.8	1.168E-02	3.516E-05	4.418E-02	5.429E-04
60	4	4.85	1.223E-02	3.861E-05	4.636E-02	5.983E-04
60	4	4.9	1.343E-02	4.659E-05	5.084E-02	7.208E-04
60	4	4.95	1.440E-02	5.354E-05	5.450E-02	8.294E-04
60	4	5	1.444E-02	5.388E-05	5.456E-02	8.312E-04
60	4	5.05	1.499E-02	5.803E-05	5.666E-02	8.970E-04
60	4	5.1	1.570E-02	6.366E-05	5.921E-02	9.806E-04
60	4	5.15	1.570E-02	6.366E-05	5.921E-02	9.806E-04
60	4	5.2	1.709E-02	7.553E-05	6.443E-02	1.163E-03
60	4	5.25	1.767E-02	8.075E-05	6.666E-02	1.246E-03
60	4	5.3	1.799E-02	8.374E-05	6.779E-02	1.289E-03
60	4	5.35	1.901E-02	9.352E-05	7.163E-02	1.442E-03
60	4	5.4	1.911E-02	9.446E-05	7.186E-02	1.451E-03
60	4	5.45	1.911E-02	9.446E-05	7.186E-02	1.451E-03
60	4	5.5	2.020E-02	1.057E-04	7.603E-02	1.627E-03
60	4	5.55	2.056E-02	1.094E-04	7.727E-02	1.681E-03
60	4	5.6	2.129E-02	1.174E-04	7.995E-02	1.801E-03
60	4	5.65	2.176E-02	1.227E-04	8.169E-02	1.882E-03
60	4	5.7	2.237E-02	1.296E-04	8.401E-02	1.992E-03
60	4	5.75	2.237E-02	1.296E-04	8.401E-02	1.992E-03
60	4	5.8	2.331E-02	1.409E-04	8.748E-02	2.162E-03
60	4	5.85	2.406E-02	1.501E-04	9.017E-02	2.300E-03
60	4	5.9	2.406E-02	1.501E-04	9.017E-02	2.300E-03
60	4	5.95	2.457E-02	1.565E-04	9.203E-02	2.398E-03
60	4	6	2.457E-02	1.565E-04	9.203E-02	2.398E-03
60	4	6.05	2.489E-02	1.606E-04	9.327E-02	2.464E-03

60	4	6.1	2.612E-02	1.770E-04	9.771E-02	2.708E-03
60	4	6.15	2.671E-02	1.851E-04	9.992E-02	2.835E-03
60	4	6.2	2.671E-02	1.851E-04	9.992E-02	2.835E-03
60	4	6.25	2.788E-02	2.018E-04	1.043E-01	3.094E-03
60	4	6.3	2.788E-02	2.018E-04	1.043E-01	3.094E-03
60	4	6.35	2.809E-02	2.048E-04	1.049E-01	3.131E-03
60	4	6.4	2.853E-02	2.115E-04	1.065E-01	3.229E-03
60	4	6.45	2.853E-02	2.115E-04	1.065E-01	3.229E-03
60	4	6.5	2.853E-02	2.115E-04	1.065E-01	3.229E-03
60	4	6.55	2.916E-02	2.209E-04	1.089E-01	3.377E-03
60	4	6.6	3.007E-02	2.350E-04	1.122E-01	3.588E-03
60	4	6.65	3.064E-02	2.440E-04	1.143E-01	3.727E-03
60	4	6.7	3.064E-02	2.440E-04	1.143E-01	3.727E-03
60	4	6.75	3.178E-02	2.627E-04	1.185E-01	4.013E-03
60	4	6.8	3.178E-02	2.627E-04	1.185E-01	4.013E-03
60	4	6.85	3.178E-02	2.627E-04	1.185E-01	4.013E-03
60	4	6.9	3.205E-02	2.672E-04	1.193E-01	4.071E-03
60	4	6.95	3.205E-02	2.672E-04	1.193E-01	4.071E-03
60	4	7	3.271E-02	2.783E-04	1.218E-01	4.246E-03
60	4	7.05	3.332E-02	2.889E-04	1.241E-01	4.409E-03
60	4	7.1	3.383E-02	2.979E-04	1.259E-01	4.543E-03
60	4	7.15	3.383E-02	2.979E-04	1.259E-01	4.543E-03
60	4	7.2	3.383E-02	2.979E-04	1.259E-01	4.543E-03
60	4	7.25	3.448E-02	3.096E-04	1.282E-01	4.713E-03
60	4	7.3	3.517E-02	3.223E-04	1.308E-01	4.913E-03
60	4	7.35	3.517E-02	3.223E-04	1.308E-01	4.913E-03
60	4	7.4	3.517E-02	3.223E-04	1.308E-01	4.913E-03
60	4	7.45	3.517E-02	3.223E-04	1.308E-01	4.913E-03
60	4	7.5	3.517E-02	3.223E-04	1.308E-01	4.913E-03
60	4	7.55	3.637E-02	3.447E-04	1.352E-01	5.256E-03
60	4	7.6	3.739E-02	3.644E-04	1.388E-01	5.549E-03
60	4	7.65	3.739E-02	3.644E-04	1.388E-01	5.549E-03
60	4	7.7	3.739E-02	3.644E-04	1.388E-01	5.549E-03
60	4	7.75	3.739E-02	3.644E-04	1.388E-01	5.549E-03
60	4	7.8	3.739E-02	3.644E-04	1.388E-01	5.549E-03
60	4	7.85	3.739E-02	3.644E-04	1.388E-01	5.549E-03
60	4	7.9	3.739E-02	3.644E-04	1.388E-01	5.549E-03
60	4	7.95	3.739E-02	3.644E-04	1.388E-01	5.549E-03
60	4	8	3.908E-02	3.983E-04	1.449E-01	6.061E-03
60	4	8.05	3.908E-02	3.983E-04	1.449E-01	6.061E-03
60	4	8.1	3.975E-02	4.124E-04	1.474E-01	6.278E-03
60	4	8.15	3.975E-02	4.124E-04	1.474E-01	6.278E-03
60	4	8.2	3.975E-02	4.124E-04	1.474E-01	6.278E-03
60	4	8.25	4.047E-02	4.276E-04	1.501E-01	6.517E-03

60	4	8.3	4.047E-02	4.276E-04	1.501E-01	6.517E-03
60	4	8.35	4.047E-02	4.276E-04	1.501E-01	6.517E-03
60	4	8.4	4.087E-02	4.362E-04	1.514E-01	6.635E-03
60	4	8.45	4.087E-02	4.362E-04	1.514E-01	6.635E-03
60	4	8.5	4.087E-02	4.362E-04	1.514E-01	6.635E-03
60	4	8.55	4.150E-02	4.497E-04	1.537E-01	6.840E-03
60	4	8.6	4.150E-02	4.497E-04	1.537E-01	6.840E-03
60	4	8.65	4.150E-02	4.497E-04	1.537E-01	6.840E-03
60	4	8.7	4.150E-02	4.497E-04	1.537E-01	6.840E-03
60	4	8.75	4.221E-02	4.655E-04	1.564E-01	7.086E-03
60	4	8.8	4.221E-02	4.655E-04	1.564E-01	7.086E-03
60	4	8.85	4.265E-02	4.753E-04	1.578E-01	7.223E-03
60	4	8.9	4.303E-02	4.839E-04	1.593E-01	7.358E-03
60	4	8.95	4.303E-02	4.839E-04	1.593E-01	7.358E-03
60	4	9	4.303E-02	4.839E-04	1.593E-01	7.358E-03
60	4	9.05	4.379E-02	5.013E-04	1.621E-01	7.632E-03
60	4	9.1	4.379E-02	5.013E-04	1.621E-01	7.632E-03
60	4	9.15	4.445E-02	5.166E-04	1.645E-01	7.865E-03
60	4	9.2	4.445E-02	5.166E-04	1.645E-01	7.865E-03
60	4	9.25	4.445E-02	5.166E-04	1.645E-01	7.865E-03
60	4	9.3	4.445E-02	5.166E-04	1.645E-01	7.865E-03
60	4	9.35	4.445E-02	5.166E-04	1.645E-01	7.865E-03
60	4	9.4	4.492E-02	5.277E-04	1.661E-01	8.022E-03
60	4	9.45	4.492E-02	5.277E-04	1.661E-01	8.022E-03
60	4	9.5	4.492E-02	5.277E-04	1.661E-01	8.022E-03
60	4	9.55	4.492E-02	5.277E-04	1.661E-01	8.022E-03
60	4	9.6	4.567E-02	5.457E-04	1.689E-01	8.303E-03
60	4	9.65	4.567E-02	5.457E-04	1.689E-01	8.303E-03
60	4	9.7	4.567E-02	5.457E-04	1.689E-01	8.303E-03
60	4	9.75	4.567E-02	5.457E-04	1.689E-01	8.303E-03
60	4	9.8	4.567E-02	5.457E-04	1.689E-01	8.303E-03
60	4	9.85	4.567E-02	5.457E-04	1.689E-01	8.303E-03
60	4	9.9	4.637E-02	5.627E-04	1.714E-01	8.565E-03
60	4	9.95	4.688E-02	5.753E-04	1.732E-01	8.743E-03
60	4	10	4.688E-02	5.753E-04	1.732E-01	8.743E-03
100	4	4.05	7.955E-04	1.625E-07	3.036E-03	2.529E-06
100	4	4.1	1.541E-03	6.100E-07	5.887E-03	9.516E-06
100	4	4.15	2.466E-03	1.563E-06	9.428E-03	2.444E-05
100	4	4.2	3.176E-03	2.593E-06	1.211E-02	4.034E-05
100	4	4.25	3.771E-03	3.656E-06	1.436E-02	5.681E-05
100	4	4.3	4.899E-03	6.174E-06	1.864E-02	9.587E-05
100	4	4.35	5.542E-03	7.903E-06	2.113E-02	1.233E-04
100	4	4.4	6.072E-03	9.492E-06	2.309E-02	1.473E-04

100	4	4.45	6.768E-03	1.179E-05	2.576E-02	1.836E-04
100	4	4.5	7.650E-03	1.507E-05	2.906E-02	2.339E-04
100	4	4.55	8.436E-03	1.834E-05	3.207E-02	2.851E-04
100	4	4.6	8.993E-03	2.084E-05	3.410E-02	3.226E-04
100	4	4.65	9.668E-03	2.410E-05	3.670E-02	3.740E-04
100	4	4.7	1.061E-02	2.905E-05	4.022E-02	4.497E-04
100	4	4.75	1.088E-02	3.055E-05	4.122E-02	4.725E-04
100	4	4.8	1.144E-02	3.375E-05	4.331E-02	5.221E-04
100	4	4.85	1.252E-02	4.048E-05	4.741E-02	6.265E-04
100	4	4.9	1.292E-02	4.310E-05	4.885E-02	6.654E-04
100	4	4.95	1.332E-02	4.583E-05	5.034E-02	7.071E-04
100	4	5	1.437E-02	5.337E-05	5.431E-02	8.242E-04
100	4	5.05	1.494E-02	5.764E-05	5.639E-02	8.893E-04
100	4	5.1	1.528E-02	6.036E-05	5.767E-02	9.307E-04
100	4	5.15	1.597E-02	6.590E-05	6.025E-02	1.017E-03
100	4	5.2	1.645E-02	6.998E-05	6.203E-02	1.078E-03
100	4	5.25	1.703E-02	7.498E-05	6.419E-02	1.156E-03
100	4	5.3	1.814E-02	8.511E-05	6.831E-02	1.311E-03
100	4	5.35	1.814E-02	8.510E-05	6.827E-02	1.309E-03
100	4	5.4	1.851E-02	8.869E-05	6.969E-02	1.365E-03
100	4	5.45	1.950E-02	9.844E-05	7.332E-02	1.513E-03
100	4	5.5	1.989E-02	1.024E-04	7.480E-02	1.575E-03
100	4	5.55	2.019E-02	1.056E-04	7.591E-02	1.623E-03
100	4	5.6	2.088E-02	1.129E-04	7.840E-02	1.733E-03
100	4	5.65	2.128E-02	1.173E-04	7.990E-02	1.801E-03
100	4	5.7	2.192E-02	1.245E-04	8.230E-02	1.912E-03
100	4	5.75	2.263E-02	1.328E-04	8.491E-02	2.037E-03
100	4	5.8	2.263E-02	1.328E-04	8.491E-02	2.037E-03
100	4	5.85	2.339E-02	1.418E-04	8.766E-02	2.174E-03
100	4	5.9	2.353E-02	1.435E-04	8.817E-02	2.200E-03
100	4	5.95	2.411E-02	1.507E-04	9.033E-02	2.310E-03
100	4	6	2.470E-02	1.582E-04	9.248E-02	2.424E-03
100	4	6.05	2.470E-02	1.582E-04	9.248E-02	2.424E-03
100	4	6.1	2.568E-02	1.711E-04	9.613E-02	2.622E-03
100	4	6.15	2.591E-02	1.742E-04	9.692E-02	2.667E-03
100	4	6.2	2.624E-02	1.788E-04	9.816E-02	2.736E-03
100	4	6.25	2.652E-02	1.826E-04	9.917E-02	2.794E-03
100	4	6.3	2.719E-02	1.920E-04	1.016E-01	2.938E-03
100	4	6.35	2.797E-02	2.033E-04	1.045E-01	3.110E-03
100	4	6.4	2.797E-02	2.033E-04	1.045E-01	3.110E-03
100	4	6.45	2.841E-02	2.098E-04	1.061E-01	3.207E-03
100	4	6.5	2.841E-02	2.098E-04	1.061E-01	3.207E-03
100	4	6.55	2.896E-02	2.179E-04	1.081E-01	3.329E-03
100	4	6.6	2.969E-02	2.291E-04	1.108E-01	3.502E-03

100	4	6.65	3.010E-02	2.356E-04	1.123E-01	3.601E-03
100	4	6.7	3.023E-02	2.377E-04	1.128E-01	3.630E-03
100	4	6.75	3.067E-02	2.447E-04	1.144E-01	3.739E-03
100	4	6.8	3.096E-02	2.493E-04	1.154E-01	3.807E-03
100	4	6.85	3.118E-02	2.528E-04	1.162E-01	3.862E-03
100	4	6.9	3.174E-02	2.620E-04	1.182E-01	4.000E-03
100	4	6.95	3.192E-02	2.651E-04	1.189E-01	4.045E-03
100	4	7	3.238E-02	2.728E-04	1.206E-01	4.164E-03
100	4	7.05	3.262E-02	2.770E-04	1.215E-01	4.230E-03
100	4	7.1	3.327E-02	2.882E-04	1.239E-01	4.402E-03
100	4	7.15	3.349E-02	2.920E-04	1.246E-01	4.453E-03
100	4	7.2	3.373E-02	2.963E-04	1.255E-01	4.521E-03
100	4	7.25	3.395E-02	3.001E-04	1.263E-01	4.579E-03
100	4	7.3	3.395E-02	3.001E-04	1.263E-01	4.579E-03
100	4	7.35	3.438E-02	3.078E-04	1.278E-01	4.688E-03
100	4	7.4	3.511E-02	3.211E-04	1.305E-01	4.897E-03
100	4	7.45	3.536E-02	3.258E-04	1.315E-01	4.970E-03
100	4	7.5	3.536E-02	3.258E-04	1.315E-01	4.970E-03
100	4	7.55	3.592E-02	3.362E-04	1.335E-01	5.127E-03
100	4	7.6	3.628E-02	3.431E-04	1.348E-01	5.229E-03
100	4	7.65	3.628E-02	3.431E-04	1.348E-01	5.229E-03
100	4	7.7	3.628E-02	3.431E-04	1.348E-01	5.229E-03
100	4	7.75	3.661E-02	3.494E-04	1.360E-01	5.322E-03
100	4	7.8	3.686E-02	3.543E-04	1.369E-01	5.398E-03
100	4	7.85	3.765E-02	3.698E-04	1.398E-01	5.637E-03
100	4	7.9	3.786E-02	3.739E-04	1.406E-01	5.699E-03
100	4	7.95	3.796E-02	3.759E-04	1.409E-01	5.723E-03
100	4	8	3.822E-02	3.811E-04	1.418E-01	5.805E-03
100	4	8.05	3.822E-02	3.811E-04	1.418E-01	5.805E-03
100	4	8.1	3.865E-02	3.897E-04	1.434E-01	5.936E-03
100	4	8.15	3.865E-02	3.897E-04	1.434E-01	5.936E-03
100	4	8.2	3.946E-02	4.065E-04	1.463E-01	6.189E-03
100	4	8.25	3.946E-02	4.065E-04	1.463E-01	6.189E-03
100	4	8.3	3.946E-02	4.065E-04	1.463E-01	6.189E-03
100	4	8.35	3.973E-02	4.121E-04	1.473E-01	6.277E-03
100	4	8.4	3.992E-02	4.160E-04	1.480E-01	6.334E-03
100	4	8.45	4.030E-02	4.240E-04	1.493E-01	6.454E-03
100	4	8.5	4.055E-02	4.294E-04	1.503E-01	6.539E-03
100	4	8.55	4.102E-02	4.395E-04	1.520E-01	6.693E-03
100	4	8.6	4.129E-02	4.453E-04	1.530E-01	6.784E-03
100	4	8.65	4.129E-02	4.453E-04	1.530E-01	6.784E-03
100	4	8.7	4.160E-02	4.521E-04	1.541E-01	6.879E-03
100	4	8.75	4.160E-02	4.521E-04	1.541E-01	6.879E-03
100	4	8.8	4.160E-02	4.521E-04	1.541E-01	6.879E-03

100	4	8.85	4.160E-02	4.521E-04	1.541E-01	6.879E-03
100	4	8.9	4.197E-02	4.603E-04	1.554E-01	7.006E-03
100	4	8.95	4.264E-02	4.751E-04	1.579E-01	7.232E-03
100	4	9	4.309E-02	4.853E-04	1.595E-01	7.388E-03
100	4	9.05	4.309E-02	4.853E-04	1.595E-01	7.388E-03
100	4	9.1	4.309E-02	4.853E-04	1.595E-01	7.388E-03
100	4	9.15	4.336E-02	4.916E-04	1.605E-01	7.486E-03
100	4	9.2	4.336E-02	4.916E-04	1.605E-01	7.486E-03
100	4	9.25	4.350E-02	4.946E-04	1.609E-01	7.527E-03
100	4	9.3	4.374E-02	5.002E-04	1.618E-01	7.611E-03
100	4	9.35	4.395E-02	5.051E-04	1.626E-01	7.683E-03
100	4	9.4	4.395E-02	5.051E-04	1.626E-01	7.683E-03
100	4	9.45	4.448E-02	5.175E-04	1.645E-01	7.878E-03
100	4	9.5	4.448E-02	5.175E-04	1.645E-01	7.878E-03
100	4	9.55	4.462E-02	5.208E-04	1.650E-01	7.923E-03
100	4	9.6	4.490E-02	5.275E-04	1.661E-01	8.028E-03
100	4	9.65	4.490E-02	5.275E-04	1.661E-01	8.028E-03
100	4	9.7	4.490E-02	5.275E-04	1.661E-01	8.028E-03
100	4	9.75	4.565E-02	5.454E-04	1.688E-01	8.303E-03
100	4	9.8	4.565E-02	5.454E-04	1.688E-01	8.303E-03
100	4	9.85	4.565E-02	5.454E-04	1.688E-01	8.303E-03
100	4	9.9	4.580E-02	5.490E-04	1.693E-01	8.352E-03
100	4	9.95	4.607E-02	5.555E-04	1.703E-01	8.454E-03
100	4	10	4.635E-02	5.624E-04	1.713E-01	8.562E-03

Table A.4: Comparison of MIs of cuboid with  $n = 4.5$  to MIs of cuboids from 4.55 to 10 using the Euclidean distance and the chi-squared distance.

length (pixels)	shape 1	shape 2	$\bar{\omega}_i$ Euc-dist	$\bar{\omega}_i$ CSD	$\bar{\tau}_i$ Euc-dist	$\bar{\tau}_i$ CSD
60	4.5	4.55	2.624E-04	1.780E-08	1.028E-03	2.960E-07
60	4.5	4.6	7.861E-04	1.598E-07	3.075E-03	2.651E-06
60	4.5	4.65	1.311E-03	4.446E-07	5.030E-03	7.098E-06
60	4.5	4.7	2.808E-03	2.041E-06	1.060E-02	3.157E-05
60	4.5	4.75	3.322E-03	2.856E-06	1.258E-02	4.452E-05
60	4.5	4.8	3.346E-03	2.897E-06	1.257E-02	4.444E-05
60	4.5	4.85	3.903E-03	3.944E-06	1.475E-02	6.125E-05
60	4.5	4.9	5.105E-03	6.750E-06	1.923E-02	1.043E-04
60	4.5	4.95	6.069E-03	9.546E-06	2.289E-02	1.480E-04
60	4.5	5	6.115E-03	9.689E-06	2.295E-02	1.488E-04
60	4.5	5.05	6.659E-03	1.149E-05	2.505E-02	1.773E-04
60	4.5	5.1	7.367E-03	1.407E-05	2.760E-02	2.155E-04
60	4.5	5.15	7.367E-03	1.407E-05	2.760E-02	2.155E-04
60	4.5	5.2	8.764E-03	1.992E-05	3.282E-02	3.053E-04

60	4.5	5.25	9.342E-03	2.264E-05	3.505E-02	3.485E-04
60	4.5	5.3	9.665E-03	2.424E-05	3.618E-02	3.716E-04
60	4.5	5.35	1.068E-02	2.963E-05	4.002E-02	4.552E-04
60	4.5	5.4	1.078E-02	3.016E-05	4.024E-02	4.605E-04
60	4.5	5.45	1.078E-02	3.016E-05	4.024E-02	4.605E-04
60	4.5	5.5	1.187E-02	3.662E-05	4.442E-02	5.616E-04
60	4.5	5.55	1.223E-02	3.884E-05	4.566E-02	5.938E-04
60	4.5	5.6	1.296E-02	4.365E-05	4.834E-02	6.663E-04
60	4.5	5.65	1.343E-02	4.691E-05	5.008E-02	7.156E-04
60	4.5	5.7	1.404E-02	5.125E-05	5.240E-02	7.841E-04
60	4.5	5.75	1.404E-02	5.125E-05	5.240E-02	7.841E-04
60	4.5	5.8	1.498E-02	5.839E-05	5.587E-02	8.924E-04
60	4.5	5.85	1.573E-02	6.437E-05	5.856E-02	9.814E-04
60	4.5	5.9	1.573E-02	6.437E-05	5.856E-02	9.814E-04
60	4.5	5.95	1.624E-02	6.860E-05	6.043E-02	1.046E-03
60	4.5	6	1.624E-02	6.860E-05	6.043E-02	1.046E-03
60	4.5	6.05	1.656E-02	7.135E-05	6.166E-02	1.090E-03
60	4.5	6.1	1.779E-02	8.242E-05	6.611E-02	1.254E-03
60	4.5	6.15	1.838E-02	8.798E-05	6.832E-02	1.341E-03
60	4.5	6.2	1.838E-02	8.798E-05	6.832E-02	1.341E-03
60	4.5	6.25	1.955E-02	9.959E-05	7.271E-02	1.521E-03
60	4.5	6.3	1.955E-02	9.959E-05	7.271E-02	1.521E-03
60	4.5	6.35	1.976E-02	1.017E-04	7.332E-02	1.547E-03
60	4.5	6.4	2.020E-02	1.064E-04	7.491E-02	1.616E-03
60	4.5	6.45	2.020E-02	1.064E-04	7.491E-02	1.616E-03
60	4.5	6.5	2.020E-02	1.064E-04	7.491E-02	1.616E-03
60	4.5	6.55	2.083E-02	1.131E-04	7.727E-02	1.721E-03
60	4.5	6.6	2.174E-02	1.232E-04	8.056E-02	1.873E-03
60	4.5	6.65	2.231E-02	1.298E-04	8.267E-02	1.974E-03
60	4.5	6.7	2.231E-02	1.298E-04	8.267E-02	1.974E-03
60	4.5	6.75	2.345E-02	1.435E-04	8.688E-02	2.183E-03
60	4.5	6.8	2.345E-02	1.435E-04	8.688E-02	2.183E-03
60	4.5	6.85	2.345E-02	1.435E-04	8.688E-02	2.183E-03
60	4.5	6.9	2.372E-02	1.469E-04	8.772E-02	2.226E-03
60	4.5	6.95	2.372E-02	1.469E-04	8.772E-02	2.226E-03
60	4.5	7	2.438E-02	1.552E-04	9.021E-02	2.356E-03
60	4.5	7.05	2.499E-02	1.630E-04	9.246E-02	2.478E-03
60	4.5	7.1	2.550E-02	1.699E-04	9.430E-02	2.579E-03
60	4.5	7.15	2.550E-02	1.699E-04	9.430E-02	2.579E-03
60	4.5	7.2	2.550E-02	1.699E-04	9.430E-02	2.579E-03
60	4.5	7.25	2.615E-02	1.787E-04	9.658E-02	2.707E-03
60	4.5	7.3	2.685E-02	1.884E-04	9.921E-02	2.859E-03
60	4.5	7.35	2.685E-02	1.884E-04	9.921E-02	2.859E-03
60	4.5	7.4	2.685E-02	1.884E-04	9.921E-02	2.859E-03

60	4.5	7.45	2.685E-02	1.884E-04	9.921E-02	2.859E-03
60	4.5	7.5	2.685E-02	1.884E-04	9.921E-02	2.859E-03
60	4.5	7.55	2.804E-02	2.056E-04	1.036E-01	3.123E-03
60	4.5	7.6	2.906E-02	2.209E-04	1.072E-01	3.350E-03
60	4.5	7.65	2.906E-02	2.209E-04	1.072E-01	3.350E-03
60	4.5	7.7	2.906E-02	2.209E-04	1.072E-01	3.350E-03
60	4.5	7.75	2.906E-02	2.209E-04	1.072E-01	3.350E-03
60	4.5	7.8	2.906E-02	2.209E-04	1.072E-01	3.350E-03
60	4.5	7.85	2.906E-02	2.209E-04	1.072E-01	3.350E-03
60	4.5	7.9	2.906E-02	2.209E-04	1.072E-01	3.350E-03
60	4.5	7.95	2.906E-02	2.209E-04	1.072E-01	3.350E-03
60	4.5	8	3.075E-02	2.475E-04	1.133E-01	3.750E-03
60	4.5	8.05	3.075E-02	2.475E-04	1.133E-01	3.750E-03
60	4.5	8.1	3.142E-02	2.586E-04	1.158E-01	3.921E-03
60	4.5	8.15	3.142E-02	2.586E-04	1.158E-01	3.921E-03
60	4.5	8.2	3.142E-02	2.586E-04	1.158E-01	3.921E-03
60	4.5	8.25	3.215E-02	2.707E-04	1.185E-01	4.111E-03
60	4.5	8.3	3.215E-02	2.707E-04	1.185E-01	4.111E-03
60	4.5	8.35	3.215E-02	2.707E-04	1.185E-01	4.111E-03
60	4.5	8.4	3.255E-02	2.775E-04	1.198E-01	4.205E-03
60	4.5	8.45	3.255E-02	2.775E-04	1.198E-01	4.205E-03
60	4.5	8.5	3.255E-02	2.775E-04	1.198E-01	4.205E-03
60	4.5	8.55	3.317E-02	2.883E-04	1.221E-01	4.368E-03
60	4.5	8.6	3.317E-02	2.883E-04	1.221E-01	4.368E-03
60	4.5	8.65	3.317E-02	2.883E-04	1.221E-01	4.368E-03
60	4.5	8.7	3.317E-02	2.883E-04	1.221E-01	4.368E-03
60	4.5	8.75	3.388E-02	3.010E-04	1.248E-01	4.566E-03
60	4.5	8.8	3.388E-02	3.010E-04	1.248E-01	4.566E-03
60	4.5	8.85	3.432E-02	3.089E-04	1.262E-01	4.675E-03
60	4.5	8.9	3.470E-02	3.158E-04	1.277E-01	4.784E-03
60	4.5	8.95	3.470E-02	3.158E-04	1.277E-01	4.784E-03
60	4.5	9	3.470E-02	3.158E-04	1.277E-01	4.784E-03
60	4.5	9.05	3.546E-02	3.299E-04	1.305E-01	5.006E-03
60	4.5	9.1	3.546E-02	3.299E-04	1.305E-01	5.006E-03
60	4.5	9.15	3.612E-02	3.423E-04	1.329E-01	5.195E-03
60	4.5	9.2	3.612E-02	3.423E-04	1.329E-01	5.195E-03
60	4.5	9.25	3.612E-02	3.423E-04	1.329E-01	5.195E-03
60	4.5	9.3	3.612E-02	3.423E-04	1.329E-01	5.195E-03
60	4.5	9.35	3.612E-02	3.423E-04	1.329E-01	5.195E-03
60	4.5	9.4	3.659E-02	3.514E-04	1.345E-01	5.323E-03
60	4.5	9.45	3.659E-02	3.514E-04	1.345E-01	5.323E-03
60	4.5	9.5	3.659E-02	3.514E-04	1.345E-01	5.323E-03
60	4.5	9.55	3.659E-02	3.514E-04	1.345E-01	5.323E-03
60	4.5	9.6	3.734E-02	3.661E-04	1.373E-01	5.552E-03

60	4.5	9.65	3.734E-02	3.661E-04	1.373E-01	5.552E-03
60	4.5	9.7	3.734E-02	3.661E-04	1.373E-01	5.552E-03
60	4.5	9.75	3.734E-02	3.661E-04	1.373E-01	5.552E-03
60	4.5	9.8	3.734E-02	3.661E-04	1.373E-01	5.552E-03
60	4.5	9.85	3.734E-02	3.661E-04	1.373E-01	5.552E-03
60	4.5	9.9	3.804E-02	3.801E-04	1.398E-01	5.767E-03
60	4.5	9.95	3.855E-02	3.904E-04	1.416E-01	5.914E-03
60	4.5	10	3.855E-02	3.904E-04	1.416E-01	5.914E-03
100	4.5	4.55	7.859E-04	1.597E-07	3.006E-03	2.532E-06
100	4.5	4.6	1.343E-03	4.663E-07	5.036E-03	7.112E-06
100	4.5	4.65	2.018E-03	1.054E-06	7.636E-03	1.636E-05
100	4.5	4.7	2.963E-03	2.272E-06	1.115E-02	3.495E-05
100	4.5	4.75	3.234E-03	2.706E-06	1.215E-02	4.151E-05
100	4.5	4.8	3.788E-03	3.715E-06	1.424E-02	5.708E-05
100	4.5	4.85	4.874E-03	6.150E-06	1.835E-02	9.482E-05
100	4.5	4.9	5.271E-03	7.196E-06	1.978E-02	1.103E-04
100	4.5	4.95	5.674E-03	8.338E-06	2.127E-02	1.277E-04
100	4.5	5	6.724E-03	1.172E-05	2.524E-02	1.800E-04
100	4.5	5.05	7.286E-03	1.376E-05	2.733E-02	2.111E-04
100	4.5	5.1	7.634E-03	1.511E-05	2.861E-02	2.315E-04
100	4.5	5.15	8.318E-03	1.794E-05	3.118E-02	2.753E-04
100	4.5	5.2	8.802E-03	2.010E-05	3.297E-02	3.078E-04
100	4.5	5.25	9.378E-03	2.281E-05	3.513E-02	3.498E-04
100	4.5	5.3	1.049E-02	2.855E-05	3.925E-02	4.373E-04
100	4.5	5.35	1.049E-02	2.854E-05	3.920E-02	4.363E-04
100	4.5	5.4	1.086E-02	3.063E-05	4.063E-02	4.689E-04
100	4.5	5.45	1.185E-02	3.647E-05	4.426E-02	5.572E-04
100	4.5	5.5	1.224E-02	3.892E-05	4.574E-02	5.954E-04
100	4.5	5.55	1.254E-02	4.087E-05	4.685E-02	6.249E-04
100	4.5	5.6	1.323E-02	4.548E-05	4.934E-02	6.937E-04
100	4.5	5.65	1.363E-02	4.825E-05	5.084E-02	7.369E-04
100	4.5	5.7	1.427E-02	5.290E-05	5.324E-02	8.089E-04
100	4.5	5.75	1.498E-02	5.838E-05	5.584E-02	8.909E-04
100	4.5	5.8	1.498E-02	5.838E-05	5.584E-02	8.909E-04
100	4.5	5.85	1.574E-02	6.441E-05	5.860E-02	9.819E-04
100	4.5	5.9	1.588E-02	6.559E-05	5.911E-02	9.992E-04
100	4.5	5.95	1.646E-02	7.048E-05	6.127E-02	1.074E-03
100	4.5	6	1.705E-02	7.563E-05	6.342E-02	1.152E-03
100	4.5	6.05	1.705E-02	7.563E-05	6.342E-02	1.152E-03
100	4.5	6.1	1.803E-02	8.460E-05	6.707E-02	1.290E-03
100	4.5	6.15	1.826E-02	8.677E-05	6.786E-02	1.321E-03
100	4.5	6.2	1.859E-02	9.003E-05	6.910E-02	1.371E-03
100	4.5	6.25	1.887E-02	9.273E-05	7.011E-02	1.412E-03

100	4.5	6.3	1.954E-02	9.949E-05	7.258E-02	1.514E-03
100	4.5	6.35	2.032E-02	1.076E-04	7.547E-02	1.639E-03
100	4.5	6.4	2.032E-02	1.076E-04	7.547E-02	1.639E-03
100	4.5	6.45	2.076E-02	1.124E-04	7.705E-02	1.709E-03
100	4.5	6.5	2.076E-02	1.124E-04	7.705E-02	1.709E-03
100	4.5	6.55	2.131E-02	1.183E-04	7.902E-02	1.799E-03
100	4.5	6.6	2.204E-02	1.267E-04	8.173E-02	1.926E-03
100	4.5	6.65	2.245E-02	1.315E-04	8.325E-02	2.000E-03
100	4.5	6.7	2.258E-02	1.330E-04	8.371E-02	2.022E-03
100	4.5	6.75	2.302E-02	1.383E-04	8.535E-02	2.103E-03
100	4.5	6.8	2.331E-02	1.418E-04	8.636E-02	2.154E-03
100	4.5	6.85	2.353E-02	1.444E-04	8.717E-02	2.196E-03
100	4.5	6.9	2.409E-02	1.514E-04	8.919E-02	2.300E-03
100	4.5	6.95	2.427E-02	1.538E-04	8.983E-02	2.334E-03
100	4.5	7	2.473E-02	1.596E-04	9.153E-02	2.425E-03
100	4.5	7.05	2.497E-02	1.628E-04	9.247E-02	2.476E-03
100	4.5	7.1	2.562E-02	1.715E-04	9.487E-02	2.608E-03
100	4.5	7.15	2.584E-02	1.744E-04	9.556E-02	2.647E-03
100	4.5	7.2	2.608E-02	1.777E-04	9.649E-02	2.700E-03
100	4.5	7.25	2.630E-02	1.807E-04	9.728E-02	2.745E-03
100	4.5	7.3	2.630E-02	1.807E-04	9.728E-02	2.745E-03
100	4.5	7.35	2.673E-02	1.866E-04	9.873E-02	2.829E-03
100	4.5	7.4	2.746E-02	1.970E-04	1.015E-01	2.992E-03
100	4.5	7.45	2.771E-02	2.007E-04	1.024E-01	3.049E-03
100	4.5	7.5	2.771E-02	2.007E-04	1.024E-01	3.049E-03
100	4.5	7.55	2.827E-02	2.089E-04	1.044E-01	3.173E-03
100	4.5	7.6	2.863E-02	2.143E-04	1.057E-01	3.253E-03
100	4.5	7.65	2.863E-02	2.143E-04	1.057E-01	3.253E-03
100	4.5	7.7	2.863E-02	2.143E-04	1.057E-01	3.253E-03
100	4.5	7.75	2.896E-02	2.194E-04	1.069E-01	3.326E-03
100	4.5	7.8	2.921E-02	2.232E-04	1.078E-01	3.387E-03
100	4.5	7.85	3.000E-02	2.355E-04	1.108E-01	3.576E-03
100	4.5	7.9	3.021E-02	2.389E-04	1.115E-01	3.626E-03
100	4.5	7.95	3.031E-02	2.404E-04	1.118E-01	3.645E-03
100	4.5	8	3.057E-02	2.446E-04	1.128E-01	3.711E-03
100	4.5	8.05	3.057E-02	2.446E-04	1.128E-01	3.711E-03
100	4.5	8.1	3.100E-02	2.515E-04	1.143E-01	3.815E-03
100	4.5	8.15	3.100E-02	2.515E-04	1.143E-01	3.815E-03
100	4.5	8.2	3.181E-02	2.650E-04	1.173E-01	4.019E-03
100	4.5	8.25	3.181E-02	2.650E-04	1.173E-01	4.019E-03
100	4.5	8.3	3.181E-02	2.650E-04	1.173E-01	4.019E-03
100	4.5	8.35	3.208E-02	2.695E-04	1.183E-01	4.090E-03
100	4.5	8.4	3.227E-02	2.727E-04	1.189E-01	4.136E-03
100	4.5	8.45	3.265E-02	2.792E-04	1.203E-01	4.233E-03

100	4.5	8.5	3.290E-02	2.836E-04	1.212E-01	4.302E-03
100	4.5	8.55	3.337E-02	2.918E-04	1.230E-01	4.427E-03
100	4.5	8.6	3.364E-02	2.965E-04	1.240E-01	4.501E-03
100	4.5	8.65	3.364E-02	2.965E-04	1.240E-01	4.501E-03
100	4.5	8.7	3.395E-02	3.021E-04	1.250E-01	4.579E-03
100	4.5	8.75	3.395E-02	3.021E-04	1.250E-01	4.579E-03
100	4.5	8.8	3.395E-02	3.021E-04	1.250E-01	4.579E-03
100	4.5	8.85	3.395E-02	3.021E-04	1.250E-01	4.579E-03
100	4.5	8.9	3.432E-02	3.088E-04	1.264E-01	4.683E-03
100	4.5	8.95	3.499E-02	3.209E-04	1.288E-01	4.868E-03
100	4.5	9	3.544E-02	3.294E-04	1.304E-01	4.996E-03
100	4.5	9.05	3.544E-02	3.294E-04	1.304E-01	4.996E-03
100	4.5	9.1	3.544E-02	3.294E-04	1.304E-01	4.996E-03
100	4.5	9.15	3.571E-02	3.345E-04	1.315E-01	5.076E-03
100	4.5	9.2	3.571E-02	3.345E-04	1.315E-01	5.076E-03
100	4.5	9.25	3.585E-02	3.370E-04	1.319E-01	5.110E-03
100	4.5	9.3	3.609E-02	3.416E-04	1.328E-01	5.180E-03
100	4.5	9.35	3.630E-02	3.456E-04	1.335E-01	5.240E-03
100	4.5	9.4	3.630E-02	3.456E-04	1.335E-01	5.240E-03
100	4.5	9.45	3.683E-02	3.559E-04	1.355E-01	5.400E-03
100	4.5	9.5	3.683E-02	3.559E-04	1.355E-01	5.400E-03
100	4.5	9.55	3.697E-02	3.587E-04	1.359E-01	5.438E-03
100	4.5	9.6	3.725E-02	3.642E-04	1.370E-01	5.525E-03
100	4.5	9.65	3.725E-02	3.642E-04	1.370E-01	5.525E-03
100	4.5	9.7	3.725E-02	3.642E-04	1.370E-01	5.525E-03
100	4.5	9.75	3.800E-02	3.791E-04	1.397E-01	5.754E-03
100	4.5	9.8	3.800E-02	3.791E-04	1.397E-01	5.754E-03
100	4.5	9.85	3.800E-02	3.791E-04	1.397E-01	5.754E-03
100	4.5	9.9	3.815E-02	3.822E-04	1.402E-01	5.794E-03
100	4.5	9.95	3.842E-02	3.876E-04	1.412E-01	5.880E-03
100	4.5	10	3.870E-02	3.933E-04	1.423E-01	5.969E-03

Table A.5: Comparison of MIs of cuboid with  $n = 5$  to MIs of cuboids from 5.05 to 10 using the Euclidean distance and the chi-squared distance.

length (pixels)	shape 1	shape 2	$\bar{\omega}_i$ Euc-dist	$\bar{\omega}_i$ CSD	$\bar{\tau}_i$ Euc-dist	$\bar{\tau}_i$ CSD
60	5	5.05	5.441E-04	7.693E-08	2.099E-03	1.255E-06
60	5	5.1	1.252E-03	4.077E-07	4.651E-03	6.172E-06
60	5	5.15	1.252E-03	4.077E-07	4.651E-03	6.172E-06
60	5	5.2	2.649E-03	1.825E-06	9.868E-03	2.784E-05
60	5	5.25	3.227E-03	2.709E-06	1.210E-02	4.189E-05
60	5	5.3	3.550E-03	3.279E-06	1.323E-02	5.012E-05
60	5	5.35	4.568E-03	5.432E-06	1.707E-02	8.354E-05

60	5	5.4	4.663E-03	5.659E-06	1.730E-02	8.578E-05
60	5	5.45	4.663E-03	5.659E-06	1.730E-02	8.578E-05
60	5	5.5	5.759E-03	8.637E-06	2.147E-02	1.323E-04
60	5	5.55	6.113E-03	9.732E-06	2.271E-02	1.482E-04
60	5	5.6	6.846E-03	1.221E-05	2.539E-02	1.854E-04
60	5	5.65	7.320E-03	1.396E-05	2.713E-02	2.118E-04
60	5	5.7	7.925E-03	1.637E-05	2.945E-02	2.498E-04
60	5	5.75	7.925E-03	1.637E-05	2.945E-02	2.498E-04
60	5	5.8	8.868E-03	2.051E-05	3.292E-02	3.125E-04
60	5	5.85	9.615E-03	2.411E-05	3.561E-02	3.660E-04
60	5	5.9	9.615E-03	2.411E-05	3.561E-02	3.660E-04
60	5	5.95	1.012E-02	2.673E-05	3.748E-02	4.057E-04
60	5	6	1.012E-02	2.673E-05	3.748E-02	4.057E-04
60	5	6.05	1.044E-02	2.846E-05	3.872E-02	4.332E-04
60	5	6.1	1.168E-02	3.559E-05	4.316E-02	5.392E-04
60	5	6.15	1.226E-02	3.927E-05	4.537E-02	5.963E-04
60	5	6.2	1.226E-02	3.927E-05	4.537E-02	5.963E-04
60	5	6.25	1.344E-02	4.716E-05	4.976E-02	7.184E-04
60	5	6.3	1.344E-02	4.716E-05	4.976E-02	7.184E-04
60	5	6.35	1.364E-02	4.862E-05	5.037E-02	7.364E-04
60	5	6.4	1.409E-02	5.187E-05	5.196E-02	7.841E-04
60	5	6.45	1.409E-02	5.187E-05	5.196E-02	7.841E-04
60	5	6.5	1.409E-02	5.187E-05	5.196E-02	7.841E-04
60	5	6.55	1.471E-02	5.660E-05	5.433E-02	8.579E-04
60	5	6.6	1.562E-02	6.382E-05	5.762E-02	9.661E-04
60	5	6.65	1.619E-02	6.859E-05	5.973E-02	1.039E-03
60	5	6.7	1.619E-02	6.859E-05	5.973E-02	1.039E-03
60	5	6.75	1.734E-02	7.864E-05	6.394E-02	1.192E-03
60	5	6.8	1.734E-02	7.864E-05	6.394E-02	1.192E-03
60	5	6.85	1.734E-02	7.864E-05	6.394E-02	1.192E-03
60	5	6.9	1.760E-02	8.111E-05	6.478E-02	1.224E-03
60	5	6.95	1.760E-02	8.111E-05	6.478E-02	1.224E-03
60	5	7	1.826E-02	8.731E-05	6.726E-02	1.321E-03
60	5	7.05	1.887E-02	9.325E-05	6.952E-02	1.413E-03
60	5	7.1	1.939E-02	9.843E-05	7.136E-02	1.489E-03
60	5	7.15	1.939E-02	9.843E-05	7.136E-02	1.489E-03
60	5	7.2	1.939E-02	9.843E-05	7.136E-02	1.489E-03
60	5	7.25	2.004E-02	1.052E-04	7.363E-02	1.587E-03
60	5	7.3	2.073E-02	1.126E-04	7.626E-02	1.704E-03
60	5	7.35	2.073E-02	1.126E-04	7.626E-02	1.704E-03
60	5	7.4	2.073E-02	1.126E-04	7.626E-02	1.704E-03
60	5	7.45	2.073E-02	1.126E-04	7.626E-02	1.704E-03
60	5	7.5	2.073E-02	1.126E-04	7.626E-02	1.704E-03
60	5	7.55	2.193E-02	1.261E-04	8.065E-02	1.909E-03

60	5	7.6	2.294E-02	1.381E-04	8.427E-02	2.087E-03
60	5	7.65	2.294E-02	1.381E-04	8.427E-02	2.087E-03
60	5	7.7	2.294E-02	1.381E-04	8.427E-02	2.087E-03
60	5	7.75	2.294E-02	1.381E-04	8.427E-02	2.087E-03
60	5	7.8	2.294E-02	1.381E-04	8.427E-02	2.087E-03
60	5	7.85	2.294E-02	1.381E-04	8.427E-02	2.087E-03
60	5	7.9	2.294E-02	1.381E-04	8.427E-02	2.087E-03
60	5	7.95	2.294E-02	1.381E-04	8.427E-02	2.087E-03
60	5	8	2.463E-02	1.592E-04	9.037E-02	2.405E-03
60	5	8.05	2.463E-02	1.592E-04	9.037E-02	2.405E-03
60	5	8.1	2.531E-02	1.682E-04	9.288E-02	2.543E-03
60	5	8.15	2.531E-02	1.682E-04	9.288E-02	2.543E-03
60	5	8.2	2.531E-02	1.682E-04	9.288E-02	2.543E-03
60	5	8.25	2.603E-02	1.780E-04	9.559E-02	2.697E-03
60	5	8.3	2.603E-02	1.780E-04	9.559E-02	2.697E-03
60	5	8.35	2.603E-02	1.780E-04	9.559E-02	2.697E-03
60	5	8.4	2.643E-02	1.835E-04	9.690E-02	2.773E-03
60	5	8.45	2.643E-02	1.835E-04	9.690E-02	2.773E-03
60	5	8.5	2.643E-02	1.835E-04	9.690E-02	2.773E-03
60	5	8.55	2.705E-02	1.923E-04	9.916E-02	2.906E-03
60	5	8.6	2.705E-02	1.923E-04	9.916E-02	2.906E-03
60	5	8.65	2.705E-02	1.923E-04	9.916E-02	2.906E-03
60	5	8.7	2.705E-02	1.923E-04	9.916E-02	2.906E-03
60	5	8.75	2.777E-02	2.027E-04	1.018E-01	3.067E-03
60	5	8.8	2.777E-02	2.027E-04	1.018E-01	3.067E-03
60	5	8.85	2.821E-02	2.091E-04	1.033E-01	3.157E-03
60	5	8.9	2.859E-02	2.149E-04	1.047E-01	3.247E-03
60	5	8.95	2.859E-02	2.149E-04	1.047E-01	3.247E-03
60	5	9	2.859E-02	2.149E-04	1.047E-01	3.247E-03
60	5	9.05	2.935E-02	2.265E-04	1.076E-01	3.430E-03
60	5	9.1	2.935E-02	2.265E-04	1.076E-01	3.430E-03
60	5	9.15	3.000E-02	2.368E-04	1.100E-01	3.587E-03
60	5	9.2	3.000E-02	2.368E-04	1.100E-01	3.587E-03
60	5	9.25	3.000E-02	2.368E-04	1.100E-01	3.587E-03
60	5	9.3	3.000E-02	2.368E-04	1.100E-01	3.587E-03
60	5	9.35	3.000E-02	2.368E-04	1.100E-01	3.587E-03
60	5	9.4	3.048E-02	2.444E-04	1.115E-01	3.693E-03
60	5	9.45	3.048E-02	2.444E-04	1.115E-01	3.693E-03
60	5	9.5	3.048E-02	2.444E-04	1.115E-01	3.693E-03
60	5	9.55	3.048E-02	2.444E-04	1.115E-01	3.693E-03
60	5	9.6	3.123E-02	2.567E-04	1.143E-01	3.885E-03
60	5	9.65	3.123E-02	2.567E-04	1.143E-01	3.885E-03
60	5	9.7	3.123E-02	2.567E-04	1.143E-01	3.885E-03
60	5	9.75	3.123E-02	2.567E-04	1.143E-01	3.885E-03

60	5	9.8	3.123E-02	2.567E-04	1.143E-01	3.885E-03
60	5	9.85	3.123E-02	2.567E-04	1.143E-01	3.885E-03
60	5	9.9	3.193E-02	2.684E-04	1.169E-01	4.065E-03
60	5	9.95	3.244E-02	2.771E-04	1.186E-01	4.189E-03
60	5	10	3.244E-02	2.771E-04	1.186E-01	4.189E-03
100	5	5.05	5.622E-04	8.215E-08	2.084E-03	1.239E-06
100	5	5.1	9.100E-04	2.153E-07	3.368E-03	3.238E-06
100	5	5.15	1.594E-03	6.607E-07	5.942E-03	1.009E-05
100	5	5.2	2.079E-03	1.124E-06	7.724E-03	1.706E-05
100	5	5.25	2.654E-03	1.832E-06	9.886E-03	2.797E-05
100	5	5.3	3.764E-03	3.687E-06	1.401E-02	5.622E-05
100	5	5.35	3.763E-03	3.685E-06	1.396E-02	5.586E-05
100	5	5.4	4.140E-03	4.461E-06	1.539E-02	6.789E-05
100	5	5.45	5.127E-03	6.846E-06	1.902E-02	1.038E-04
100	5	5.5	5.518E-03	7.931E-06	2.050E-02	1.207E-04
100	5	5.55	5.820E-03	8.824E-06	2.161E-02	1.342E-04
100	5	5.6	6.506E-03	1.103E-05	2.409E-02	1.670E-04
100	5	5.65	6.903E-03	1.242E-05	2.560E-02	1.886E-04
100	5	5.7	7.542E-03	1.483E-05	2.800E-02	2.258E-04
100	5	5.75	8.260E-03	1.779E-05	3.060E-02	2.701E-04
100	5	5.8	8.260E-03	1.779E-05	3.060E-02	2.701E-04
100	5	5.85	9.012E-03	2.118E-05	3.336E-02	3.212E-04
100	5	5.9	9.156E-03	2.187E-05	3.387E-02	3.311E-04
100	5	5.95	9.735E-03	2.472E-05	3.603E-02	3.750E-04
100	5	6	1.032E-02	2.782E-05	3.818E-02	4.215E-04
100	5	6.05	1.032E-02	2.782E-05	3.818E-02	4.215E-04
100	5	6.1	1.130E-02	3.335E-05	4.183E-02	5.066E-04
100	5	6.15	1.153E-02	3.472E-05	4.262E-02	5.262E-04
100	5	6.2	1.187E-02	3.680E-05	4.386E-02	5.574E-04
100	5	6.25	1.215E-02	3.853E-05	4.487E-02	5.837E-04
100	5	6.3	1.282E-02	4.293E-05	4.734E-02	6.503E-04
100	5	6.35	1.360E-02	4.832E-05	5.023E-02	7.329E-04
100	5	6.4	1.360E-02	4.832E-05	5.023E-02	7.329E-04
100	5	6.45	1.404E-02	5.152E-05	5.181E-02	7.801E-04
100	5	6.5	1.404E-02	5.152E-05	5.181E-02	7.801E-04
100	5	6.55	1.458E-02	5.559E-05	5.378E-02	8.412E-04
100	5	6.6	1.532E-02	6.134E-05	5.649E-02	9.289E-04
100	5	6.65	1.573E-02	6.469E-05	5.801E-02	9.803E-04
100	5	6.7	1.586E-02	6.580E-05	5.847E-02	9.959E-04
100	5	6.75	1.630E-02	6.951E-05	6.011E-02	1.053E-03
100	5	6.8	1.659E-02	7.197E-05	6.112E-02	1.089E-03
100	5	6.85	1.680E-02	7.389E-05	6.193E-02	1.119E-03
100	5	6.9	1.736E-02	7.889E-05	6.395E-02	1.194E-03

100	5	6.95	1.755E-02	8.061E-05	6.459E-02	1.218E-03
100	5	7	1.800E-02	8.485E-05	6.629E-02	1.284E-03
100	5	7.05	1.825E-02	8.720E-05	6.723E-02	1.321E-03
100	5	7.1	1.890E-02	9.353E-05	6.963E-02	1.418E-03
100	5	7.15	1.911E-02	9.570E-05	7.032E-02	1.447E-03
100	5	7.2	1.936E-02	9.818E-05	7.125E-02	1.486E-03
100	5	7.25	1.957E-02	1.004E-04	7.204E-02	1.519E-03
100	5	7.3	1.957E-02	1.004E-04	7.204E-02	1.519E-03
100	5	7.35	2.000E-02	1.048E-04	7.349E-02	1.582E-03
100	5	7.4	2.073E-02	1.127E-04	7.624E-02	1.705E-03
100	5	7.45	2.098E-02	1.154E-04	7.720E-02	1.748E-03
100	5	7.5	2.098E-02	1.154E-04	7.720E-02	1.748E-03
100	5	7.55	2.154E-02	1.217E-04	7.921E-02	1.842E-03
100	5	7.6	2.191E-02	1.258E-04	8.049E-02	1.903E-03
100	5	7.65	2.191E-02	1.258E-04	8.049E-02	1.903E-03
100	5	7.7	2.191E-02	1.258E-04	8.049E-02	1.903E-03
100	5	7.75	2.224E-02	1.297E-04	8.166E-02	1.960E-03
100	5	7.8	2.249E-02	1.327E-04	8.261E-02	2.006E-03
100	5	7.85	2.328E-02	1.422E-04	8.552E-02	2.152E-03
100	5	7.9	2.349E-02	1.448E-04	8.627E-02	2.191E-03
100	5	7.95	2.359E-02	1.460E-04	8.657E-02	2.206E-03
100	5	8	2.385E-02	1.492E-04	8.754E-02	2.257E-03
100	5	8.05	2.385E-02	1.492E-04	8.754E-02	2.257E-03
100	5	8.1	2.427E-02	1.547E-04	8.909E-02	2.339E-03
100	5	8.15	2.427E-02	1.547E-04	8.909E-02	2.339E-03
100	5	8.2	2.509E-02	1.653E-04	9.204E-02	2.499E-03
100	5	8.25	2.509E-02	1.653E-04	9.204E-02	2.499E-03
100	5	8.3	2.509E-02	1.653E-04	9.204E-02	2.499E-03
100	5	8.35	2.536E-02	1.689E-04	9.305E-02	2.555E-03
100	5	8.4	2.554E-02	1.714E-04	9.370E-02	2.592E-03
100	5	8.45	2.592E-02	1.765E-04	9.505E-02	2.668E-03
100	5	8.5	2.618E-02	1.800E-04	9.601E-02	2.723E-03
100	5	8.55	2.665E-02	1.866E-04	9.773E-02	2.823E-03
100	5	8.6	2.691E-02	1.903E-04	9.873E-02	2.882E-03
100	5	8.65	2.691E-02	1.903E-04	9.873E-02	2.882E-03
100	5	8.7	2.723E-02	1.948E-04	9.977E-02	2.945E-03
100	5	8.75	2.723E-02	1.948E-04	9.977E-02	2.945E-03
100	5	8.8	2.723E-02	1.948E-04	9.977E-02	2.945E-03
100	5	8.85	2.723E-02	1.948E-04	9.977E-02	2.945E-03
100	5	8.9	2.760E-02	2.002E-04	1.011E-01	3.028E-03
100	5	8.95	2.826E-02	2.100E-04	1.036E-01	3.177E-03
100	5	9	2.872E-02	2.169E-04	1.052E-01	3.281E-03
100	5	9.05	2.872E-02	2.169E-04	1.052E-01	3.281E-03
100	5	9.1	2.872E-02	2.169E-04	1.052E-01	3.281E-03

100	5	9.15	2.899E-02	2.210E-04	1.062E-01	3.346E-03
100	5	9.2	2.899E-02	2.210E-04	1.062E-01	3.346E-03
100	5	9.25	2.912E-02	2.231E-04	1.067E-01	3.374E-03
100	5	9.3	2.936E-02	2.268E-04	1.075E-01	3.431E-03
100	5	9.35	2.957E-02	2.301E-04	1.083E-01	3.479E-03
100	5	9.4	2.957E-02	2.301E-04	1.083E-01	3.479E-03
100	5	9.45	3.011E-02	2.385E-04	1.103E-01	3.610E-03
100	5	9.5	3.011E-02	2.385E-04	1.103E-01	3.610E-03
100	5	9.55	3.025E-02	2.408E-04	1.107E-01	3.641E-03
100	5	9.6	3.053E-02	2.453E-04	1.118E-01	3.712E-03
100	5	9.65	3.053E-02	2.453E-04	1.118E-01	3.712E-03
100	5	9.7	3.053E-02	2.453E-04	1.118E-01	3.712E-03
100	5	9.75	3.128E-02	2.576E-04	1.145E-01	3.900E-03
100	5	9.8	3.128E-02	2.576E-04	1.145E-01	3.900E-03
100	5	9.85	3.128E-02	2.576E-04	1.145E-01	3.900E-03
100	5	9.9	3.143E-02	2.601E-04	1.150E-01	3.934E-03
100	5	9.95	3.170E-02	2.646E-04	1.160E-01	4.004E-03
100	5	10	3.198E-02	2.693E-04	1.170E-01	4.078E-03

Table A.6: Comparison of MIs of cuboid with  $n = 5.5$  to MIs of cuboids from 5.55 to 10 using the Euclidean distance and the chi-squared distance.

length (pixels)	shape 1	shape 2	$\bar{\omega}_i$ Euc-dist	$\bar{\omega}_i$ CSD	$\bar{\tau}_i$ Euc-dist	$\bar{\tau}_i$ CSD
60	5.5	5.55	3.537E-04	3.267E-08	1.243E-03	4.476E-07
60	5.5	5.6	1.087E-03	3.085E-07	3.924E-03	4.465E-06
60	5.5	5.65	1.560E-03	6.360E-07	5.666E-03	9.314E-06
60	5.5	5.7	2.166E-03	1.225E-06	7.987E-03	1.852E-05
60	5.5	5.75	2.166E-03	1.225E-06	7.987E-03	1.852E-05
60	5.5	5.8	3.109E-03	2.527E-06	1.145E-02	3.813E-05
60	5.5	5.85	3.856E-03	3.887E-06	1.414E-02	5.821E-05
60	5.5	5.9	3.856E-03	3.887E-06	1.414E-02	5.821E-05
60	5.5	5.95	4.363E-03	4.977E-06	1.601E-02	7.465E-05
60	5.5	6	4.363E-03	4.977E-06	1.601E-02	7.465E-05
60	5.5	6.05	4.684E-03	5.739E-06	1.725E-02	8.668E-05
60	5.5	6.1	5.917E-03	9.163E-06	2.169E-02	1.373E-04
60	5.5	6.15	6.505E-03	1.108E-05	2.390E-02	1.668E-04
60	5.5	6.2	6.505E-03	1.108E-05	2.390E-02	1.668E-04
60	5.5	6.25	7.676E-03	1.543E-05	2.829E-02	2.341E-04
60	5.5	6.3	7.676E-03	1.543E-05	2.829E-02	2.341E-04
60	5.5	6.35	7.882E-03	1.627E-05	2.891E-02	2.445E-04
60	5.5	6.4	8.329E-03	1.817E-05	3.049E-02	2.722E-04
60	5.5	6.45	8.329E-03	1.817E-05	3.049E-02	2.722E-04
60	5.5	6.5	8.329E-03	1.817E-05	3.049E-02	2.722E-04

60	5.5	6.55	8.955E-03	2.101E-05	3.286E-02	3.164E-04
60	5.5	6.6	9.863E-03	2.550E-05	3.615E-02	3.834E-04
60	5.5	6.65	1.044E-02	2.855E-05	3.826E-02	4.298E-04
60	5.5	6.7	1.044E-02	2.855E-05	3.826E-02	4.298E-04
60	5.5	6.75	1.158E-02	3.515E-05	4.247E-02	5.304E-04
60	5.5	6.8	1.158E-02	3.515E-05	4.247E-02	5.304E-04
60	5.5	6.85	1.158E-02	3.515E-05	4.247E-02	5.304E-04
60	5.5	6.9	1.185E-02	3.681E-05	4.331E-02	5.518E-04
60	5.5	6.95	1.185E-02	3.681E-05	4.331E-02	5.518E-04
60	5.5	7	1.250E-02	4.102E-05	4.580E-02	6.175E-04
60	5.5	7.05	1.311E-02	4.513E-05	4.805E-02	6.803E-04
60	5.5	7.1	1.363E-02	4.875E-05	4.989E-02	7.340E-04
60	5.5	7.15	1.363E-02	4.875E-05	4.989E-02	7.340E-04
60	5.5	7.2	1.363E-02	4.875E-05	4.989E-02	7.340E-04
60	5.5	7.25	1.428E-02	5.352E-05	5.217E-02	8.032E-04
60	5.5	7.3	1.497E-02	5.888E-05	5.480E-02	8.871E-04
60	5.5	7.35	1.497E-02	5.888E-05	5.480E-02	8.871E-04
60	5.5	7.4	1.497E-02	5.888E-05	5.480E-02	8.871E-04
60	5.5	7.45	1.497E-02	5.888E-05	5.480E-02	8.871E-04
60	5.5	7.5	1.497E-02	5.888E-05	5.480E-02	8.871E-04
60	5.5	7.55	1.617E-02	6.870E-05	5.918E-02	1.036E-03
60	5.5	7.6	1.719E-02	7.765E-05	6.281E-02	1.169E-03
60	5.5	7.65	1.719E-02	7.765E-05	6.281E-02	1.169E-03
60	5.5	7.7	1.719E-02	7.765E-05	6.281E-02	1.169E-03
60	5.5	7.75	1.719E-02	7.765E-05	6.281E-02	1.169E-03
60	5.5	7.8	1.719E-02	7.765E-05	6.281E-02	1.169E-03
60	5.5	7.85	1.719E-02	7.765E-05	6.281E-02	1.169E-03
60	5.5	7.9	1.719E-02	7.765E-05	6.281E-02	1.169E-03
60	5.5	7.95	1.719E-02	7.765E-05	6.281E-02	1.169E-03
60	5.5	8	1.887E-02	9.371E-05	6.890E-02	1.410E-03
60	5.5	8.05	1.887E-02	9.371E-05	6.890E-02	1.410E-03
60	5.5	8.1	1.955E-02	1.006E-04	7.141E-02	1.516E-03
60	5.5	8.15	1.955E-02	1.006E-04	7.141E-02	1.516E-03
60	5.5	8.2	1.955E-02	1.006E-04	7.141E-02	1.516E-03
60	5.5	8.25	2.027E-02	1.082E-04	7.412E-02	1.635E-03
60	5.5	8.3	2.027E-02	1.082E-04	7.412E-02	1.635E-03
60	5.5	8.35	2.027E-02	1.082E-04	7.412E-02	1.635E-03
60	5.5	8.4	2.067E-02	1.125E-04	7.544E-02	1.694E-03
60	5.5	8.45	2.067E-02	1.125E-04	7.544E-02	1.694E-03
60	5.5	8.5	2.067E-02	1.125E-04	7.544E-02	1.694E-03
60	5.5	8.55	2.129E-02	1.194E-04	7.769E-02	1.798E-03
60	5.5	8.6	2.129E-02	1.194E-04	7.769E-02	1.798E-03
60	5.5	8.65	2.129E-02	1.194E-04	7.769E-02	1.798E-03
60	5.5	8.7	2.129E-02	1.194E-04	7.769E-02	1.798E-03

60	5.5	8.75	2.201E-02	1.276E-04	8.037E-02	1.926E-03
60	5.5	8.8	2.201E-02	1.276E-04	8.037E-02	1.926E-03
60	5.5	8.85	2.245E-02	1.328E-04	8.182E-02	1.997E-03
60	5.5	8.9	2.283E-02	1.373E-04	8.325E-02	2.069E-03
60	5.5	8.95	2.283E-02	1.373E-04	8.325E-02	2.069E-03
60	5.5	9	2.283E-02	1.373E-04	8.325E-02	2.069E-03
60	5.5	9.05	2.359E-02	1.467E-04	8.610E-02	2.216E-03
60	5.5	9.1	2.359E-02	1.467E-04	8.610E-02	2.216E-03
60	5.5	9.15	2.425E-02	1.550E-04	8.849E-02	2.342E-03
60	5.5	9.2	2.425E-02	1.550E-04	8.849E-02	2.342E-03
60	5.5	9.25	2.425E-02	1.550E-04	8.849E-02	2.342E-03
60	5.5	9.3	2.425E-02	1.550E-04	8.849E-02	2.342E-03
60	5.5	9.35	2.425E-02	1.550E-04	8.849E-02	2.342E-03
60	5.5	9.4	2.472E-02	1.611E-04	9.007E-02	2.428E-03
60	5.5	9.45	2.472E-02	1.611E-04	9.007E-02	2.428E-03
60	5.5	9.5	2.472E-02	1.611E-04	9.007E-02	2.428E-03
60	5.5	9.55	2.472E-02	1.611E-04	9.007E-02	2.428E-03
60	5.5	9.6	2.547E-02	1.711E-04	9.288E-02	2.584E-03
60	5.5	9.65	2.547E-02	1.711E-04	9.288E-02	2.584E-03
60	5.5	9.7	2.547E-02	1.711E-04	9.288E-02	2.584E-03
60	5.5	9.75	2.547E-02	1.711E-04	9.288E-02	2.584E-03
60	5.5	9.8	2.547E-02	1.711E-04	9.288E-02	2.584E-03
60	5.5	9.85	2.547E-02	1.711E-04	9.288E-02	2.584E-03
60	5.5	9.9	2.617E-02	1.807E-04	9.544E-02	2.732E-03
60	5.5	9.95	2.668E-02	1.879E-04	9.716E-02	2.833E-03
60	5.5	10	2.668E-02	1.879E-04	9.716E-02	2.833E-03
100	5.5	5.55	3.021E-04	2.382E-08	1.110E-03	3.571E-07
100	5.5	5.6	9.875E-04	2.547E-07	3.597E-03	3.752E-06
100	5.5	5.65	1.384E-03	5.006E-07	5.099E-03	7.540E-06
100	5.5	5.7	2.024E-03	1.070E-06	7.503E-03	1.634E-05
100	5.5	5.75	2.742E-03	1.965E-06	1.011E-02	2.968E-05
100	5.5	5.8	2.742E-03	1.965E-06	1.011E-02	2.968E-05
100	5.5	5.85	3.494E-03	3.191E-06	1.286E-02	4.812E-05
100	5.5	5.9	3.637E-03	3.459E-06	1.337E-02	5.200E-05
100	5.5	5.95	4.217E-03	4.649E-06	1.553E-02	7.022E-05
100	5.5	6	4.806E-03	6.041E-06	1.768E-02	9.109E-05
100	5.5	6.05	4.806E-03	6.041E-06	1.768E-02	9.109E-05
100	5.5	6.1	5.785E-03	8.757E-06	2.133E-02	1.328E-04
100	5.5	6.15	6.014E-03	9.464E-06	2.213E-02	1.429E-04
100	5.5	6.2	6.352E-03	1.056E-05	2.336E-02	1.594E-04
100	5.5	6.25	6.628E-03	1.150E-05	2.437E-02	1.736E-04
100	5.5	6.3	7.301E-03	1.396E-05	2.685E-02	2.107E-04
100	5.5	6.35	8.080E-03	1.710E-05	2.974E-02	2.588E-04

100	5.5	6.4	8.080E-03	1.710E-05	2.974E-02	2.588E-04
100	5.5	6.45	8.522E-03	1.903E-05	3.131E-02	2.872E-04
100	5.5	6.5	8.522E-03	1.903E-05	3.131E-02	2.872E-04
100	5.5	6.55	9.063E-03	2.152E-05	3.328E-02	3.247E-04
100	5.5	6.6	9.797E-03	2.516E-05	3.599E-02	3.800E-04
100	5.5	6.65	1.021E-02	2.732E-05	3.752E-02	4.131E-04
100	5.5	6.7	1.034E-02	2.804E-05	3.797E-02	4.233E-04
100	5.5	6.75	1.078E-02	3.048E-05	3.961E-02	4.609E-04
100	5.5	6.8	1.107E-02	3.212E-05	4.062E-02	4.849E-04
100	5.5	6.85	1.129E-02	3.340E-05	4.143E-02	5.047E-04
100	5.5	6.9	1.184E-02	3.680E-05	4.345E-02	5.555E-04
100	5.5	6.95	1.203E-02	3.797E-05	4.410E-02	5.723E-04
100	5.5	7	1.248E-02	4.090E-05	4.580E-02	6.176E-04
100	5.5	7.05	1.273E-02	4.254E-05	4.674E-02	6.434E-04
100	5.5	7.1	1.338E-02	4.699E-05	4.913E-02	7.116E-04
100	5.5	7.15	1.360E-02	4.854E-05	4.983E-02	7.321E-04
100	5.5	7.2	1.384E-02	5.031E-05	5.075E-02	7.599E-04
100	5.5	7.25	1.406E-02	5.188E-05	5.154E-02	7.839E-04
100	5.5	7.3	1.406E-02	5.188E-05	5.154E-02	7.839E-04
100	5.5	7.35	1.448E-02	5.509E-05	5.300E-02	8.292E-04
100	5.5	7.4	1.521E-02	6.081E-05	5.575E-02	9.184E-04
100	5.5	7.45	1.547E-02	6.285E-05	5.670E-02	9.505E-04
100	5.5	7.5	1.547E-02	6.285E-05	5.670E-02	9.505E-04
100	5.5	7.55	1.602E-02	6.748E-05	5.872E-02	1.020E-03
100	5.5	7.6	1.639E-02	7.059E-05	6.000E-02	1.066E-03
100	5.5	7.65	1.639E-02	7.059E-05	6.000E-02	1.066E-03
100	5.5	7.7	1.639E-02	7.059E-05	6.000E-02	1.066E-03
100	5.5	7.75	1.672E-02	7.349E-05	6.117E-02	1.108E-03
100	5.5	7.8	1.697E-02	7.572E-05	6.211E-02	1.143E-03
100	5.5	7.85	1.776E-02	8.297E-05	6.503E-02	1.254E-03
100	5.5	7.9	1.797E-02	8.494E-05	6.578E-02	1.284E-03
100	5.5	7.95	1.807E-02	8.587E-05	6.607E-02	1.295E-03
100	5.5	8	1.833E-02	8.836E-05	6.705E-02	1.334E-03
100	5.5	8.05	1.833E-02	8.836E-05	6.705E-02	1.334E-03
100	5.5	8.1	1.875E-02	9.254E-05	6.860E-02	1.397E-03
100	5.5	8.15	1.875E-02	9.254E-05	6.860E-02	1.397E-03
100	5.5	8.2	1.957E-02	1.008E-04	7.154E-02	1.522E-03
100	5.5	8.25	1.957E-02	1.008E-04	7.154E-02	1.522E-03
100	5.5	8.3	1.957E-02	1.008E-04	7.154E-02	1.522E-03
100	5.5	8.35	1.984E-02	1.036E-04	7.256E-02	1.566E-03
100	5.5	8.4	2.002E-02	1.056E-04	7.321E-02	1.594E-03
100	5.5	8.45	2.040E-02	1.096E-04	7.456E-02	1.654E-03
100	5.5	8.5	2.066E-02	1.124E-04	7.552E-02	1.698E-03
100	5.5	8.55	2.113E-02	1.176E-04	7.723E-02	1.777E-03

100	5.5	8.6	2.139E-02	1.206E-04	7.823E-02	1.824E-03
100	5.5	8.65	2.139E-02	1.206E-04	7.823E-02	1.824E-03
100	5.5	8.7	2.171E-02	1.241E-04	7.928E-02	1.874E-03
100	5.5	8.75	2.171E-02	1.241E-04	7.928E-02	1.874E-03
100	5.5	8.8	2.171E-02	1.241E-04	7.928E-02	1.874E-03
100	5.5	8.85	2.171E-02	1.241E-04	7.928E-02	1.874E-03
100	5.5	8.9	2.208E-02	1.284E-04	8.065E-02	1.940E-03
100	5.5	8.95	2.274E-02	1.363E-04	8.307E-02	2.060E-03
100	5.5	9	2.320E-02	1.418E-04	8.471E-02	2.144E-03
100	5.5	9.05	2.320E-02	1.418E-04	8.471E-02	2.144E-03
100	5.5	9.1	2.320E-02	1.418E-04	8.471E-02	2.144E-03
100	5.5	9.15	2.347E-02	1.452E-04	8.574E-02	2.197E-03
100	5.5	9.2	2.347E-02	1.452E-04	8.574E-02	2.197E-03
100	5.5	9.25	2.360E-02	1.469E-04	8.616E-02	2.219E-03
100	5.5	9.3	2.385E-02	1.499E-04	8.704E-02	2.265E-03
100	5.5	9.35	2.406E-02	1.526E-04	8.778E-02	2.305E-03
100	5.5	9.4	2.406E-02	1.526E-04	8.778E-02	2.305E-03
100	5.5	9.45	2.459E-02	1.595E-04	8.977E-02	2.412E-03
100	5.5	9.5	2.459E-02	1.595E-04	8.977E-02	2.412E-03
100	5.5	9.55	2.473E-02	1.613E-04	9.022E-02	2.437E-03
100	5.5	9.6	2.501E-02	1.650E-04	9.128E-02	2.495E-03
100	5.5	9.65	2.501E-02	1.650E-04	9.128E-02	2.495E-03
100	5.5	9.7	2.501E-02	1.650E-04	9.128E-02	2.495E-03
100	5.5	9.75	2.576E-02	1.751E-04	9.402E-02	2.650E-03
100	5.5	9.8	2.576E-02	1.751E-04	9.402E-02	2.650E-03
100	5.5	9.85	2.576E-02	1.751E-04	9.402E-02	2.650E-03
100	5.5	9.9	2.591E-02	1.772E-04	9.450E-02	2.678E-03
100	5.5	9.95	2.618E-02	1.809E-04	9.550E-02	2.736E-03
100	5.5	10	2.646E-02	1.848E-04	9.655E-02	2.797E-03

Table A.7: Comparison of MIs of cuboid with  $n = 6$  to MIs of cuboids from 6.05 to 10 using the Euclidean distance and the chi-squared distance.

length (pixels)	shape 1	shape 2	$\bar{\omega}_i$ Euc-dist	$\bar{\omega}_i$ CSD	$\bar{\tau}_i$ Euc-dist	$\bar{\tau}_i$ CSD
60	6	6.05	3.216E-04	2.710E-08	1.240E-03	4.498E-07
60	6	6.1	1.555E-03	6.337E-07	5.681E-03	9.474E-06
60	6	6.15	2.142E-03	1.204E-06	7.891E-03	1.829E-05
60	6	6.2	2.142E-03	1.204E-06	7.891E-03	1.829E-05
60	6	6.25	3.314E-03	2.881E-06	1.228E-02	4.438E-05
60	6	6.3	3.314E-03	2.881E-06	1.228E-02	4.438E-05
60	6	6.35	3.519E-03	3.250E-06	1.289E-02	4.894E-05
60	6	6.4	3.967E-03	4.130E-06	1.448E-02	6.177E-05
60	6	6.45	3.967E-03	4.130E-06	1.448E-02	6.177E-05

60	6	6.5	3.967E-03	4.130E-06	1.448E-02	6.177E-05
60	6	6.55	4.593E-03	5.537E-06	1.685E-02	8.369E-05
60	6	6.6	5.501E-03	7.945E-06	2.014E-02	1.197E-04
60	6	6.65	6.073E-03	9.686E-06	2.225E-02	1.462E-04
60	6	6.7	6.073E-03	9.686E-06	2.225E-02	1.462E-04
60	6	6.75	7.214E-03	1.368E-05	2.646E-02	2.071E-04
60	6	6.8	7.214E-03	1.368E-05	2.646E-02	2.071E-04
60	6	6.85	7.214E-03	1.368E-05	2.646E-02	2.071E-04
60	6	6.9	7.483E-03	1.472E-05	2.730E-02	2.206E-04
60	6	6.95	7.483E-03	1.472E-05	2.730E-02	2.206E-04
60	6	7	8.141E-03	1.742E-05	2.979E-02	2.628E-04
60	6	7.05	8.750E-03	2.013E-05	3.204E-02	3.043E-04
60	6	7.1	9.265E-03	2.258E-05	3.388E-02	3.405E-04
60	6	7.15	9.265E-03	2.258E-05	3.388E-02	3.405E-04
60	6	7.2	9.265E-03	2.258E-05	3.388E-02	3.405E-04
60	6	7.25	9.914E-03	2.586E-05	3.616E-02	3.881E-04
60	6	7.3	1.061E-02	2.962E-05	3.879E-02	4.471E-04
60	6	7.35	1.061E-02	2.962E-05	3.879E-02	4.471E-04
60	6	7.4	1.061E-02	2.962E-05	3.879E-02	4.471E-04
60	6	7.45	1.061E-02	2.962E-05	3.879E-02	4.471E-04
	6	7.5	0.0106088	2.96E-05	0.038788	0.00044712
60	6	7.55	1.181E-02	3.670E-05	4.317E-02	5.548E-04
60	6	7.6	1.282E-02	4.331E-05	4.680E-02	6.528E-04
60	6	7.65	1.282E-02	4.331E-05	4.680E-02	6.528E-04
60	6	7.7	1.282E-02	4.331E-05	4.680E-02	6.528E-04
60	6	7.75	1.282E-02	4.331E-05	4.680E-02	6.528E-04
60	6	7.8	1.282E-02	4.331E-05	4.680E-02	6.528E-04
60	6	7.85	1.282E-02	4.331E-05	4.680E-02	6.528E-04
60	6	7.9	1.282E-02	4.331E-05	4.680E-02	6.528E-04
60	6	7.95	1.282E-02	4.331E-05	4.680E-02	6.528E-04
60	6	8	1.451E-02	5.549E-05	5.289E-02	8.358E-04
60	6	8.05	1.451E-02	5.549E-05	5.289E-02	8.358E-04
60	6	8.1	1.519E-02	6.081E-05	5.540E-02	9.179E-04
60	6	8.15	1.519E-02	6.081E-05	5.540E-02	9.179E-04
60	6	8.2	1.519E-02	6.081E-05	5.540E-02	9.179E-04
60	6	8.25	1.591E-02	6.675E-05	5.812E-02	1.011E-03
60	6	8.3	1.591E-02	6.675E-05	5.812E-02	1.011E-03
60	6	8.35	1.591E-02	6.675E-05	5.812E-02	1.011E-03
60	6	8.4	1.631E-02	7.017E-05	5.943E-02	1.058E-03
60	6	8.45	1.631E-02	7.017E-05	5.943E-02	1.058E-03
60	6	8.5	1.631E-02	7.017E-05	5.943E-02	1.058E-03
60	6	8.55	1.693E-02	7.565E-05	6.168E-02	1.140E-03
60	6	8.6	1.693E-02	7.565E-05	6.168E-02	1.140E-03
60	6	8.65	1.693E-02	7.565E-05	6.168E-02	1.140E-03

60	6	8.7	1.693E-02	7.565E-05	6.168E-02	1.140E-03
60	6	8.75	1.765E-02	8.221E-05	6.436E-02	1.243E-03
60	6	8.8	1.765E-02	8.221E-05	6.436E-02	1.243E-03
60	6	8.85	1.809E-02	8.635E-05	6.581E-02	1.300E-03
60	6	8.9	1.847E-02	9.003E-05	6.724E-02	1.358E-03
60	6	8.95	1.847E-02	9.003E-05	6.724E-02	1.358E-03
60	6	9	1.847E-02	9.003E-05	6.724E-02	1.358E-03
60	6	9.05	1.922E-02	9.761E-05	7.010E-02	1.477E-03
60	6	9.1	1.922E-02	9.761E-05	7.010E-02	1.477E-03
60	6	9.15	1.988E-02	1.044E-04	7.249E-02	1.581E-03
60	6	9.2	1.988E-02	1.044E-04	7.249E-02	1.581E-03
60	6	9.25	1.988E-02	1.044E-04	7.249E-02	1.581E-03
60	6	9.3	1.988E-02	1.044E-04	7.249E-02	1.581E-03
60	6	9.35	1.988E-02	1.044E-04	7.249E-02	1.581E-03
60	6	9.4	2.036E-02	1.095E-04	7.407E-02	1.652E-03
60	6	9.45	2.036E-02	1.095E-04	7.407E-02	1.652E-03
60	6	9.5	2.036E-02	1.095E-04	7.407E-02	1.652E-03
60	6	9.55	2.036E-02	1.095E-04	7.407E-02	1.652E-03
60	6	9.6	2.111E-02	1.178E-04	7.687E-02	1.781E-03
60	6	9.65	2.111E-02	1.178E-04	7.687E-02	1.781E-03
60	6	9.7	2.111E-02	1.178E-04	7.687E-02	1.781E-03
60	6	9.75	2.111E-02	1.178E-04	7.687E-02	1.781E-03
60	6	9.8	2.111E-02	1.178E-04	7.687E-02	1.781E-03
60	6	9.85	2.111E-02	1.178E-04	7.687E-02	1.781E-03
60	6	9.9	2.181E-02	1.257E-04	7.943E-02	1.904E-03
60	6	9.95	2.232E-02	1.317E-04	8.115E-02	1.988E-03
60	6	10	2.232E-02	1.317E-04	8.115E-02	1.988E-03
100	6	6.05	0.000E+00	0.000E+00	0.000E+00	0.000E+00
100	6	6.1	9.791E-04	2.514E-07	3.650E-03	3.912E-06
100	6	6.15	1.208E-03	3.825E-07	4.445E-03	5.805E-06
100	6	6.2	1.546E-03	6.271E-07	5.680E-03	9.484E-06
100	6	6.25	1.822E-03	8.707E-07	6.694E-03	1.318E-05
100	6	6.3	2.495E-03	1.633E-06	9.166E-03	2.472E-05
100	6	6.35	3.275E-03	2.814E-06	1.206E-02	4.281E-05
100	6	6.4	3.275E-03	2.814E-06	1.206E-02	4.281E-05
100	6	6.45	3.716E-03	3.625E-06	1.363E-02	5.479E-05
100	6	6.5	3.716E-03	3.625E-06	1.363E-02	5.479E-05
100	6	6.55	4.257E-03	4.759E-06	1.560E-02	7.182E-05
100	6	6.6	4.991E-03	6.543E-06	1.831E-02	9.901E-05
100	6	6.65	5.402E-03	7.667E-06	1.984E-02	1.163E-04
100	6	6.7	5.537E-03	8.053E-06	2.029E-02	1.217E-04
100	6	6.75	5.976E-03	9.382E-06	2.193E-02	1.422E-04
100	6	6.8	6.261E-03	1.030E-05	2.294E-02	1.557E-04

100	6	6.85	6.479E-03	1.103E-05	2.375E-02	1.670E-04
100	6	6.9	7.038E-03	1.302E-05	2.577E-02	1.967E-04
100	6	6.95	7.225E-03	1.372E-05	2.642E-02	2.067E-04
100	6	7	7.679E-03	1.550E-05	2.812E-02	2.343E-04
100	6	7.05	7.926E-03	1.652E-05	2.906E-02	2.503E-04
100	6	7.1	8.574E-03	1.934E-05	3.145E-02	2.935E-04
100	6	7.15	8.791E-03	2.033E-05	3.215E-02	3.068E-04
100	6	7.2	9.036E-03	2.148E-05	3.307E-02	3.248E-04
100	6	7.25	9.250E-03	2.252E-05	3.386E-02	3.406E-04
100	6	7.3	9.250E-03	2.252E-05	3.386E-02	3.406E-04
100	6	7.35	9.677E-03	2.465E-05	3.532E-02	3.707E-04
100	6	7.4	1.041E-02	2.852E-05	3.807E-02	4.311E-04
100	6	7.45	1.066E-02	2.992E-05	3.902E-02	4.532E-04
100	6	7.5	1.066E-02	2.992E-05	3.902E-02	4.532E-04
100	6	7.55	1.122E-02	3.314E-05	4.104E-02	5.015E-04
100	6	7.6	1.158E-02	3.533E-05	4.232E-02	5.336E-04
100	6	7.65	1.158E-02	3.533E-05	4.232E-02	5.336E-04
100	6	7.7	1.158E-02	3.533E-05	4.232E-02	5.336E-04
100	6	7.75	1.191E-02	3.739E-05	4.349E-02	5.638E-04
100	6	7.8	1.217E-02	3.899E-05	4.443E-02	5.887E-04
100	6	7.85	1.296E-02	4.424E-05	4.735E-02	6.693E-04
100	6	7.9	1.317E-02	4.568E-05	4.810E-02	6.909E-04
100	6	7.95	1.326E-02	4.636E-05	4.839E-02	6.994E-04
100	6	8	1.352E-02	4.819E-05	4.937E-02	7.282E-04
100	6	8.05	1.352E-02	4.819E-05	4.937E-02	7.282E-04
100	6	8.1	1.395E-02	5.129E-05	5.092E-02	7.750E-04
100	6	8.15	1.395E-02	5.129E-05	5.092E-02	7.750E-04
100	6	8.2	1.476E-02	5.749E-05	5.387E-02	8.683E-04
100	6	8.25	1.476E-02	5.749E-05	5.387E-02	8.683E-04
100	6	8.3	1.476E-02	5.749E-05	5.387E-02	8.683E-04
100	6	8.35	1.503E-02	5.961E-05	5.488E-02	9.016E-04
100	6	8.4	1.522E-02	6.110E-05	5.553E-02	9.233E-04
100	6	8.45	1.560E-02	6.418E-05	5.688E-02	9.693E-04
100	6	8.5	1.585E-02	6.632E-05	5.784E-02	1.003E-03
100	6	8.55	1.632E-02	7.032E-05	5.956E-02	1.064E-03
100	6	8.6	1.659E-02	7.263E-05	6.055E-02	1.100E-03
100	6	8.65	1.659E-02	7.263E-05	6.055E-02	1.100E-03
100	6	8.7	1.690E-02	7.540E-05	6.160E-02	1.139E-03
100	6	8.75	1.690E-02	7.540E-05	6.160E-02	1.139E-03
100	6	8.8	1.690E-02	7.540E-05	6.160E-02	1.139E-03
100	6	8.85	1.690E-02	7.540E-05	6.160E-02	1.139E-03
100	6	8.9	1.727E-02	7.877E-05	6.297E-02	1.191E-03
100	6	8.95	1.794E-02	8.497E-05	6.539E-02	1.285E-03
100	6	9	1.839E-02	8.934E-05	6.703E-02	1.351E-03

100	6	9.05	1.839E-02	8.934E-05	6.703E-02	1.351E-03
100	6	9.1	1.839E-02	8.934E-05	6.703E-02	1.351E-03
100	6	9.15	1.866E-02	9.203E-05	6.806E-02	1.393E-03
100	6	9.2	1.866E-02	9.203E-05	6.806E-02	1.393E-03
100	6	9.25	1.880E-02	9.336E-05	6.848E-02	1.411E-03
100	6	9.3	1.904E-02	9.578E-05	6.936E-02	1.448E-03
100	6	9.35	1.925E-02	9.791E-05	7.010E-02	1.480E-03
100	6	9.4	1.925E-02	9.791E-05	7.010E-02	1.480E-03
100	6	9.45	1.978E-02	1.034E-04	7.209E-02	1.566E-03
100	6	9.5	1.978E-02	1.034E-04	7.209E-02	1.566E-03
100	6	9.55	1.992E-02	1.049E-04	7.254E-02	1.586E-03
100	6	9.6	2.021E-02	1.079E-04	7.360E-02	1.633E-03
100	6	9.65	2.021E-02	1.079E-04	7.360E-02	1.633E-03
100	6	9.7	2.021E-02	1.079E-04	7.360E-02	1.633E-03
100	6	9.75	2.095E-02	1.161E-04	7.634E-02	1.759E-03
100	6	9.8	2.095E-02	1.161E-04	7.634E-02	1.759E-03
100	6	9.85	2.095E-02	1.161E-04	7.634E-02	1.759E-03
100	6	9.9	2.110E-02	1.178E-04	7.683E-02	1.781E-03
100	6	9.95	2.137E-02	1.208E-04	7.783E-02	1.829E-03
100	6	10	2.165E-02	1.240E-04	7.887E-02	1.879E-03

Table A.8: Comparison of MIs of cuboid with  $n = 6.5$  to MIs of cuboids from 6.55 to 10 using the Euclidean distance and the chi-squared distance.

length (pixels)	shape 1	shape 2	$\bar{\omega}_i$ Euc-dist	$\bar{\omega}_i$ CSD	$\bar{\tau}_i$ Euc-dist	$\bar{\tau}_i$ CSD
60	6.5	6.55	6.260E-04	1.030E-07	2.369E-03	1.661E-06
60	6.5	6.6	1.534E-03	6.186E-07	5.657E-03	9.493E-06
60	6.5	6.65	2.106E-03	1.167E-06	7.769E-03	1.792E-05
60	6.5	6.7	2.106E-03	1.167E-06	7.769E-03	1.792E-05
60	6.5	6.75	3.247E-03	2.775E-06	1.198E-02	4.268E-05
60	6.5	6.8	3.247E-03	2.775E-06	1.198E-02	4.268E-05
60	6.5	6.85	3.247E-03	2.775E-06	1.198E-02	4.268E-05
60	6.5	6.9	3.516E-03	3.254E-06	1.282E-02	4.889E-05
60	6.5	6.95	3.516E-03	3.254E-06	1.282E-02	4.889E-05
60	6.5	7	4.174E-03	4.588E-06	1.530E-02	6.974E-05
60	6.5	7.05	4.783E-03	6.025E-06	1.756E-02	9.188E-05
60	6.5	7.1	5.298E-03	7.394E-06	1.940E-02	1.122E-04
60	6.5	7.15	5.298E-03	7.394E-06	1.940E-02	1.122E-04
60	6.5	7.2	5.298E-03	7.394E-06	1.940E-02	1.122E-04
60	6.5	7.25	5.947E-03	9.319E-06	2.167E-02	1.402E-04
60	6.5	7.3	6.642E-03	1.163E-05	2.431E-02	1.765E-04
60	6.5	7.35	6.642E-03	1.163E-05	2.431E-02	1.765E-04
60	6.5	7.4	6.642E-03	1.163E-05	2.431E-02	1.765E-04

60	6.5	7.45	6.642E-03	1.163E-05	2.431E-02	1.765E-04
60	6.5	7.5	6.642E-03	1.163E-05	2.431E-02	1.765E-04
60	6.5	7.55	7.839E-03	1.621E-05	2.869E-02	2.464E-04
60	6.5	7.6	8.856E-03	2.069E-05	3.232E-02	3.130E-04
60	6.5	7.65	8.856E-03	2.069E-05	3.232E-02	3.130E-04
60	6.5	7.7	8.856E-03	2.069E-05	3.232E-02	3.130E-04
60	6.5	7.75	8.856E-03	2.069E-05	3.232E-02	3.130E-04
60	6.5	7.8	8.856E-03	2.069E-05	3.232E-02	3.130E-04
60	6.5	7.85	8.856E-03	2.069E-05	3.232E-02	3.130E-04
60	6.5	7.9	8.856E-03	2.069E-05	3.232E-02	3.130E-04
60	6.5	7.95	8.856E-03	2.069E-05	3.232E-02	3.130E-04
60	6.5	8	1.054E-02	2.935E-05	3.841E-02	4.432E-04
60	6.5	8.05	1.054E-02	2.935E-05	3.841E-02	4.432E-04
60	6.5	8.1	1.122E-02	3.324E-05	4.092E-02	5.035E-04
60	6.5	8.15	1.122E-02	3.324E-05	4.092E-02	5.035E-04
60	6.5	8.2	1.122E-02	3.324E-05	4.092E-02	5.035E-04
60	6.5	8.25	1.194E-02	3.767E-05	4.364E-02	5.730E-04
60	6.5	8.3	1.194E-02	3.767E-05	4.364E-02	5.730E-04
60	6.5	8.35	1.194E-02	3.767E-05	4.364E-02	5.730E-04
60	6.5	8.4	1.234E-02	4.025E-05	4.495E-02	6.083E-04
60	6.5	8.45	1.234E-02	4.025E-05	4.495E-02	6.083E-04
60	6.5	8.5	1.234E-02	4.025E-05	4.495E-02	6.083E-04
60	6.5	8.55	1.297E-02	4.443E-05	4.720E-02	6.715E-04
60	6.5	8.6	1.297E-02	4.443E-05	4.720E-02	6.715E-04
60	6.5	8.65	1.297E-02	4.443E-05	4.720E-02	6.715E-04
60	6.5	8.7	1.297E-02	4.443E-05	4.720E-02	6.715E-04
60	6.5	8.75	1.368E-02	4.949E-05	4.988E-02	7.504E-04
60	6.5	8.8	1.368E-02	4.949E-05	4.988E-02	7.504E-04
60	6.5	8.85	1.412E-02	5.271E-05	5.133E-02	7.952E-04
60	6.5	8.9	1.450E-02	5.560E-05	5.276E-02	8.407E-04
60	6.5	8.95	1.450E-02	5.560E-05	5.276E-02	8.407E-04
60	6.5	9	1.450E-02	5.560E-05	5.276E-02	8.407E-04
60	6.5	9.05	1.526E-02	6.159E-05	5.562E-02	9.350E-04
60	6.5	9.1	1.526E-02	6.159E-05	5.562E-02	9.350E-04
60	6.5	9.15	1.592E-02	6.704E-05	5.801E-02	1.018E-03
60	6.5	9.2	1.592E-02	6.704E-05	5.801E-02	1.018E-03
60	6.5	9.25	1.592E-02	6.704E-05	5.801E-02	1.018E-03
60	6.5	9.3	1.592E-02	6.704E-05	5.801E-02	1.018E-03
60	6.5	9.35	1.592E-02	6.704E-05	5.801E-02	1.018E-03
60	6.5	9.4	1.639E-02	7.109E-05	5.959E-02	1.075E-03
60	6.5	9.45	1.639E-02	7.109E-05	5.959E-02	1.075E-03
60	6.5	9.5	1.639E-02	7.109E-05	5.959E-02	1.075E-03
60	6.5	9.55	1.639E-02	7.109E-05	5.959E-02	1.075E-03
60	6.5	9.6	1.714E-02	7.778E-05	6.239E-02	1.180E-03

60	6.5	9.65	1.714E-02	7.778E-05	6.239E-02	1.180E-03
60	6.5	9.7	1.714E-02	7.778E-05	6.239E-02	1.180E-03
60	6.5	9.75	1.714E-02	7.778E-05	6.239E-02	1.180E-03
60	6.5	9.8	1.714E-02	7.778E-05	6.239E-02	1.180E-03
60	6.5	9.85	1.714E-02	7.778E-05	6.239E-02	1.180E-03
60	6.5	9.9	1.784E-02	8.429E-05	6.495E-02	1.280E-03
60	6.5	9.95	1.835E-02	8.919E-05	6.667E-02	1.350E-03
60	6.5	10	1.835E-02	8.919E-05	6.667E-02	1.350E-03
100	6.5	6.55	5.415E-04	7.711E-08	1.969E-03	1.150E-06
100	6.5	6.6	1.275E-03	4.277E-07	4.678E-03	6.495E-06
100	6.5	6.65	1.687E-03	7.484E-07	6.203E-03	1.143E-05
100	6.5	6.7	1.821E-03	8.722E-07	6.657E-03	1.316E-05
100	6.5	6.75	2.260E-03	1.344E-06	8.298E-03	2.046E-05
100	6.5	6.8	2.545E-03	1.705E-06	9.308E-03	2.576E-05
100	6.5	6.85	2.764E-03	2.010E-06	1.012E-02	3.047E-05
100	6.5	6.9	3.322E-03	2.905E-06	1.214E-02	4.387E-05
100	6.5	6.95	3.509E-03	3.242E-06	1.279E-02	4.868E-05
100	6.5	7	3.963E-03	4.136E-06	1.449E-02	6.251E-05
100	6.5	7.05	4.210E-03	4.668E-06	1.542E-02	7.089E-05
100	6.5	7.1	4.858E-03	6.217E-06	1.782E-02	9.470E-05
100	6.5	7.15	5.075E-03	6.786E-06	1.851E-02	1.023E-04
100	6.5	7.2	5.320E-03	7.458E-06	1.944E-02	1.128E-04
100	6.5	7.25	5.535E-03	8.072E-06	2.023E-02	1.222E-04
100	6.5	7.3	5.535E-03	8.072E-06	2.023E-02	1.222E-04
100	6.5	7.35	5.962E-03	9.367E-06	2.168E-02	1.405E-04
100	6.5	7.4	6.692E-03	1.181E-05	2.443E-02	1.785E-04
100	6.5	7.45	6.945E-03	1.272E-05	2.539E-02	1.928E-04
100	6.5	7.5	6.945E-03	1.272E-05	2.539E-02	1.928E-04
100	6.5	7.55	7.503E-03	1.485E-05	2.740E-02	2.248E-04
100	6.5	7.6	7.866E-03	1.632E-05	2.869E-02	2.465E-04
100	6.5	7.65	7.866E-03	1.632E-05	2.869E-02	2.465E-04
100	6.5	7.7	7.866E-03	1.632E-05	2.869E-02	2.465E-04
100	6.5	7.75	8.198E-03	1.773E-05	2.985E-02	2.671E-04
100	6.5	7.8	8.449E-03	1.884E-05	3.080E-02	2.843E-04
100	6.5	7.85	9.240E-03	2.254E-05	3.372E-02	3.411E-04
100	6.5	7.9	9.449E-03	2.357E-05	3.447E-02	3.566E-04
100	6.5	7.95	9.546E-03	2.406E-05	3.476E-02	3.627E-04
100	6.5	8	9.805E-03	2.538E-05	3.574E-02	3.835E-04
100	6.5	8.05	9.805E-03	2.538E-05	3.574E-02	3.835E-04
100	6.5	8.1	1.023E-02	2.765E-05	3.729E-02	4.177E-04
100	6.5	8.15	1.023E-02	2.765E-05	3.729E-02	4.177E-04
100	6.5	8.2	1.105E-02	3.225E-05	4.023E-02	4.869E-04
100	6.5	8.25	1.105E-02	3.225E-05	4.023E-02	4.869E-04

100	6.5	8.3	1.105E-02	3.225E-05	4.023E-02	4.869E-04
100	6.5	8.35	1.132E-02	3.383E-05	4.125E-02	5.119E-04
100	6.5	8.4	1.150E-02	3.496E-05	4.190E-02	5.283E-04
100	6.5	8.45	1.188E-02	3.730E-05	4.325E-02	5.633E-04
100	6.5	8.5	1.214E-02	3.893E-05	4.421E-02	5.887E-04
100	6.5	8.55	1.261E-02	4.201E-05	4.592E-02	6.357E-04
100	6.5	8.6	1.287E-02	4.381E-05	4.692E-02	6.639E-04
100	6.5	8.65	1.287E-02	4.381E-05	4.692E-02	6.639E-04
100	6.5	8.7	1.319E-02	4.596E-05	4.797E-02	6.941E-04
100	6.5	8.75	1.319E-02	4.596E-05	4.797E-02	6.941E-04
100	6.5	8.8	1.319E-02	4.596E-05	4.797E-02	6.941E-04
100	6.5	8.85	1.319E-02	4.596E-05	4.797E-02	6.941E-04
100	6.5	8.9	1.356E-02	4.860E-05	4.934E-02	7.348E-04
100	6.5	8.95	1.422E-02	5.350E-05	5.176E-02	8.094E-04
100	6.5	9	1.468E-02	5.698E-05	5.340E-02	8.619E-04
100	6.5	9.05	1.468E-02	5.698E-05	5.340E-02	8.619E-04
100	6.5	9.1	1.468E-02	5.698E-05	5.340E-02	8.619E-04
100	6.5	9.15	1.495E-02	5.912E-05	5.443E-02	8.957E-04
100	6.5	9.2	1.495E-02	5.912E-05	5.443E-02	8.957E-04
100	6.5	9.25	1.508E-02	6.019E-05	5.485E-02	9.099E-04
100	6.5	9.3	1.532E-02	6.214E-05	5.573E-02	9.397E-04
100	6.5	9.35	1.553E-02	6.386E-05	5.647E-02	9.651E-04
100	6.5	9.4	1.553E-02	6.386E-05	5.647E-02	9.651E-04
100	6.5	9.45	1.607E-02	6.833E-05	5.846E-02	1.035E-03
100	6.5	9.5	1.607E-02	6.833E-05	5.846E-02	1.035E-03
100	6.5	9.55	1.621E-02	6.955E-05	5.891E-02	1.051E-03
100	6.5	9.6	1.649E-02	7.199E-05	5.997E-02	1.090E-03
100	6.5	9.65	1.649E-02	7.199E-05	5.997E-02	1.090E-03
100	6.5	9.7	1.649E-02	7.199E-05	5.997E-02	1.090E-03
100	6.5	9.75	1.724E-02	7.870E-05	6.271E-02	1.193E-03
100	6.5	9.8	1.724E-02	7.870E-05	6.271E-02	1.193E-03
100	6.5	9.85	1.724E-02	7.870E-05	6.271E-02	1.193E-03
100	6.5	9.9	1.739E-02	8.008E-05	6.319E-02	1.212E-03
100	6.5	9.95	1.766E-02	8.259E-05	6.419E-02	1.251E-03
100	6.5	10	1.794E-02	8.523E-05	6.524E-02	1.292E-03

Table A.9: Comparison of MIs of cuboid with  $n = 7$  to MIs of cuboids from 7.05 to 10 using the Euclidean distance and the chi-squared distance.

length (pixels)	shape 1	shape 2	$\bar{\omega}_i$ Euc-dist	$\bar{\omega}_i$ CSD	$\bar{\tau}_i$ Euc-dist	$\bar{\tau}_i$ CSD
60	7	7.05	6.085E-04	9.770E-08	2.255E-03	1.524E-06
60	7	7.1	1.124E-03	3.332E-07	4.095E-03	5.031E-06
60	7	7.15	1.124E-03	3.332E-07	4.095E-03	5.031E-06

60	7	7.2	1.124E-03	3.332E-07	4.095E-03	5.031E-06
60	7	7.25	1.773E-03	8.296E-07	6.370E-03	1.219E-05
60	7	7.3	2.468E-03	1.608E-06	9.003E-03	2.436E-05
60	7	7.35	2.468E-03	1.608E-06	9.003E-03	2.436E-05
60	7	7.4	2.468E-03	1.608E-06	9.003E-03	2.436E-05
60	7	7.45	2.468E-03	1.608E-06	9.003E-03	2.436E-05
60	7	7.5	2.468E-03	1.608E-06	9.003E-03	2.436E-05
60	7	7.55	3.665E-03	3.549E-06	1.339E-02	5.395E-05
60	7	7.6	4.682E-03	5.794E-06	1.701E-02	8.727E-05
60	7	7.65	4.682E-03	5.794E-06	1.701E-02	8.727E-05
60	7	7.7	4.682E-03	5.794E-06	1.701E-02	8.727E-05
60	7	7.75	4.682E-03	5.794E-06	1.701E-02	8.727E-05
60	7	7.8	4.682E-03	5.794E-06	1.701E-02	8.727E-05
60	7	7.85	4.682E-03	5.794E-06	1.701E-02	8.727E-05
60	7	7.9	4.682E-03	5.794E-06	1.701E-02	8.727E-05
60	7	7.95	4.682E-03	5.794E-06	1.701E-02	8.727E-05
60	7	8	6.368E-03	1.073E-05	2.311E-02	1.613E-04
60	7	8.05	6.368E-03	1.073E-05	2.311E-02	1.613E-04
60	7	8.1	7.045E-03	1.313E-05	2.562E-02	1.985E-04
60	7	8.15	7.045E-03	1.313E-05	2.562E-02	1.985E-04
60	7	8.2	7.045E-03	1.313E-05	2.562E-02	1.985E-04
60	7	8.25	7.768E-03	1.597E-05	2.833E-02	2.430E-04
60	7	8.3	7.768E-03	1.597E-05	2.833E-02	2.430E-04
60	7	8.35	7.768E-03	1.597E-05	2.833E-02	2.430E-04
60	7	8.4	8.168E-03	1.766E-05	2.964E-02	2.662E-04
60	7	8.45	8.168E-03	1.766E-05	2.964E-02	2.662E-04
60	7	8.5	8.168E-03	1.766E-05	2.964E-02	2.662E-04
60	7	8.55	8.791E-03	2.046E-05	3.190E-02	3.085E-04
60	7	8.6	8.791E-03	2.046E-05	3.190E-02	3.085E-04
60	7	8.65	8.791E-03	2.046E-05	3.190E-02	3.085E-04
60	7	8.7	8.791E-03	2.046E-05	3.190E-02	3.085E-04
60	7	8.75	9.507E-03	2.394E-05	3.457E-02	3.627E-04
60	7	8.8	9.507E-03	2.394E-05	3.457E-02	3.627E-04
60	7	8.85	9.944E-03	2.620E-05	3.602E-02	3.940E-04
60	7	8.9	1.032E-02	2.824E-05	3.746E-02	4.262E-04
60	7	8.95	1.032E-02	2.824E-05	3.746E-02	4.262E-04
60	7	9	1.032E-02	2.824E-05	3.746E-02	4.262E-04
60	7	9.05	1.108E-02	3.256E-05	4.031E-02	4.941E-04
60	7	9.1	1.108E-02	3.256E-05	4.031E-02	4.941E-04
60	7	9.15	1.174E-02	3.655E-05	4.270E-02	5.549E-04
60	7	9.2	1.174E-02	3.655E-05	4.270E-02	5.549E-04
60	7	9.25	1.174E-02	3.655E-05	4.270E-02	5.549E-04
60	7	9.3	1.174E-02	3.655E-05	4.270E-02	5.549E-04
60	7	9.35	1.174E-02	3.655E-05	4.270E-02	5.549E-04

60	7	9.4	1.221E-02	3.956E-05	4.428E-02	5.972E-04
60	7	9.45	1.221E-02	3.956E-05	4.428E-02	5.972E-04
60	7	9.5	1.221E-02	3.956E-05	4.428E-02	5.972E-04
60	7	9.55	1.221E-02	3.956E-05	4.428E-02	5.972E-04
60	7	9.6	1.297E-02	4.459E-05	4.709E-02	6.759E-04
60	7	9.65	1.297E-02	4.459E-05	4.709E-02	6.759E-04
60	7	9.7	1.297E-02	4.459E-05	4.709E-02	6.759E-04
60	7	9.75	1.297E-02	4.459E-05	4.709E-02	6.759E-04
60	7	9.8	1.297E-02	4.459E-05	4.709E-02	6.759E-04
60	7	9.85	1.297E-02	4.459E-05	4.709E-02	6.759E-04
60	7	9.9	1.367E-02	4.955E-05	4.965E-02	7.521E-04
60	7	9.95	1.417E-02	5.332E-05	5.137E-02	8.058E-04
60	7	10	1.417E-02	5.332E-05	5.137E-02	8.058E-04
60	7	7.05	2.469E-04	1.608E-08	9.389E-04	2.638E-07
60	7	7.1	8.950E-04	2.114E-07	3.334E-03	3.331E-06
60	7	7.15	1.112E-03	3.264E-07	4.029E-03	4.871E-06
60	7	7.2	1.357E-03	4.862E-07	4.956E-03	7.370E-06
60	7	7.25	1.572E-03	6.520E-07	5.744E-03	9.904E-06
60	7	7.3	1.572E-03	6.520E-07	5.744E-03	9.904E-06
60	7	7.35	1.999E-03	1.055E-06	7.198E-03	1.557E-05
60	7	7.4	2.729E-03	1.967E-06	9.948E-03	2.975E-05
60	7	7.45	2.982E-03	2.349E-06	1.091E-02	3.577E-05
60	7	7.5	2.982E-03	2.349E-06	1.091E-02	3.577E-05
60	7	7.55	3.540E-03	3.310E-06	1.292E-02	5.023E-05
60	7	7.6	3.904E-03	4.026E-06	1.420E-02	6.073E-05
60	7	7.65	3.904E-03	4.026E-06	1.420E-02	6.073E-05
60	7	7.7	3.904E-03	4.026E-06	1.420E-02	6.073E-05
60	7	7.75	4.235E-03	4.740E-06	1.537E-02	7.117E-05
60	7	7.8	4.486E-03	5.319E-06	1.631E-02	8.021E-05
60	7	7.85	5.277E-03	7.363E-06	1.923E-02	1.116E-04
60	7	7.9	5.486E-03	7.958E-06	1.998E-02	1.205E-04
60	7	7.95	5.583E-03	8.243E-06	2.027E-02	1.241E-04
60	7	8	5.843E-03	9.027E-06	2.125E-02	1.364E-04
60	7	8.05	5.843E-03	9.027E-06	2.125E-02	1.364E-04
60	7	8.1	6.270E-03	1.040E-05	2.280E-02	1.571E-04
60	7	8.15	6.270E-03	1.040E-05	2.280E-02	1.571E-04
60	7	8.2	7.086E-03	1.329E-05	2.575E-02	2.005E-04
60	7	8.25	7.086E-03	1.329E-05	2.575E-02	2.005E-04
60	7	8.3	7.086E-03	1.329E-05	2.575E-02	2.005E-04
60	7	8.35	7.354E-03	1.431E-05	2.676E-02	2.167E-04
60	7	8.4	7.540E-03	1.505E-05	2.741E-02	2.274E-04
60	7	8.45	7.919E-03	1.660E-05	2.876E-02	2.505E-04
60	7	8.5	8.175E-03	1.769E-05	2.972E-02	2.675E-04

60	7	8.55	8.645E-03	1.979E-05	3.144E-02	2.996E-04
60	7	8.6	8.910E-03	2.102E-05	3.244E-02	3.190E-04
60	7	8.65	8.910E-03	2.102E-05	3.244E-02	3.190E-04
60	7	8.7	9.223E-03	2.252E-05	3.348E-02	3.400E-04
60	7	8.75	9.223E-03	2.252E-05	3.348E-02	3.400E-04
60	7	8.8	9.223E-03	2.252E-05	3.348E-02	3.400E-04
60	7	8.85	9.223E-03	2.252E-05	3.348E-02	3.400E-04
60	7	8.9	9.594E-03	2.438E-05	3.486E-02	3.687E-04
60	7	8.95	1.026E-02	2.788E-05	3.728E-02	4.221E-04
60	7	9	1.071E-02	3.041E-05	3.892E-02	4.603E-04
60	7	9.05	1.071E-02	3.041E-05	3.892E-02	4.603E-04
60	7	9.1	1.071E-02	3.041E-05	3.892E-02	4.603E-04
60	7	9.15	1.099E-02	3.199E-05	3.994E-02	4.851E-04
60	7	9.2	1.099E-02	3.199E-05	3.994E-02	4.851E-04
60	7	9.25	1.112E-02	3.277E-05	4.037E-02	4.955E-04
60	7	9.3	1.136E-02	3.421E-05	4.125E-02	5.175E-04
60	7	9.35	1.157E-02	3.549E-05	4.199E-02	5.364E-04
60	7	9.4	1.157E-02	3.549E-05	4.199E-02	5.364E-04
60	7	9.45	1.210E-02	3.885E-05	4.397E-02	5.888E-04
60	7	9.5	1.210E-02	3.885E-05	4.397E-02	5.888E-04
60	7	9.55	1.225E-02	3.976E-05	4.443E-02	6.011E-04
60	7	9.6	1.253E-02	4.162E-05	4.549E-02	6.304E-04
60	7	9.65	1.253E-02	4.162E-05	4.549E-02	6.304E-04
60	7	9.7	1.253E-02	4.162E-05	4.549E-02	6.304E-04
60	7	9.75	1.328E-02	4.676E-05	4.823E-02	7.094E-04
60	7	9.8	1.328E-02	4.676E-05	4.823E-02	7.094E-04
60	7	9.85	1.328E-02	4.676E-05	4.823E-02	7.094E-04
60	7	9.9	1.343E-02	4.782E-05	4.871E-02	7.238E-04
60	7	9.95	1.369E-02	4.976E-05	4.971E-02	7.541E-04
60	7	10	1.397E-02	5.182E-05	5.076E-02	7.865E-04

## BIBLIOGRAPHY

- [1] J. MacSleyne, M.D. Uchic, J.P. Simmons, and M. De Graef. Three-dimensional analysis of secondary precipitates in René-88 {DT} and UMF-20 superalloys. *Acta Materialia*, 57(20):6251 – 6267, 2009.
- [2] L. Wojnar, K.J. Kurzydowski, and J. Szala. *ASM Handbook*, volume 9. ASM International, 2004.
- [3] G.B. Olson. Computation Design of Hierarchically Structured Materials. *Science*, 277(1237):1237–1242, 1997.
- [4] J.P. MacSleyne, J.P. Simmons, and M. De Graef. On the use of 2-D moment invariants for the automated classification of particle shapes moment invariants for the automated classification of particle shapes. *Acta Materialia*, 56(3):427 – 437, 2008.
- [5] J P MacSleyne, J P Simmons, and M De Graef. On the use of moment invariants for the automated analysis of 3D particle shapes. *Modelling and Simulation in Materials Science and Engineering*, 16(4):045008, 2008.
- [6] S. Ghosh and D. Dimiduk. *Computational Methods for Microstructure-Property Relationships*. Springer, 2010.
- [7] A. Maheshwari and A.J. Ardell. Morphological Evolution of Coherent Misfitting Precipitates in Anisotropic Elastic Media. *Phys. Rev. Lett.*, 70(15):2305–2309, April 1993.
- [8] N. Zhou, C. Shen, M. Mills, and Y. Wang. Large-scale three-dimensional phase field simulation of  $\gamma$ -rafting and creep deformation. *Philosophical Magazine*, 90(1-4):405–436, 2010.
- [9] S.V. Prikhodko and A.J. Ardell. Coarsening of  $\gamma'$  in Ni-Al alloys aged under uniaxial compression: III. Characterization of the morphology. *Acta Materialia*, pages 5021–5036, 2003.
- [10] J. Flusser, T. Suk, and B. Zitova. *Moments and Moment Invariants in Pattern Recognition*. John Wiley and Sons Ltd., 2009.
- [11] R.A. Lebensohn. N-site modeling of a 3D viscoplastic polycrystal using fast Fourier transform. *Acta Materialia*, 49:2723–2737, 2001.
- [12] White House. Materials Genome Initiative. <http://www.whitehouse.gov/mgi>.

- [13] J.P. MacSleyne. *Moment Invariants for 2-D and 3-D Characterization of the Morphology of Gamma-Prime Precipitates in Ni-base Superalloys*. PhD thesis, Carnegie Mellon University, November 2008.
- [14] P.G. Callahan. *Quantitative characterization and comparison of precipitate and grain shape in Ni-base superalloys using moment invariants*. PhD thesis, Carnegie Mellon University, August 2012.
- [15] P.G. Callahan and M. De Graef. Precipitate shape fitting and reconstruction by means of 3D Zernike functions. *Modeling and Simulation in Materials Science and Engineering*, 20(1):015003, 2012.
- [16] P G Callahan, J P Simmons, and M De Graef. A quantitative description of the morphological aspects of materials structures suitable for quantitative comparisons of 3D microstructures. *Modelling and Simulation in Materials Science and Engineering*, 21(1):015003, 2013.
- [17] D. Kammer and P.W. Voorhees. The morphological evolution of dendritic microstructures during coarsening. *Acta Materialia*, 54:1549–1558, 2006.
- [18] K. Geels. *Metallographic and Materialographic Specimen Preparation, Light Microscopy, Image Analysis and Hardness Metallographic and Materialographic Specimen Preparation, Light Microscopy, Image Analysis and Hardness Testing*. ASTM International, West Conshohocken, PA, 2007.
- [19] J. Alkemper and P.W. Voorhees. Quantitative serial sectioning analysis. *Journal of Microscopy*, 201(3):388–394, March 2001.
- [20] R.T. DeHoff. Quantitative serial sectioning analysis: preview. *Journal of Microscopy*, 131(3):259–263, 1983.
- [21] W.D. Callister and D.G. Rethwisch. *Materials Science and Engineering: An Introduction*. Wiley, 2013.
- [22] O. Forsman. Undersoknin av rymdstrukturen hos ett kolsta av hypereutectoid sammansattning. *Jern-Kontorets Ann*, 102:1–30, 1918.
- [23] E.A. Holm and P.M. Duxbury. Three-dimensional materials science. *Scripta Materialia*, 54:1035–1040, 2006.
- [24] AC Lewis and D. Howe. The first international conference on 3d materials science. *The Journal of The Minerals, Metals & Materials Society*, 65(2), 2013.
- [25] M.A. Groeber, B.K. Haley, M.D. Uchic, D.M. Dimiduk, and S. Ghosh. 3D reconstruction and characterization of polycrystalline microstructures using a FIB–SEM system. *Materials Characterization*, 57(4–5):259 – 273, 2006.
- [26] M.A. Groeber, S. Ghosh, M.D. Uchic, and D.M. Dimiduk. A framework for automated analysis and simulation of 3D polycrystalline microstructures. Part1: Statistical characterization. *Acta Materialia*, 56:1257–1273, 2008.
- [27] M.D. Uchic, M.A. Groeber, D. Dimiduk, and J.P. Simmons. 3D microstructural characterization of nickel superalloys via serial-sectioning using a dual beam FIB–SEM. *Scripta Materialia*, 55:23–28, 2006.

- [28] M. Echlin, A. Mottura, C.J. Torbet, and T.M. Pollock. A new TriBeam system for three-dimensional multimodal materials analysis. *Review of Scientific Instruments*, 83(023701), 2012.
- [29] Wikipedia. Henry Clifton Sorby. [http://en.wikipedia.org/wiki/Henry\\_Clifton\\_Sorby](http://en.wikipedia.org/wiki/Henry_Clifton_Sorby), 2014.
- [30] D. Juul Jensen, E.M. Lauridsen, L. Margulies, H.F. Poulsen, S. Schmidt, H.O. Sørensen, and G.B.M. Vaughan. X-ray microscopy in four dimensions. *Materials Today*, 9(1–2):18 – 25, 2006.
- [31] U. Lienert, J. Almer, B. Jakobsen, W. Pantleon, H.F. Poulsen, D. Hennessy, C. Xiao, and R.M. Suter. 3-dimensional characterization of polycrystalline bulk materials using high-energy synchrotron radiation. *Materials Science Forum*, 2353-2358:539–543, 2007.
- [32] U Lienert, SF Li, CM Hefferan, J Lind, RM Suter, JV Bernier, NR Barton, MC Brandes, MJ Mills, MP Miller, et al. High-energy diffraction microscopy at the advanced photon source. *JOM*, 63(7):70–77, 2011.
- [33] MA Groeber and A Jackson. DREAM. 3D: A digital representation environment for the analysis of microstructure in 3D. *Integrating Materials and Manufacturing Innovation*, 3(1):5, 2014.
- [34] A. Rollett. Overview of Microstructures in 3D. CMU Summer School for 3D Microstructural Studies, July 2012.
- [35] E.E. Underwood. *Quantitative Stereology for Microstructural Analysis*. Springer, 1973.
- [36] A.D. Rollett. Stereology. <http://neon.materials.cmu.edu/rollett/27750/L19-Stereology-21Apr14.pdf>, April 2014.
- [37] G. Krauss. Martensite in steel: strength and structure. *Materials Science and Engineering: A*, A273-275:40–57, 1999.
- [38] J.S. Van Sluytman and T.M. Pollock. Optimal precipitate shapes in nickel-base  $\gamma - \gamma'$  alloys. *Acta Materialia*, 60(4):1771 – 1783, 2012.
- [39] J. Flusser. Moment Invariants in Image Analysis. *World Academy of Science, Engineering and Technology*, 11, 2005.
- [40] D. Hilbert. *Theory of Algebraic Invariants*. Cambridge University Press, 1993.
- [41] M.K. Hu. Visual pattern recognition by moment invariants. *IEEE Transactions on Information Theory*, 8:179–187, 1962.
- [42] J. Flusser. On the independence of rotation moment invariants. *Pattern Recognition*, 33:1405–1410, 2000.
- [43] J. Flusser and T. Suk. Rotation moment invariants for recognition of symmetric objects. *IEEE Trans. Image Processing*, 15(12):3384–3790, December 2006.

- [44] J. Flusser and T. Suk. Affine moment invariants: A new tool for character recognition. *Pattern Recognition Letters*, 15:433–436, 1994.
- [45] J. Flusser and T. Suk. Degraded image analysis: An invariant approach. *IEEE Trans. Pattern Analysis and Machine Intelligence*, 20(6):590–603, 1998.
- [46] M. Novotni and R. Klein. Shape Retrieval using 3D Zernike Descriptors. *Computer Aided Design*, 36(1047-1062), 2004.
- [47] S. Ghosh, Z. Nowak, and K. Lee. Quantitative characterization and modeling of composite microstructure by voronoi cells. *Acta Materialia*, 45(6):2215–2234, 1997.
- [48] A.G. Mamistvalov. n-Dimensional moment invariants and conceptual mathematical theory of recognition n-dimensional solids. *IEEE Transactions on Pattern Analysis and Machine Intelligence*, 20(8):819–831, August 1998.
- [49] F. Sadjadi and E. Hall. Three-Dimensional Moment Invariants. *IEEE Transactions on Pattern Analysis and Machine Intelligence*, 2:127–136, March 1980.
- [50] C. Aviles-Cruz, J. Villegas-Cortez, J. Ocampo-Hidalgo, and R. Arechiga-Martinez. Principal components and invariants moments analysis - font recognition applied. *WSEAS Transactions on Computers*, 5:1041–1046, 2006.
- [51] H. Hadwiger. Konkave eikorperfunktionale und hoehere tragheitsmomente. *Comment. Math. Helv.*, 39:285–296, 1955.
- [52] I. Icke. Content Based 3D Shape Retrieval, A Survey of State of the Art. <http://www.cs.gc.cuny.edu/iicke>.
- [53] S. Torquato. *Random Heterogeneous Materials*. Springer, 2002.
- [54] A.A. Salem, J.B. Shaffer, D.P. Satko, S.L. Semiatin, and S.R. Kalidindi. Workflow for integrating mesoscale heterogeneities in materials structure with process simulation of titanium alloys. *Integrating Materials and Manufacturing Innovation*, 3(24), 2014.
- [55] S.R. Niezgoda, Y.C. Yabansu, and S.R. Kalidindi. Understanding and visualizing microstructure and microstructure variance as a stochastic process. *Acta Materialia*, 59:6387–6400, 2011.
- [56] D.T. Fullwood, S.R. Niezgoda, and S.R. Kalidindi. Microstructure reconstructions from 2-point statistics using phase-recovery algorithms. *Acta Materialia*, 56:942–948, 2008.
- [57] M.A. Groeber and M.A. Jackson. DREAM.3D: A Digital Representation Environment for the Analysis of Microstructure in 3D. *Integrating Materials and Manufacturing Innovation*, 3(5), 2014.
- [58] A.L.C. Barczak, M.J. Johnson, and C.H. Messom. Revisiting Moment Invariants: Rapid Feature Extraction and Classification for Handwritten Digits. In *Proceedings of Image and Vision Computing New Zealand*, pages 137–142, Dec 2007.
- [59] S.O. Belkasim, M. Shridhar, and M. Ahmadi. Pattern recognition with moment invariants: a comparative study and new results. *Pattern Recognition*, 24(12):1117–1138, 1991.

- [60] S.A. Dudani, K.J. Breeding, and R.B. McGhee. Aircraft identification by moment invariants. *IEEE Transactions Computers*, 26:33–45, 1977.
- [61] L. Wang and G. Healey. Using Zernike moments for the illumination and geometry invariant classification of multispectral texture. *IEEE Trans. Image Processing*, 16:196–203, 1998.
- [62] L. Guo, M. Dai, and M. Zhu. Quaternion moment and its invariants for color object classification. *Information Sciences*, pages 132–143, 2014.
- [63] L. van Gool, T. Moons, and D. Ungureanu. Affine/photometric invariants for planar intensity patterns. In *Proc. 4th ECCV'96*, volume LNCS 1064, pages 642–651. Springer, 1996.
- [64] F. Mindru, T. Moons, and L. van Gool. Recognizing color patterns irrespective of viewpoint and illumination. In *Proc. IEEE Conf. Computer Vision Pattern Recognition CVPR'99*, volume 1, pages 368–373, 1999.
- [65] J. Flusser and T. Suk. Recognition of blurred images by method of moments. *IEEE Trans. Image Processing*, 5:533–538, 1996.
- [66] Y. Zhang, C. Wen, and Y. Zhang. Estimation of motion parameters from blurred images. *Pattern Recognition Letters*, 21:425–433, 2000.
- [67] J. Lu and Y. Yoshida. Blurred image recognition based on phase invariants. *IEICE Trans. Fundamentals of Il. Comm. and and Comp. Sci.*, E82A:1450–1455, 1999.
- [68] J. Flusser, B. Zitova, and T. Suk. Invariant-based registration of rotated and blurred images. In *EEE 1999 International Geoscience and Remote Sensing Symposium. Proceedings*, pages 1262–1264. IEEE Computer Society, 1999.
- [69] G. Kindlmann, D.B. Ennis, R.T. Whitaker, and C-F. Westin. Diffusion Tensor Analysis With Invariant Gradients and Rotation Tangents. *IEEE Transactions on Medical Imaging*, 26(11):1483–1499, 2007.
- [70] D.B. Ennis and G. Kindlmann. Orthogonal Tensor Invariants and the Analysis of Diffusion Tensor Magnetic Resonance Images. *Magnetic Resonance in Medicine*, 55:136–146, 2006.
- [71] T.H. Reiss. The revised fundamental theorem of moment invariants. *IEEE Trans. Pattern Analysis and Machine Intelligence*, 13(8):830–834, August 1991.
- [72] L. Wojnar. *Image Analysis, Applications in Materials Engineering*. CRC Press, 1999.
- [73] M. Fahrman, P. Fratzl, O. Paris, E. Fahrman, and W.C. Johnson. Influence of Coherency Stress on Microstructural Evolution in Model Ni-Al-Mo Alloys. *Acta Metallurgicalica Materialia*, 43(3):1007–1022, 1995.
- [74] G. Polya and G. Szego. *Isoperimetric Inequalities in Mathematical Physics*. Princeton University Press, 1951.
- [75] J. Ohser and F. Mucklich. *Statistical Analysis of Microstructures in Materials Science*. John Wiley, 2000.

- [76] A. Gray, E. Abbena, and S. Salamon. *Modern Differential Geometry of Curves and Surfaces with Mathematica*. Chapman and Hall CRC, 2006.
- [77] R. Mendoza, I. Savin, K. Thornton, and P.W. Voorhees. Topological complexity and the dynamics of coarsening. *Nature Materials*, 3:385–388, June 2004.
- [78] F.C. Campbell. *Elements of Metallurgy and Engineering Alloys*. ASM International, Materials Park, Ohio, 2008.
- [79] R.O. Duda, P.E. Hart, and D.G. Stork. *Pattern Classification*. Wiley, 2001.
- [80] E. Deza and M.M. Deza. *Dictionary of Distances*. Elsevier, 2006.
- [81] S. Cha. Comprehensive Survey on Distance/Similarity Measures between Probability Density Functions. *International Journal of Mathematical Models and Methods in Applied Sciences*, 1(4):300–307, 2007.
- [82] A. Basu, H. Shioya, and C. Park. *Statistical Inference: The Minimum Distance Approach*. Chapman and Hall, 2011.
- [83] A. Bhattacharyya. On a measure of divergence between two statistical populations defined by their probability distribution. *Bulletin of the Calcutta Mathematical Society*, 35:99–110, 1943.
- [84] E. Choi and C. Lee. Feature extraction based on the Bhattacharyya distance. *Pattern Recognition*, 36:1703–1709, 2003.
- [85] D. Comaniciu, V. Ramesh, and P. Meer. Kernel-based object tracking. *IEEE Trans. Pattern Analysis and Machine Intelligence*, 25:564–577, 2003.
- [86] N. Saito, R.R. Coifman, F.B. Geshwind, and F. Warner. Discriminant feature extraction using empirical probability density estimation and a local basis library. *Pattern Recognition*, 35(12):2841–2852, 2002.
- [87] H. Zhao, A. Robles-Kelly, and J. Zhou, editors. *On the Use of the Chi-Squared Distance for the Structured Learning of Graph Embeddings*. International Conference on Digital Image Computing: Techniques and Applications, 2011.
- [88] O. Pele and M. Werman. The Quadratic-Chi Histogram Distance Family. In K. Daniilidis, P. Maragos, and N. Paragios, editors, *Computer Vision - ECCV 2010*, volume 6312 of *Lecture Notes in Computer Science*, pages 749–762. Springer Berlin Heidelberg, 2010.
- [89] S. Patil and S. Talbar. Content Based Image Retrieval Using Various Distance Metrics. *ICDEM*, 6411:154–161, 2010.
- [90] JK Tien and SM Copley. The effect of uniaxial stress on the periodic morphology of coherent gamma prime precipitates in nickel-base superalloy crystals the effect of uniaxial stress on the periodic morphology of coherent gamma prime precipitates in nickel-base superalloy crystals. *Metallurgical Transactions*, 2(1):215–219, 1971.
- [91] T.M. Pollock and A.S. Argon. Creep resistance of CMSX-3 nickel base superalloy single crystals. *Acta Metallurgica et Materialia*, 40(1):1–30, 1992.

- [92] T.M. Pollock and A.S. Argon. Directional coarsening in nickel-base single crystals with high volume fractions of coherent precipitates. *Acta Metallurgicalica et Materialia*, 42(6):1859–1874, 1994.
- [93] A. Pineau. Influence of uniaxial stress on the morphology of coherent precipitates during coarsening—elastic energy considerations. *Acta Metallurgicalica*, 24(6):483–592, 1976.
- [94] M. Kamaraj. Rafting in single crystal nickel-base superalloys — An overview. *Sadhana*, 28(1-2):115–128, 2003.
- [95] R.C. Reed. *The superalloys: fundamentals and applications*. Cambridge University Press, 2006.
- [96] M. Fahrman, W. Hermann, E. Fahrman, A. Boegli, T.M. Pollock, and H.G. Sockel. Determination of matrix and precipitate elastic constants in  $(\gamma - \gamma')$  Ni-base model alloys, and their relevance to rafting. *Materials Science and Engineering: A*, 260(1–2):212 – 221, 1999.
- [97] L.G. Carroll, Q. Feng, J.F. Manfield, and T.M. Pollock. High Refractory, Low Misfit Ru-Containing Single-Crystal Superalloys. *Metallurgical and Materials Transactions A*, 37:2927–2938, 2006.
- [98] A. Fredholm and J.L. Strudel. *Superalloys 1984*. AIME, Warrendale, PA, 1984.
- [99] J.Z. Zhu, Z.K. Liu, V. Vaithyanathan, and L.Q. Chen. Linking phase-field model to CALPHAD: application to precipitate shape evolution in Ni-base alloys. *Scripta Materialia*, 46(401), 2002.
- [100] Q. Chen, N. Ma, K. Wu, and Y. Wang. Quantitative phase field modeling of diffusion-controlled precipitate growth and dissolution in Ti–Al–V. *Scripta Materialia*, 50(4):471–476, 2004.
- [101] C.A. Schneider, W.S. Rasband, and K.W. Eliceiri. NIH Image to ImageJ: 25 years of image analysis. *Nature Methods*, pages 671–675, 2012.
- [102] M. Koiwa, K. Otsuka, and T. Miyazaki, editors. *Morphological Evolution of  $\gamma'$  Particles in Ni-Base Alloys: Shape Characterization*, number 3. Proceedings of the International Conference on Solid-Solid Phase Transformations, The Japanese Institute of Metals, 1999.
- [103] S.V. Prikhodko and A.J. Ardell. Coarsening of  $\gamma'$  in Ni–Al alloys aged under uniaxial compression: I. Early-stage kinetics. *Acta Materialia*, 51:5001–5012, 2003.
- [104] K. Otsuka and C.M. Wayman. *Shape memory materials*. Cambridge University Press, New York, 1998.
- [105] K. Otsuka and X. Ren. Physical metallurgy of ti–ni-based shape memory alloys. *Progress in Materials Science*, 50(5):511 – 678, 2005.
- [106] Shampa Sarkar, Xiaobing Ren, and Kazuhiro Otsuka. Evidence for Strain Glass in the Ferroelastic-Martensitic System  $\text{ti}_{50-x}\text{ni}_{50+x}$ . *Phys. Rev. Lett.*, 95:205702, Nov 2005.

- [107] D. Wang, Z. Zhang, J. Zhang, Y. Zhou, Y. Wang, X. Ding, Y. Wang, and X. Ren. Strain glass in Fe-doped Ti–Ni. *Acta Materialia*, 58(18):6206 – 6215, 2010.
- [108] P. Lloveras, T. Castán, M. Porta, A. Planes, and A. Saxena. Influence of Elastic Anisotropy on Structural Nanoscale Textures. *Phys. Rev. Lett.*, 10:165707, 2008.
- [109] R. Vasseur and T. Lookman. Effects of disorder in ferroelastics: A spin model for strain glass. *Phys. Rev. B*, 81:094107, 2010.
- [110] D. Wang, Y. Wang, Z. Zhang, and X. Ren. Modeling Abnormal Strain States in Ferroelastic Systems: The Role of Point Defects. *Phys. Rev. Lett.*, 105:205702, Nov 2010.
- [111] X. Ren, Y. Wang, and Y. Zhou. Strain glass in ferroelastic systems: Premartensitic tweed versus strain glass. *Philosophical Magazine*, 90(1-4):141–157, 2010.
- [112] D. Wang, S. Hou, Y. Wang, X. Ding, S. Ren, X. Ren, and Y. Wang. Superelasticity of slim hysteresis over a wide temperature range by nanodomains of martensite. *Acta Materialia*, 66:349–359, 2014.
- [113] D. Wang, Y. Ni, J. Gao, Z. Zhang, X. Ren, and Y. Wang. Unique properties associated with normal martensitic transition and strain glass transition - A simulation study. *Journal of Alloys and Compounds*, 577S:S102–S106, 2013.
- [114] Y. Wang, X. Ren, K. Otsuka, and A. Saxena. Evidence for broken ergodicity in strain glass. *Phys. Rev. B*, 76:132201, Oct 2007.
- [115] Y. Zhou, D. Xue, X. Ding, K. Otsuka, J. Sun, and X. Ren. High temperature strain glass in  $\text{Ti}_{50}(\text{Pd}_{50-x}\text{Cr}_x)$  alloy and shape memory effect and superelasticity. *Applied Physics Letters*, 95:151906, 2009.
- [116] Z. Zhang, Y. Wang, D. Wang, Y. Zhou, K. Otsuka, and X. Ren. Phase diagram of  $\text{ti}_{50-x}\text{ni}_{50+x}$ : Crossover from martensite to strain glass. *Phys. Rev. B*, 81(22):224102, June 2010.
- [117] S. Semenovskaya and A.G. Khachaturyan. Coherent structural transformations in random crystalline systems. *Acta Materialia*, 45:4367–4384, 1997.
- [118] A.P. Levaniuk and A.S. Sigov. *Defects and structural phase transitions*. Gordon and Breach Science Publishers, New York, 1988.
- [119] G. Eggeler, J. Khalil-Aflafi, S. Gollerthan, C. Somsen, W. Schmahl, and D. Sheptyakov. On the effect of aging on martensitic transformations in Ni-rich NiTi shape memory alloys. *Smart Mater. Struct.*, 14:S186–S191, 2005.
- [120] A.G. Khachaturyan. *Theory of Structural Transformations in Solids*. John Wiley and Sons Ltd., 1983.
- [121] R. Szeliski. *Computer Vision: Algorithms and Applications*. Springer, 2010.
- [122] T.M. Cover and J.A. Thomas. *Elements of Information Theory*. Wiley Interscience, New York, 1991.

- [123] E.B. Gulsoy, J.P. Simmons, and M. De Graef. Application of joint histogram and mutual information to registration and data fusion problems in serial sectioning microstructure studies. *Scripta Materialia*, 60:381–384, 2009.
- [124] M. Baurer, D. Weygand, P. Gumbsch, and M.J. Hoffmann. Grain growth anomaly in strontium titanate. *Scripta Materialia*, 61:584–587, 2009.
- [125] T. Sano. *Interface Anisotropy and its Effect on Microstructural Evolution During Coarsening*. PhD thesis, Carnegie Mellon University, 2005.
- [126] T. Sano, D. Saylor, and G.S. Rohrer. Surface Energy Anisotropy of  $\text{SrTiO}_3$  at 1400 C in Air. *Journal of the American Ceramic Society*, 86(1933-1939):11, November 2003.
- [127] M. Syha, W. Rheinheimer, M. Bäurer, E.M. Lauridsen, W. Ludwig, D. Weygand, and P. Gumbsch. Three-dimensional grain structure of sintered bulk strontium titanate from x-ray diffraction contrast tomography. *Scripta Materialia*, 66(1):1 – 4, 2012.
- [128] W. Rheinheimer. *Zur Grenzflächenanisotropie von  $\text{SrTiO}_3$* . Universitätsverlag Karlsruhe, 2013.
- [129] M. Syha, M. Baurer, M.J. Hoffmann, E.M. Lauridsen, W. Ludwig, D. Weygand, and P. Gumbsch, editors. *Comparing grain growth experiments and simulations in 3D*, Denmark, 2010. 31st Riso International Symposium on Materials Science.
- [130] M. Syha. *Microstructure evolution in strontium titanate investigated by means of grain growth simulations and x-ray diffraction contrast tomography experiments*. PhD thesis, Karlsruhe Institute of Technology, Karlsruhe, Germany, April 2014.
- [131] M. Baurer, M. Syha, and D. Weygand. Combined experimental and numerical study on the effective grain growth dynamics in highly anisotropic systems: Application to barium titanate. *Acta Materialia*, 61:5664–5673, 2013.
- [132] M. Syha, A. Trenkle, B. Lodermann, A. Graff, W. Ludwig, D. Weygand, and P. Gumbsch. Validation of three-dimensional diffraction contrast tomography reconstructions by means of electron backscatter diffraction characterization. *Journal of Applied Crystallography*, 46:1145–1150, 2013.
- [133] Committee on Integrated Computational Materials Engineering. *Integrated Computational Materials Engineering: A Transformational Discipline for Improved Competitiveness and National Security*. The National Academies Press, 2008.